Università degli Studi di Padova

Dipartimento di Fisica e Astronomia G. Galilei

Dottorato di Ricerca in Astronomia Ciclo XXXI

ANALYSIS OF IMAGES OF COMET 67P/CHURYUMOV-GERASIMENKO OBTAINED BY OSIRIS/ROSETTA: DUST PARTICLES INVESTIGATION

Coordinatore: Prof. Giampaolo Piotto
Supervisore: Dott. Gabriele Cremonese
Co-Supervisori: Dott. Ivano Bertini
Dott.ssa Monica Lazzarin

Valutatori: Dott. Marco Fulle
Dott. Pedro J. Gutiérrez

Dottoranda: Elisa Frattin

Riassunto

Lo scopo di questa tesi consiste nello studio e nella caratterizzazione della polvere nella chioma della cometa 67P/Churyumov-Gerasimenko al fine di arricchire ed approfondire la nostra conoscenza sulla natura e il comportamento delle comete.
Esse infatti sono tra i corpi più antichi del nostro sistema solare e la loro analisi consente di comprendere le condizioni fisiche e chimiche che hanno avuto luogo nell'ambiente in cui si sono formate. La polvere, a sua volta, è un costituente fondamentale delle comete e fornisce informazioni sulla loro composizione, struttura ed evoluzione.
L'importanza dello studio della polvere consiste nella possibilità di essere usata come tracciante per derivare le proprietà dell'interno del nucleo cometario. Infatti, quando la cometa si avvicina al Sole e diventa attiva rilascia sia materiale superficiale che materiale primitivo dall'interno del nucleo, che non potrebbe essere raggiunto altrimenti.
La missione dell'ESA Rosetta, con obiettivo la cometa 67P/Churyumov-Gerasimenko, ha fornito una prospettiva completamente nuova sulla polvere cometaria, regalando informazioni dettagliate sulla sua composizione, dimensione e struttura. Per la prima volta è stato possibile acquisire immagini di singoli aggregati di polvere e fornire una descrizione completa delle loro proprietà, grazie alle informazioni ottenute dagli strumenti a bordo del veicolo.
L'insieme dei processi che agiscono sulle comete non sono stati ancora compresi appieno e rimangono molte questioni aperte che richiedono indagini accurate. È quindi essenziale continuare a studiare questi oggetti primitivi al fine di svelare la loro vera natura.

Il primo lavoro di questa tesi riguarda l'analisi fotometrica di immagini di grani di polvere, acquisite dalla Narrow Angle Camera (NAC) dello strumento OSIRIS. L'ingente mole di dati ha richiesto lo sviluppo di una routine automatica in grado di identificare e analizzare le tracce di grani presenti nelle immagini fornendo alcuni parametri fotometrici e geometrici distintivi.
Abbiamo misurato la pendenza spettrale di circa 2000 grani in 555 immagini appartenenti a 18 giorni di osservazione a partire da luglio 2015 fino a gennaio 2016. Abbiamo quindi valutato la variazione delle pendenze spettrali rispetto alle distanze eliocentriche e nucleocentriche.

Per caratterizzare al meglio la composizione dei grani abbiamo eseguito anche un'analisi spettrofotometrica di un sottogruppo di 339 grani. Gli spettri a tre punti così ottenuti sono stati poi confrontati con quelli di diversi terreni del nucleo identificando tre diversi tipi di spettri.

Il secondo lavoro di questa tesi tratta le proprietà ottiche di alcuni analoghi di polvere cometaria. Questo progetto è stato realizzato in collaborazione con l'Instituto de Astrofísica de Andalusía di Granada presso il Laboratorio di Polvere Cosmica.
Gli esperimenti di laboratorio sono di fondamentale importanza per l'interpretazione dei dati poiché consentono di studiare fenomeni complessi in condizioni controllate permettendo di valutare gli effetti dovuti a specifiche proprietà fisiche e chimiche della polvere. Abbiamo misurato sperimentalmente la funzione di fase e la curva di polarizzazione lineare di 7 campioni: 4 meteoriti, 2 silicati e 1 composto organico, con lo scopo di confrontare i nostri risultati con i dati osservativi riguardanti la 67P ed altre comete.

Il nostro ultimo lavoro è ancora in corso e consiste nell'analisi del moto della polvere cometaria con lo scopo di fornire vincoli osservativi ai modelli dinamici che descrivono la polvere nella chioma.
Abbiamo focalizzato la nostra indagine su 15 gruppi di immagini fornite dallo strumento NAC/OSIRIS a partire da luglio 2015 fino a gennaio 2016. Abbiamo misurato i periodi di rotazione, la deviazione dalla forma sferica e infine la direzione del moto di un campione costituito da oltre 500 grani.

La tesi è strutturata come segue:
Nel Capitolo 1 presentiamo una panoramica delle principali caratteristiche delle comete.
Nel Capitolo 2 illustriamo la storia e gli strumenti della missione Rosetta, insieme alle principali scoperte riguardanti la cometa 67P/Churyumov-Gerasimenko.
Nel Capitolo 3 introduciamo alcuni concetti fisici di base sulla teoria dello scattering.
Nel Capitolo 4 presentiamo la fotometria e la spettrofotometria elaborata su singoli grani di polvere, suggerendo delle possibili composizioni.
Nel Capitolo 5 discutiamo i risultati degli esperimenti di laboratorio svolti sulle proprietà di dispersione di alcuni analoghi della polvere cometaria. Ci concentriamo sulla loro funzione di fase e sulla curva di polarizzazione introducendo un confronto con le osservazioni della cometa 67P/Churyumov-Gerasimenko e altre comete.
Nel Capitolo 6 descriviamo alcuni risultati osservativi riguardanti il comportamento dinamico della polvere nella chioma allo scopo di fornire dei vincoli per i modelli dinamici.
Nel capitolo 7 traiamo le conclusioni generali di questo lavoro di tesi.

Abstract

The aim of this thesis is to study and characterize the dust in the coma of the comet 67P/Churyumov-Gerasimenko in order to increase our knowledge about the nature and behavior of comets.
These objects are the most pristine of our solar system and their investigation allows to understand the physical and chemical conditions that took place in the primordial environment where they formed. In turn, dust is a fundamental constituent of comets and provides valuable information on their composition, structure and evolution. The importance of the dust lies in the possibility to use it as a proxy to derive properties of the interior of the cometary nuclei. Indeed, the activity produced when the comet approaches the Sun releases both surface material and pristine matter from the inside of the nucleus that cannot be reached otherwise.
The ESA Rosetta mission to the comet 67P/Churyumov-Gerasimenko revealed a new insight of the cometary dust providing precious information about its composition, dimension, size distribution and structure. For the first time it was possible to acquire images of single dust aggregates and to give a comprehensive description of their properties, thanks to the information obtained by all the instrumentation on board the spacecraft.
The overall processes that act on the comets are not yet fully understood and there are still open questions that need to be clarified. It is therefore essential to continue to investigate this complex scenario to unveil the real nature of these primordial objects.

The first work of this thesis concerns the photometric analysis of images of dust grains, taken by the OSIRIS Narrow Angle Camera (NAC). The large amount of data forced us to develop an automatic pipeline to identify and to analyze the particle tracks present in the images. We measured the spectral slope of about 2000 grains in 555 images taken in 18 days of observation from July 2015 to January 2016. Then we evaluate their variability with respect to the distance from the nucleus and from the Sun.
To better characterize the grains composition we perform also a spectrophotometric analysis of a subgroup of 339 grains. To check their nature, we compared their three

point spectra with the ones of several nucleus terrains identifying different types of grains spectra.

The second work of this thesis treats the scattering properties of cometary dust analogs, in collaboration with the Instituto de Astrofísica de Andalusía, Granada at the Cosmic Dust Laboratory.
Laboratory experiments are of fundamental importance to interpret the data since they allow to study complex phenomena in a monitored environment, favoring the evaluation of the effects due to specific physical and chemical properties of the dust. We measure the phase function and the linear polarization curve of 7 samples, consisting on 4 meteorites, 2 silicates and 1 organic compound with the aim to compare our results with the observational data of 67P and other comets.

Our last work, which is still in progress, consists in the analysis of dust motion with the aim to provide observational constraints to the dynamical models of cometary dust in the inner coma as well as to the shape of the single grains. We focus our investigation on the 15 groups of images taken from July 2015 to January 2016 and we measure the rotational periods, the axis ratio and the direction of motion on a dataset of more than 500 grains.

In the following we give a summary of the thesis.
In Chapter 1 we present an overview of the main characteristics of the comets.
In Chapter 2 we illustrate the history and instrumentations of the Rosetta space mission, together with the main findings about its primary target, the comet 67P/Churyumov-Gerasimenko.
In Chapter 3 we introduce some physical concepts about the scattering theory.
In Chapter 4 we present the photometry and spectrophotometry of single dust grains in the coma, suggesting possible compositions.
In Chapter 5 we discuss the results of laboratory experiments about the scattering properties of some cometary dust analogs. We focus on their phase function and polarization curve introducing a comparison with 67P/Churyumov-Gerasimenko and comets observations.
In Chapter 6 we describe some observational results about the dynamical behavior of the dust in the coma with the aim to provide constraints for the dynamical models.
In Chapter 7 we give some conclusions of this thesis work.

Contents

List of Figures

List of Tables

Chapter 1

Introduction

In this chapter we present a brief review of the main properties of comets. For a comprehensive dissertation of the topic refer to the books of Huebner (1990), Festou et al. (2004), Swamy (2010b) and Rickman (2017).

Comets are thought to be the most pristine objects of our solar system. The investigation of these ancient bodies therefore expands our knowledge about the physical and chemical conditions underlying the primitive environment in which they formed. There are still a lot of information that lack to achieve a comprehensive understanding of the formation and evolution processes that took place in the primitive solar system, for instance the accretion mechanisms, the relation between the protoplanetary disk and the growing up planetesimals, the thermodynamical condition and so on. Indeed, the comets are promising objects to answer to these questions.

The evolution of the comets around the Sun slightly affects the inner part of the nucleus that remains intact and undergoes a low degree of thermal metamorphism and chemical alteration. When the comets approach the Sun, they start to show activity, unveiling the pristine material covered by the outward layers. The refractory and volatile materials ejected into the cometary coma are a fundamental target of the observations, exactly because they represent the most untouched material.

There are a lot of processes that act on the comet that need to be analyzed in order to correctly interpret the incoming information, as for example what rules the activity of the comet, how the relation between gas and dust in the coma develops, how the surface of the nucleus changes, what chemical reactions take place into the coma, what mineralogical composition the comets conceal.

Other reasons to investigate the comets lie in the possibility to consider these bodies as carriers of organic molecules and water on the Earth. The comets indeed contain a lot of water ice and also amino acids such as the glycine and other molecules progenitors of life that might be brought on our planet through impacts. These scenario gives an

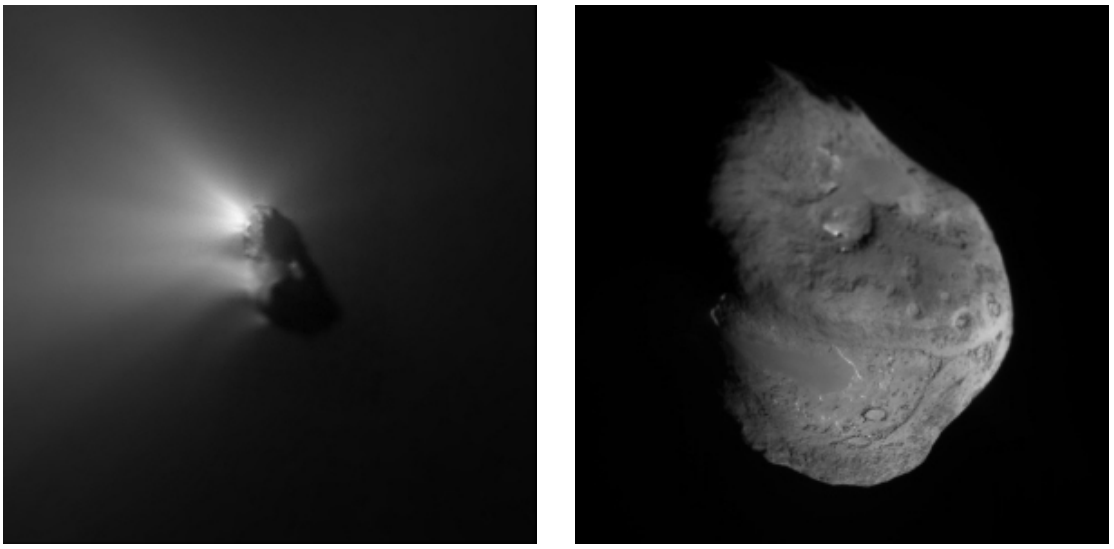

FIGURE 1.1: The nucleus of Comet Halley by ESA's Giotto in 1986, from a distance of about 2000 km (on the left). Credit: ESA/MPS. Comet Tempel-1, by NASA's Deep Impact in 2005. The nucleus is 7.6 x 5 km (on the right). Credit: NASA/JPL/UMD.

important role to these bodies in the development of the Earth as we know it.
Moreover, comets constitute a cosmic laboratory to study those processes that cannot be reproduced in the Earth environment, allowing the study for example of the interactions of the plasma tail with the solar wind and the optical properties of dust and surfaces.
Several space missions were developed during the last 30 years to unveil the nature of these fascinating bodies. A huge amount of data was provided by the in-situ measurements that allowed to define the main characteristics of the comets. However the data were limited in time and the differences among the objects made the development of an overall picture quite difficult. The ESA mission Rosetta was in this sense revolutionary since it followed the comet 67P Churyumov-Gerasimenko during 2 years, providing data that described the evolution of the comet around its perihelion passage.
The relation between the comets and the origin of the solar system is still an issue of current and deep interest. The future missions and instrumentation will be increasingly sophisticated and will lead a new generation of explorations and discoveries trying to answer to the still open questions about the most ancient (and fascinating) bodies of our solar system.

1.1 Comets

Comets are primitive bodies, composed by a solid *nucleus*, a transient atmosphere called *coma* and from different *tails*, extended for $10^6 - 10^8$ km. In the following we give a brief description of these features.

1.1.1 Classification

Comets are classified mainly according with their dynamical properties. They are divided into two main groups: the Long Period Comets (LPCs) and the Short Period Comets (SPCs). LPCs are *new* ($a > 10^4$ AU) but also *returning* comets ($a < 10^4$ AU) with periods $T > 200$ yr and quasi-parabolic or even hyperbolic orbits characterized by high eccentricity and inclination. Otherwise the SPCs are periodic with elliptic orbits, low inclinations and their aphelion can reach 40-70 AU. They are divided into two subgroups depending on their periods: the Halley-type Comets (HCs) with $T > 20$ yrs, and the Jupiter Family Comets (JFCs) with $T < 20$ yrs. LPCs likely come from the Oort cloud while SPCs origin from the Scattered disk (Nesvorný et al., 2017).
Nowadays the classification is based on a dynamical parameter called the Tisserand invariant which is a quantity approximately conserved after an encounter between a planet and a comet. Therefore it allows to recognize the same comets even if they have changed their orbital parameters due to perturbations. The most important perturber in the Solar System is Jupiter, therefore the Tisserand parameter is commonly computed with respect to Jupiter and is defined as follows by Levison (1996):

$$T_J = \frac{a_J}{a} + 2[(1-e^2)\frac{a}{a_J}]^{1/2}\cos i \tag{1.1}$$

where a_J is the Jupiter semimajor-axis, and a, e and i are the semimajor axis, the eccentricity and the inclination of the comet.
Comets with $T_J < 2$ are called *nearly-isotropic*, corresponding to the LPCs in the classical classification, which are in turn subdivided into *new* and *returning* comets. Otherwise, when the Tisserand parameter is $T_J > 2$ we have the so-called *ecliptic* comets subdivided into the Enke-type, with $T_J > 3$ and $a < a_J$, the Jupiter family with $2 < T < 3$ and the Chiron type with $T_J > 3$ and $a > a_J$ (Levison, 1996).

1.1.2 Nucleus

After the first in situ observations it was clear that comet nuclei were not spherical (Keller et al., 2004). On the contrary, they have irregular shapes and surface structures that characterize their morphology like craters, valleys, hills etc. As example of cometary nuclei in Figs. 1.1 and 1.2 we report comet Halley, Wild2, Hartley and 67P.
The first approach for the modelization of cometary nuclei analyses the energetic balance between absorbed and reflected energy from the nucleus (see Meech & Svoren (2004) and references therein). The energy depends in turn on the type of materials that compose the comet, on its albedo and on its structure. The absorbed energy is responsible for the nucleus temperature increase, depending on its thermal inertia, and consequently of

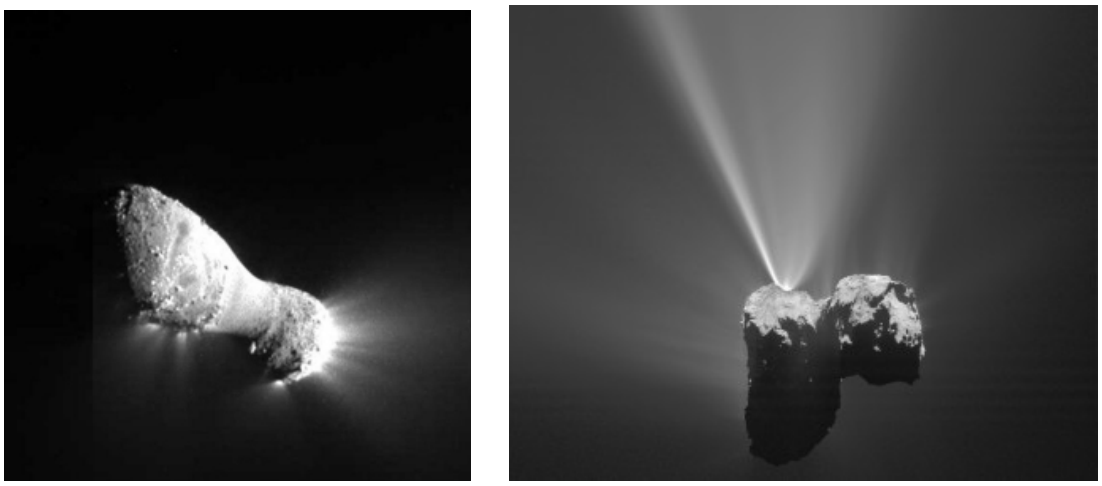

FIGURE 1.2: Comet Hartley-2 by NASA's EPOXI in 2010, from a distance of about 700 km. The nucleus is 2.2 km long (on the left). Credit: NASA/JPL-Caltech/UMD. Comet 67p/Churyumov-Gerasimenko by ESA's Rosetta mission, 2015. The nucleus is about 4 km (on the right). Credits: ESA/Rosetta/NAVCAM – CC BY-SA IGO 3.0.

gas sublimation. It is also responsible for the nucleus thermal emission itself.
The simplest model of energy balance considers a spherical nucleus and no energy exchange with the interior. It can be written as follows:

$$\frac{F_{\odot}(1-A_v)}{r^2}\cos z = (1-A_{IR})\sigma T^4 + Z(T)L(T) \tag{1.2}$$

where $F_{\odot}$ is the solar radiation at 1 AU, z is the solar zenith distance, A_v and A_{IR} are the albedo in visual and infrared, r is the heliocentric distance and T the temperature. The first term describes the incoming solar radiation, the second term is the thermal energy emitted, $Z(T)$ represents the vaporization rate of the gas in mol/cm^2 sec and $L(T)$ the latent heat of sublimation in erg/mol.
Actually the models need to take into account more physical processes to be realistic (Prialnik et al., 2004). Basically, there are three sources of energy to be considered: the solar radiation, the radioactivity (i.e. due to ^{26}Al decay) and the process of crystallization (i.e. of amorphous ice). The first who considered the ^{26}Al decay as source of energy in cometary nuclei were Whipple & Stefanik (1965), followed by Lee et al. (1976) who presented evidences of the presence of this isotope in the primordial nebula. Then, the studies of Irvine et al. (1980) showed that the internal heating due to the decay could melt the ices that compose the comet.
The phase transition from amorphous to crystalline ice is a spontaneous process which specific rate is continuous function of the temperature (Schmitt et al., 1989; Tancredi et al., 1994). The phase change releases latent heat, which contributes to the energy sources of the nucleus. Moreover, the heat release induces a more efficient crystallization which, in turn, releases more latent heat and also the volatiles that could be possibly

trapped in the ice. This runaway process has been recognized as a mechanism for explaining nuclei activity at high distance from the Sun (Patashnick, 1974; Weissman, 1991). Each of these sources dominates in a precise stage of cometary evolution: the solar radiation prevails of course when the comet is approaching the Sun, radioactive heating becomes important during the comet formation, even if it is not yet clear if it acted during all the growth phase (Davidsson et al., 2016). Eventually the crystallization process occurs whenever the comet reaches the threshold temperature (Prialnik et al., 2004).

Finally, the heat propagates into the nucleus depending on its physical characteristics, producing a layers differentiation. The refractory material lies on the top and the volatiles and ices lie more in the inner part. Also the nucleus structure plays an important role in energy transportation. Nowadays, the more accredited models consist on a porous aggregates made of dust, ices and volatiles (see Weissman & Lowry (2008) and reference therein), quite different from the dirty snowball mainly composed of ices, theorized by Whipple (1950). Therefore, a comprehensive model should take into account all these physical processes, starting from the energy sources, the heat propagation mechanism, the nucleus structure and also the thermo-chemical interaction with the coma. Only in this way the model might explain the overall comet activity.

Outbursts Those typical events consist on a quick increase of brightness (up to a factor 100), due to a sudden and fast production of volatiles, basically triggered by ice sublimation for solar irradiation. These phenomena occur for instance when a patch of ice sublimates or when a pit collapses and exposed fresh material or gases (Meech & Svoren, 2004; Prialnik et al., 2004).

Comets show evidences of activity also at high distance from the Sun, as 3-5 AU, thus beyond the *snow line* which is defined as the distance from the Sun where the temperature is such to allows the volatiles to condense into ices (Jewitt et al., 2007). The explanation of this phenomenon involves the ice crystallization process, as mentioned in the last paragraph. When the ices condensed from gaseous phase in conditions of very low temperature and pressure, they can occur in different metastable states. All these amorphous states tend to crystallize when the proper threshold temperature is reached, releasing latent heat (Jenniskens et al., 1998). When the conduction timescale of the material surpasses the crystallization timescale, the runaway process develops, producing the outburst (Patashnick, 1974; Weissman, 1991).

When the comet approaches the Sun, the heat propagates inward, to the colder layers, where it induces the crystallization with consequent release of the gas trapped inside the ice. Part of the gas is ejected, the other reaches the cooler outer regions where eventually condenses. The heat produced in this process further affects the chemical composition

of the surrounding material. The effect of heat and gas diffusion results in layers of different chemical structure (Prialnik, 1997). Following this mechanism, the successive perihelion passage will implicate the release of gas from the same layer in which the crystallization had already occurred. Eventually, each perihelion passage will produce alternate layers of amorphous and crystalline ices (Prialnik et al., 2004).
Due to the volatile sublimation and material ejection, the comets lose mass. From the mass loss rate computation it is possible to obtain an estimate of the comets lifetime. Given the typical value of revolution period of 5 yr, for the short period comets the value ranges between $5 \cdot 10^3 - 3 \cdot 10^4$ years.

1.1.3 Coma

Cometary coma is the transient atmosphere composed by dust, molecules, atomic species and ions that surrounds the nucleus and extends for $10^4 - 10^5$ km. It is divided into three main zones. The *inner coma*, where the mother molecules are directly produced from ice sublimation. The *visible zone* corresponds to the part of the coma in which the species generated, called daughter molecules, expand outward. Finally, the *atomic or UV coma* is the outer part of the coma in which the particles are destroyed for ionization and interaction with solar wind.
Among the many types of molecules production mechanisms, the main ones are the photodissociation, in which a compound is broken by a photon, generating new lighter species and the photoionization, in which a photon excites an electron that is ejected from the atom or molecule, thus generating an ion.
Many models have been developed during the years with the intent to describe the whole coma. If only the gas is considered it is possible to describe the inner coma as a collisional gas and therefore to apply the hydrodynamical equilibrium, while the outer coma as a collisionless gas. However, an extended zone of transition stays in between ($10^3 - 10^5$ km), which is difficult to describe (Combi et al., 2004). The Haser model (Haser, 1957) and the following Festou (Festou, 1981) generalized model allowed to determine several fundamental parameters as the radicals lifetime, the density distribution, the surface brightness as function of the distance from the nucleus:

$$I(\rho) = (g/4\pi)N(\rho) \tag{1.3}$$

where ρ is the distance from the nucleus projected in the plane of the sky, $N(\rho)$ the column density and g is the emission coefficient measured in erg/mol sec, and the production rate:

$$Q(r) = n(r)v4\pi r^2 \tag{1.4}$$

where $n(r)$ is the volume density of the particles, v is their velocity and r is the radius at which the production rate $Q(r)$ is computed in mol/sec.
However, a realistic and complete description of the coma is more complicated and it requires to consider also the dust component and its interaction with the gas. Hydrodynamic codes able to provide the velocity profile of gas and dust were implemented for example by Gombosi et al. (1985) but Direct Simulation Monte Carlo methods (DSMC) are among the more accurate methods to describe the complexity of the processes involved in cometary comae (Crifo et al., 2005).

1.1.4 Tails

The last typical feature of a comet is the tail. There are many kind of tails, the two main types are: the *dust tail* generated by the dust, yellowish in colour and extended for $10^6 - 10^7$ km, and the *plasma tail*, composed by ionized gas, bluish and extended for $10^7 - 10^8$ km.
The first one undergoes the effect of two forces: the gravitational force $F_G = GM_\odot m/r^2$ and the force generated by the solar radiation pressure:

$$F_{RAD} = (L_\odot/4\pi r^2 c)\pi a^2 Q \tag{1.5}$$

with $L_\odot$ the luminosity of the Sun at 1 AU, r the heliocentric distance, a the size of the dust particles and Q the dust production rate. The effect of radiation on the dynamics of dust particles is studied through the effective gravity parameter $\beta = F_{RAD}/F_G$ which does not depend on the distance form the nucleus and the Sun, but it still depends on the size of the particles. In the nucleus reference frame, there are two main trajectories the particles can sweep: the so-called *syndines* and the *synchrones*. The first one describes the place in which the particles share the same value of β, and it basically identifies the place in which the particles have the same size. In the second type of trajectory, the particles have different value of β but they have the same age, since they were ejected at the same time (i.e. during an emission event).
Otherwise, the plasma tail is generated by the interaction between solar wind and cometary plasma. It is interesting to notice that the solar wind existence was hypothesized by Biermann (1951) just because of observational evidences provided by the cometary tails. Indeed, the speed of some features on the tail of the comets he observed were too high (100 km/s) to be explained only as an effect of the radiation pressure. The acceleration at which the feature underwent was therefore produced by the interaction with solar wind and it was defined as:

$$\frac{dv}{dt} = \frac{e^2 N_e v_e m_e}{\sigma m_i} \tag{1.6}$$

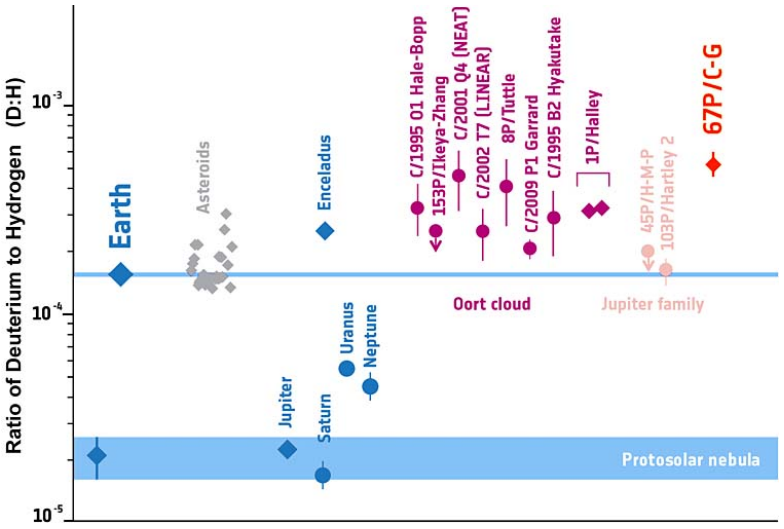

FIGURE 1.3: The different values of the deuterium-to-hydrogen ratio (D/H) in water observed in various bodies in the Solar System (Altwegg et al., 2015).

with N_e electron density, v_e electron velocity, σ conductivity, m_e mass of the electron and m_i mass of the ion.

In 1997 Cremonese et al. (1997) observed a tail in the sodium filter at $\lambda = 5890\mathring{A}$, in comet Hale-Bopp. This third type of tail, the *sodium tail*, is likely generated by the dissociation for solar radiation of molecules release from the nucleus or from the dust grains themselves.

In 2007 Fulle et al. (2007) provided evidence of the presence of a tail composed by neutral Fe atoms on the comet McNaught, demonstrating the existence of a forth type of tail, the *iron tail*.

Lastly, the so called *anti-tail* is a feature that seems to point toward the solar direction but that is actually generated by a specific geometrical configuration among Sun, Earth (observer) and comet.

1.1.5 Isotopic abundances

Isotopes can be used as a fingerprint to constrain the environment conditions in which Solar System objects have formed. They are difficult to detect and high resolution spectra are required since it is necessary to distinguish all the molecular bands to identify the small shift from the normal molecule line and the isotopic line. One of the most significant indicator is the D/H ratio. Almost all the deuterium formed only few seconds after the Big Bang, during the primordial nucleosynthesis and fixed the value of D/H in the H_2 at $25 \cdot 10^{-6}$. At the time of Solar System formation the H_2O produced in the interstellar medium was enriched in deuterium with respect to H_2, thanks to mechanisms that took place at low temperature < 50 K, reaching values of $10^{-2} - 10^{-3}$ (Hallis,

2017). When the D-rich water ice in the protoplanetary disk arrived to the inner part of the Solar System beyond the snow line, it equilibrated with the H_2 by means of isotopic exchange reactions, reducing drastically the level of deuterium in the medium. Therefore the D/H ratio is expected to increase with the distance from the Sun, preserving its primitive higher value in the colder region and low value in the hotter inner region. Giant gaseous planets have formed directly from the protosolar nebula, gathering a lot of H_2 with low value of D/H ratio, while the icy planets have a slightly higher value since they grew up by accretion of planetesimals with high fraction of deuterium (Robert, 2006).

As shown in Fig. 1.3 the typical value of D/H ratio is around $1-6\cdot10^{-4}$ for Oort comets and $1-2\cdot10^{-4}$ for JFCs, indicating that those objects have formed in the outer part of the Solar System and contain primitive water ice (Altwegg et al., 2015). The value of D/H ratio is quite relevant to constrain the origin of water in the Earth. From a direct comparison appears that the value of cometary D/H is higher than the value of terrestrial water D/H, except for some JFCs. These results do not exclude the possibility for the comet to be source of water on the Earth, but limit their contribution at most at the 10% (Robert, 2006).

1.1.6 Comets reservoir

The existence of a spherical cloud surrounding the Solar System, mainly composed by icy objects was proposed by the Dutch astronomer Jan Oort in 1950 as an attempt to explain the dynamical behaviors of the long period comets (Oort, 1950). Those with long orbital periods seamed in fact to come from all over the sky directions otherwise those with short orbital periods showed low inclinations. He saw that the majority of the 19 comets known at the time showed values of the parameter $1/a$ very close to zero. This implies that the objects had almost parabolic orbits, not yet perturbed by passages through the Solar System. These *new comets* would have came from a region at 3-5·10^4 AU from the Sun, very far from the inner system, suggesting the existence of the **Oort cloud** that extends from 10^4 to 10^5 AU.

The injection of these comets toward the inner part of the Solar System is a consequence of various perturbations as the passage of a distance star. Other important sources are the encounters with the Giant Molecular Cloud, each 3-4·10^8 yr and the galactic tides generated by the stars distribution in the Galaxy.

Comets are thus deviated toward the Sun, and they can undergo different destinies: they can be affected by a Jupiter encounter and then ejected from the system, they can maintain their trajectory or they can eventually become short period comets, after

numerous planets encounters. However, the number of observed SPCs are not explained by this mechanism, which produces only few of them (Swamy, 2010a). Therefore, there should have been another source of comets able to produce low inclination orbits. This source is the **Scattered Disk** (SD), which extends beyond 50 AU and is populated by objects with highly unstable orbits, scattered by Neptune during the instability phases of the Solar System formation. It is actually this region which is thought to be the source of SPCs and of Centaurus (Morbidelli & Brown, 2004; Nesvorný et al., 2017). The latter is a group of objects considered as dormant cometary nuclei since some of them have shown the presence of a coma and of activity. They lie between 5-30 AU and they have very short life time, due to the strong interaction with the outer planets of solar system. Examples of this group are Chiron, which was the first Centaurus discovered (Kowal et al., 1979) and Chariklo.

Also the **Kuiper belt** (KB), the inner part of the SD, that lies on the ecliptic plane beyond 30 AU, is a source of JPCs. This structure was hypothesized by Kuiper in 1951 and by Edgeworth already in 1949 and the existence of a comet belt beyond Neptune was proposed also by Fernandez (1980). The simulated comets production results more efficient considering the existence of the Kuiper belt. Moreover, the simulations are able to reproduce also the distribution of JFCs which in turn originate from the KB. The median life time of JFCs is $\tau = 4.5 \cdot 10^5$ yr (Swamy, 2010a).

The existence of the theorized KB was confirmed by the discovery of 1992 QB1, the first object of the KB (Jewitt & Luu, 1993), which gave the name to the classical, stable population of the belt, the *cubewanos*. Together with them there is a second group, the *resonant* population, which are locked in specific resonances with Neptune (3:2 for the Plutinos, but also 4:3, 5:3 and 1:2) which offer a protection mechanism from the perturbations.

Another class of objects with cometary characteristics consists in the Main Belt Comets (MBCs). They are main belt objects dynamically stable, on scale of billion yr that show seasonal activity (Hsieh & Jewitt, 2006). The mechanisms that trigger the activity can be (1) the sublimation of crystalline water ice, the only volatile able to survive inside the snow line during the period of formation (Bertini, 2011), or (2) the collision of small bodies and the exposition of ices trapped under the surface, as the case of 596 Schila (Moreno et al., 2011). The first object of this group was the asteroid 7968 Elst-Pizarro that was indeed classified also as comet 133P/Elst-Pizarro after showing activity near the perihelion (Hsieh et al., 2004).

1.2 Dust

Dust is a main constituent of comets. It covers the surface of the nucleus, composes the nucleus and the coma and generates the tail. It is mainly composed by silicates, refractory organic compound called 'CHON' and ices.
Dust has a key role in the understanding of the environment in which the comet formed and the ongoing physical and chemical conditions. Dust particles in the coma are easier to analyze than the surface and interior of the nucleus and they are thought to be a good proxy to understand nucleus characteristics. In the following a brief description of the main dust components is reported.

1.2.1 Composition

Silicates Silicon (Si) is about the 30% of the Earth in weight. All the compounds with group SiO_4 are called *silicates*. They have tetrahedral structure and are classified depending on the bonds among single tetrahedra. They are divided into:
-Nesosilicates: composed by an isolated tetrahedra as Olivine $(Mg,Fe)_2SiO_4$;
-Inosilicates: composed by single chains as Piroxenes $(Mg,Fe)_2SiO_3$;
-Phyllosilicates: when multiple chains form a layer.
IR observations result fundamental for the composition analysis since many molecular absorption lines lie in the range of 5-35 μm.
Several lines represent material common in each comet, as for example the silicates features near 10 μm, identified for the first time in the comet Bennett in 1970 (Maas et al., 1970). Laboratory measurements revealed that the stretching vibrations of Si-O compounds are responsible for this lines. Another important feature is the one at 20 μm, generated by the bending vibrations of Si-O-Si compounds. Other common features are those at 30-33 μm, but they are characteristic of the chemical composition of different materials therefore difficult to identify.

Organics Organic material consists of chemical compounds based on carbon. Organic matter can appear as volatile, stored in ices of water or CO or CO_2, or as refractory material. During the comet approach toward the Sun the ices sublimate directly from the nucleus or from the ejected material, thus releasing these organic molecules.
There are several typical lines responsible of the presence of organics. The feature at 3.4 μm revealed by Vega1 on comet Halley spectra was attributed to the C-H stretching vibrations. This spectral signature is associated with the presence of functional groups as CH_3 or CH_2, therefore organic matter. Another important feature is located around 3.29 μm and, together with other lines, is associated with the presence of Polycyclic Aromatic

Hydrocarbons (PAH): organic compound that are composed of multiple aromatic rings (i.e. cyclic, ring shaped, planar molecules that result very stable) (Kissel & Krueger, 1987a).

Ice Water ice is a major component of comets. It can be found in two different phase depending on the temperature at the time of formation. It is amorphous, if it has experienced a fast cooling reaching T$<$ 50 K, or crystalline, in the case it has frozen at T$= 120 - 180$ K. There are several techniques to detect it involving different wavelength ranges. In the UV and visible regime the water ice presence is observed taking the photodissociation products, such as OH radical, atomic hydrogen H and atomic oxygen O(^{1}D), as proxy. Strong OH production was detected on comet Bowell at heliocentric distances > 4 AU from the emission at $\lambda = 3080$ Å, and it was attributed to the presence of a population of icy grains not yet sublimated in the coma (Hanner & Campins, 1986). Otherwise, the characteristic H emission is due to the Lyman-α transition at 1216 Å. The O(^{1}D) emission lines are instead located in the visible range, consisting in three forbidden transitions respectively at 5577, 6300 and 6363 Å. Those lines are not unambiguous since they are generated by photodissociation of various molecules such as H_2O but also CO_2, CO and O_2.
On the other hand, water can be directly revealed from the IR absorption lines in the reflected solar spectrum and not through the detection of daughter species. The problem is that the main water bands are not visible form the ground-based observations, due to the atmosphere absorption. Therefore space observations are needed. The main features observed are generated by the stretching modes of crystalline ice: at 3.1 μm due to the Fresnel reflection peak and at 1.65μm, due to the temperature sensitive absorption.
Finally, the ice can be seen directly from in-situ images and measurements. The mass spectrometer ROSINA/Rosetta was able to measure the relative abundances of water and other volatiles providing the value of water production rate $Q = 5 \cdot 10^{25}$mol/sec at 100 km from the nucleus at heliocentric distance of 3.5 AU during August 2014 (Hansen et al., 2016). Otherwise on the nucleus, several icy patches was detected and studied in relation with their evolution due to physical processes as sublimation and recondensation (Deshapriya et al., 2018; Fornasier et al., 2016) .

1.2.2 Dust in comets

Before Halley Before the Halley encounters very little was known about cometary dust. Spectral emission feature at 10 μm of comet Bennett (Maas et al., 1970) revealed the presence of silicates. Other elements were identified in various spectra, as Fe Ca Na

K etc., but the overall information was very limited. The dominant idea was that the dust composition should be compared with the one of carbonaceous chondrites.

Halley The flyby missions that first revealed the nature of cometary dust with in-situ measurements were the European Space Agency (ESA) Giotto mission (Reinhard, 1986) and the soviet mission Vega 1 and Vega 2 (Sagdeev et al., 1986) to 1P/Halley.
The mass spectrometers on board the spacecrafts provided for the first time *in situ* analysis of the solids in the coma. [libro grun]
The dust impact mass analyzer PUMA 1 and 2 on Vega and PIA on Giotto revealed the chemical composition of the coma. Basically three main spectra have been found:
1. those made of light elements, composed by CHON elements; 2. those similar to CI meteorites but enriched in C (therefore more pristine); 3. those comparable to silicates (Mg,O,Si,Fe); (Kissel & Krueger, 1987b). Schulze et al. (1997) used the cluster analysis method to classify the Halley's inorganic dust particles. They found that the dominant components were the Mg-rich olivine and pyroxene ($> 20\%$) with density $\rho = 2.5$ gr/cm^3. Then the Fe and Ni sulfides (10%) as pyrrhotite ($Fe_{1-x}S$) and pentlandite $(FeNi)_9S_8$ and the Fe oxide as magnetite ($< 1\%$).
The emission features near 3.4 μm generally correspond to C-H stretching of some organic material. The emissions detected by Vega 1 have been associated with the presence of -CH_3 and -CH_2 functional groups (e.g. methanol CH_3OH etc.) (Swamy, 2010b).

Hale-Bopp The spectra obtained by the Infrared Space Observatory show 5 major features at 10-30 μm which correspond to Mg-rich crystalline olivine (forsterite Mg_2SiO_4). Minor features of Mg-rich pyroxene (enstatite $MgSiO_3$) have been revealed when compared with laboratory spectra by Crovisier et al. (1997). The mineralogy of Comet Hale-Bopp is clearly Mg-rich and it is similar to the one of IDPs aggregates (Swamy, 2010b).

Tempel 1 The Spitzer Space Telescope obtained spectra of the material ejected by the comet after the Deep Impact mission visited it (2005). An accurate analysis (best fit model) of the spectra revealed the ejected material was composed mainly of:
-silicates: olivines (11 μm), pyroxenes ($8 - 10$ μm) phyllosilicates (due to the impact).
-carbonates: magnesite ($MgCO_3$), siderite ($FeCO_3$) ($6.5 - 7.2$ μm);
-water ice;
-metal sulphides ($27 - 29$ μm);
-organics: PAH, amorphous carbon;
This composition results comparable with the one of CI meteorites (Lisse et al., 2007).

Wild 2 The Stardust mission was the first able to collect samples of dust particles and brought them back to Earth. The samples showed the presence of amorphous silicates and crystalline silicates, among which forsterite and enstatite. CIDA mass spectrometer found that the dominant ion was CN^-, while O^- and OH^- were less abundant, indicating the importance of the nitrogen chemistry. Also the sulphur chemistry has an important role, due to the presence of SH^- probably generated from troilite (FeS) through radiative processes.
Stardust revealed also the presence of PAH as benzene C_6H_6, fenolo C_6H_5OH and naftalene $C_{10}H_8$. For the first time was revealed the presence of the aminoacid glicina (Elsila et al., 2009). Moreover, dust particles with mineralogical composition similar to the one of meteoritic Calcium-Alluminium-Inclusions (CAIs) have been found. CAIs are the oldest minerals formed in the solar system. They condensed out the solar nebula at very high temperature and this is why they are composed by very refractory material. CAIs show a typical excess in ^{26}Mg, due to the β-decay of ^{26}Al, a very abundant element in the early Solar System. The enrichment in ^{16}O with respect to the other two oxygen isotopes, reveals the outer solar system origin of this material.

1.3 Dust role in planetary formation

One of the most important issue in planetary formation models is the understanding of dust grains growth processes that will lead to the accretion of large aggregate and eventually to the formation of planetesimals. The condensation of dust particles depends on the different materials of which they are composed and on their distance from the Sun. Refractory material such as silicates and metals condense in the inner part of the disk, semi-volatiles and organic material in the middle disk and finally the cold matter as ices and volatiles as H_2O, CO_2, CO, NH_3, CH_4 in the outer disk (Blum, 2018).
The collision models needed to explain the first aggregation phases was deeply explored with laboratory experiments. Blum & Münch (1993) started demonstrating that aggregates of mm-size, composed by monomers of μm size, did not stick together but fragmented into smaller pieces. After that the whole space parameter of collision velocity, type of material and size was largely investigated, leading to the results graphically summarized in Fig. 1.4. In each region, defined by the size of particles that will collide, a specific mechanism dominates which could or not eventually contribute to planetary formation. In the following the main grain growth mechanisms are illustrated.

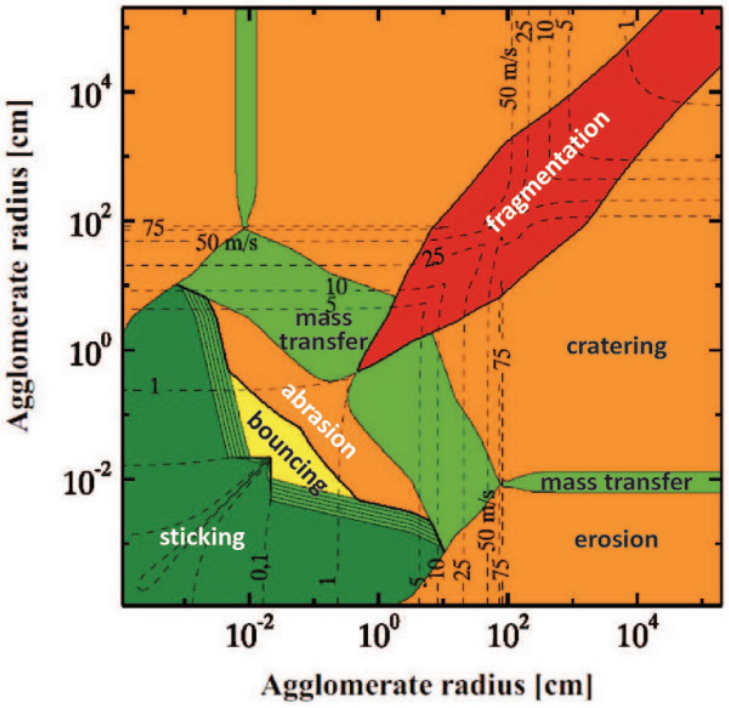

FIGURE 1.4: Collision model for SiO_2 monomer particles with radius $r = 0.75$ μm. Coloured regions identify the collisional outcomes and the dash lines mark the mean collision velocities in m/s (Blum, 2018).

1.3.1 Dust growth mechanisms

There are several processes involved in the growth of dust grains. In the case in which the collision is between particles of approximately the same size, the following phenomena can occur:

Sticking When the collision energy is less than the Van der Waals bounding energy (i.e. for velocities less than 0.1 m/s and particles size of 1-100 μm) the hit and stick mechanism takes place and gives rise to a fractal aggregate.

Bouncing As the energy of collision increases the particles start to bounce but there is not yet enough energy to destroy the body. The outcome is a grain with more compact structure.

Fragmentation For even higher energies and for particles larger than cm-size, the the collision leads to the fragmentation of the objects.

When the colliding particles have different sizes, i.e. a projectile hit a bigger target, the phenomena that take place are the following:

Erosion When the projectile is very small it erodes the bigger body causing a mass loss.

Mass transfer In a very little region of space parameter (see Fig. 1.4) the mass of the smaller projectile is transferred to the bigger mass with consequent compaction of the object.

Cratering As the dimension of the projectile increases the impact causes the excavation of the bigger object and a remarkable mass loss.

In the protoplanetary disk (PPD) the dust particles are not free to orbit, but they undergo the effect of the gas component. According with the streaming instability model (Johansen & Youdin, 2007) a series of spontaneous turbulences develop inside the PPD leading to clump particles thus creating zones of overdensities. Particles in these regions are more in contact with each other and feel the effect of the Van der Waals forces that stick them together. This happens for typical aggregate dimension of 1 μm at $v = 1$ m/s (Poppe et al., 2000). The threshold velocity for sticking depends on the size and morphology of the materials involved and is defined as:

$$\frac{v_{th}}{1m/s} = \left(\frac{s}{1\mu m}\right)^{-x} \qquad \begin{cases} x \sim 1 & 0.1 < s < 10\mu m \\ x < 1 & s > 10 \\ x < 1 & s < 0.1 \end{cases} \tag{1.7}$$

where s is the size of the particle (Blum & Wurm, 2008).
As long as the grains do aggregate, collisions became more efficient in absorbing part of the kinetic energy and in converting it into more compact structures. At this point the grains can not stick anymore since they have reached the bouncing barrier. As in the case of the sticking process, the bouncing barrier has a threshold which varies with the characteristics of the material, for instance icy grains are able to stick together for higher collision velocities than refractory material. Therefore, bouncing barrier and compaction put a limit to the maximum size the sticking grown up aggregates could achieve, which coincide approximately with pebbles of 1 cm. At this point the accretion process leads to the formation of a planetesimal only through mass transfer but this is an efficient mechanism only under restricted conditions, otherwise it causes fragmentation or erosion. The mass transfer is very slow in accreting a planetesimal, due to the small size of the impactors. On the other hand, the gravitational collapse of clouds of pebbles (built-up by e.g. streaming instability) is faster. Indeed, the formation of km-size planetesimals should have been very fast, taking 100 yr through collisions with $v > 100$ m/s, given their trend to drift inward to the Sun (Weidenschilling, 1977).

Chapter 2

Rosetta mission

In this chapter we present the Rosetta mission and we illustrate the instrumentation on board the spacecraft. Then we give a brief description of the main findings about the primary target of the mission, the comet 67P/Churyumov-Gerasimenko.

2.1 Rosetta mission

Rosetta was an European Space Agency (ESA) mission with primary target the comet 67P/Churyumov-Gerasimenko (hereafter 67P). The name is a tribute to the Rosetta stone, as the stele was a joining link between the past and the present allowing the interpretation of the ancient hieroglyphics, so the mission should have helped in the interpretation of the origin of the Solar System. The main goal of the mission was trying to generalize the findings about 67P to the whole cometary population.
Originally the mission had a different target: the comet 46P/Wirtanen. A failed launch of an Ariane 5 caused a delay that affect the mission, loosing the possibility to reach the established comet and forcing to consider a new target. Therefore the comet 67P, discovered by the soviet astronomers Klym Ivanovyč Čurjumov and Svetlana Ivanovna Gerasimenko in 1969 and belonging to the Jupiter family, was a suitable alternative. This comet underwent a close encounter with Jupiter, responsible for a change in the orbit that moved the perihelion closer to the Sun, from 2.7 AU to 1.2 AU. This was an additional contribution to the mission, allowing the analysis of especially fresh material. Rosetta was selected in 1993 as cornerstone of the ESA Horizon 2000 program. Cornerstone means a large mission implying innovation and new technologies for the payload and the spacecraft, and involving a large scientific community. Rosetta was launched on March 2004. After 10 years of travel in the interplanetary space, three gravity assists at close encounters with Earth and one with Mars, it reached comet 67P. During its

long trip it met 2 main belt asteroids: Šteins in 2008 and Lutetia in 2010, getting a big amount of scientific data. On January 2014, after 32 months of deep space hibernation, the spacecraft woke up. On August 2014 the rendezvous started and it would last 26 months. The approach took place at 3.7 AU and the spacecraft followed the comet toward the perihelion, occurred on August 2015 at 1.2 AU. It continued orbiting the object until the end of the mission, when it landed on the comet surface, the 30^{th} September 2016 at 3.8 AU from the Sun, providing the last extraordinary images, with resolution of few cm. During the rendezvous the spacecraft orbited the nucleus at various distances, approaching the nucleus up to few tenth of km, as for example during the fly-by, to come back to 1200 km at perihelion, due to the higher activity.
On November 2014, at 3 AU from the Sun, the spacecraft deployed the Philae probe, designed to study the comet directly form the surface. Due to an unlucky dysfunction of the harpoons during the touchdown, the lander bounced few times before stopping in a shadow zone. The solar panels were thus useless and consequently it was impossible to communicate with the orbiter. The exact position of Philae was discovered at the end of the mission thanks to the image taken by OSIRIS NAC at 2.7 km from the surface and shown in Fig. 2.1). Rosetta was the first mission at all to provide in-situ data for such a long period of time, allowing the study of physical, chemical and dynamical punctual characteristics but also their evolution along the orbit.

2.1.1 Instrumentation

Rosetta probe was composed by two main members: the orbiter and the lander (see Fig. 2.2) .
Rosetta orbiter [1] was a large aluminium box with dimensions 2.8 x 2.1 x 2.0 metres equipped with 11 different instruments. On the top of the box were mounted the instruments, while on the opposite side were located the antenna and the lander. The orbiter was equipped with two solar panels, each of 32 m^2 in area, able to make a complete turn and to catch the maximum amount of energy from the Sun. The propulsion system includes two tanks, one containing the fuel and the other the oxidiser. The spacecraft was provided with 24 thrusters for attitude control able to push it with a force of 10 newtons.
The instruments on board the spacecraft were:

ALICE was the Ultraviolet Imaging Spectrometer addressed to the characterization of the nucleus and the coma composition. It was designed to observe spectral features in the extreme and far ultraviolet spectral regions ranging from 70 to 205 nm. Alice measured the presence of H_2O and O_2 in the comet and investigated the gas outburst

[1] http://sci.esa.int/rosetta/35061-instruments/

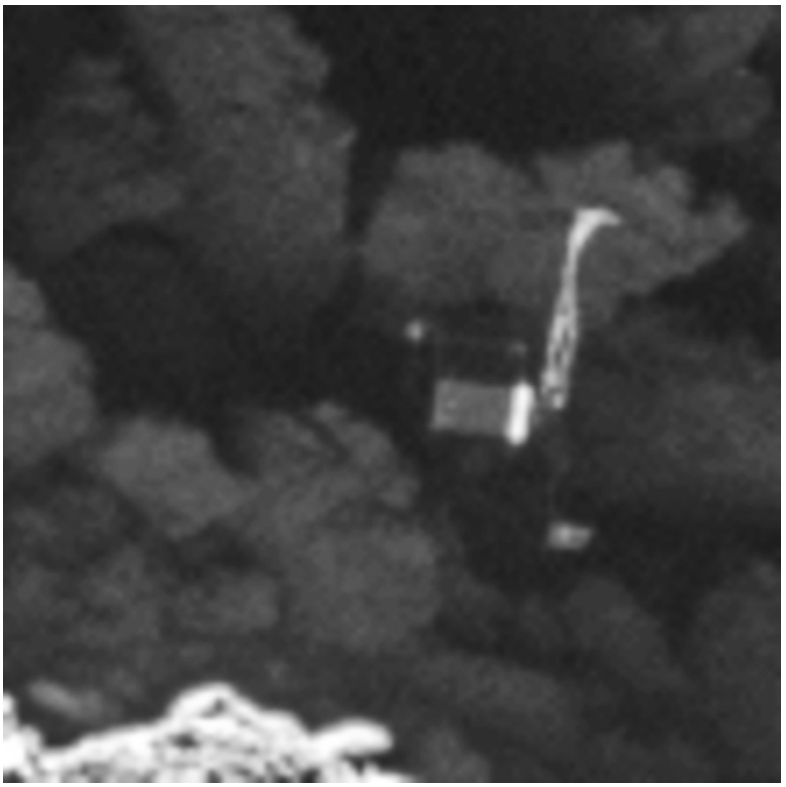

FIGURE 2.1: Philae imaged by OSIRIS NAC on 2 September 2016. Credits: ESA/Rosetta/MPS for OSIRIS Team MPS/UPD/LAM/IAA/SSO/INTA/UPM/-DASP/IDA

(Feldman et al., 2016; Keeney et al., 2017). Alice mapped also the cometary nucleus in the FUV and during the travel to 67P studied Mars and the asteroids Steins and Lutetia.

CONSERT was the COmet Nucleus Sounding Experiment by Radio wave Transmission. It was intended to perform the tomography of the nucleus and to determine the dielectric properties of the nuclear material (Ciarletti et al., 2017). It was composed of two modules, one that landed on the comet and the other that remained in orbit with the comet. The radio signal transmitted from the orbiting component was expected to be received by the lander, and then immediately re-transmitted back to the orbiter, measuring the variations in phase and amplitude that occur as the radio waves pass through different parts of the cometary nucleus.

COSIMA was the Cometary Secondary Ion Mass Analyser. The target of the instrument was the individual dust particles in the near comet environment. COSIMA was a secondary ion mass spectrometer equipped with a dust collector. The particles that entered the instrument were then moved under a microscope to determine their positions. After that, the particles underwent the bombardment of indium ions from the primary ion gun and then the secondary ions were extracted into the mass spectrometer.

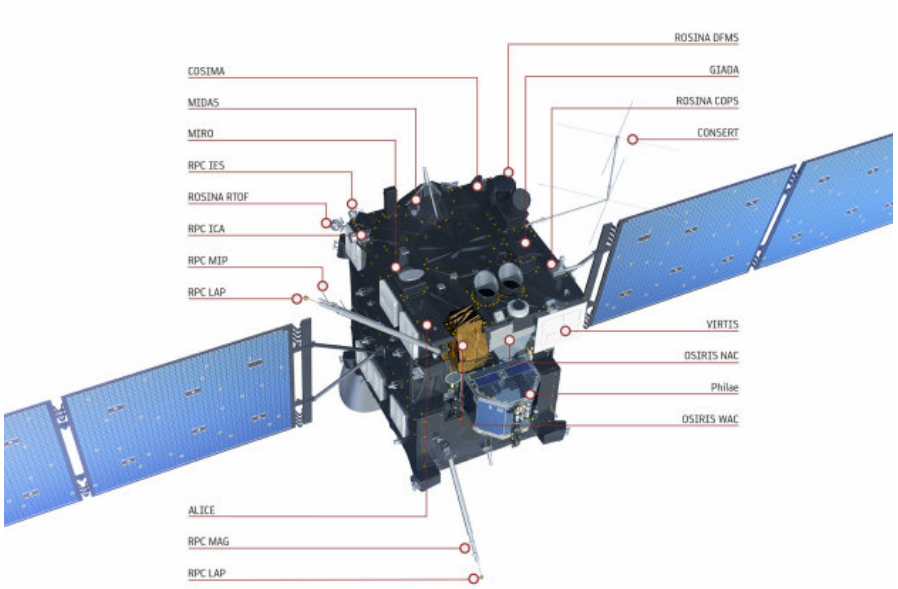

FIGURE 2.2: Instrumentation on board the Rosetta spacecraft. Credits: ESA/ATG medialab.

GIADA was the Grain Impact Analyser and Dust Accumulator, developed to characterize the dust grains in the inner coma providing measurements of the number, mass, momentum and velocity distribution of the particles. GIADA was divided into three modules. The first one consisted in the Grain Detection System (GDS) and the Impact Sensor (IS). The second one contained the main electronics (ME) and it controlled the acquisition of data. The last module consisted of five microbalances that measured the dust flux.

MIDAS the Micro-Imaging Dust Analysis System, was intended to study the dust environment around the comet and to perform statistical analysis on it. The instrument took advantage of the technique of atomic force microscopy, that allowed analysis at a spatial resolution of 4 nm. MIDAS also studied the dust environment of the two asteroids Šteins and Lutetia.

MIRO was the Microwave Instrument for the Rosetta Orbiter committed to the investigation of the cometary nucleus, the coma and the outgassing. MIRO was programmed to be a high spectral resolution line receiver that operated at frequencies that ranged from 188 GHz (1.6 mm) to 562 GHz (0.5 mm), but also as a continuum line receiver. It obtained measurements of the abundance, velocity and temperature of coma species and in the continuum channels at millimetre and submillimetre wavelengths it sensed the subsurface temperature of the nucleus to depths of several centimetre.

ROSINA the Rosetta Orbiter Spectrometer for Ion and Neutral Analysis, consisted of two mass spectrometers and a pressure sensor. The spectrometers were intended for

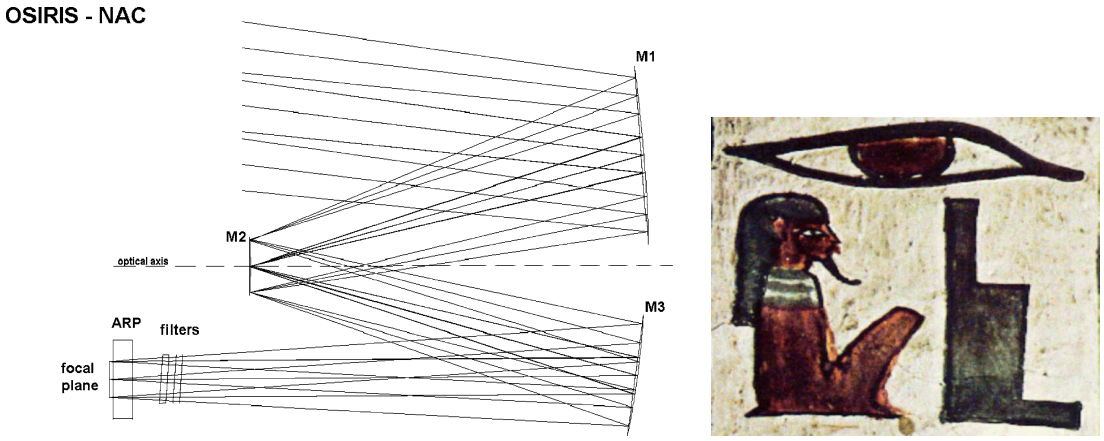

FIGURE 2.3: Ray tracing diagram of the NAC optical system, left panel (Keller et al., 2007). The hieroglyphic of Osiris in the tomb of Nefertari, right panel.

the investigation of the cometary coma, providing measurements of temperature and velocity of gas and ions. The pressure sensor was able to determine the gas density and rate of gas flow.

RPC the Rosetta Plasma Consortium, consisted on a set of five instruments sharing a common electrical and data interface with the Rosetta orbiter. The RPC instruments were designed to make complementary measurements of the plasma environment around comet.

RSI was the Radio Science Investigation devoted to the control of the spacecraft motion and of the perturbing forces acting on it. It used the communication system of the Rosetta spacecraft to communicate with the ground stations on Earth.

VIRTIS was an imaging spectrometer. It combined three data channels in one instrument: two data channels were committed to spectral mapping while the third channel was devoted entirely to spectroscopy. The mapping channel utilized a CCD to detect wavelengths from 0.25 μm to 1 μm and a mercury cadmium telluride (HgCdTe) infrared focal plane array to detect from 0.95 μm to 5 μm. The high resolution channel was an echelle spectrometer, sensitive to the wavelength range from 2 μm to 5μm.

OSIRIS The Optical, Spectroscopic and Infrared Remote Imaging System (OSIRIS) was the scientific camera system on board the spacecraft Keller et al. (2007). The name derived form the Egyptian god of underworld and vegetation who symbolizes the creative forces of nature and the indestructibility of life. In the hieroglyphics he was represented as äll-seeing eyeänd for this reason it was considered an appropriate name for the instrument (see Fig. 2.3). The telescope consisted on 2 cameras: the Narrow Angle Camera (NAC) and the Wide Angle Camera (WAC), both equipped with a CCD of 2048 x 2048 and with a set of various filters. The two cameras were designed as complementary pair with different purposes. The WAC was more suitable for long-term monitoring,

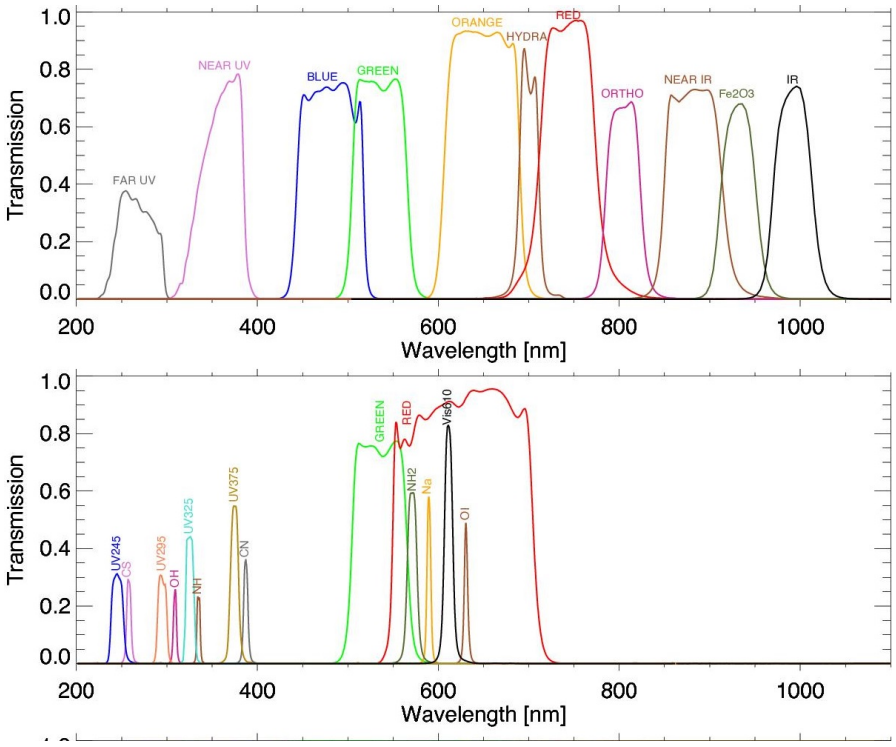

FIGURE 2.4: NAC and WAC transmission curves (Tubiana et al., 2015).

	NAC	WAC
Optical design	3-mirror off-axis	2-mirror off-axis
Detector type	$2k$ x $2k$ CCD	$2k$ x $2k$ CCD
FoV (°)	2.20 x 2.22	11.35 x 14.4
Angular resolution (μrad/px)	18	101
Focal length (mm)	717.4	140.131
Mass (kg)	13.2	9.48
F number	8	5.6
Spatial scale from 1 km (cm/px)	1.86	10.1
Filter bandpass (nm)	40	5
Wavelength range (nm)	250-1000	240-720
Number of filters	12	14

TABLE 2.1: OSIRIS cameras characteristics (Keller et al., 2007).

to analyze the 3D flow-field of the dust and gas and to take images of extended zones. Otherwise, the NAC was more appropriate to detect the nucleus at high distances, to study the morphology and the mineralogy of the surface and to detect details of dust single grains.

OSIRIS took more than 98000 images during the entire mission, for a totality of more than 22000 hours of operation. In Tab. 2.1 are shown the main characteristic of the instrument.

We focus on the NAC since during the thesis work we have used images taken indeed with that camera. NAC optical design is shown in Fig. 2.3, the camera was composed of

three mirrors, 2 aspheric and 1 spheric made of Silicon Carbide (SiC). The system was equipped with two filter wheels placed in front of the CCD, containing bandpass filters and a neutral density filter that controlled the intensity of the photon flux. Moreover, two anti-reflection-coated focusing plates were added to the front of the CCD and used together with bandpass filters allowed 2 different focus ranges: Far Focus Plate (FFP), from infinity to 2 km and Near Focus Plane (NFP), from 2 km to 1 km.
The nominal operations were defined as far focused with orange filter (at 649 nm with bandwidth of 94 nm). The transmission curves of the NAC and WAC filters are shown in Fig. 2.4.
The structure was designed to maintain the camera components in the proper position during the travel. That structure was mounted on the main spacecraft by means of 3 titanium bipods in a way to reduce the thermal flow from the main structure and possible distortion Keller et al. (2007).
The acquired images needed to be calibrated before using them for accurate data analysis. The OSIRIS calibration pipeline , OsiCalliope, is a complex software which converts the raw CCD images into calibrated ones. The main steps to obtain level 2 corrected images are the following: (1) Bias subtraction, (2) Coherent random noise removal, (3) dark current removal, (4) flat field correction, (5) bad pixel removal, (6) ghost correction, (7) exposure time normalization, (8) radiometric correction to convert from DN (digital numbers) to W/m^2 sr nm. Level 3 of correction includes (9) geometric distortion correction and level 4 is the (10) georeferenced one (Tubiana et al., 2015).

Rosetta lander Philae [2] was a probe design to land on the comet surface. It was 100 kg in weight, composed by a base and an instrument platform in carbon fiber. The instrumentation carried by Philae were:
APXS: Alpha Proton X-ray Spectrometer.
CIVA: Panoramic imaging system and spectrometer.
CONSERT: COmet Nucleus Sounding Experiment by Radio-wave Transmission.
COSAC: COmetary SAmpling and Composition experiment. Gas analyzer.
MODULUS Ptolemy: Methods Of Determining and Understanding Light elements from Unequivocal Stable isotope compositions. Geochemistry of light elements.
MUPUS: MUlti-PUrpose Sensors for Surface and Sub-Surface Science.
ROLIS: Rosetta Lander Imaging System.
ROMAP: Rosetta Lander Magnetometer and Plasma Monitor.
SD2: Sampling, Drilling and Distribution Subsystem.
SESAME: Surface Electric Sounding and Acoustic Monitoring Experiment.

[2] http://sci.esa.int/rosetta/31445-instruments/

FIGURE 2.5: An amazing image of a jet on comet 67P taken by the NAC OSIRIS on July 2015. Credits: ESA/Rosetta/MPS for OSIRIS Team MPS/UPD/LAM/IAA/SSO/INTA/UPM/DASP/IDA

2.2 67P main findings

In this section we list some of the main findings about 67P, obtained from the huge amount of data provided by the Rosetta instrumentation during the 26 months of rendezvous. In Tab.2.2 we resume the main characteristic parameters of the comet.

Bilobate nucleus The in-situ images revealed a bilobate nucleus composed by a smaller lobe, named *head*, a bigger lobe, the *body* and a thin contact zone, the *neck*. Therefore, the comet is thought to be the result of a fusion process of 2 cometesimals through slow-collisions (Massironi et al., 2015). The 2 lobes show independent surface stratification of material that confirm the different origin of the 2 previous bodies (Penasa et al., 2017). In Fig. 2.6 is shown the regional morphology of the comet.

Dust to water ratio The dust to water ratio (DWR) is a parameter with important implications for the nucleus structure. It confirms that 67P is a very dusty comet, contrary to what predicted the dirty snowball model accepted before the Halley exploration. A value of DWR of 6 implies an erosion of 1-15 m at perihelion and an average contents of 15% of water on the nucleus surface. This water corresponds to the more internal

Parameter	**Value**	**References**
Size	4.3 x 4.1 km	Rickman (2017)
Big lobe	4.1 x 3.3 x 1.8 km	Jorda et al. (2016)
Small lobe	2.6 x 3.3 x 1.8 km	Jorda et al. (2016)
Neck	2.2 x 0.8 km	Jorda et al. (2016)
Density	532 kg/m^3	Jorda et al. (2016)
Dust bulk density	795 kg/m^3	Fulle et al. (2016b)
Mass	$1.0 \cdot 10^{13}$ kg	*
Volume	18.7 m^3	*
Perihelion	1.243 AU	*
Aphelion	5.68 AU	*
Orbital eccentricity	0.640	*
Orbital inclination	7.04 deg	*
Revolution period	6.45 yr	*
Rotational period	12.4043 h	Sierks et al. (2015)
Dust/water	6 6-100 perihelion	Fulle et al. (2016b) Rotundi et al. (2015)
Dust/gas	4 3 perihelion	Hässig et al. (2015)
Albedo geo	0.06	Rickman (2017)
Water production	$7 - 8 \cdot 10^{27}$ mol./sec	Rickman (2017)
Dust bulk density	$1 \cdot 10^3 - 3 \cdot 10^3$ kg/m^3	Rotundi et al. (2015)
Thermal inertia	20 J/K m^2 s$^{1/2}$	Schloerb et al. (2015)
D/H	0.053%	Altwegg et al. (2015)

TABLE 2.2: 67P main characteristic parameters. *http://sci.esa.int/rosetta/14615-comet-67p/.

layers of the comet, exposed during the perihelion. This value indicates that the comet is less hydrated and quite porous, with value ranging between 75-85% (Kofman et al., 2015). Therefore the nucleus is mainly composed by non-volatile materials.
A value of DWR = 6 corresponds to a value of dust to gas ratio DGR = 4-5 taking into account the minor species abundances (Hässig et al., 2015).

Distributed sources The water component revealed in the comet might come from the nucleus or from the dust particles in the coma, in the second case they are called distributed sources. For 67P the distributed sources are less then 5%, which is less than the nucleus with its value of 15% of the mass (derived from DWR = 6, see previous paragraph). That means that the ejected material forming the coma is particularly dry. Therefore the dust is confirmed to be mainly compact and homogeneous in structure, since it was not revealed a variation in size distribution, which would have been an evidence of processes like fragmentation or sublimation Fulle et al. (2016a).

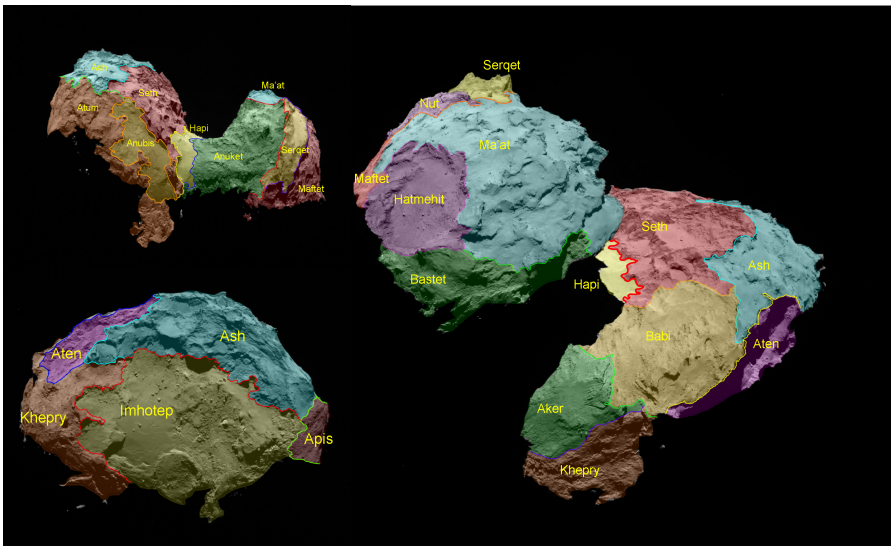

FIGURE 2.6: Regional maps of 67P (El-Maarry et al., 2015).

Seasons activity The comet shape, together with the nucleus spin obliquity rule the activity in a crucial manner. 67P shows the importance of considering seasons in modelling activity, which results heterogeneous depending on the structure and composition of different zones of the nucleus. The emission of material is a complex process that evolves with the seasons of the comet. One of the main seasonal events is the transfer of material from the south hemisphere to the north hemisphere. This material passage affects the dust size distribution which is steeper in the south ($\alpha = -4$) with a major contribution of small particles, while in the north is flatter ($\alpha = -2, -3$) (Fulle et al., 2016c).

D/H The D/H value for 67P is 0.053%, a value three time higher than the Earth and of other comets, approaching indeed the value for molecular clouds Altwegg et al. (2015). It means that not only comets brought water to the Earth but they are responsible only for the 10% of the total amount of terrestrial water Robert (2006).
D/H is different among comets and this is a signature of the physical condition of the place in which they formed. That is an evidence that 67P developed in a cold region. Other evidences of this fact is the presence of supervolatiles as N_2, O_2, Argon etc., which are trapped into the clathrate hydrates or into crystalline ices, implying a maximum temperature reached from the body of 40 K (Davidsson et al., 2016).

Oxygen detection The measurements of more than 3000 spectra taken by ROSINA mass spectrometer from September 2014 to March 2015, revealed the presence of oxygen molecule in the coma of 67P, with local abundances ranging from 1% to 10% relative to H_2O (Bieler et al., 2015). The O_2/H_2O ratio does not show significant variations with

FIGURE 2.7: The dust environment at 10 km from the nucleus. Credits: ESA/Rosetta/MPS for OSIRIS Team MPS/UPD/LAM/IAA/S-SO/INTA/UPM/DASP/IDA

the heliocentric distance, suggesting that oxygen is coming not from surface for radiolysis or photolysis processes while form the interior of the nucleus. Oxygen has never been detected before in comets and in very low abundances in interstellar clouds, probably due to its high reactivity with other molecules. Therefore an explanation for the presence of O_2 in 67P suggests that primordial oxygen was incorporated into water ices in the primordial nebula and during the successive phase of cooling of the protoplanetary disk, amorphous water ice with trapped O_2 condensed on dust grains.

Glycine detection The amino acids are organic molecules fundamental for the development of life as we know it. ROSINA mass spectrometer detected the presence of the amino acids glycine for the first time in October 2014 at 10 km from the nucleus at 3 AU from the Sun, and the second time on March 2015 at 15 km from the nucleus at 2 AU (Altwegg et al., 2016). The density profiles show a glycine distribution quite diffuse in the coma and correlated with the dust. Moreover, the glycine was detected together with methylamine and ethylamine which is consistent with the models that predict they have formed from UV irradiation directly in the interstellar medium at T = 40 - 120 K, without the need of water. This scenario supports the idea that the comets brought prebiotic molecules onto the young Earth.

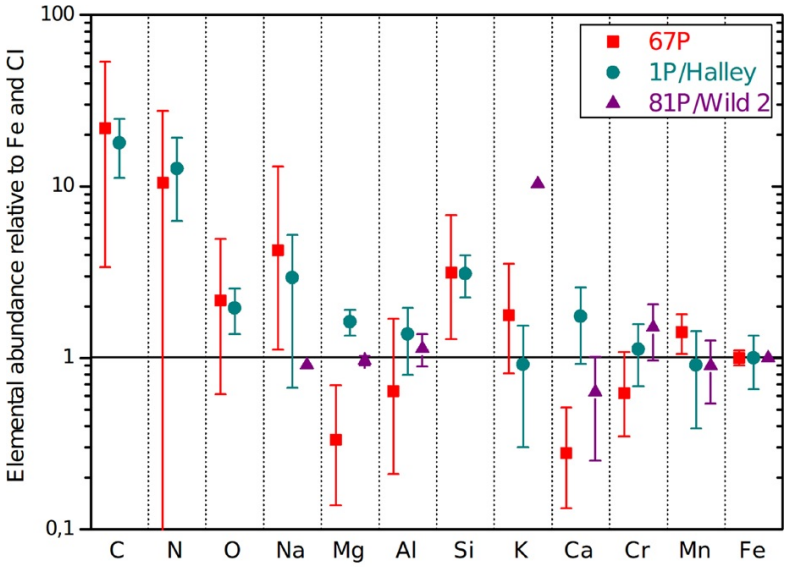

FIGURE 2.8: Elemental composition of C, N, O, Na, Mg, Al, Si, K, Ca, Cr, Mn and Fe, relative to Fe and CI composition, measured on 30 particles (Levasseur-Regourd et al., 2018).

Origin The presence of fractal dust in 67P put some constrains to the processes involved in its formation and evolution. In fact, in order to preserve fractal dust it is necessary that the object would accrete through gentle gravitational collapse at velocity not higher than 1 m/s (Fulle & Blum, 2017). This fact implies that the comet did not undergo high velocity collisions but that it is a primordial rubble pile that does not derive from a larger body (Davidsson et al., 2016).

2.2.1 Dust in 67P

In the following we summarize the actual knowledge about the cometary dust as seen from Rosetta instrumentation. In Fig. 2.7 we see the extraordinary dust environment of the 67P at 10 km from the surface of the nucleus.

Composition During the 26 months of the mission, COSIMA have revealed 35000 particles of various dimensions, from 10 to 100 μm, collected at different distances from the nucleus and experiencing specific activity phase (Merouane et al., 2017). The particles kept an impact velocity < 10 m/s, on the contrary to the Stardust mission that trapped the particles in the aerogel with velocity of the order of 6 km/s (Rotundi et al., 2015). This allowed the material to keep the original structure and the physico-chemical properties of the dust particles.

The relative chemical abundances can be used as a proxy to determine how primitive

	67P	protosolar	CI
C/Si	5.5	7.19	0.76
N/C	0.035	0.3	0.04

TABLE 2.3: Relative elemental abundances of 67P dust measured by COSIMA (Levasseur-Regourd et al., 2018).

material	% vol.	ρ [kg/m^{-3}]
sulfides	4 ± 1	4600
ices	20 ± 8	917
silicates	22 ± 2	3200
hydrocarbons	54 ± 5	1200

TABLE 2.4: 67P composition in volume (Fulle & Blum, 2017).

is an object. The more similar with the solar photosphere and the more pristine is the body.

The elemental composition of 67P relative to C, N, O, Na, Mg, Al, Si, K, Ca, Cr, Mn and Fe, has been measured on 30 particles (see Fig. 2.8). It results close to the one of carbonaceous chondrite of type CI, except for the higher abundances of C and N (see Tab. 2.3) (Bardyn et al., 2017; Fray et al., 2017) The percentage of atoms obtained by COSIMA is the following: 30% O, 30% H, 30% C, 5.5% Si, 1.6% Fe, 0.6% Mg, 2.4% of N, Na, Mn and minor elements.

Otherwise, the analysis of size and density of the pebbles revealed by GIADA provided an estimate of the mineralogy of 67P. The measurements are compatible with a composition including hydrocarbons, silicates, ices and sulfides. In Tab. 2.4 is reported the average composition in volume abundances. Moreover, among all the organic compounds detected on 67P, the simplest aminoacid, the glycine, was found by ROSINA. From its distribution in the coma, glycine was likely released by heated particles, rather than from direct sublimation from the surface (Altwegg et al., 2016).

Morphology Define the dust morphology and structure is not a trivial issue. In fact the shape of the particles depends on some crucial parameters for comets, such as porosity, strength and thermal properties. Stardust collection was the first that reveal the aggregate structure of particles (even if the analysis was biased by the impacts). COSIMA/Rosetta detected more than 10000 cometary particles $> 14\mu$m. Fig. 2.9 shows four particles collected by the instrument and illustrates how differentiated the population could be, including compact particles (a) and more clustered aggregates (b, c, d). Following the classification of Guettler (in prep.), the dust particles can be divided into three main groups:

- **Solid**: those particles with low value of porosity, $< 10\%$, consolidated structure similar to rocks, with high strength, i.e. of the order of MPa or more. These

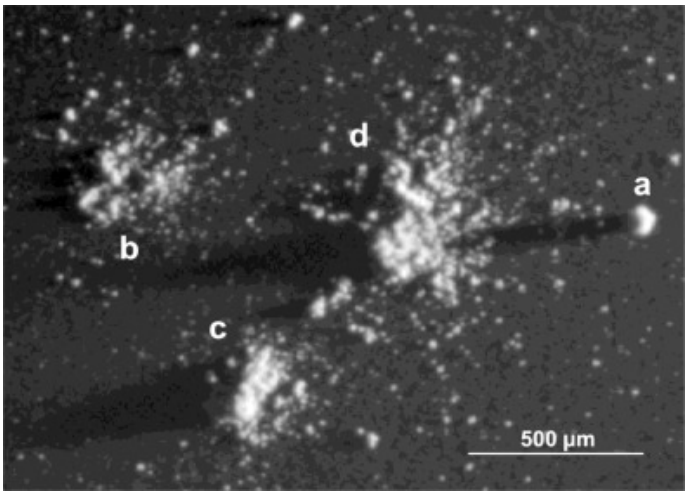

FIGURE 2.9: Morphology of particles collected by COSIMA. The classification used by Langevin et al. (2016) defines: (a) *compact* particle; (b) *glued cluster*; (c) *rubble pile*; (d) *shattered cluster*.

particles formed by thermal processing as for instance the compaction through melting.

- **Fluffy**: particles with high porosity $> 95\%$, fractal structure, necessary to justify the high porosity and with low strength, of the order of Pa.
- **Porous**: particles with porosity between 10-95%, aggregates structure taken together by the Van Der Waals force with low strength, of the order of KPa.

Fractality The porosity of the aggregate particles is strictly correlated with the fractal dimension of the dust. An object is a fractal when it shows similar pattern at different scales, it has indeed the property of self-similarity. Fractal dimension is a characteristic of fractal objects, that quantify their complexity and is defined as $D_f = \frac{\log N(l)}{\log l}$ where l is the scale and $N(l)$ is the number of single elements. Dimension 1 describes the 1-dimensional objects composed by lines, dimension 2 describes surfaces and dimension 3 volumes. Moreover, it can assume intermediate values depending on how the object fills the space. Another important quantity that characterizes the particles structure is the filling factor, defined as $\phi = (\frac{R}{r})^{D_f - 3}$ with R the dimension of the aggregate and r the dimension of the monomers that compose the aggregate. Consequently, the porosity is define as $1 - \phi$. In the case of 67P, Fulle et al. (2016b) measured an average dust porosity of 60%. Fractality is a signature of how pristine the dust is and moreover put constraints on the processes that led the evolution of the comet. Fulle & Blum (2017) measured the nucleus volume fraction occupied by fractal dust in 67P, finding a value of $37 \pm 5\%$ (with fractal dimension $D_f = 1.7 \pm 0.1$, from MIDAS and GIADA direct observations (Mannel et al., 2016)). The presence of such percentage of fractal particles

demonstrates that the comet did not undergo very fast collision, instead it grew by gentle gravitational collapse triggered by velocity of the order of 1 m/s, which is the only way to preserve fractal aggregates.

Size Distribution For the first time with Rosetta mission it was possible to take images of the coma and provide measurements at different distances from the nucleus and during a consistent interval of time and therefore to obtain the dust size distribution of the cometary dust in different moments. Before the 2015 equinox the dust came mainly from the Hapi region, in the north hemisphere, and showed a power low index $\alpha = -3$ which implies that both the dust mass and cross-section mainly depend on mm-sized particles. The steeper is the curve, the more important is the contribution of small particles. After the equinox 2015 the dust came mainly from the erosion in the south hemisphere of the comet, following a power law with index of $\alpha = -4$. It implies the presence of a bigger amount of pristine material, likely preserved in the interior of the nucleus and lift by the increasing activity approaching the perihelion passage (Fulle et al., 2016c; Merouane et al., 2017; Rotundi et al., 2015).

Dust to ice ratio Dust to ice ratio (DIR) is a fundamental parameter to characterize the comets. Before perihelion the dust to ice ratio of 67P was measured by Rotundi et al. (2015), finding a value of 6 at 3.6 AU. During the perihelion and immediately after, dust to ice ratio reached values up to 100 (Fulle et al., 2016b), implying a high percentage of dust ejected from the nucleus with respect to water ices. 67P is indeed a particularly dusty comet, probably formed in a region of the protosolar nebula drier than the region in which CI formed (Fulle et al., 2016b). It is important to notice that there are boulders of several meters that were lift up during the perihelion activity, which increase the overall mass loss rate of one order of magnitude (see Tab. 2.5, the last two cases). Dust loss rate is computed as follows: $Q_m = 2\pi R^2 v \rho m$, where R is the nucleocentric distance, v is the mean dust velocity in each mass bin, ρ is the space density, m the mass relative to certain mass bin. GIADA obtains velocity and mass from direct measurements, while from the OSIRIS images it is not direct. It is necessary to determine the distance first with parallax methods (Ott et al., 2017) and then to derive the size, to assume a density ($10^3 kg/m^3$) and to compute finally the mass.

r_h [AU]	Q_m dust [Kg/s]	Q_w water [Kg/s]	ref
3.6	-	1.2	Rotundi et al. (2015)
2.2	60 ± 10	11	Fulle et al. (2016c)
2.1	70 ± 30	13	Fulle et al. (2016c)
perihelion[a]	$(1.7 \pm 0.9)10^4$	150	Fulle et al. (2016c)
perihelion[b]	$(1.5 \pm 0.5)10^3$	150	Fulle et al. (2016c)
perihelion[c]	8297	-	Ott et al. (2017)

TABLE 2.5: Values of dust and water mass loss rate. r_h heliocentric distance. Q_m is the dust loss rate and Q_w the water loss rate. Dust mass loss rate for perihelion[a] considers all mass bins, for perihelion[b] considers only mass less than 1 kg and for perihelion[c] is computed from the analysis of 250 particles near perihelion (Ott et al., 2017).

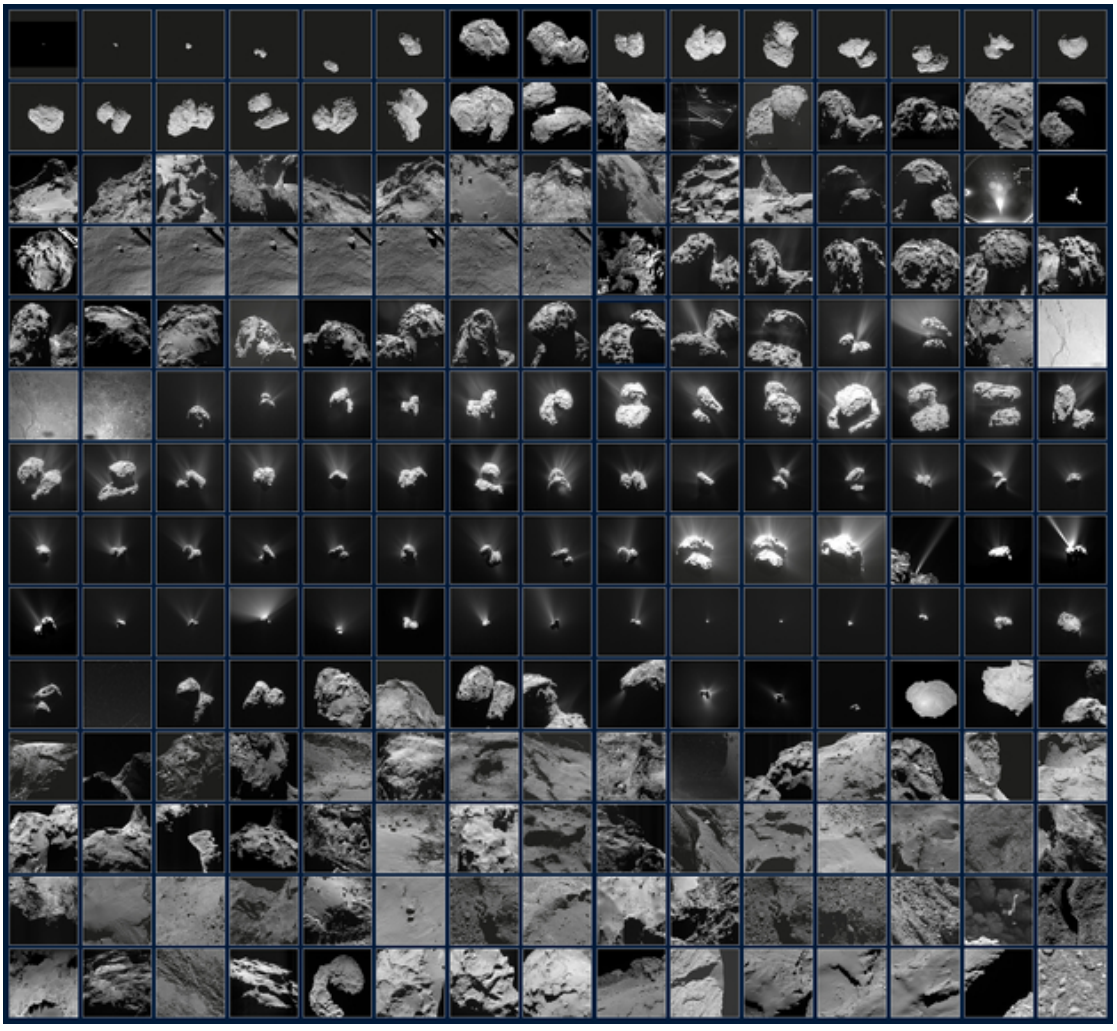

FIGURE 2.10: These mosaic composed by 210 images reflects the Rosetta view of comet 67P/Churyumov–Gerasimenko between July 2014 and September 2016. [Credit: ESA/Rosetta/NavCam–CC BY-SA IGO 3.0; ESA/Rosetta/MPS for OSIRIS Team MPS/UPD/LAM/IAA/SSO/INTA/UPM/DASP/IDA; ESA/Rosetta/Philae/-CIVA; ESA/Rosetta/Philae/ROLIS/DLR].

Chapter 3

Scattering Theory

In this chapter we explain the basic concepts of the scattering theory. Given the vastness of the topic, we refer to the exhaustive books of Hapke (2012) and Van de Hulst (1957) and to the reviews of Kimura et al. (2016) and Bagnulo et al. (2015). In the last section we present a brief description of the meteorites classification and properties, based on the book of Richard Norton (2002).

The basic to understand and interpret the data provided by in situ measurements or ground and space-based observations of cometary dust, lies in the scattering theory. In fact, the dust particles interact with solar radiation partly absorbing and partly scattering it and it is exactly the scattered light that makes the dust coma and tail visible.

The theory describes quantitatively the behavior of the electromagnetic field interacting with one or more particles. Two of the most representative quantities to be determined that characterized the behavior of the radiation are the *phase function*, defined as the distribution of the radiation intensity with respect to the phase angle, and the *linear polarization curve*, which evaluates the degree of polarization at each phase angle.

Several scattering models have been developed for different particle shapes, starting from the classical sphere (Mie theory) to more complicated structures, as cylinder or spheroids. Actually in nature we find irregular particles, as the case of planetary regolith or atmospheric aerosol, moreover, from the measurements provided by space mission such as Vega1 and Vega2, Stardust, Rosetta and also from the analysis of stratospheric interplanetary dust of cometary origin (Rotundi et al., 2014), we know that cometary dust grains are fluffy aggregates with irregular structure (Fulle et al., 2015a; Langevin et al., 2016). Certainly the theory of scattering for those grains is very complex and needs to be supported by laboratory experiments.

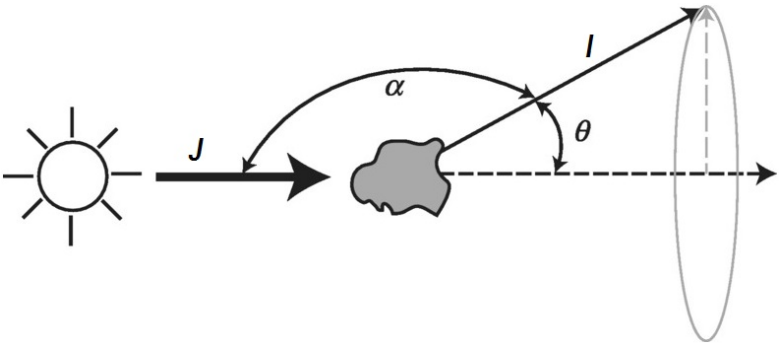

FIGURE 3.1: A schematic diagram of the scattering. J is the incoming light beam, I the scattered beam, α the phase angle and θ the scattering angle.

3.1 Mie theory for spherical and homogeneous particles

The Mie theory solves the scattering problem in the simplest case of spherical and homogeneous particles. The method basically consists in solving the Maxwell equations in spherical coordinates, given the appropriate set of boundary conditions on the surface of a sphere. The procedure is quite complex and if the reader wants to go deeper in the details of the mathematical computation can refers to the work of Hapke (2012). As result we left with an expression that describes the external and internal electromagnetic fields as function of the scattering angle and of the distance from the center of the sphere. Let **J** be the incoming *irradiance* (power per unit area of a collimated beam) and **I** the scattered *radiance* (power per unit area per unit solid angle of an uncollimated beam), see Fig. 3.1. We define the quantity P_{ext} the amount of power of **J** that affect the particle. Therefore, the *extinction cross section* is:

$$\sigma_{ext} = P_{ext}/J, \tag{3.1}$$

and accordingly, we define the *scattering cross section* as $\sigma_{sca} = P_{sca}/J$ and the *absorption cross section* as $\sigma_{abs} = P_{abs}/J$ that are related by $\sigma_{ext} = \sigma_{sca} + \sigma_{abs}$.
One of the aim of the scattering theory is to determine the efficiency factors Q_{ext}, Q_{sca} and Q_{abs}. These three dimensionless quantities describe the amount of radiation extincted, scattered and absorbed by the particle. They are defined as:

$$Q_{ext} = \sigma_{ext}/\pi r^2, \tag{3.2}$$

and thus $Q_{sca} = \sigma_{sca}/\pi r^2$ and $Q_{abs} = \sigma_{abs}/\pi r^2$. Therefore, the following relation is satisfied:

$$Q_{ext} = Q_{sca} + Q_{abs}. \tag{3.3}$$

One of the most important physical quantity defined by the theory is the *phase function* $\Pi(\alpha)$, which describes the angular pattern into which the light is scattered. In the case

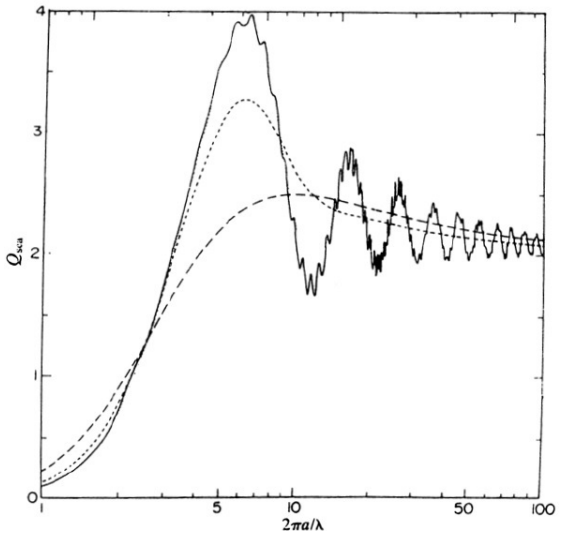

FIGURE 3.2: The scattering efficiency as function of the size parameter X. Refractive index is $n_r = 1.33$, $n_i = 0$. The solid curve refers to the case of single particle, the dotted and dashed lines refer to different particles distributions. (Hansen & Travis, 1974a).

of unpolarized incoming light it is defined by the following equation:

$$I = \frac{\varpi}{4\pi}\Pi(\alpha)J \tag{3.4}$$

where $\varpi = Q_{sca}/Q_{ext}$ is the so-called single-scattering albedo. In the case of a incident and scattered light beams partially polarized, the relation becomes:

$$\mathbf{I} = \frac{\varpi}{4\pi}\mathbf{MJ} \tag{3.5}$$

where **J** and **I** are incident irradiance and scattered radiance in form of Stokes vectors (see paragraph 3.3). **M** is the scattering matrix, or *Mueller matrix* that is a 4x4 matrix in which each element is function of the phase angle α. In particular the first element is the phase function $\Pi(\alpha) = M_{11}$ and $P(\alpha) = -M_{12}/M_{11}$ represents the polarization. These fundamental quantities depend on the characteristic parameters of the particles such as the size, the shape and the composition and therefore give important information about the nature of the dust.

The Mie solutions for the scattering problem depend only on two parameters: the refractive index of the medium, n, and on the size parameter, $X = 2\pi r/\lambda$, where r is the radius of the particle. Therefore, it is possible to define three main scattering regimes based on the size parameter value: for $X << 1$ we are in the Rayleigh region, for $X = 1$ in the resonance region and for $X >> 1$ in the geometric-optics region.

In Fig. 3.2 is shown the dependence of the extinction efficiency Q_{ext} with the size

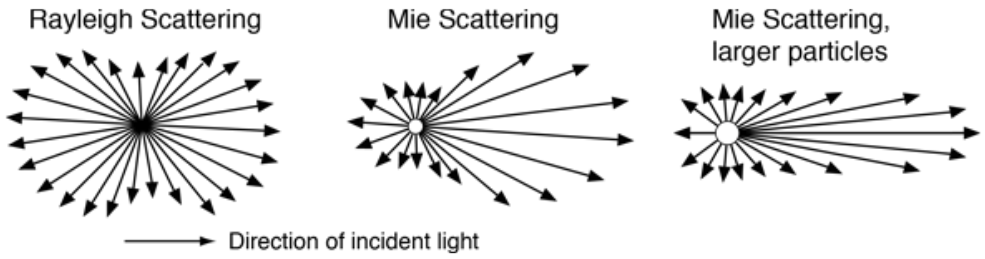

FIGURE 3.3: Scattered light directions in the case of Rayleigh and Mie scattering.

parameter, for different value of refractive index. For small value of X the curve refers to the Rayleigh regime and it varies proportional to $1/\lambda^4$, in the intermediate region it varies as $1/\lambda$ while in the geometric-optics it approaches the value 2. The effect of higher absorption (dotted and pointed curves) reduces the strength of the resonances (solid curve), making the curve smoother. These relations are responsible of the color of the sky, in fact the aerosol in the atmosphere smaller than the wavelength of visible light (called *Rayleigh scatterers*) favour the scattering of blue wavelengths rather than the red ones, given the dependence with $1/\lambda^4$. In the case of clouds, instead, we are in the intermediate regime since the water droplets are bigger, therefore the dependence with the wavelength is such that all the spectrum is scattered in the same way, producing the typical white colour of the clouds.
Also the phase function shows a dependence from the scattering regime considered. In Fig. 3.3 we see the schematic diagrams that illustrate the direction of the scattered beams. In the case of small particles we expect an equivalent forward and backward scattering while for larger size of particles the forward scattering becomes more and more dominant.

3.2 The case of irregular particles

In the last section we have illustrated the case of spherical and homogeneous particle. However, in nature the dust is far from being spherical, favouring instead more irregular shapes. There are several theoretical approaches to solve the complex problem of irregular particles scattering. The more common and widespread approaches are the following:

DDA The *Discrete Dipole Approximation* is a technique that approximates the particles by a series of electric dipoles which field results as a combination of all the individual oscillations. The advantage of this method is that it can be applied to particles of any shape. For N dipoles there are $3N$ linear equation to be solved, so the complexity is quite

high and requires a lot of CPU time. It was theorized firstly by Purcell & Pennypacker (1973) and then reviewed by Draine & Flatau (2000).

T-matrix This method, known also under the name of "extended boundary condition", is a technique in which the incident and scattered fields are described with an expansion in spherical function on a sphere that circumscribes the nonspherical particles. It is particularly efficient for axisymmetric particles and aggregates of spheres. Initially proposed by Waterman in 1965-79, then reviewed by Mishchenko et al. (2000) who made available the program for download.

RTMCA The *Ray-tracing Monte Carlo Approximation* is applied in geometric optics regime. Actually, when the particles are quite bigger than the wavelength the light rays can be treated with the laws of refraction and reflection. This approach has been used by several authors, as for instance by Muinonen & Saarinen (2000).

Laboratory experiments Laboratory experiments are of fundamental importance to interpret the data. The scattering problem solution is quite complex, especially if applied to the cometary dust. Theoretical models are based on the caveat of particles spherical shape, but it is necessary to consider the complexity of the structure and the physical and chemical properties of the dust to study it in a reliable way. Therefore it rises up the necessity to produce cometary analogs and measured their characteristics, such as phase function and polarization degree, with a direct methodology, in laboratory. The IAA group in Spain has set up a laboratory that allows to measure the 16 elements of the scattering matrix. They provide a database (Muñoz et al., 2012) of measurements for various materials at different wavelengths, as volcanic hashes (Muñoz et al., 2002), fluffy aggregates (Volten et al., 2007) and more recently the mm particles (Muñoz et al., 2017).

3.3 Polarization

An electromagnetic wave can be represented by two waves with electric field vectors perpendicular one with respect to the other:

$$\mathbf{E}_x = E_{x_0} cos(kx - \omega t + \phi_x)\mathbf{u_x} \tag{3.6}$$

$$\mathbf{E}_y = E_{y_0} cos(kx - \omega t + \phi_y)\mathbf{u_y} \tag{3.7}$$

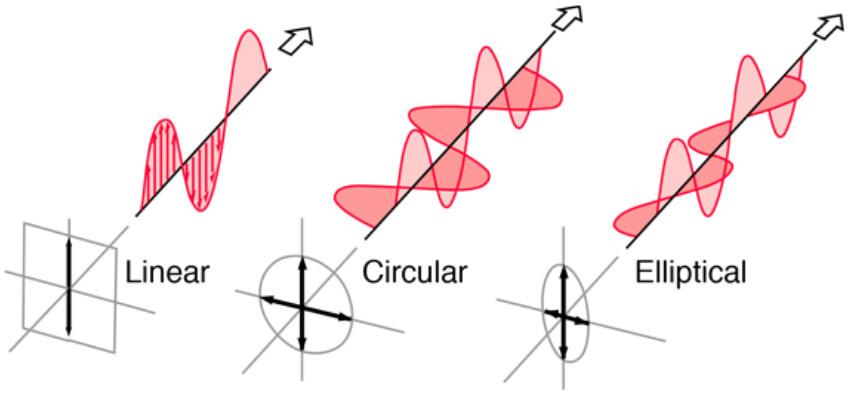

FIGURE 3.4: The linear circular and elliptic polarization. The wave represents the electric field.

with k the wave vector, ω the angular frequency and ϕ the phase.
Basically the polarization is the ability of the radiation waves to oscillate or not in a preferential plane and is defined as follows:

$$P_r = \frac{I_\perp - I_\parallel}{I_\perp + I_\parallel} \tag{3.8}$$

where $I_\perp$ is the component of intensity with the electric vector pointing perpendicularly with respect to the scattering plane and $I_\parallel$ the component parallel to the plane. There are different type of polarization, the *linear polarization* occurs when $\phi_x = \phi_y = 0$, i.e. when the parallel and perpendicular components of electric field are in phase and consequently the vector $\mathbf{E}$ oscillates on the same plane (see Fig. 3.4). *Circular polarization* occurs when $\phi_x \neq \phi_y$ and the intensity of the two components is the same $E_{x_0} = E_{y_0}$. Therefore the vector $\mathbf{E}$ projects a circle on a the plane perpendicular to the scattering plane. Finally, when $E_{x_0} \neq E_{y_0}$ we have the more general case of *Elliptic polarization.*

Stokes vectors A propagating wave of partially polarized light can be also represented in terms of the Stokes vectors as $\mathbf{I} = [I, Q, U, V]$, which components are defined as follows:

$$\begin{aligned} I &= \mathbf{E_x}^2 + \mathbf{E_y}^2 \\ Q &= \mathbf{E_x}^2 - \mathbf{E_y}^2 \\ U &= 2\mathbf{E_x}\mathbf{E_y} cos(\phi_y - \phi_x) \\ V &= 2\mathbf{E_x}\mathbf{E_y} sin(\phi_y - \phi_x). \end{aligned}$$

Those vectors have physical meaning: I represents the total intensity, Q the difference between the linearly polarized intensity along the x-axis and that along the y-axis. U is defined by the difference of the linearly polarized intensity along the directions rotated

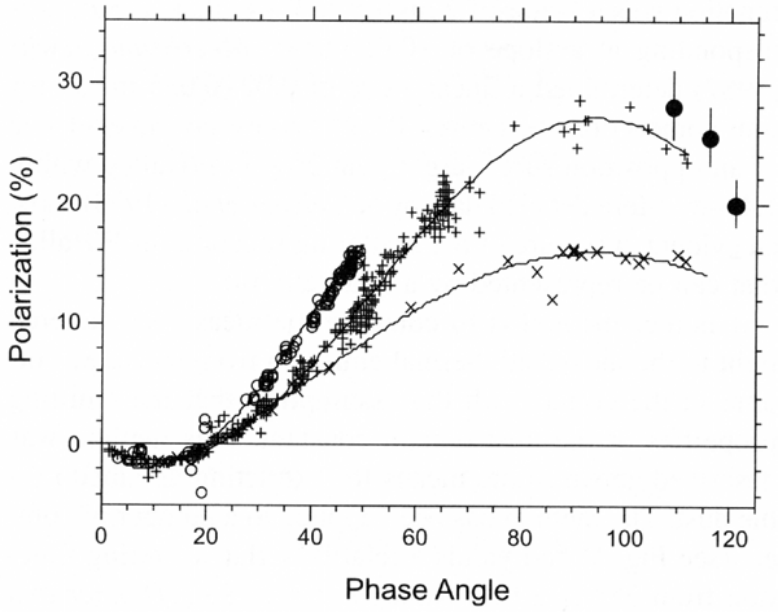

FIGURE 3.5: Two classes of comets are recognized, (x) comets with low maximum in polarization, with low value of dust to gas ratio and (+) comets with higher maximum, corresponding to higher value of dust to gas ratio. In the panel appear also the (○) Comet C/1995 O1 Hale-Bopp and the (●) Comet C/1999 S4 LINEAR at disruption, (Kolokolova et al., 2004).

by 45° and -45° from the x. V is related to the circular polarization, defined as the left-handed polarized intensity minus the right-handed polarized intensity.
Following this formalism the polarization is defined as $P = -Q/I$.

3.3.1 Polarimetry of comets and asteroids

Polarimetry is a technique that allows to measure the degree of polarization of an electromagnetic radiation. It is a very important tool to investigate planetary surfaces, asteroids, comets and atmospheres.
Generally light scattered by a surface or by a cloud of particles results (partially) polarized, thus it has a preferred plane of oscillation. In case of analysis of point sources the linear polarization curves is computed putting together all the measurements obtained at different points of the trajectory which correspond to different phase angles.
Otherwise, in case of extended objects it is possible to obtain extended maps to be compared with color maps and photometric observations, in order to reveal the features responsible of specific behaviour.
Finally, the spectropolarimetry is a technique that provides polarimetric measurements at different wavelengths. One of the evidence of these measurements concerns the cometary dust morphology, showing that to explain such observations it is necessary to consider aggregates and not compact particles (Kolokolova et al., 2004).

Polarization parameters	References
$P_{max} \propto X$ $(X >> 1)$	Liu et al. (2015)
$P_{max} \propto 1/\sigma$	Liu et al. (2015)
$P_{max} \propto \kappa$	Zubko et al. (2016)
$\alpha_{max} \propto Im(n)$	Zubko et al. (2009)
$P_{max} \propto Im(n)$	Zubko et al. (2009)
$A \propto 1/Im(n)$	Zubko et al. (2009)
$P_{min} \propto Im(n)$	Zubko et al. (2015)
$\alpha_{min} \propto Re(n)$	Zubko et al. (2015)
$P_{max} \propto V_{inc.}$	Escobar-Cerezo et al. (2017)
$P_{max} \propto 1/rough.$	Escobar-Cerezo et al. (2017)

TABLE 3.1: Some dependence of polarization parameters with physical parameters characterizing the dust particles. P_{max} is the maximum value of linear polarization, σ is the deviation from a gaussian sphere, κ is the absorption coefficient, $Im(n)$ the imaginary part of the refractive index, $Re(n)$ the real part of the refractive index, $V_{inc.}$ is the volume of inclusions of various material embedded in a particle, $rough.$ is the surface roughness of the particle.

In the study of comets, polarimetry helps in the interpretation of different types of observations, especially focused on the coma. The main results regarding cometary population, obtained with this technique are summarized in the following:

1. The polarization curves are qualitatively similar to that of asteroids. They have the typical bell-shape with small negative branch for the low values of phase angle.

2. The maximum value of polarization defines two classes of comets depending on the dust to gas ratio, being higher for dusty comets (see Fig. 3.5).

3. Multiwavelengths observations reveal that to fit the data aggregates shapes are required instead of compact structures.

4. The value of inversion angle is linked with the composition, while the value of minimum polarization varies with both the surface roughness and the composition.

5. Size, shape, absorption properties, composition etc. are entangled quantities. Only with the help of the simulations and experiments it is possible to constrain the nature of the observed material.

In the asteroids research field, polarimetry is useful to determine some specific quantities. In the following a brief list of the main application is presented:

1. The minimum value of polarization allows to compute the geometrical albedo p through an empirical relationship: $log_{10}(p) = -1.419 log_{10}(P_{min}) - 0.918$.

2. Polarization, combined with photometry, allows to estimate the size of the asteroids, thanks to the following empirical relationship: $log(D) = 3.1236 - 0.2H - 0.5log(p_v)$, where D is the diameter, H the absolute magnitude and p_v the geometrical albedo.

3. Polarimetry helps in the taxonomic classification, bringing some parameters, as the inversion angle α_{inv}, as new constraints.

4. The parameter space defined by $\alpha_{inv} - P_{min}$ plot generates additional constraints on

Family	Class
Chondrites	Carbonaceous chondrite (CC): CI, CM, CR, CO, CV, CK, CH Ordinary chondrites (OC): H, L, LL Enstatite chondrites: EH, EL R chondrites
Primitive achondrites	Acapulcoites Londranites Winonaites
Differentiated meteorites	Asteroidal achondrites Martian meteorites Lunar meteorites Stony irons Irons

TABLE 3.2: Meteorites classification by Rubin (1997).

the size of the material that cover the asteroid surface (thin powder or rocks).

Opposition effect

The presence of a negative branch in the polarization curves is a phenomenon not yet fully explained. For the low values of phase angles the polarization becomes negative, i.e. the oscillation plane is inverted and the scattering of parallel component is favoured, rather than the perpendicular one. This effect happens in correspondence with a brightness enhancement in the backscattering regime. The possible explanations are two, depending basically on the size of the particles involved.

The Shadow-Hiding Opposition Effect (SHOE) occurs in particulate medium in which the particles are big enough to shadow each other. This is what happened on the regolith surfaces, causing an increase in brightness when observed at zero phase angle.

A second explanation consists in the Coherent Backscatter Opposition Effect (CBOE). It occurs both if particles are bigger or smaller than the incident wavelength. Part of the wave front is scattered many times before escaping the medium. For each path followed by the light beam, an opposite path exists, travelled by the other portion of the wave front. This results in a brightness enhancement at low values of phase angle, due to the superposition of the two wave fronts once come out from the scattering material. They will be in coherent phase since they have travelled the same path, therefore they will superpose making constructive interference producing a brightness 4 time higher than the initial one.

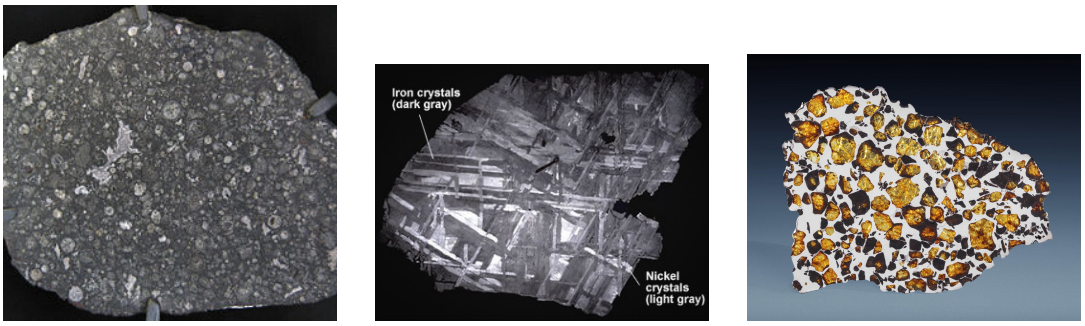

FIGURE 3.6: The Allende meteorite on the left panel, which is an example of carbonaceous chondrite. In the left part of the slice a CAI can be seen. In the center panel are shown an iron meteorite called otahedrite, and on the right panel a stony iron meteorite named pallasite.

3.4 Meteorites as cometary analogs

Meteorites are fragments of asteroids, comets and interplanetary medium that cross the Earth atmosphere and reach the ground. Every year $4{\cdot}10^4$ tons of material smaller than 1 mm fall on the Earth (Cremonese et al., 2012). The exterior of the meteorites is modified by several factors: the friction during the passage through the atmosphere that creates a fusion crust, the mechanical weathering due to rapid fluctuations in temperature or chemical weathering that happens when the sample is exposed to water and oxygen. Otherwise the interior remains rather unaltered. Antarctica is a favoured sites for the conservation and research of meteorites since the low temperature and low degree of weathering limit their degradation.

The classical classification by Prior (1920) divided the meteorites into the following major groups: *chondrites*, *achondrites*, *stony-irons* and *irons*. The current classification by Rubin (1997) replaces the previous one and is reported in Tab. 3.2. Meteorites are divided into three main groups and various subgroups: *chondrites*, *Primitive achondrites* and *differentiated meteorites*, see Tab. 3.2.

Among all the classes we focus on the chondrites family and in the following we give a brief description of their characteristics.

3.4.1 Chondrites

Chondrites are the most common type of meteorites, in fact they include the 82% of the total catalogue. They give their name to their typical texture, mainly composed by chondrules: spheroidal structures dispersed in an homogeneous matrix. They can reach the 70 % of the total volume of the meteorite, with size ranging from 0.1 to 4 mm (even cm in few cases).

Type	Name	Texture	Abundance (%)
Porphyritic	PO	porphyritic olivine	23
	PP	porphyritic pyroxene	10
	POP	porphyritic olivine-pyroxene	48
Nonporphyritic	RP	radial pyroxene	7
	BO	barred olivine	4
	C	cryptocrystalline	5
Granular	GOP	granular olivine-pyroxene	3

TABLE 3.3: Chondrules classification by Gooding et al. (1980).

Chondrules Chondrules are classified based on their texture which depends on their mineral composition, the cooling rates and the degree of melting [p107]. Gooding et al. (1980) recognized three main groups and various subgroups: porphyritic, nonporphyritic and granular types (see Tab. 3.3). Their differences provide information about the environment in which they have formed.
First group is the most common, including about the 80% of the total amount of chondrules. They likely formed around dust grains, helping the condensation of material from the solar nebula, therefore they did not undergo melting processes. The granular type is an intermediate group characterized by the particularly small dimension of olivine and pyroxene grains, uniformely distributed into a glassy mesostasis. The nonporphyritic chondrules instead, experienced a fully molten phase. They condensed in the external region of the solar nebula and completely liquefied into spherical droplets after heating, to quickly cool down and solidify after.

Carbonaceous chondrites Among the overall chondritic classes the carbonaceous chondrites are the most primitive and rare, representing only the 3.8% of the total family. Radiometric dating determines that CC formed around 4.5 Gyr ago (Chen & Wasserburg, 1981; Mahnes et al., 1987) and it is confirmed by the similarity with the solar photosphere composition of some of them (CI class). Moreover, in the matrix of CC are trapped presolar grains (diamond, graphite, PAH, ecc.), likely injected into the system from nucleosynthetic sites as supernovae (Lugaro, 2007).
The main differences among the CC types are summarized in Tab. 3.4. This type of meteorites look like dark charcoal and this is due to the large amount of carbonaceous material that characterizes their composition, which includes also aminoacids. Since they have formed in the cold outer disk, they are enriched in volatile elements with respect to the ordinary chondrites. The ferrous matrix proves they have formed in a more oxidate environment, necessarily in the outer part of the Solar System. They have experienced aqueous alteration within the first 10Myr of accretion. The water likely percolated through the rocks and reacted with the refractory silicates producing hydrated silicate minerals, similar to terrestrial phyllosilicates. Those meteorites did not

	CI	CH	CV	CO	CR	CK
Chondrule size (μm)	-	270	1000	150	700	700
Aqueous alteration	high	high	low	low	moderate	moderate
CAI (Vol%)	-	2-8	6-13	10-18	0.1-1	$\sim$4
ρ (g/cm^3)	2.2	2.5-2.9	3.5	-	-	-
Chondrule (vol%)	-	12 sparse	sparse	38 abundant	abundant	abundant
Petrographic type	1	2	3	3	2	3-6

TABLE 3.4: Characteristic of carbonaceous chondrites.

experienced high temperature or pressure, therefore they did not undergo high thermal metamorphism and they are preserved intact as in the moment they have formed.
The parameter that specifies the degree of alteration of the meteorites is the petrographic type. Tab. 3.5 shows the main features associated with this parameter. Low values as 1 or 2 indicate almost no thermal metamorphism but high water alteration. Those meteorites show high percentage of carbon while are depleted in minerals and they have an opaque matrix. The successive petrographic types are associated with phases of high temperature, they show a remarkable presence of minerals and a transparent matrix. Usually CC have value 2 or 3, therefore they have experimented a low degree of water and thermal alteration.
Primitive meteorites like CC could represent fragments of asteroids or NEOs that include also a percentage of extinct comets (DeMeo & Binzel, 2008).

	1	2	3	4	5	6
	Aqueous alteration $\longleftarrow$			Thermal metamorphism $\longrightarrow$		
T (C°)	< 150	< 200	400	600	700	750-950
a	-	$\geq 5\%$	more homogeneous			
b	3-5%	0.2%	-	-	$< 0.2\%$	-
c	22%	-	-	-	-	
d	-	Ni<200 mg/g	-	-	$> 20\%$	-
e	opaque			transparent		

TABLE 3.5: A chemical-petrologic classification for the chondritic meteorites. Petrographic types from 1 to 6 are on the first line. a: olivine and pyroxene homogeneity; b:carbon (% weight); c: water; d: metallic minerals; e: matrix Van Schmus & Wood (1967).

Chapter 4

Post-perihelion photometry of dust

This chapter is taken from the published work of Frattin et al. (2017). We present a photometric analysis of individual dust grains in the coma of comet 67P/Churyumov -Gerasimenko using OSIRIS images taken from July 2015 to January 2016. We analyzed a sample of 555 taken during 18 days at heliocentric distances ranging between 1.25 AU and 2.04 AU and at nucleocentric distances between 80 km and 437 km. An automated method to detect the tracks was specifically developed. The images were taken by OSIRIS NAC in four different filters: Near-IR (882 nm), Orange (649nm), FarOrange (649 nm) and Blue (480 nm). It was not always possible to recognize all the grains in the four filters, hence we measured the spectral slope in two wavelengths ranges: in the interval [480-649] nm, for 1179 grains, and in the interval [649-882] nm, for 746 grains. We studied the evolution of the two populations' average spectral slopes. The data result scattered around the average value in the range [480-649] nm, while in the [649-882] nm we observe a slight decreasing moving away from the Sun as well as a slight increasing with the nucleocentric distance. A spectrophotometric analysis was performed on a subsample of 339 grains. Three major groups were defined, based on the spectral slope between [535-882] nm: (i) the steep spectra that may be related with organic material, (ii) the spectra with an intermediate slope, likely a mixture of silicates and organics, (iii) flat spectra that may be associated to a high abundance of water ice.

4.1 Introduction

The Rosetta spacecraft orbited around Jupiter family comet 67P/Churyumov-Gerasimenko for 2 years, reaching distances from the nucleus smaller than 10 km. For the first time

in the history of space missions a spacecraft arrived so close to a comet, allowing observations of the development of the inner coma from inside. During this time range the Optical, Spectroscopic and Infrared Remote Imaging System (OSIRIS by Keller et al. (2007)) mapped the coma from different configurations, providing a detailed understanding of its nature. The large amount of OSIRIS images clearly revealed the presence of individual dust grains, characterizing the overall coma (Davidsson et al., 2015; Fulle et al., 2015b). We focused our investigation on these single grains.

In the past, a coma of icy grains was revealed on Hartley 2 by Kelley et al. (2013) that, for the first time, detected and analyzed single objects of cm-size in a comet's coma. The Rosetta spacecraft permitted a more detailed study of dust grains. For instance, Fulle et al. (2016c) derived a dust size distribution consistent with a differential power law index of -4 for sizes >1 mm and with a power index of -2 for sizes <1 mm at 2 AU. During the perihelion passage, the index decreased to -3.7, indicating a major contribution of grains smaller than 1 mm. An estimation of the masses of cm-size grains is given by Ott et al. (2017), finding values ranging between 10^{-6} kg and 10^{-2} kg on a sample of more than 200 particles.

Dust analysis shows that several complex processes work on the grains, driving their release and changing their behaviour. The increasing activity at short heliocentric distances corresponds to a larger dust grains ejection rate. Such grains are accelerated by gas drag and rocket force due to sublimation of the ice (Agarwal et al., 2016; Gicquel et al., 2016), and undergo different fates: part of them exceeds escape velocity (about 1 m/s) and leaves the cometary coma (Thomas et al., 2015), while another part falls back on the surface (Kramer & Noack, 2015; La Forgia et al., 2015; Lai et al., 2016). Aeolian structures like ripples or dunes are related to this process and to the surface dust transport (Thomas et al., 2015). The dynamics involved in the releasing, and eventually in the falling back, depends on several grains properties as their shapes and rotational state, intimately related with the gas production rate (Fulle et al., 2015b).

A deeper knowledge of the dust nature, through the study of physical and compositional properties of single grains, allows a better understanding of the relationship with the nucleus and the mechanisms involved in the ejection.

In this work we present a spectrophotometric analysis of a wide sample of dust grains, which provides some possible hints on the grain composition. The colour characteristics of single grains were previously measured by Cremonese et al. (2016) on a sample of 70 grains, finding a spectral slope value peaked between 12 and 16 %/100 nm in the wavelength range [480-743 nm]. They also measured a negative spectral slope for 16 grains, associated with the presence of water ice. Now, a larger amount of data and the information coming from an extended range of filters allow to realize a more accurate statistics to describe them.

STP	Epoch	rc (km)	rh (AU)	$\alpha_N(^\circ)$	$\#_{649-882}$	$\#_{480-649}$	$\#_{spectra}$
066GC	2015-07-24	183	1.26	90	41	51	27
067GC2	2015-08-04	238	1.25	89	52	82	28
070GC3	2015-08-25	403	1.25	85	29	29	2
071GC3	2015-08-31	404	1.26	70	38	59	6
073GC1	2015-09-11	326	1.31	119	9	19	5
073GC4	2015-09-15	327	1.31	92	8	13	2
075GC2	2015-09-28	1220	1.37	50	26	43	9
078GC4	2015-10-18	437	1.47	65	35	58	14
079GC1	2015-10-23	389	1.51	63	62	83	21
081GC2	2015-11-06	244	1.61	63	70	91	32
081GT3	2015-11-10	201	1.63	63	83	108	24
082GT4	2015-11-17	141	1.68	62	57	136	47
083GC1	2015-11-19	126	1.70	74	30	44	9
083GT1	2015-11-27	144	1.70	88	31	49	15
086GT3	2015-12-10	99	1.86	89	57	101	39
085GC5	2015-12-14	100	1.90	89	78	116	25
087GT1	2015-12-17	99	1.90	89	26	49	16
089GT2	2016-01-04	80	2.04	89	50	82	18

TABLE 4.1: MTP: Medium Term Planning (1 month); STP: Short Term Planning (1 week); Type: Grain Colours or Grain Track; rc: nucleocentric distance; rh: heliocentic distance;α_N: phase angle of the nucleus; $\#_{649-882}$: number of grains detected with Near-IR and FarOrange filters; $\#_{480-649}$: number of grains detected with Orange and Blue filters; $\#_{spectra}$: number of spectra.

4.2 Detection method

The large amount of data obtained by OSIRIS, (including the dust grains observations), required us to develop an automatic routine able to identify and to analyze the particle tracks present in several images, corresponding to the passage of the particles during the time of integration.

The main aim of this program is to detect the grains tracks and their orientation in the reference system of the image. At the same time it can analyze the point-by-point intensities of the grains tracks as well, thus providing their light curves. The latter show evidences in some cases of periodic oscillations, corresponding to rotating grains Duda & Hart (1973).

The detection of the tracks can be performed taking advantage of a similarity function, a window-based matching function, commonly used in photogrammetry to define the homologues between two images. Dust track features can be easily modeled and the match between the model and the image is a valid probability operator for the presence of the dust grain.

Dust tracks can be modeled by two parameters: their orientation Φ in the reference system of the image and their Full Width at Half Maximum (FWHM), here approximated with a mean value of 1 px. For each orientation (considered with a sampling of

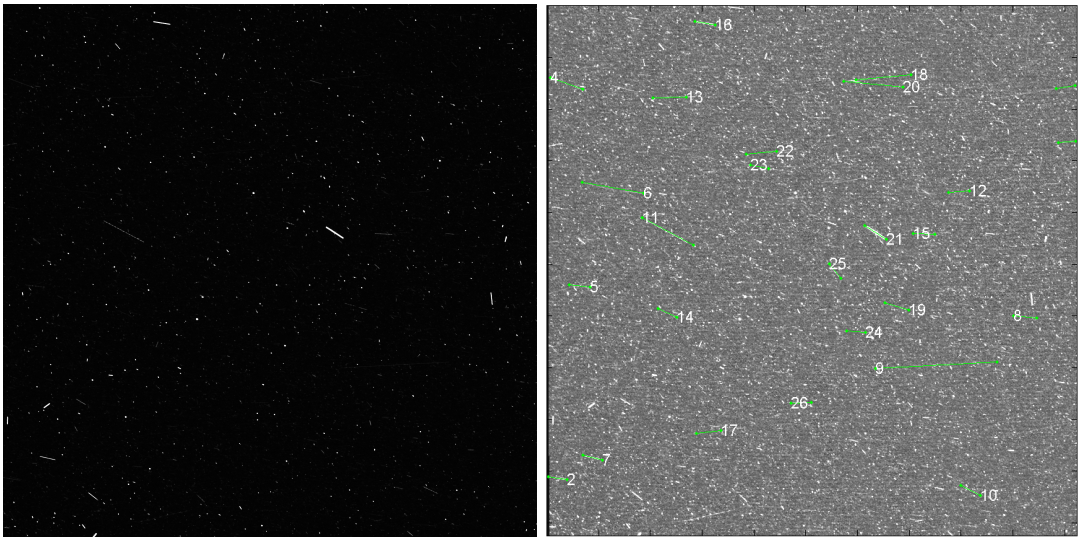

FIGURE 4.1: Final step of the detection on a portion of a NAC image. The detected tracks are identified with a number.

4°), a squared window (classically defined as template T^{Φ}) representing the trail can be synthetically generated simply using a line convolved with a bi-dimensional Gaussian (representing both the grain and the instrument point spread function, PSF). An image representing a subset of templates is shown in Figure 4.2. This bench of templates can be used to detect at the same time the presence and the orientation of the tracks by using, as similarity function, the Normalised Cross Correlation (NCC). The NCC is an important tool in image processing, pattern recognition, and other fields. A common approach to features detection makes use of the correlation between two signals as well as more sophisticated recognition techniques or photogrammetric pipelines. The NCC ($\overline{\otimes}$) evaluates the similarity of a local zone on the image with respect to the generated synthetic tracks. Considering two templates A and B, the NCC is defined as:

$$A\overline{\otimes}_{i,j}B = \sum_{\omega} \frac{(A_{i,j} - m_{i,j}(A))(B_{i,j} - mi, j(B))}{\sigma_{i,j}(A)\sigma_{i,j}(B)} \tag{4.1}$$

Where ω represents the semi-dimension of the squared template, $m_{i,j}$ represents the local mean of the template size, and $\sigma_{i,j}$ the local standard deviation of the template size. The NCC is invariant to local mean and standard deviation, it means it is not influenced by star variability or signal variation. For each orientation Φ the NCC between the template T^{Φ} and the image is computed as:

$$SM^{\Phi}_{(i,j)} = I\overline{\otimes}T^{\Phi} \tag{4.2}$$

The similarity map $SM^{\Phi}_{(i,j)}$ associates to each pixel coordinates and to a defined orientation Φ the probability to find a track in this location with the considered orientation. Despite of image operators (Sobel, Surf), which require to define different threshold

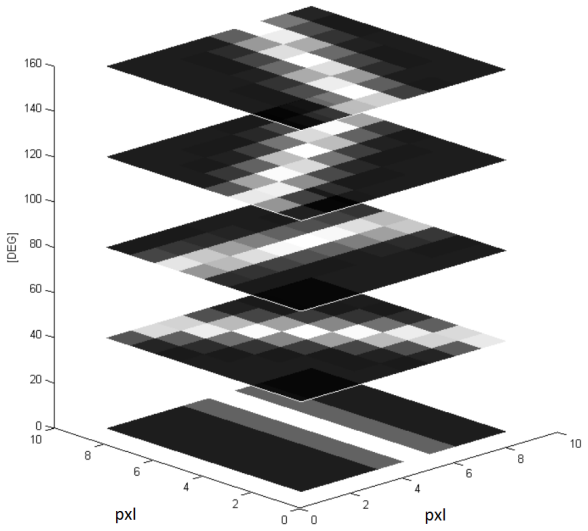

FIGURE 4.2: Subset of templates used to model the tracks. For each orientation, with 4° angular step, a template representing the synthetic trail is defined

depending by background variability, noise, SNR and flux of the trails considered, the NCC approach needs a unique threshold and preserve in $SM^{\Phi}_{(i,j)}$ the information on the track orientation allowing to discriminate overlapped signals.
Relative Standard Deviation (RSD) indicates the ratio between the effective mean signal (with respect to the background) and the standard deviation of the noise. The usage of NCC allows to reach a detection probability of 90 % also in the case of a RSD of 1.75. In fact, given an angle Φ, the presence of a track influences the similarity function of the pixels (i,j) along the direction Φ. This correlation can be detected convolving any level of the $SM^{\Phi}_{(i,j)}$ with the same Template function T^{Φ}, which represents a mono directional low pass filter in the direction considered:

$$SM^{\Phi\prime} = I^{\prime}\overline{\otimes}T^{\Phi} \otimes T^{\Phi} \tag{4.3}$$

allows to increase the performance of the detection (by imposing continuity of the track along its orientation, even where different tracks overlap). Segmentation process (isocurves based on Boolean morphological operators) allows at this point to extract the tracks distinguished by their orientation. This information can be used to avoid fake tracks. An example of the final detection is shown in Figure 4.1.

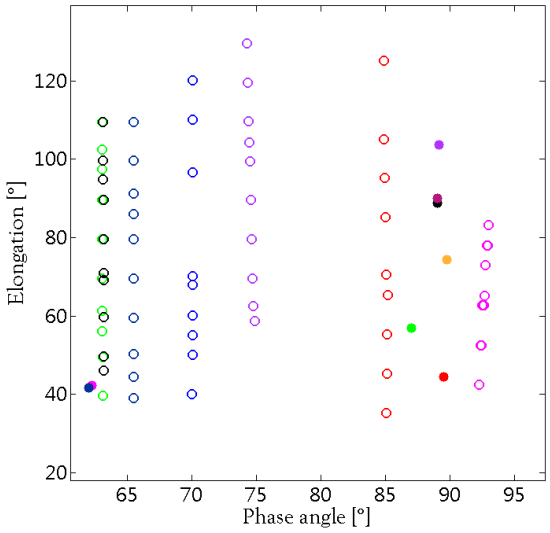

FIGURE 4.3: The empty circles represent the geometry of the sequences taken at different Sun elongation (i.e. the angle formed by the Sun-spacecraft and spacecraft-line of sight directions) keeping fixed the phase angle. The filled circles represent the images taken with both phase angle and elongation fixed. The colours indicate different set of observations.

4.3 Observations

We focused our analysis on images taken in the post-perihelion period, i.e. from the end of August 2015 to January 2016 (two sequences were taken before the perihelion). The images were chosen from the series devoted to grain colour (GC) and grain track (GT) acquired by the NAC (Narrow Angle Camera) in 4 different filters: Near-IR (λ = 882.1 nm, bandwidth = 65.9 nm), FarOrange (λ = 649.7 nm, bandwidth = 84.5 nm), Orange (λ = 649.7 nm, bandwidth = 84.5 nm) and Blue (λ = 400 nm, bandwidth = 74.9 nm). The difference between FarOrange and Orange filters lies in the presence of a focusing plate: the first one focuses from infinity to 2 km, while the second one from 2 to 1 km (Tubiana et al., 2015). These two types of series were taken with different observational geometries. In GC dataset the camera scans the coma in the Sun-comet-spacecraft plane at a fixed phase angle α (i.e. the angle formed by the Sun-comet and comet-spacecraft directions). In the GT dataset, the camera orientation remains fixed, so observing always the same coma region.

The angles describing the above mentioned configurations are shown in Figure 4.3, where the empty circles refer to GC images and the filled ones to GT. In total, we analyzed 555 images taken during 18 days at heliocentric distances ranging between 1.25 AU and 2.04 AU and at distances from the nucleus between 80 km and 437 km (one set being taken at 1220 km). The entire dataset is reported in Table 4.1.
In each image we identified 2 types of grains: those in bound orbits with the nucleus

$s(m)$	p	$\Delta(km)$
10^{-2}	0.04	20
10^{-3}	0.04	2.0
10^{-6}	0.04	0.0020
10^{-2}	0.10	31
10^{-3}	0.10	3.1
10^{-6}	0.10	0.0031

TABLE 4.2: Maximum distance Δ at which the camera is able to observe an aggregate of dimension s, according to equation 4.4. The dimension s is related to the albedo p and to the phase function ϕ. The values are obtained considering a radiance $J = 10^{-7} W m^{-2} nm^{-1} sr^{-1}$ at heliocentric distance $r_h = 1.5$ AU.

and those outflowing. The bound grains appeared as faint dots in the background, far from the spacecraft, while the outflowing grains appeared as tracks and are closer to the spacecraft (Rotundi et al., 2015). To estimate the distance at which the camera is still able to detect a particle we used the equation by Agarwal et al. (2016):

$$\Delta = \sqrt{I_{\odot} \frac{s^2 p \phi(\alpha)}{J r_h^2}} \tag{4.4}$$

where Δ is the distance of the grain from the camera, $I_{\odot} = 1.565\ W m^{-2} nm^{-1}$ is the solar flux at 1 AU in the Orange NAC filter (F22), s is the grain size in m, p the albedo, $\phi(\alpha)$ is the phase function of the coma, J is the flux of the aggregate in $W m^{-2} nm^{-1} sr^{-1}$ and r_h is the heliocentric distance measured in AU. In Table 6.3 we report the maximum distance Δ at which the camera is able to observe an aggregate of dimension s, extended on a 4 pixels area. Clearly this quantity depends on the object's composition and on the illumination's conditions. We considered, as reference, the lower value of radiance measured for a grain $J = 10^{-7} W m^{-2} nm^{-1} sr^{-1}$. Since the dust material is supposed to be dark, we used 2 values for the albedo: 0.04 and 0.1. The phase function is that determined by Fornasier et al. (2015) for the nucleus at 90°, $\phi = 0.02$. During the period of our analysis the spacecraft was at heliocentric distances ranging between 1.3 AU at perihelion and 2 AU on January 2016, so we used an average value of $r_h = 1.5$ AU for our estimates. As an example of the camera sensitivity, we obtain from equation 4.4 that the camera is able to resolve an aggregate of 1 cm with low albedo at a range of 20 km. Generally, the images were taken in groups of 3 or 4, following the filter sequence: Near-IR, FarOrange, Orange, Blue. The exposure time was 12.5 s and the gap between two observations was about 11 s, short enough to follow the grain motions in more than one image. In fact, we were able to detect a large amount of grains: 746 with Near-IR and Orange and 1179 with Orange and Blue. Most of the grains we detected with the first two filters are not the same we found with the last two. However, there were 339 cases in which we could find the same grain in all the filters. We will describe them in

the section 4.5.

4.4 Colors of the grains

In order to characterize the photometric properties of the dust grains, we measured their spectral slopes using the formula by Jewitt & Meech (1986):

$$S = \frac{I/F_{Red} - I/F_{Blue}}{\lambda_{Red} - \lambda_{Blue}} \frac{20000}{I/F_{Red} + I/F_{Blue}} \tag{4.5}$$

where I/F is the reflectance of the grain in the two filters, with I the radiance of the object and F the solar flux, λ is the central wavelength of the filter. The spectral slope S is expressed in units of %/100 nm.
To perform a statistical analysis, we decided to consider the data set collected on the same day as a group, even if they were taken at different phase angles. These corresponds to assume that phase reddening in the dust coma was negligible. Actually, on the surface of the nucleus, a variation of the spectral slope of about 0.1%/° was measured in the range of phase angle of $[1.3° - 52°]$ and in the wavelength range of [535-882] nm (Fornasier et al., 2015). This effect has been attributed to the multiple scattering, due to the roughness of the surface, and it becomes more important at large phase angles. However, for what concerns the dust coma, we do not expect any significant correlation between the reflectivity gradient and the phase angle (Jewitt & Meech, 1986). In fact, the coma of the comet is effectively optically thin, likely composed by absorbent material with a low albedo, supporting the assumption that the multiple scattering is not an important contribution (Fink & Rinaldi, 2015).
Bertini et al. (2017) studied the variations of the coma colours as function of phase angle and deduced that the single scattering is the dominant process on the 67P coma. Therefore measured colours are not affected by a systematic effect depending on the geometry of observation.

Under this assumption, we could derive the spectral slope for all the grains detected and group them depending on the dates.
We measured the spectral slopes of 1179 grains in the wavelengths range [480-649] nm and 746 in the range [649-882] nm. The two populations represent a different sample, since it was not always possible to identify the same grain in all the filters. A subset of 339 grains was recognized in the four filters and will be analyzed in Section 4.5. An example of our results is shown in Figure 4.4. The histograms represent the number of grains with certain values of spectral slope for both the wavelengths ranges. These data were taken on October 2015. The grain distribution appears spread around a central

Epoch	$S_{480-649}$	*se*	$S_{649-882}$	*se*
2015-07-24	15.8	0.9	7.8	0.5
2015-08-04	12.9	0.7	6.8	0.5
2015-08-25	12.8	1.5	6.9	0.8
2015-08-31	12.4	0.9	8.8	0.4
2015-09-11	12.8	1.3	7.7	1.0
2015-09-15	13.5	1.3	8.5	1.3
2015-09-28	13.1	1.0	8.7	0.7
2015-10-18	14.6	1.9	7.7	0.7
2015-10-23	13.5	0.6	7.5	0.4
2015-11-06	11.6	0.7	8.3	0.5
2015-11-10	11.9	0.9	7.4	0.5
2015-11-17	11.8	0.6	7.3	0.5
2015-11-19	14.2	0.9	6.4	0.7
2015-11-27	12.0	0.8	7.4	0.6
2015-12-10	12.0	0.6	6.7	0.3
2015-12-14	12.0	0.8	7.2	0.5
2015-12-17	13.2	0.8	5.4	0.6
2016-01-04	12.9	0.7	5.3	0.4

TABLE 4.3: Values of average spectral slope in the range of wavelengths [480-649] nm and in the range [649-882] nm with associated standard errors (*se*). Each measurement refers to a specific epoch.

peak, with spectral slope that ranges from negative to large positive values. Therefore we decided to fit it with a Gaussian normalized to the total counts, which provided a statistic value for the means and the errors. The standard error of the mean was computed as $se = \sigma/\sqrt{N}$, where σ is the standard deviation of the Gaussian distribution and N the number of grains for which the spectral slope was measured. This type of analysis was performed for the whole set of images, finding the average values with the relative errors for each day of the sample. The results are reported in Table 4.3. On average, we found a spectral slope of $12.9 \pm 0.2\%/100$ nm in the range Orange Blue and of $7.3 \pm 0.2\%/100$ nm in the range Near-IR Orange. The two slopes are different also for the normalization used: at about 550 nm for the first one and at about 770 nm for the second one.

These results describe a general behaviour of the grains in the coma. Therefore, we can infer that the bulk of the grain population has a steeper spectral slope in the blue part of the spectrum and a flatter spectral slope in the red part of the spectrum.

It is interesting to note that sometimes the distributions extend also in the region of negative values. We found about 6% of grains have spectral slope ¡ 0 in the range [480-649] nm and about 8% in the range [649-882] nm. High abundance of water ice, for instance, is associated with neutral or negative values of spectral slope (Fornasier et al., 2016; Oklay et al., 2016; Rotundi et al., 2015). Therefore, for those grains presenting low or negative spectral slope values in both wavelengths intervals, we can infer a water

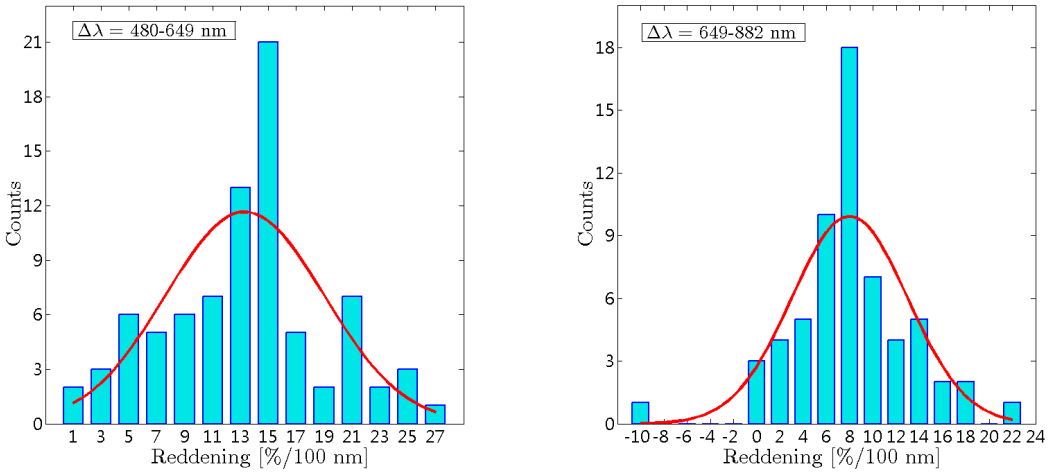

FIGURE 4.4: In the panels are represented the spectral slope distribution in the range of Orange and Blue (on the left) and in the range of NearIR and Orange (on the right) for a set of images taken on October 2015. The distributions are fitted with a Gaussian, normalized to the area of the histogram.

ice composition. Also the presence of silicates could justify a negative value in the range [649-882] nm (DeMeo & Carry, 2013).

4.4.1 Evolution of spectral slope

In order to analyze the possible variations of the spectral slopes with time, we studied the evolution with respect to the heliocentric and nucleocentric distances. The images analyzed in this work were taken with different geometry of acquisition and with a nucleus distance ranging between 100 km and 400 km. Assuming that the camera was able to see grain tracks up to the distance of 10-20 km (see Table 6.3), it has been possible to characterize the grain populations at relative distances from the nucleus, even if we do not know the real distance of the dust grains from the spacecraft.

Figure 4.5 shows the values of the average spectral slope measured for each sequence. The data result scattered within the values of 11.6-15.8 %/100 nm in the range [480-649] nm (blue points), but no particular trend is revealed. This peculiar variability was observed also by Bertini et al. (2017), in the trend of the spectral slope of the overall coma in a similar wavelength range. In fact, they measured a slope of 11-14 %/100 nm between 376 and 744 nm. The evolution of the spectral slope in the range [649-882] nm shows variations as well, within the values of 5.3-8.8 %/100 nm,(red points), but on average it seems to decrease moving away from the Sun, and to increase with the distance from the comet.

Therefore the red part of the spectrum seems to be more sensitive to the changes the grains undergo. Since the spectral slope computed up to 744 nm does not reveal any

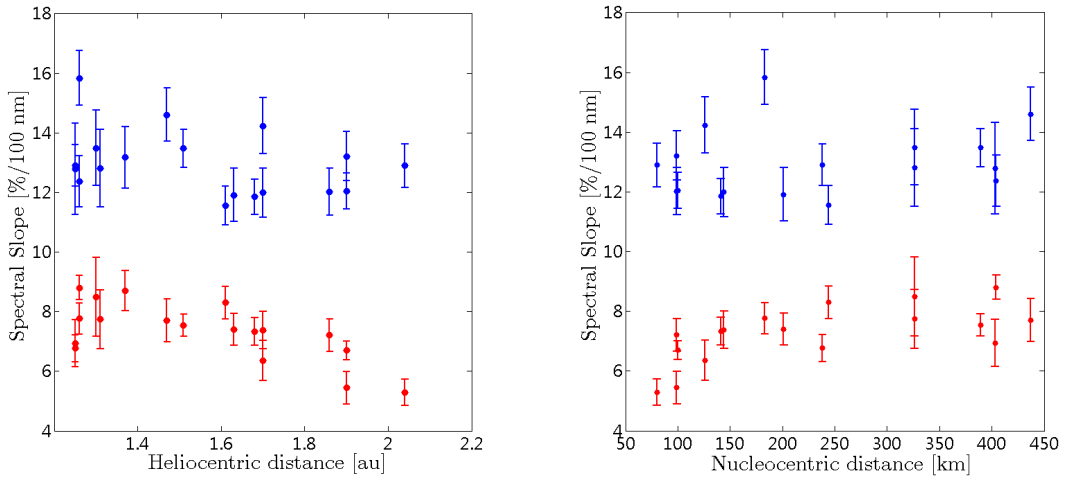

FIGURE 4.5: Daily average spectral slopes between [649-882] nm (red) and between [480-649] nm (blue) versus heliocentric distance (on the left) and versus nucleocentric distance (on the right). The standard errors of the mean ($se = \sigma/\sqrt{N}$) are associated to each measurement.

significant trend with respect to the distances, we expect that the characteristic feature responsible for the increasing or decreasing spectral slope lies between [744-882] nm. This variability may hint at a certain degree of heterogeneity in the coma properties, depending on the on-going evolution of the comet's environment.

4.5 Spectrophotometry

To better characterized the grains composition, we performed also the spectrophotometric analysis of the grains. Indeed, when the time interval between two consecutive images was sufficiently short, we were able to identify the same grain in the four filters. Overall, we derived 339 3-point spectra. An example is reported in Figure 4.6. The flux's value in each filter was obtained integrating all the track's signal. Since it can show fluctuations due to the grain spin, we measured an estimate of this effect. We analyzed a sample of WAC (Wide Angle Camera) images taken simultaneously to the NAC ones with F21 Green filter (537 nm, bandwidth = 63.2 nm). Their long exposure time (90 seconds) covered four NAC images (12.5 seconds), allowing to quantify the track luminosity's changes that possibly occurred. The statistics was performed on 200 tracks belonging to images taken on August and September 2015. A typical light curve of an aggregate taken with the WAC is shown in Figure 4.7. To be consistent with the NAC's exposure time intervals, we divided the WAC tracks signal into two groups: the one corresponding to the NAC images and the one corresponding to the time interval between consecutive shots. Then, we measured the mean reflectance and the variance for the intervals corresponding to the NAC images. It resulted that the most probable

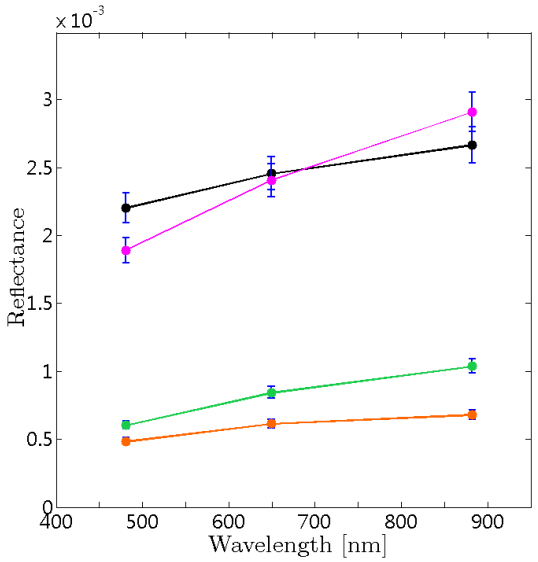

FIGURE 4.6: 3-point spectra of four grains taken on November 2015. The black one is supposed to be a grain composed by water ice. Indeed, the high reflectance and the flat spectrum are two conditions associated with the presence of water ice in the aggregate.

value for the error, in terms of flux's average percentage, was about 5%. Assuming a comparable filters' sensitivity we could apply a variability of about 5% on the flux's measurements even for the other NAC filters.

We basically identified three types of spectra: a) very steep slope spectra, b) spectra with intermediate slope values, and c) spectra presenting a flat slope trend. The same spectra of Figure 4.6 are shown in Figure 4.8 in terms of Relative Reflectance.

Moreover, we decided to measure the spectral slope of the subsample of grains between Green and Near-IR, [535-882] nm, with the following formula, reported by Fornasier et al. (2015):

$$S = \frac{I/F_{882} - I/F_{535}}{I/F_{535}(882nm - 535nm)} 10000 \tag{4.6}$$

I/F is the reflectance of the grain, with I the radiance of the object and F the solar flux.

This is a slight different wavelength interval respect to the previous measurements, usually applied at the nucleus analysis. Indeed, this choice allows a further consistent comparison with the nucleus surface, which will be discuss in the next section.

Since we do not have measurements with the Green filter, we decided to fit the 3-point spectra with a linear interpolation. Then, we extrapolated the values of the spectra at the required wavelengths and measured the spectral slope between 535 nm and 882 nm for the 339 grains of the sample. We measured an average value for the spectral slope of 11±3 %/100 nm, quite in agreement with the values of the overall coma found by Bertini et al. (2017), which range between 11-14 %/100 nm. The result is inconsistent also with the values of about 11%/100 nm obtained by Ott et al. (2017) on a sample of

Population [%]	Spectral slope [%/100 nm]	Composition
10	<5	Water ice/Carbonaceous material
77	5-15	Mixture of Silicates and Organics
13	>15	Organics

TABLE 4.4: Percentage of grain populations, grouped for different range of spectral slope (derived by (4.6)), and relative possible composition.

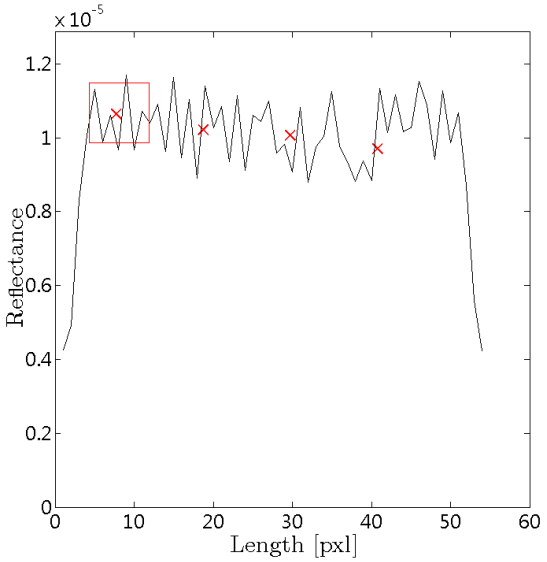

FIGURE 4.7: Light curve profile obtained from the track of a rotating grain acquired with the WAC. The red box highlights the part of WAC curve corresponding to simultaneous NAC track. The red star points show the average values of the flux measured in the box interval.

more than 100 single grains. The values of the average spectral slope computed for each day, with relative statistical errors, are reported in Table 4.5.

Then, we analyzed the spectral slope with respect to the heliocentric and nucleocentric distances. Few dataset were not statistically relevant so we neglected them (i.e those taken on August 25, on September 11 and on September 15). The results are shown in Figures 4.9. Each point represents the spectral slope obtained with equation 4.6 for the 339 grains of the subsample. We found that the average values of spectral slope, measured for each day, don't follow any particular trend with these distances.

4.5.1 Comparison with the nucleus

To check the nature of the dust grains, we compared the 3-point spectra with the spectra of several nucleus terrains. We took as reference the nucleus terrains spectra taken at phase angle 90°, provided by Barucci et al. (2016), where a distinction has been done between dust terrains and icy patches. Following the results by Fornasier et al. (2015)

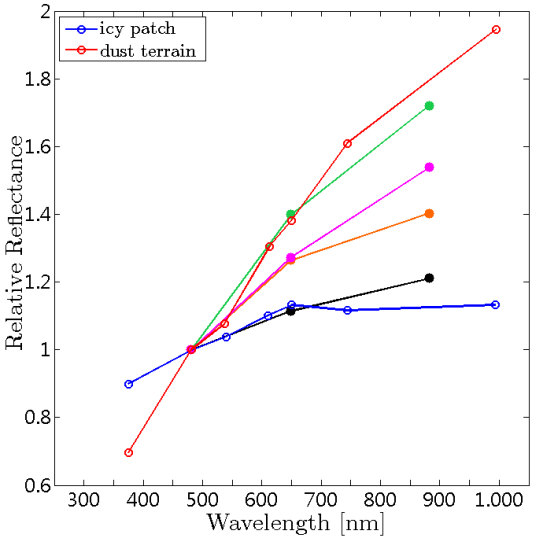

FIGURE 4.8: Normalized spectra of the same four grains of Figure 4.6. They are superimposed to two terrains on the nucleus. In red a dust terrain and in blue an ice patch, ($\alpha = 90°$). The steepest spectrum (green), is related with the dust terrain and probably mostly composed by organics; the two intermediate spectra (pink and orange), are associated with a mixture of organics and silicates and the flatter spectrum (black), is similar to the one of icy patch on the surface of the nucleus and likely composed by water ice.

for low heliocentric distances, the nucleus undergoes a phase reddening effect. This produces an increasing of the spectral slope of about 5 %/100 nm for phase angle varying from 0° to 60°. On the contrary the dust is not affected by any phase reddening. Our analysis and consequent nucleus-dust comparison is therefore applicable for nucleus parameters obtained with a phase angle $\alpha = 90°$.

We found that (see Figure 4.8) the first type of spectrum, the ones with the highest value of spectral slope, well fits the spectral behaviour of nucleus dust terrains, and might be composed by organics (Pommerol et al., 2015). The second type instead, could be associated with a mixture of silicates and organics. Spectra of S-type asteroids show a peak around 0.7 μm and an absorption band around 1 μm due to olivine. Since we do not have sensitivity between 600 nm and 900 nm, we are not able to observe the peak and we see only a neutral trend or a low positive slope (DeMeo & Carry, 2013). The measurement done by Cremonese et al. (2016) may strengthen this hypothesis. In fact, they found a red slope of 16%/100 nm between blue (480.7 nm) and red (743.7 nm) filters, implying that the intensity might grow until the peak associated with the silicates around 700 nm and then decreases.

Finally, the flat type seems to superimpose to the spectrum of the icy patch. Usually we expect to see icy grains with flat spectrum and high reflectance (black spectrum in Figure 4.6 and Figure 4.8), but we found also grains with flat trend and low reflectance. Since we were not able to estimate the absolute distance from the nucleus, we may have

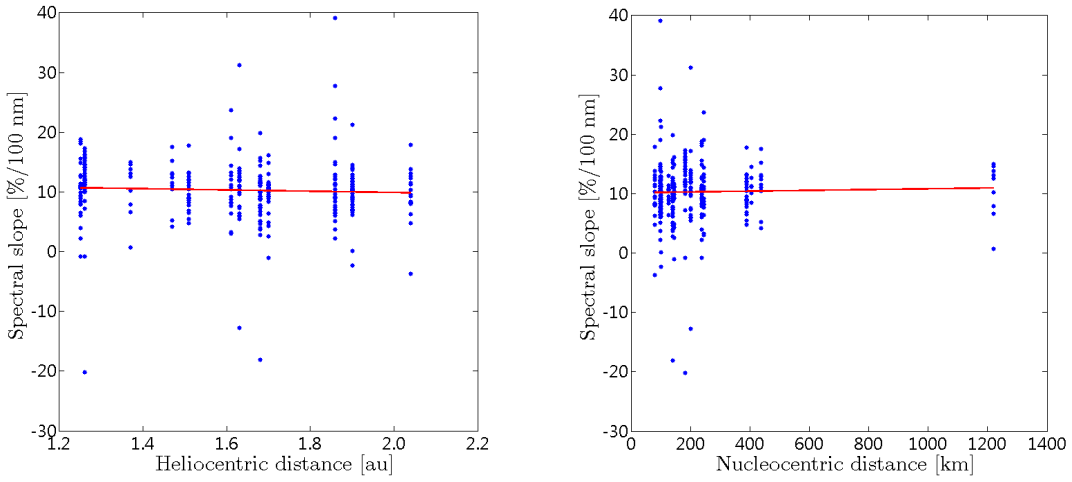

FIGURE 4.9: Spectral slopes between [535-882] nm versus the heliocentric distance, on the left panel, and versus the nucleocentric distance, on the right panel. Each blue point represents the spectral slope obtained from the 3-point spectra fit.

observed small particle of ice very far from the spacecraft. Assuming that the water ice sublimation depends on the nucleus distance and on the ejection time, we do not expect to see a large amount of water ice in the coma (Gicquel et al., 2016). Alternatively this third type of flat spectra might represent carbonaceous material with very low albedo (DeMeo & Carry, 2013).

Moreover, we considered the laboratory experiments of Pommerol et al. (2015) and Poch et al. (2016a) to test the sublimation of water ice mixed with silicates and organic material. They found that such mixture changed its spectral slope during the sublimation process. Starting from a flat spectrum, they demonstrated that, after just 10 hours, the trend of the spectrum changed, becoming steeper. At the end of the experiment the resulting spectrum could be related to a very pristine organic material.

Since the grains were ejected with a velocity of the order of few m/s (Rotundi et al., 2015), they needed about 1 day to arrive at more than 100 km from the nucleus when we observed them. Therefore the 3 types of spectra we measured could represent different phases of an on-going sublimation process active on the grains themselves.

Another approach to interpret the different grain spectra was based on the spectral slope classification. A correspondence between surface features and values of the spectral slope was introduced by Fornasier et al. (2015) and Oklay et al. (2016). We decided to arrange the grains into three categories, consistently with the spectra types we defined earlier. The relative composition of the grains is estimated to be: organics in the case of great values of spectral slope (>15 %/100 nm), a mixture of organics and silicates in the intermediate interval (5-15 %/100 nm), and ices or carbonaceous material in the case of lowest values (<5 %/100 nm). The results are resumed in Table 4.4. The intermediate group is the most populated.

Epoch	$S_{535-882}$	*se*
2015-07-24	11.3	1.4
2015-08-04	10.3	0.9
2015-08-25	23.3	1.5
2015-08-31	11.4	0.8
2015-09-11	6.6	1.5
2015-09-15	13.4	2.3
2015-09-28	10.5	1.6
2015-10-18	11.3	0.9
2015-10-23	9.9	0.7
2015-11-06	10.6	1.0
2015-11-10	10.5	1.5
2015-11-17	9.1	0.8
2015-11-19	10.0	0.6
2015-11-27	9.0	1.2
2015-12-10	11.2	1.1
2015-12-14	9.6	0.9
2015-12-17	10.9	0.6
2016-01-04	9.4	1.1

TABLE 4.5: Daily average spectral slope computed for 339 grains in the wavelength range [535-882] nm. The standard error of the mean *se* is associated.

4.6 Conclusions

We analyzed the photometric behaviour of the grains in the coma of 67P in the time range from July 2015 and January 2016. We extracted geometric and photometric parameters with an automatic method specifically developed. The results can be summarized as follows:

- We measured the average spectral slope of the grains for each set of images obtaining the total average value of $12.9 \pm 0.2\%/100$ nm in the range [480-649] nm and $7.3 \pm 0.2\%/100$ nm in the range [649-882] nm.
- We analyzed the reddening in the two wavelength ranges with respect to the heliocentric and nucleocentric distances. We revealed a variability in the behaviour of the spectral slope that could hint at heterogeneity in the coma due to physical processes affecting the released material.
- We performed a spectrophotometric analysis of 339 grains observed in three filters (Blue, Orange and Near-IR). We divided the spectra into three major groups:
  - steep, which may be connected with the presence of organics, with a slope values >15 %/100 nm;
  - intermediate, which are supposed to be a mixture of silicates and organics, corresponding to a slope range between 5 and 15 %/100 nm;

  - flat, most likely due to much higher abundance of water ice, that should be suitable for a comet, but in case of very low albedo grains we have to mention a possible higher abundance of carbonaceous material.

- We found an average value for the spectral slope of the grains subsample of about 11 %/100 nm in the wavelength range [535-882] nm. No trend of the spectral slope with respect to the heliocentric and nucleocentric distances was measured.

- We compared the spectra with two characteristic terrains of the nucleus, finding a correspondence between the steeper spectra and the dust terrain, while the flatter one is compatible with the icy patch.

Chapter 5

Experimental phase function and degree of linear polarization of cometary dust analogs

This chapter is taken from the submitted work of Frattin et al. (2018). We present experimental phase function and degree of linear polarization curves for seven samples of cometary dust analogues namely, ground pieces of Allende, DaG521, FRO95002 and FRO99040 meteorites, Mg-rich olivine and pyroxene, and a sample of organic tholins. The experimental curves have been obtained at the IAA Cosmic Dust Laboratory at a wavelength of 520 nm covering a phase angle range from 3° to 175°. We also provide values of the backscattering enhancement (BCE) four our cometary analogue samples. The final goal of this work is to compare our experimental curves with observational data of comets and asteroids to better constrain the nature of cometary and asteroidal dust grains. All measured phase functions present the typical behavior for μm-sized cosmic dust grains. Direct comparison with data provided by the OSIRIS/Rosetta camera for comet 67P Churyumov-Gerasimenko reveals significant differences and supports the idea of a coma dominated by big chunks, larger than μm. The polarization curves are qualitatively similar to ground-based observations of comets and asteroids. The position of the inversion polarization angle seems to be dependent on the composition of the grains. We find opposite dependence of P_{max} for grains sizes in the Rayleigh-resonance and geometric optics domains, respectively.

5.1 Introduction

Dust is a fundamental constituent of planetary systems in all their stages of development. For example, the origin of planetary systems involves a phase of aggregation of submicron-sized dust grains by streaming instability into protoplanetary disks (Blum et al., 2014; Blum & Wurm, 2008; Johansen & Youdin, 2007). In our mature Solar System, dust can be found in the interplanetary medium orbiting around the Sun as a product of the disintegration of comets and asteroidal collisional cascading (the Zodiacal Cloud), as well as in the rings of the giant planets. In addition, dust is present in the regolith surfaces of planets, asteroids and comets, and in dense atmospheres (e.g. Venus, the Earth, Mars, Titan) in the form of aerosol. Because of the ubiquity of dust and its involvement in countless physical phenomena, from atmospheric radiative transfer to cometary activity through the tracing of Solar System primitive materials, it is important to study its nature and properties.

Comets are the most appropriate targets to study the early Solar System, since they are among the most pristine objects orbiting the Sun. Because of their low-velocity, gentle accretion process, some of their most primitive constituents (the grains) have remained intact, i.e. as they were when the comets formed (Fulle et al., 2016b). During their passage at perihelion, these objects release refractory materials driven by the sublimation of trapped ices, generating a bright dust coma dominated by μm-sized particles composed of silicate minerals and organics. Comets unveil the composition of the primordial material from which they accreted, namely material located in the outer regions of the Solar System, and put some constraints to the processes involved in its origin. The flyby missions that first revealed the nature of cometary dust with in-situ measurements were the *Giotto* (Reinhard, 1986) and *Vega* (Sagdeev et al., 1986) missions to 1P/Halley in 1986. The 'Halley Armada' was followed up by the Deep Space 1 mission to comet 19P/Borrelly in 2001 (Soderblom et al., 2002). A major breakthrough came with the *Stardust* mission flyby of comet 81P/Wild in 2004 (Hörz et al., 2006), and subsequent return to Earth of samples of dust collected directly from the coma of the comet. More recently, the Rosetta mission has been able, for the first time, to orbit around a cometary nucleus and observe its evolution during its trajectory before and after perihelion. The coma of comet 67P/Churyumov-Gerasimenko (hereafter 67P) was observed during two entire years (2014-2016) from the very inside, reaching distances of few km from the nucleus. The astonishing images obtained by the OSIRIS instrument on board the spacecraft have shed new light into the properties of cometary dust. There is now evidence that 67P formed by gentle accretion of pebbles smaller than 1 cm at velocities of the order of 1 m/s (Fulle & Blum, 2017). Moreover, photometric analysis of the overall coma and single grains reveal that the majority of the material has similar spectral properties to those of nucleus surface (Frattin et al., 2017), which enables using

the dust coma as a proxy indicator of nucleus properties.
The sunlight incident on a cometary dust envelope is partly absorbed and partly scattered by the particle cloud. Spacecraft and ground based observations of scattered light show characteristics strictly dependent on the nature and physical properties (composition, size distribution, shape, roughness, etc) of the material composing the coma. Since each material has characteristic scattering signatures, scattering theory can be used to interpret observations and retrieve from them some of the properties of the dust. Experimental data of the angular distribution of the scattered intensity and degree of linear polarization of clouds of cosmic dust analogs assist in the interpretation of in-situ and remote sensing observations. Since these quantities are intimately related to the nature of the particles, laboratory data are used as a reference for comparison and interpretation, allowing a correct analysis of the observational data (Muñoz et al., 2017, 2000; Volten et al., 2006). Modeling of the interaction between electromagnetic radiation and particles in turn, supports the experiments, helping to discriminate unambiguously dust features corresponding to specific observables (Escobar-Cerezo et al., 2017; Liu et al., 2015; Zubko, 2015). All these different approaches (observations, laboratory experiments and theoretical simulations) provide essential contributions to the investigation of the behavior of dust particles as radiation scatterers.

In this work we present experimental phase function and degree of linear polarization curves as functions of the observational phase angle of a selected set of cometary dust analogs: four meteoritic samples, two minerals (Mg-rich olivine and pyroxene), and a sample of organic particles (tholins). Light scattering measurement have been performed at the Cosmic Dust Laboratory (CODULAB) (Muñoz et al., 2011) at the Instituto de Astrofísica de Andalucía (IAA), spanning a phase angle range from 3° to 175° at a wavelength of 520 nm. We combine the new measurements presented in this work with the scattering matrices at 442 nm and 633 nm of a sample of the Allende meteorite and of size-segregated Mg-rich olivine samples that have been previously presented by Muñoz et al. (2000). Finally, we compare the experimental data with observations of asteroids and cometary dust envelops, with special emphasis on the observations of 67P by Rosetta, in order to put constrains on the nature of cometary dust.

5.2 Light scattering theory

A beam of quasi-monochromatic light is physically defined by the Stokes vector $\mathbf{I} = \{I, Q, U, V\}$, where I is proportional to the total flux of the light beam and Q is related to the linear polarization of the light beam, representing the difference between the two components of the flux along the x-axis and the y-axis. U is defined by the difference

of the two components of the flux along the directions rotated by 45° from the x and y axis. V is related to the circular polarization, defined as the difference between the left-handed and the right-handed polarized components of the flux.

The interaction between a light beam and a cloud of particles results in scattering of the incident light. The Stokes vector of the scattered beam $\mathbf{I}_{sc}$ is related to the one of the incident beam $\mathbf{I}_{in}$ by the so-called scattering matrix $\mathbf{F}$, through the following expression:

$$\begin{pmatrix} I_{sc} \\ Q_{sc} \\ U_{sc} \\ V_{sc} \end{pmatrix} = \frac{\lambda^2}{4\pi^2 D^2} \begin{pmatrix} F_{11} & F_{12} & F_{13} & F_{14} \\ F_{21} & F_{22} & F_{23} & F_{24} \\ F_{31} & F_{32} & F_{33} & F_{34} \\ F_{41} & F_{42} & F_{43} & F_{44} \end{pmatrix} \begin{pmatrix} I_{in} \\ Q_{in} \\ U_{in} \\ V_{in} \end{pmatrix}, \tag{5.1}$$

where λ is the wavelength of the incident beam and D is the distance of the detector from the particles. The 16 dimensionless elements of the matrix depend on physical characteristics of the particles such as their number, shape, dimension (through the size parameter $x = 2\pi r/\lambda$) and refractive index, as well as on geometrical parameters such as their orientation in the space and scattering direction.

When the particles are randomly oriented all scattering planes are equivalent. Therefore, the scattering direction is fully described by the scattering angle, θ, defined by the angle between the directions of propagation of the incident and scattered beams. To facilitate direct comparison with astronomical observations of comets and asteroids we use the phase angle, $\alpha = 180° - \theta$, throughout the text. Furthermore, if the ensemble of particles presents mirror symmetry, the matrix is simplified as follows (van de Hulst, 1957):

$$\mathbf{F} = \begin{pmatrix} F_{11} & F_{12} & 0 & 0 \\ F_{12} & F_{22} & 0 & 0 \\ 0 & 0 & F_{33} & F_{34} \\ 0 & 0 & -F_{34} & F_{44} \end{pmatrix} \tag{5.2}$$

5.3 Experimental apparatus

The CODULAB facility is dedicated to measuring the elements of the scattering matrix (eq. 5.1 and 5.2) as a function of the scattering angle of clouds of randomly oriented cosmic dust analogs. This is achieved by means of a gonio-nephelometer that has been described in detail previously by Muñoz et al. (2010). In the experiments carried out for this work we employed an Argon-Kripton laser tuned to 520 nm as our light source. The scattering apparatus is shown in Fig. 5.1. The laser beam passes through a polarizer and an electro-optic modulator before encountering a jet stream of randomly oriented

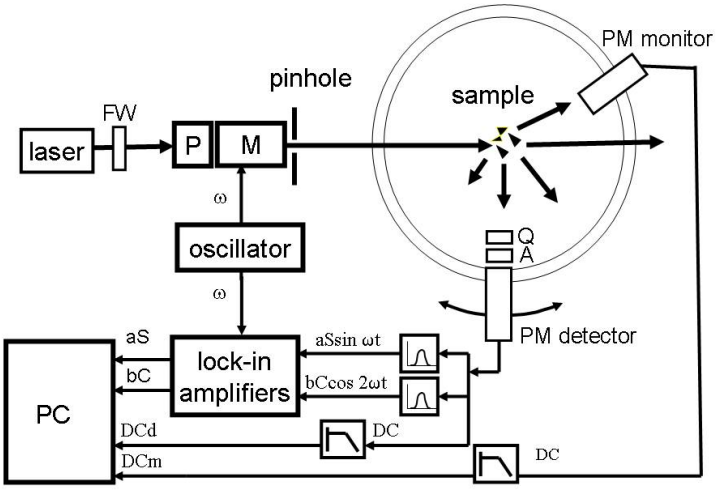

FIGURE 5.1: The scattering apparatus at the CODULAB.

particles produced by an aerosol generator (Muñoz et al., 2011). The powder under analysis is contained in a cylindrical reservoir, and is pushed by a piston in a controlled manner towards a rotating brush, which disperses the particles into a flow of air which carries them trough a nozzle to the scattering volume. The particle density in the scattering volume, which is controlled by the speed of the piston, must be high enough to produce a detectable scattering signal, but low enough to avoid multiple scattering. In this way it better approximates the low density cometary coma. The scattered light passes through optional optics before being detected by a photomultiplier, the *detector*, which is mounted on a 1 m ring rail centered at the aerosol jet. In the measurements presented in this paper we have covered the phase angle range from 3° to 175° in steps of 5° within the $10° - 20°$ and $40° - 175°$ ranges, and in steps of 1° within the $3° - 10°$ and $25° - 40°$ ranges. Sinusoidal electro-optic modulation combined with lock-in detection allows determining all elements of the scattering matrix from eight different configurations of the optical components (eq. 5.1) (Muñoz et al., 2010). In order to keep the scattered intensity within the linearity range of the detector, a wheel of neutral density filters is placed between the laser head and the polarizer, which allows adapting the beam intensity to the scattering behavior of the aerosol sample at each particular angle. A second photomultiplier placed at a fixed angle, the *monitor*, corrects for fluctuations in the aerosol beam. For each position of the detector, 1000 measurements are conducted in about 2 seconds. The final value at each phase angle is obtained from the average of such measurements, with an associated error given by the standard deviation. Three measurement runs are carried out for each optical configuration in order to achieve further noise reduction. Due to the limited amount of material, we did not measure the complete scattering matrix but only the elements F_{11} and F_{12}. For unpolarized incident

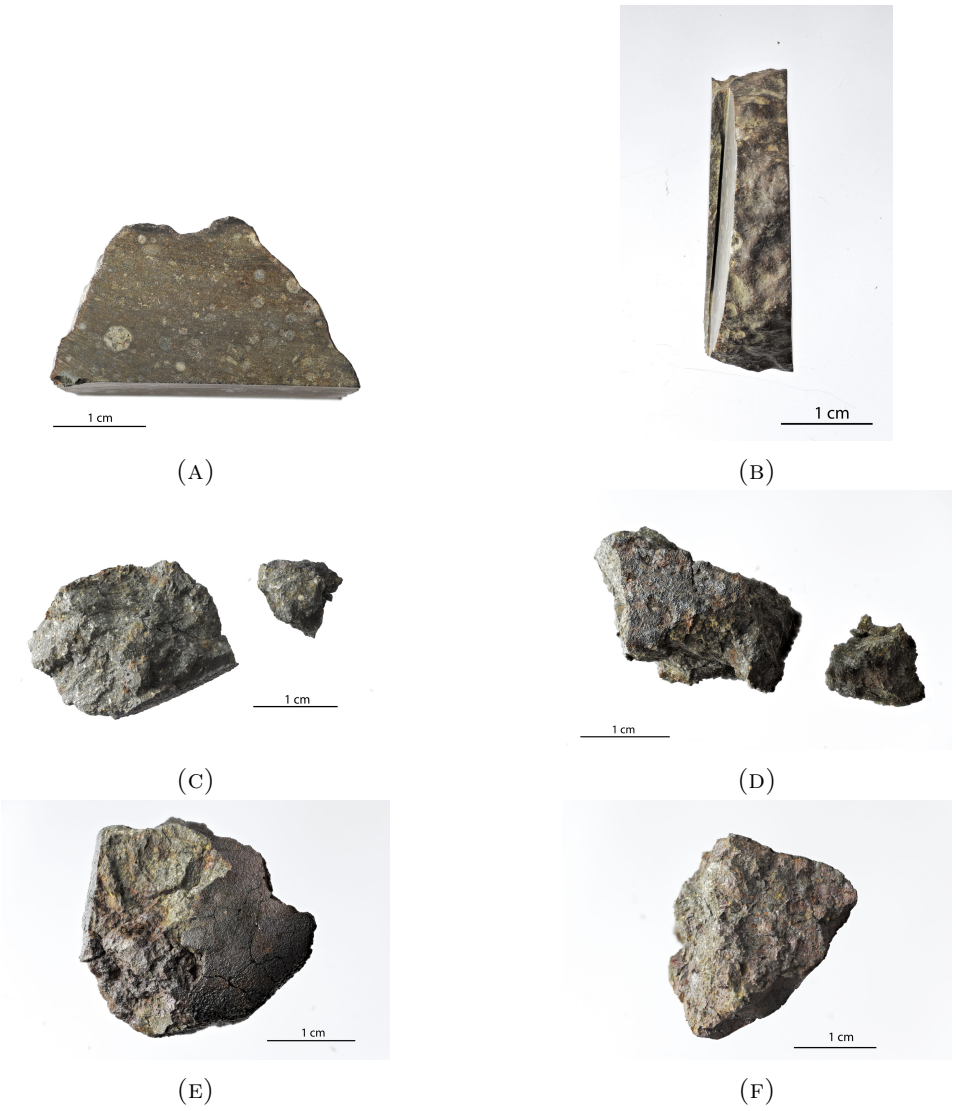

(A) (B)

(C) (D)

(E) (F)

FIGURE 5.2: In panel 5.2a and 5.2b are shown the meteorite DaG521, in panel 5.2d and 5.2e the meteorite FRO95002 and in panel 5.2e and 5.2f the meteorite FRO99040. The three meteorites were provided by the Museo dell'Antartide Felice Ippolito, Siena.

light the F_{11} is proportional to the scattered flux. The measured values of the F_{11} are arbitrarily normalized so that they are equal to 1 at $\alpha = 150°$. The F_{11} normalized in this way is called the *phase function*. The $-F_{12}/F_{11}$ ratio is equal to the degree of linear polarization, P, for unpolarized incident light, expressed in terms of Stokes parameters as $P = -Q/I$.

5.4 Materials

We have selected four Carbonaceous Chondrites (CCs), two silicate minerals and one organic powder as sources of cometary dust analogs. Bulk samples of the meteorites DaG521, FRO95002 and FRO99040 were provided by the Museo dell'Antartide Felice

Ippolito, Siena especially for this work (see Fig. 5.2). Batches of particulate tholins were synthesized at the Laboratoire Inter-Universitaire des Systemes Atmospheriques (LISA), Paris. The Allende, olivine, and pyroxene samples belong to the IAA-CODULAB collection and have been used in a previous work (Muñoz et al., 2000). Below we describe the bulk properties of these materials, the methods employed to obtain particulate samples suitable for our light scattering experiments, and the physical properties of the particles (optical constants, size distribution and morphology).

5.4.1 Meteorites

Carbonaceous Chondrites meteorites are among the oldest and most primitive materials in the Solar System. Age determination techniques indicate that they formed around 4.5 Gyr ago (Chen & Wasserburg, 1981; Mahnes et al., 1987). Since they are very old, these rocks suffered different primary processes, which record pre-accretionary histories in the solar nebula, and secondary processes like aqueous alteration, thermal metamorphism and shock metamorphism (Brearley & Jones, 1998).
CCs are divided in several classes based on composition: CI, CH, CO, CV, CK, CR. Most of them are fragments of primitive asteroids. They come from the NEO population, which includes about 10% of extinct comets, in addition to former asteroids.
The bulk composition of the Carbonaceous Ivuna (CI) group of chondrites is very close to the composition of the solar photosphere. Furthermore, interstellar grains that predate the Solar System formation are found in the matrix of these primitive chondrites (Brearley & Jones, 1998). CCs are characterized by chondrule sizes ranging from 1 mm in the CV group down to around 0.15 mm and 0.02 mm in the CO and CH groups, respectively. The CV and CO chondrites have the highest abundances of refractory inclusions, while CR and, above all, CH chondrites have the highest content of metals (Brearley & Jones, 1998; Weisberg et al., 2006). In Tab. 5.1 we report the mean composition of CO and CV chondrites.

DaG521 and Allende The meteorites DaG521 (Dar al Gani 521, found in Lybia in 1997 Grossman (1999)) and Allende (fallen near Parral, Chihuahua, Mexico, in 1969) Clarke (1970) are classified as CV3. CVs chondrites are characterized by large mm-sized chondrules, large refractory inclusions and abundant matrix (40 %vol). They are divided into oxidized CV_{OX} and reduced CV_{RED} subgroups based on abundances of metal, magnetite and Ni content (McSween, 1977). The main component of CV matrices is Fe-rich olivine (fayalite Fa$\sim$30-60 and in some cases Fa$>$90), but there are substantial differences among the subgroups due to different late stage metasomatism and aqueous alteration (Krot et al., 1998, 1995). Other mineral constituents are Ca-Fe-pyroxene, andradite,

	CO	CV
Si	15.8	16.0
Ti	0.08	0.15
Al	1.58	2.19
Cr	0.36	0.35
Fe	24.3	23.1
Mn	0.18	0.15
Mg	14.4	14.4
Ca	1.62	2.57
K	0.05	0.03
S	1.94	1.63
P	0.11	0.13
Na	0.35	0.35
Ni	1.31	1.11
O	37.9	37.9

TABLE 5.1: Mean composition of CV and CO chondrites.

Fe-Ni sulfides and magnetite. Some chemical and textural features of the CV chondrites evidence a phase in which the parent body experienced temperatures <300°C (Krot et al., 1998).

DaG521 is the only meteorite of our set with reddish colour, probably due to iron oxide generated by weathering in the Lybian desert.

Allende is classified as CV_{OX}. This group displays Calcium-Aluminum-rich Inclusions (CAIs) and ameboid olivine refractory elements and this suggests they have been formed at high temperature during the early stages of Solar System formation. A recent discovery of a class of asteroids (the so-called Barbarians) seems to have a composition unusually enriched in CAI minerals, like spinel (Cellino et al., 2014). Allende differs from other CV_{OX} meteorites in its lower matrix-chondrule ratio and in having chondrules with more opaque minerals (Brearley & Jones, 1998). Fe/Mg exchange took place between matrix and inclusions. Secondary fayalite is found around forsterite phenocrysts and replaces also low-Ca pyroxenes (Krot et al., 1998).

FRO95002 and FRO99040 These two meteorites were found in Antarctica, in the region of the Frontier Mountain in 1995 and 1999, respectively. Both belong to the CO3 class, which presents similar characteristic of CV3 regarding chondrules and matrix abundance, but differ in the chondrule dimensions, which in the CO3 case are μm-sized. The CO chondrites are all of petrologic type 3, showing slightly different metamorphic stages, ranging from 3.0 to 3.7 (McSween, 1977). CO chondrites usually have low Fe compositions with olivine with Fa<1 (Brearley & Jones, 1998). Also Fe-pyroxenes are rare, only a few pyroxenes with Fs$\sim$10 are reported (Brearley & Jones, 1998).

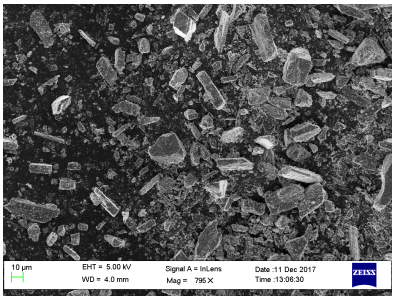
10 µm
EHT = 5.00 kV
WD = 4.0 mm
Signal A = InLens
Mag = 795 X
Date :11 Dec 2017
Time :13:06:30
ZEISS

(A)

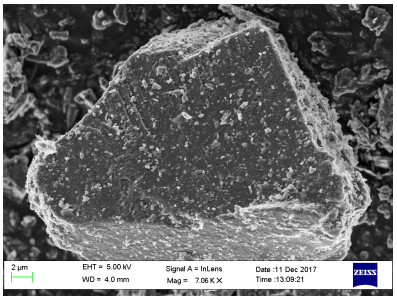
2 µm
EHT = 5.00 kV
WD = 4.0 mm
Signal A = InLens
Mag = 7.06 K X
Date :11 Dec 2017
Time :13:09:21
ZEISS

(B)

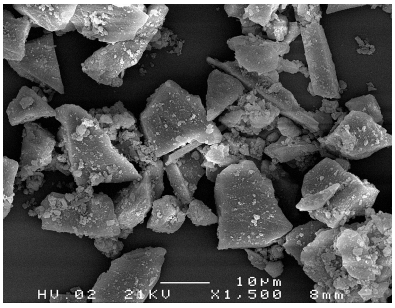
10µm
HV 02 21KV X1,500 8mm

(C)

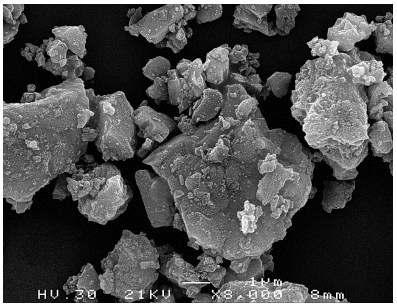
1µm
HV 30 21KV X8,000 8mm

(D)

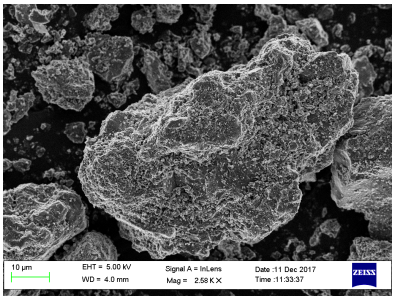
10 µm
EHT = 5.00 kV
WD = 4.0 mm
Signal A = InLens
Mag = 2.58 K X
Date :11 Dec 2017
Time :11:33:37
ZEISS

(E)

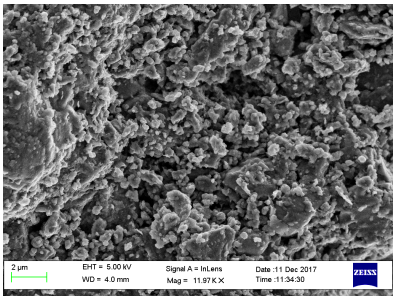
2 µm
EHT = 5.00 kV
WD = 4.0 mm
Signal A = InLens
Mag = 11.97 K X
Date :11 Dec 2017
Time :11:34:30
ZEISS

(F)

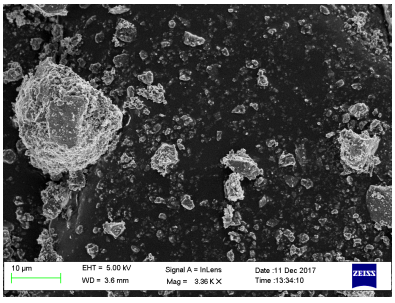
10 µm
EHT = 5.00 kV
WD = 3.6 mm
Signal A = InLens
Mag = 3.36 K X
Date :11 Dec 2017
Time :13:34:10
ZEISS

(G)

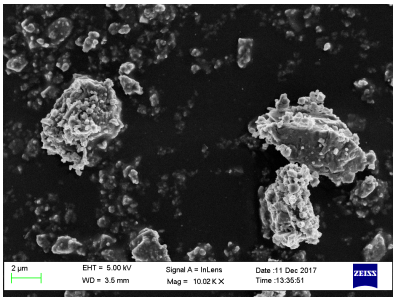
2 µm
EHT = 5.00 kV
WD = 3.5 mm
Signal A = InLens
Mag = 10.02 K X
Date :11 Dec 2017
Time :13:35:51
ZEISS

(H)

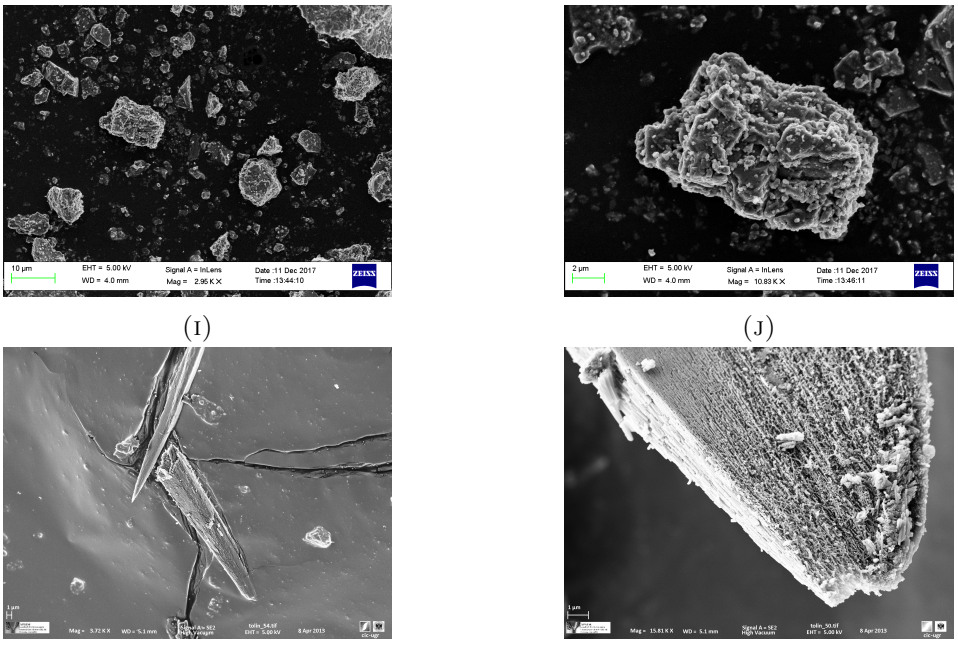

(I) (J)

(K) (L)

FIGURE 5.3: Photographs taken with the FSEM. **a** and are enstatite, **c** is olivina, **d** Allende, **e** and **f** are DaG521, **g** and **h** FRO95002, **i** and **j** are FRO99040, **k** and **l** are tholine.

5.4.2 Minerals

The first hint of the presence of silicates in the cometary dust dates back to the observation of the emission feature at 10 μm in comet Bennett and its consequent laboratory modeling (Maas et al., 1970). The measurements of 1P/Halley mineralogical composition revealed Mg-rich olivine (forsterite) and pyroxene (enstatite) as dominant compounds from in-situ mass spectra of particles provided by Giotto and Vega Spacecraft (Schulze et al., 1997). Crystalline forsterite and enstatite have been detected also on comet Hale-Bopp (Crovisier et al., 1997) and 9P/Tempel from space-based infrared spectra (Lisse et al., 2007) and on 81P/Wild2 from direct measurement of particles collected by Stardust mission (Clemett et al., 2007). These silicates are predicted by thermodynamic models to condense in a hot gas at 1200-1400 K, while the reaction with Fe occurs only at lower temperature. Thus, the preponderance of Mg-rich silicates in cometary dust can be explained by direct condensation in the inner primordial nebula (Hanner & Bradley, 2004). The olivine and pyroxene samples used in this work have respectively the composition $Mg_{1.85}Fe_{0.14}SiO_4$ and $Mg_{0.85}Fe_{0.08}Si_{0.99}O_3$, and are therefore close to the Mg-rich endmembers, i.e. forsterite and enstatite. Thus, in the following we will refer to the olivine and pyroxene samples as forsterite and enstatite. The forsterite sample is the one identified as 'Olivine S' in Muñoz et al. (2000).

5.4.3 Organics

Tholins are organic compounds generated by irradiation (solar UV, high energy particles, electrons) of mixtures of common compounds of carbon, oxygen and nitrogen, e.g. CO_2, CH_4 and HCN (Sagan & Khare, 1979). They are thought to be present on the surfaces and/or in the atmospheres of several Solar System bodies. For example, they are likely responsible for the reddish color of many objects such as Pluto (Gladstone, 2016) and Ceres (Combe et al., 2017), and are believed to be responsible for Titan's atmospheric haze (Brassé et al., 2015).
Analysis of 1P/Halley dust mass spectra indicated for the first time the existence of CHON particles in comets (Kissel & Krueger, 1987b). The complex nature and variety of organics in cometary dust was revealed by analysis of samples returned from 81P/Wild, obtained by *Stardust* (Clemett et al., 2007). More recently, the in situ analysis of 67P coma dust by COSIMA/*Rosetta* mass spectrometer has confirmed the presence of abundant high-molecular weight organic matter, nearly 50% in mass (Bardyn et al., 2017; Fray et al., 2017). Thus, the abundance of CHON compounds in cometary dust suggests that tholins are likely to form in this environment as well. Tholins have been previously used in laboratory studies as cometary dust simulants, often mixed with other components, typically silicates and ices (Jost et al., 2017; Poch et al., 2016b,c).
The tholins sample used in this work was synthesized using the PLASMA experimental setup described previously by Brassé et al. (2017). It allows the production and sampling of tholins from N_2-CH_4 electron irradiation in a glove box without contamination by the air of the laboratory. The elemental composition of these tholins has been determined (Brassé, 2014). They are carbon rich (C/N = 2.2 to 2.4) with a C/H of 0.7 to 0.8. Several grams of tholins were prepared to perform the CODULAB measurements.

5.4.4 Sample preparation

In order to obtain particulate samples with different size distributions within the typical size range of cosmic dust particles, the DaG521, FRO95002 and FRO99040 samples were milled and dry-sieved at the Department of Geoscience of the University of Padua. After milling, the three samples were first size-segregated using a 71 μm sieve. The fraction of sample that passed through the sieve was subsequently sieved using a 53 μm sieve. This procedure generated three subsamples designated as DaG521M, FRO99040M and FRO95002M with diameters, d, in the range 53 μm $< d <$ 71 μm. The fractions of DaG521M and FRO99040M that passed through the 53 μm sieve were subsequently sieved through a 45 μm sieve producing subsamples DaG521S and FRO99040S (45 μm $< d <$ 53 μm). A similar sieving procedure was used to produce the olivine samples

Sample	Refractive Index	Appearance
DaG521	$1.65 + i10^{-3}$	reddish
FRO99040	$1.65 + i10^{-3}$	dark grey
FRO95002	$1.65 + i10^{-3}$	dark grey
Allende	$1.65 + i10^{-3}$	dark grey
Forsterite	$1.62 + i10^{-5}$	white
Enstatite	$1.58 + i10^{-5}$	white
Tholins	$1.35 + i2.3 \cdot 10^{-2}$	dark

TABLE 5.2: Refractive index of each sample and their relative appearance.

described by Muñoz et al. (2000). As far as the organic sample is concerned, after their synthesis, the tholins were kept in gas proof vials under dry N_2 atmosphere, to avoid their chemical evolution. Just before measurements with CODULAB the tholins were first homogenized with a mortar to break the agglomerates and sieved to obtain an homogeneous powder. Then, these tholins were introduced into the cylindrical stainless steel tank of the aerosol generator.

5.4.5 Sample characterization

Refractive index The refractive index of a medium is defined as:

$$m = c\sqrt{\epsilon\mu} = n + ik \tag{5.3}$$

where ϵ is the electric permittivity, μ is the magnetic permeability and c the speed of light in vacuum. The optical constants n and k represent, respectively, the phase velocity of the wave in the medium and the absorption coefficient of the material.
Estimates of the refractive indices of our samples are compiled in Table 5.2. The refractive indices of forsterite and enstatite (Dorschner et al. (1995)) have been obtained from the Jena-St. Petersburg Database of Optical Constants [1]. The refractive index of tholins at 532 nm has been reported by Hasenkopf et al. (2010); for a detailed analysis of the tholins optical properties see Brassé et al. (2015).
The refractive indexes of the Allende, DaG521, FRO99040, and FRO95002 meteorite samples are unknown. Therefore, we have assumed estimates based on literature values of the main constituents. The imaginary part of the refractive index of the terrestrial samples is significantly smaller than that of the meteorites and tholins, which indicates a smaller absorbance of these materials, consistent with their light colour. By contrast, the meteorite powders are darker as a result of the higher bulk Fe content and organic components.
It should be kept in mind that the refractive index generally depends on the wavelength

[1] http://www.astro.uni-jena.de/Laboratory/Database/jpdoc/index.html

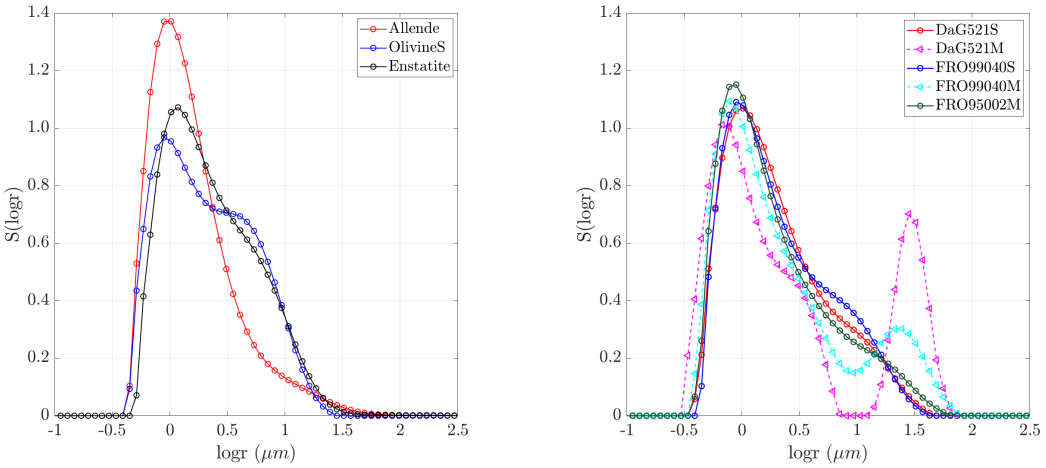

FIGURE 5.4: Size distribution of samples of Allende meteorite, Olivine and Enstatite, on the left panel and the size distribution of two different samples of DaG521, FRO95002 and FRO99040, on the right.

of the incident light. While the Mg-rich forsterite and enstatite present a flat wavelength dependence in the visible, the Fe content of the meteorite samples is expected to produce an effect on the refractive index at different visible wavelengths. This fact has been recently taken into account by Devogèle et al. (2018) to interpret the observed wavelength dependence of the inversion angle of polarization of asteroid (234) Barbara as a consequence of the imaginary refractive index, in turn a consequence of the presence of nano-iron phase particles.

Size distribution The size distributions of our samples have been estimated using a low angle laser light scattering (LALLS) particle sizer (Malvern Mastersizer 2000, Rawle (1993)). The LALLS method relies on the measurement of the phase function of samples dispersed in a carrier fluid at 633 nm within a range of low scattering angles (0.02°-30°). The volume distribution of equivalent spherical particles that best reproduces the observed phase function is obtained by inverting a light scattering model based on Mie theory, which requires knowing the complex refractive index of the samples (eq. 5.3). Since the refractive indexes of our meteorite samples are unknown, we have carried out a sensitivity study of the impact on the retrieved size distributions of varying n and k within wide ranges. In these sensitivity tests we have used as reference value the estimated refractive index for the Allende meteorite ($m = 1.65, k = i0.001$) (Muñoz et al., 2000). First, the imaginary part of the refractive index, k, was fixed to the reference value ($k = 0.001$). The value of real part, n, was then varied between 1.5 and 1.7 in steps of 0.5. Second, the real part was fixed to the reference value ($n = 1.65$), and the imaginary part, k, was varied from 10^{-5} to 10^{-1} in factor of 10 steps. Artifacts are found in the retrieved size distributions in the small size range (r < 1 μm) when low

Sample	r_{eff} (μm)	v_{eff}	$P_{min}(\%)$	$\alpha_{min}(deg)$	$\alpha_0(deg)$	$P_{max}(\%)$	$\alpha_{max}(deg)$	h(%/deg)
DaG521S	3.58	1.96	-3.3 ± 0.7	15 ± 5	32 ± 1	11.3 ± 0.91	80 ± 5	0.24
DaG521M	8.69	2.43	-4.9 ± 1.6	20 ± 5	34 ± 1	12.6 ± 1.4	75 ± 5	0.31
FRO95002M	3.92	2.72	-3.9 ± 0.1	20 ± 5	35 ± 1	10.0 ± 0.3	85 ± 5	0.20
FRO99040S	3.68	1.72	-3.3 ± 0.3	20 ± 5	33 ± 1	10.1 ± 0.3	80 ± 5	0.21
FRO99040M	5.90	3.10	-3.5 ± 0.6	20 ± 5	34 ± 1	10.7 ± 0.1	90 ± 5	0.19
Forsterite	3.06	1.04	-3.1 ± 0.3	15 ± 5	30 ± 1	9.9 ± 0.2	75 ± 5	0.22
Enstatite	3.70	3.13	-2.1 ± 0.3	15 ± 5	26 ± 1	11.3 ± 0.2	85 ± 5	0.19
Allende	2.44	3.42	-3.3 ± 0.3	22 ± 1	36 ± 1	7.5 ± 0.2	85 ± 5	0.15
Tholins	-	-	-6.7 ± 1.5	15 ± 5	35 ± 1	19.1 ± 3.3	90 ± 5	0.35

TABLE 5.3: Polarimetric parameters of the samples. r_{eff} and v_{eff} are the effective radius and effective variance. P_{min} is the minimum of polarization and α_{min} the relative phase angle. P_{max} is the maximum of polarization at phase angle α_{max} and α_0 is the inversion angle. h(%/deg) is the slope of the polarization curves computed between α_{max} and α_0. Tholins measurements were taken in the red domain, at $\lambda = 632$nm.

values of the real part ($n = 1.5$; $n = 1.55$) or extreme values of the imaginary part ($k = 10^{-5}$; $k = 10^{-2}$; $k = 10^{-1}$) are assumed. Therefore, we consider the reference value $n = 1.65 + i0.001$ as a reasonable estimate of the refractive index of our meteorite samples.

In spite of the sieving procedure described in Section 5.4.4, the meteorite samples show broad size distributions with volume equivalent radii ranging from 0.3 μm to $\sim$ 100 μm. Fig. 5.4 shows the $S(logr)$ size distributions of the samples. Here, $S(logr)$ is the projected-surface-area for a volume equivalent sphere with radius r. Size distributions are commonly characterized by the effective radio r_{eff} and effective variance v_{eff} as defined by Hansen & Travis (1974b). These parameters have a straightforward interpretation for mono-modal distributions, while for multi-modal distributions, the r_{eff} and v_{eff} are only first order indicators of the particles size. For example, the DaG521M and FRO99040M samples show bi-modal size distributions with secondary peaks at $\sim$ 30 μm and $\sim$ 20 μm, respectively.

Due to the limited amount of the tholins sample, we could not measure its size distribution. Based on the SEM images (Figs. 5.3k and 5.3l) we can estimate a broad size distribution with sizes ranging from sub-micron up to hundred of microns.

Morphology Fig. 5.3 shows Field Emission Scanning Electron Microscope (FSEM) images of our samples. It can be seen that in all cases the particles present a wide variety of irregular shapes. Figs. 5.3a - 5.3d show that the enstatite, forsterite and Allende meteorite particles present sharp edges and relatively clean flat surfaces compared with the other samples. The DaG521, FRO95002 and FRO99040 particles (Figs. 5.3e - 5.3j) present more rounded shapes with rough surfaces covered by a layer of small particles. These morphological differences could be partially caused by the powder preparation method. The dry-sieving procedure could not remove small particles that remained stuck on the surface of the large particles by electrostatic forces. By contrast, the enstatite, forsterite and Allende meteorite samples underwent wet-sieving, which removed a large fraction of the finest particles from the original sample. For this reason the grain surfaces appear generally smoother than for the other samples. Tholins show peculiar structures due to the synthesis process that produced very elongated particles of the order of 10 μm with layered substructure and sub-μm surface roughness (Figs. 5.3k - 5.3l).

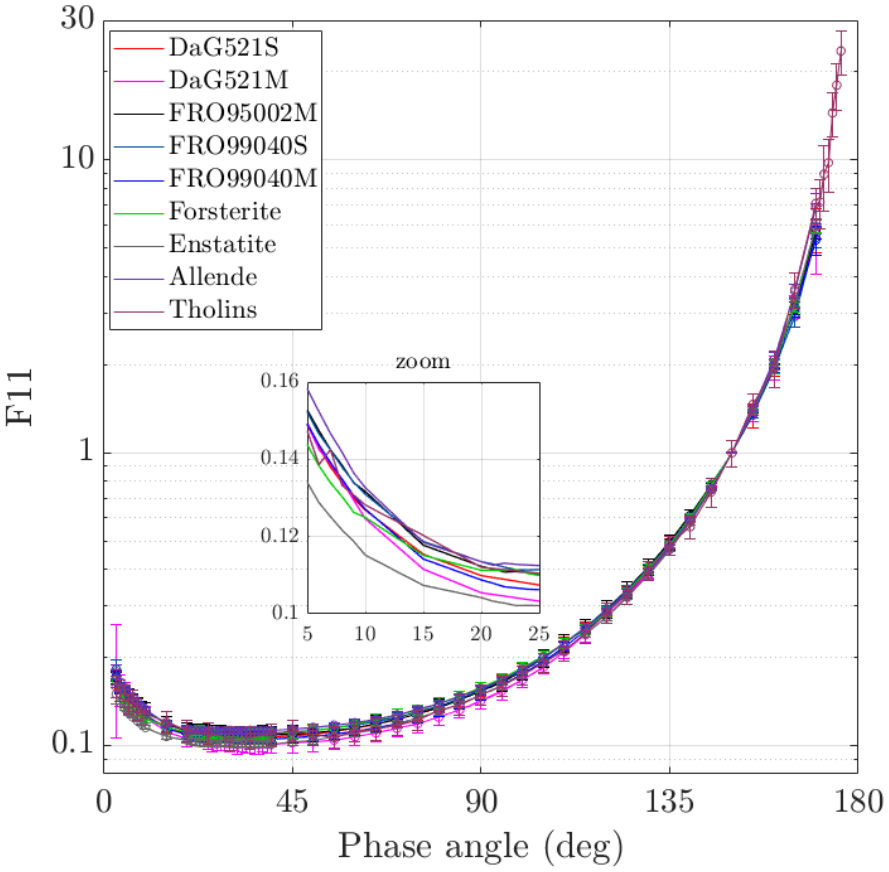

FIGURE 5.5: Phase function of samples with comparable effective radius.

5.5 Results and discussion

5.5.1 Measurements

In this section we present the measured phase functions $F_{11}(\alpha)$ (Fig. 5.5) and degree of linear polarization for unpolarized incident light $P(\alpha) = -F_{12}(\alpha)/F_{11}(\alpha)$ (Fig. 5.6) for all samples studied in this work. The measurements were performed at a wavelength of 520 nm covering the phase angle range from 3° to 175°. As mentioned, the measured phase functions are normalized to unity at $\alpha = 150°$. The experimental phase function and polarization curves are freely available in the Amsterdam-Granada Light Scattering Database [2] under request of citation of this paper and Muñoz et al. (2012). The light scattering behavior of the samples considered in this work is qualitatively similar to that of other types of irregular mineral dust investigated in the laboratory (see Muñoz et al. (2012) and references therein). The measured phase functions show a strong peak at large phase angles, a plateau with almost no structure at intermediate angles and

[2] www.iaa.es/scattering

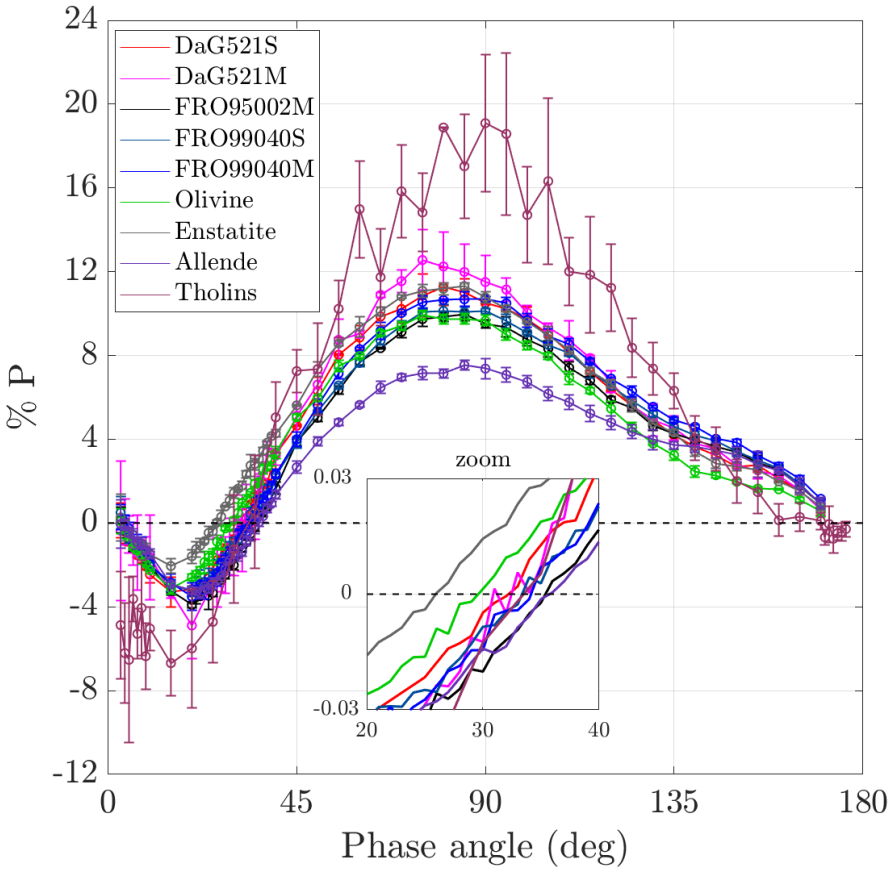

FIGURE 5.6: Polarization curve of samples with comparable effective radius.

a moderate increase at small phase angles. Fig. 5.5 does not reveal large differences between samples. The measured P curves display the typical bell-shape with a small negative branch starting at an inversion angle, α_0 and reaching a minimum at α_{min} (Fig. 5.6). The wide positive branch has a maximum P_{max} at $\alpha_{max} = 75° - 90°$. These polarization curves are also similar to those observed by remote sensing for a variety of Solar System objects such as comets and asteroids. In contrast to the phase functions, the polarization curves of our samples do show significant variability. Table 5.3 summarizes the main parameters of the degree of linear polarization curve in the region of minimum polarization (P_{min}, α_{min}), inversion angle (α_0), and maximum polarization (P_{max}, α_{max}).

Among our samples, tholins show the highest maximum values of linear polarization ($P_{max} = 19\%$) and the deepest negative branch ($P_{min} = -6.7\%$). Note that the empirical relationship known as *Umov's effect* indicates an inverse relationship between the maximum value of polarization and the geometric albedo (Zubko et al., 2011), and tholins are indeed the darkest material considered in this study. However, for a cloud of irregular particles in single scattering conditions the interrelation between P_{max} and the geometric albedo is dependent on the size distribution of the particle cloud (Zubko

et al., 2017, 2018). Thus, the Allende meteorite sample, which has the smallest effective radii, also presents the lowest maximum of the degree of linear polarization in spite of its dark color. Interestingly, the polarization curve of the Allende sample has a distinct feature compared to the pure silicate samples, showing a shoulder near $\alpha = 150°$ at all wavelengths (see Fig. 5.7). In the case of (the still few) Near-Earth Asteroids (NEA) observed so far, the maximum of positive polarization can reach, for low-albedo objects like (3200) Phaethon and (101955) Bennu, much higher values of linear polarization (up to 40%), whereas S-class objects have P_{max} values between 7% and 10%. The measured values of α_0 range from 26° for enstatite to 36° for the Allende sample. We do not find a clear relation between size distribution and position of the inversion angle. By contrast, for the range of sizes of our samples, the location of the inversion angle seems to be dependent on the composition. This is also found by Devogèle et al. (2018) in their analysis of Barbarian asteroids. On the other hand, other polarimetric evidence (P_{min} versus inversion angle plot) suggest that these objects should have a very fine surface regolith. This is also in agreement with some estimate of a low thermal inertia for (21) Lutetia, which has also a large inversion angle, not much smaller than that of Barbarians (Cellino et al., 2016).

Terrestrial materials consisting of pure non-absorbing minerals show lower inversion angles than the meteorites and tholins, which present iron and organic material in different proportions.

A fully satisfactory explanation of the negative branch of the linear polarization curve is still missing. Numerous Solar System objects such as asteroids and comets, which are covered by a thick regolith layer, show this feature.

Even quite small asteroids, for which we might assume that the surface regolith layer is thinner, generally exhibit the same general polarimetric behaviour as larger asteroids.

In principle, each powdered material should produce negative values of polarization at low phase angles, when coherent backscattering by small particles is considered. This physical effect results from the interference of wavelets scattered by the particulate medium. At zero phase angle the wavelets are in phase and they combined positively enhancing the intensity. The linear polarization reflects this effect as well, inverting the plane of wave polarization and favoring the parallel component of electromagnetic wave to be scattered, rather than the perpendicular one. The role of coherent backscattering in the development of a negative polarization branch and a backscattering enhancement in the phase function has been discussed by Muinonen et al. (2012) using the exact method known as the superposition T-Matrix (Mackowski & Mishchenko, 1996).

The origin of the negative branch of clouds of particles in single scattering conditions and corresponding particulate surfaces has also been investigated in several laboratory

Sample	r_{eff} (μm)	v_{eff}	x_{eff}	$F_{11}^{syn}(0°)$	$F_{11}^{syn}(30°)$	BSE (520 nm)
DaG521S	3.58	1.96	43.3	0.384	0.191	2.01
DaG521M	8.69	2.43	105.0	0.419	0.214	1.96
FRO95002M	3.92	2.72	47.4	0.390	0.201	1.94
FRO99040S	3.68	1.72	44.5	0.612	0.270	2.27
FRO99040M	5.90	3.10	71.3	0.427	0.203	2.10
Forsterite	3.06	1.04	37.0	0.384	0.197	1.95
Enstatite	3.70	3.13	44.7	0.369	0.188	1.96
Allende	2.44	3.42	29.5	0.519	0.266	1.95

TABLE 5.4: Parameters related to the backscattering enhancement computed for the samples at different wavelengths. BSE= $F_{11}(0°)/F_{11}(30°)$.

studies (e.g. Escobar-Cerezo et al. (2018); Shkuratov et al. (2007, 2006)). In a recent work, Escobar-Cerezo et al. (2018) compare the scattering behavior of two samples of the same lunar simulant with different size distributions. The effect of removing particles smaller than ~ 1 μm from the pristine sample on the polarization curve is noticeable. The maximum of the linear polarization increases by a factor of 1.5. Apparently the small particle fraction of the pristine sample was limiting the maximum of the degree of linear polarization. Further, the negative polarization branch (absolute values) is decreased from 2.4% to 0.8% after removing particles smaller than 1 μm. This result seem to indicate that sub-micron scale features might be responsible for the negative branch of the degree of linear polarization.

In summary, it is quite difficult to disentangle all the effects responsible for the polarization curve shape, we can only highlight some empiric relations, but it is essential to further investigate the subject. In sections 5.5.2 and 5.5.3 the differences observed in the phase function and degree of linear polarization are discussed in terms of different physical properties (size, color, shape), in order to disentangle their influence on the scattering behavior of the samples.

5.5.2 Backscattering enhancement

In order to give an estimation of the trend of the phase function in the backward region for all studied samples, we compute the backscattering enhancement (BSE), defined as the ratio of measured phase function values at $\alpha = 0°$ and $\alpha = 30°$ (Bertini et al., 2007). Since our laboratory measurements do not cover the whole phase angle range we extrapolated a synthetic phase function, F_{11}^{syn}, from our measurements that range from 3° to 175°. The synthetic phase function is defined in the full angle range from 0° to 180° and is normalized according to:

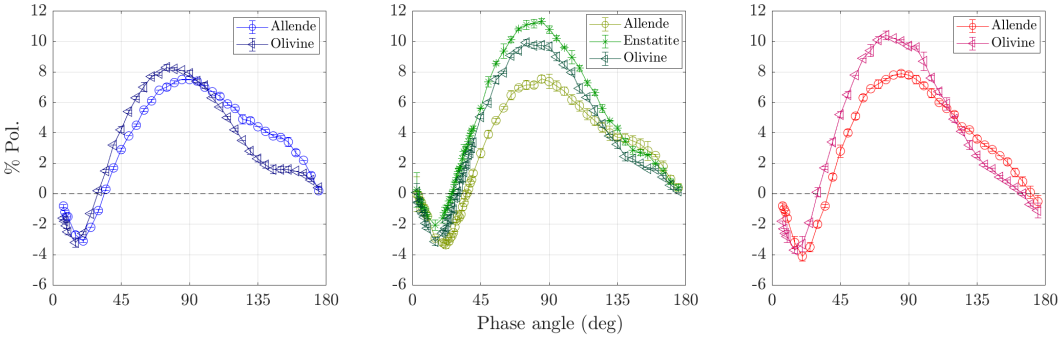

FIGURE 5.7: Polarization curves measured for Allende meteorite, Olivine and Enstatite in three different wavelengths.

$$\frac{1}{2}\int_0^{\pi} d\alpha sin\alpha F_{11}^{syn}(\alpha) = 1. \tag{5.4}$$

The extrapolation of the measured phase function in the forward direction is based on the assumption that the forward scattering peak for randomly oriented particles with moderate aspect ratios is mainly dependent on the size and refractive indices of the particles, but not on their shapes (Liu et al., 2003). Between 175° and 180°, we produce Mie calculations for projected-surface-area equivalent spheres. For the Mie computations we use the measured size distribution of the corresponding sample and the value of the refractive indices presented in Tab. 5.2. For the backward direction, we first generate a value for the phase function at 0° by a quadratic function generated by least squares with the measured data points from 3° to 30°. Then all values between 3° and 30° are produced by a cubic splines interpolation considering an additional condition that must be fulfilled in all cases: the first derivative of the phase function at 0° must be zero (Hovenier & Guirado, 2014). At this stage, both the forward peak ($175° - 180°$) and the rest of the phase function ($0° - 175°$) are defined, but they are normalized in a different way: the forward peak belongs to a function normalized according to eq. 5.4 and the normalization of the rest of the function is arbitrary. The function defined by the measured ($3° - 175°$) plus the extrapolated ($0° - 3°$) data points is then vertically shifted until the computed $F_{11}^{syn}(175°)$ matches the measured $F_{11}(175°)$. The normalization condition (eq. 5.4) is then checked. If it is not satisfied within a 0.1% accuracy, the value of the measurement at 175° is increased or decreased (within the experimental error bars) until the normalization condition is fulfilled. The backscattering enhancement for all our samples lays in the range [1.94-2.27] (see Table 5.4).

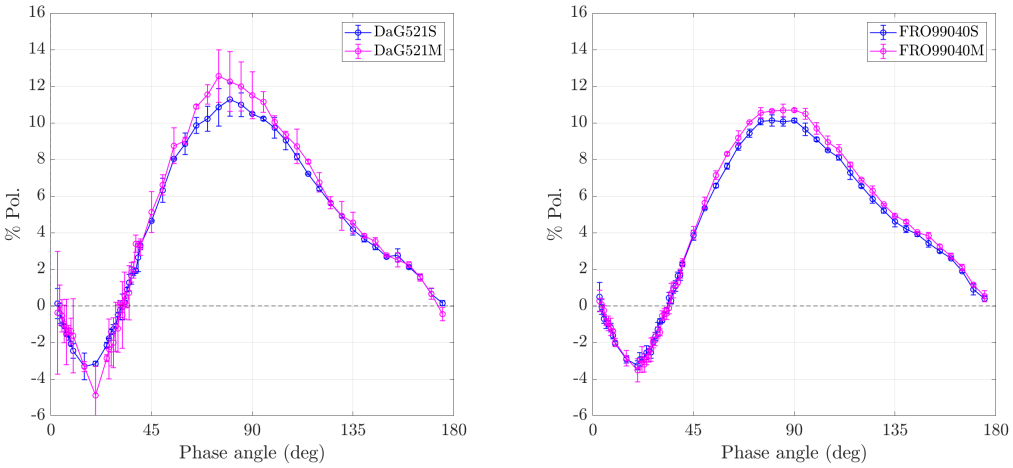

FIGURE 5.8: Comparison of polarization curves of DaG521S and DaG521M, on the left, and of FRO99040S and FRO99040M samples on the right.

5.5.3 The effect of size and color on polarization

The degree of linear polarization of the DaG521S and DaG521M, and the FRO99040S and FRO99040M samples are plotted in Fig. 5.8. Since each figure refers to the same material, the differences observed are only attributable to the different size distributions of the S and M samples. The salient feature of this comparison is an increase of the maximum polarization with size. In fact, it can be seen in Fig. 5.4, right panel, that the size distributions of the samples with a higher P_{max} (DaG521M and FRO99040M) present a secondary maximum at larger sizes. Thus, the contribution of particles with large size parameters ($x_{eff} = 2\pi r_{eff}/\lambda$) is most likely responsible for the measured increase in P_{max}.

The direct relationship between P_{max} and r_{eff} (or x_{eff}) apparent in Fig. 5.8 suggests an inverse relationship between P_{max} and wavelength, since the size parameter is inversely proportional to wavelength.

In the case of asteroids, there are spectropolarimetric data showing that the gradient of linear polarization for increasing wavelength depends on the taxonomic class and upon the phase angle. In the positive polarization branch, the polarization tends to decrease for increasing wavelength for S-class objects (moderate albedo). Low-albedo objects do just the opposite. Note also that, for any given object of any class, the polarimetric gradient changes sign if the object is observed in the negative or in the positive polarization branch (Bagnulo et al., 2015).

The polarization curves for the forsterite sample at three different wavelengths (442 nm, 520 nm, and 633 nm) are plotted in Fig. 5.9. The measurements at 442 nm and 633 nm have been published previously (Muñoz et al., 2000). It can be seen that P_{max} increases as the size parameter of the particles decreases (λ increases for a fixed r_{eff}). In this

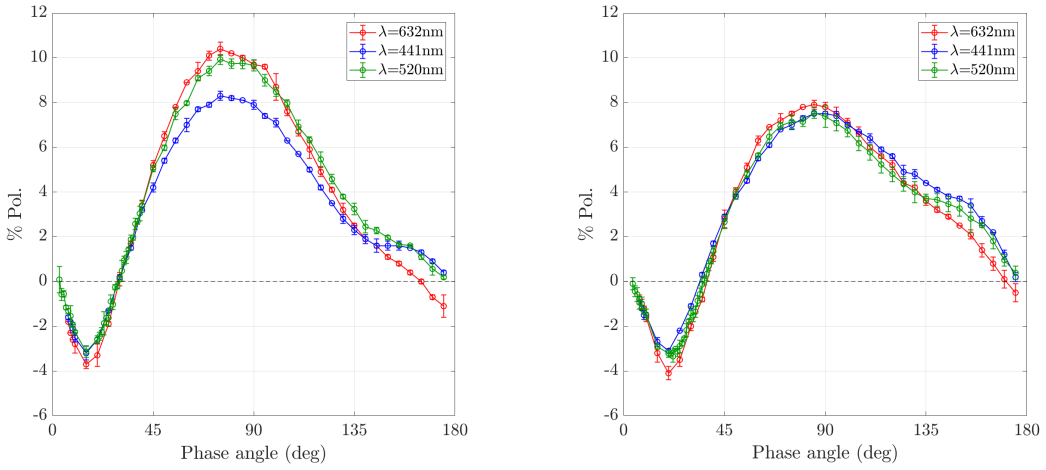

FIGURE 5.9: Polarization curves of OlivineS and Allende meteorite at three different wavelengths.

case the differences in the measured degree of linear polarization are also likely related to the size parameter of the grains, since the refractive index of forsterite presents a flat dependence on wavelength in the studied region.

The apparent contradiction between Fig. 5.8 on one side and Fig. 5.9 on the other can be explained by the broad size range of our samples. The scattering properties of dust grains are described by three regimes: Rayleigh, resonance and geometric optics. When particles are smaller than the wavelength (Rayleigh regime), P_{max} tends to decrease as the size parameter increases. In that case, P_{max} increases with wavelength if the refractive index is constant, i.e. $P_{max} \propto 1/x \propto \lambda$. By contrast, in the geometric optics regime ($x_{eff} \gg \lambda$), P_{max} tends to increase as the size parameter becomes larger, i.e. $P_{max} \propto x \propto 1/\lambda$. These trends are well illustrated by computed polarization data for Gaussian random shapes from the Rayleigh to the geometric optics regimes reported by Liu et al. (2015). As shown in Fig. 5.4, right panel, the contribution of grains in the geometric optics domain for samples DaG521M and FRO95002M is relatively large. Therefore, the P_{max} tends to increase as x_{eff} increases (Fig. 5.8). The majority of the grains in the forsterite sample belong to the Rayleigh and resonance ($x_{eff} \approx \lambda$) domains where the dependence of P_{max} with size is nearly opposite, i.e. it increases as x_{eff} decreases (Fig.5.9,left).

The degree of linear polarization curves for the Allende meteorite sample at three wavelengths (442 nm, 520 nm, and 633 nm) are plotted in Fig. 5.9, (right panel). As shown In Fig. 5.4 (left panel), the Allende sample mainly consists of particles in the Rayleigh and resonance regimes. In this case there is no clear trend of P_{max} with wavelength. The higher Fe content of the Allende meteorite compared to forsterite indicates a higher imaginary part of the refractive index at shorter wavelengths, implying a higher reflectance at red wavelengths. According to the Umov effect, the larger reflectance, the

Comet	λ (nm)	$P_{min}(\%)$	$\alpha_{min}(^\circ)$	$\alpha_0(^\circ)$	$P_{max}(\%)$	$\alpha_{max}(^\circ)$	h (%/deg)
High	515	-1.5 ± 0.5	9 ± 2	22.2 ± 0.5	26 ± 2	103 ± 10	0.22 ± 0.02
	670	-1.5 ± 0.5	11 ± 2	22.6 ± 0.5	28 ± 3	95 ± 10	0.25 ± 0.03
Low	515	-1.7 ± 0.5	6 ± 3	19.0 ± 0.5	10 ± 3	80 ± 10	0.20 ± 0.02
	670	-1.9 ± 0.5	6 ± 3	20.5 ± 0.5	18 ± 3	95 ± 10	0.22 ± 0.02
67P	red	-1.7 ± 0.1	12 ± 3	22 ± 2	-	-	0.35 ± 0.02*

TABLE 5.5: Polarimetric parameters of two classes of comets from Levasseur-Regourd et al. (1996). High stands for high P_{max} and Low stands for Low P_{max}. Values for 67P correspond to post-perihelion period and are taken from Hadamcik et al. (2016). *The h value for 67P is the slope at the inversion angle, since no value for P_{max} are available.

lower the maximum of the degree of linear polarization. Thus, the increase of P_{max} with wavelength seems to be balanced by a lower albedo at shorter wavelengths. Therefore, the maximum of the degree of linear polarization is dependent not only on the size of the grains but also on their refractive index.

It is worth noting that in the case of the forsterite sample (Fig. 5.9, left), the inversion angle α_0 does not change with wavelength. However, some wavelength dependence of the negative branch minimum can be distinguished at 633 nm. In the case of the Allende sample both, of the minimum of the negative branch and inversion angle vary with wavelength. The apparent dependence of the negative branch parameters with the composition (i.e. refractive index) seems to be in agreement with the simulations of Zubko et al. (2009, 2015), which demonstrate that the negative polarization parameters strongly depend not only on size parameter but also on the material absorption properties.

5.5.4 Comparison with asteroids and comets

Ground-based observations of the intensity of light scattered by cometary dust grains are usually limited to certain observational geometries. Moreover, time variations of the brightness of the coma as observed from Earth do not only depend on the phase angle but also on changes of the dust production rate as the comet moves in its orbit around the Sun (see e.g. Kolokolova et al. (2004)). The OSIRIS camera on board the Rosetta spacecraft revealed the behavior of comet 67P/Churyumov-Gerasimenko phase functions from inside the coma (Bertini et al., 2017). They were obtained in a short time period (about 2.5 h) covering an unprecedented broad phase angle range (from $\sim 10^\circ$ to $\sim 155^\circ$). The measured phase functions show a peculiar u-shape with a minimum at a phase angle around 100° 5.10. That phase function is not reproduced for any of the μm-sized randomly oriented particles studied in this work or previously presented in the Amsterdam-Granada Light Scattering Database (Muñoz et al., 2012). However, laboratory measurements of the phase function of mm-sized particles (Muñoz et al.,

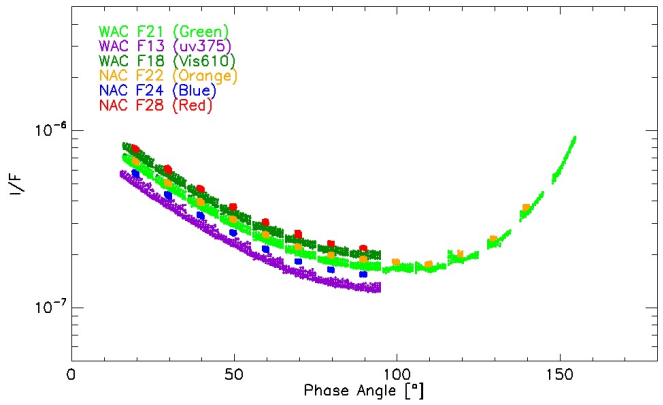

FIGURE 5.10: Multiwavelength phase function of 67P/Churyumov-Gerasimenko computed by (Bertini et al., 2017). The reflectivity in all used filters is plotted against the phase angle.

2017) show a distinct behavior compared to μm-sized particle clouds, with a minimum placed at much larger phase angles more in line with the 67P phase curve. Further, recent analysis of the OSIRIS phase functions at low phase angles provides a range of BSE values broader [1.7-3.6] (Bertini et al., in prep.) than that based on ground-based observations [1.7-2.7] (Ishiguro et al., 2013). As shown in Table 5.4, the BSE values obtained for our μm-sized cometary dust analogues are within the range obtained from ground-based observations. The highest BSE value obtained from the OSIRIS data (3.6) seem to be produced by a cloud of decimetric chunks orbiting 67P nucleus at distances smaller than 100 km (Bertini et al., in prep.). All in all our experimental data suggest that 67P phase function is not dominated by randomly-oriented μm-sized particles in line with the conclusions of multi-instrument analysis on board Rosetta (Guettler, in prep.).

Polarization is a powerful tool to investigate the nature of particles populating cometary comae and asteroidal regoliths. The value of the minimum of the degree of linear polarization together with the slope of polarization curve is generally used to determine the albedo of asteroids.

Moreover, polarimetric criteria are used to classify and refine the asteroid taxonomy (Belskaya et al., 2017).

In the case of asteroids, the angle of inversion of polarization is usually around 20 deg. A few objects, and also a few cometary nuclei, exhibit an inversion angle at lower phase angles ($15° - 17°$). Only a few rare objects, the so-called Barbarians, show high values of inversion angles, up to 28° (Cellino et al., 2006; Devogèle et al., 2018). We also note that some low-albedo near-Earth asteroids observed at large phase angles show much higher values of positive polarization, well above the limits reach by the samples analysed in this work. Only S-class NEAs show P_{max} values compatible with those values.

As opposite, there are no asteroids reaching negative polarization deeper than -2,-3.
As shown in Section 5.5.1, for the size range of the samples presented in this work, the position of the inversion angle depends on sample composition. A caveat to direct comparisons between observations and laboratory results is that the assumption of single scattering is no longer valid for such bodies, since they are covered by a layer of regolith. Single scattering is considered to be more adequate to explain the behaviour of low-albedo objects, for which multiple scattering is less important. As a result of multiple scattering the minimum polarization value approaches zero, and the inversion angle α_0 decreases (Shkuratov et al., 2006, 2004).
The condition of single scattering holds for cometary comae. Observational data show the existence of two classes of comets, based on the degree of linear polarization (Levasseur-Regourd et al., 1996; Shestopalov & Golubeva, 2017). The high polarization comets, which are considered dust-rich, and the low polarization comets, which have a higher gas component (Table 5.5). The measurements of the samples presented in this work seems to be of the order of the low polarization group. Generally, cometary comae behave qualitatively in a similar manner to our analog particle clouds: they show a negative polarization branch at small phase angles, and a bell-shaped curve at side and backscattering angles, with a maximum of polarization at a phase angle near 90°. However, the exact parameters defining the cometary polarization phase curve (see Table 5.5 for comet 67P in particular), are different from our laboratory measurements. The 67P polarization phase curve might be shaped by particles larger than the wavelength, but with wavelength-scale surface features that could produce a polarization roughly similar that of a cloud of isolated scatterers. Moreover, the h slope observed for 67P seems to indicate that it belongs to the family of "high polarization" comets (Rosenbush et al., 2017). This might be in agreement with the depletion of small particles (<1 μm) observed with Rosetta.
Our laboratory data support the interpretation of the decreasing polarization outward the nucleus of 67P, according to which this results from larger particles near the nucleus and smaller particles moving away from it (Rosenbush et al., 2017). In order to enable a more consistent comparison between astronomical observations and laboratory data, future studies need to consider more appropriate mixtures of components such as silicates, organics and ices, with improved control on other characteristics such as size, shape and surface roughness.

5.6 Conclusions

Our results are summarized as follows:

- All measured phase functions present the typical behavior of μm-sized irregular compact dust particles in random orientation. They show strong peaks at large phase angles, almost no structure at side phase angles and soft increase at small phase angles.

- The measured values of backscattering enhancement (BSE) of our samples are within the range obtained from ground-based observations of cometary comae. According to our experimental data small BSE values seem to indicate a coma population of μm-sized grains.

- The dependence of P_{max} with size is opposite for particle sizes belonging to Rayleigh-resonance ($x_{eff} \approx \lambda$) and geometric optic ($x_{eff} \gg \lambda$) regimes. When particles are smaller or of the order of the wavelength (Rayleigh-resonance regimes), P_{max} decreases with size whereas in the geometric optics regime P_{max} tend to increase with size.

- For the range of sizes of our samples, the minimum of the negative polarization branch seems to be dependent on both, size and composition of the grains whereas the inversion angle value, α_0, depends on the refractive index.

- The measured degree of linear polarization curves are qualitatively similar to that obtained from ground-based observations of cometary comae. This is in line with the finding that the main scatterers in the coma are larger than the wavelength of the incident light, where the surface features of the particles are of the order of the incident wavelength.

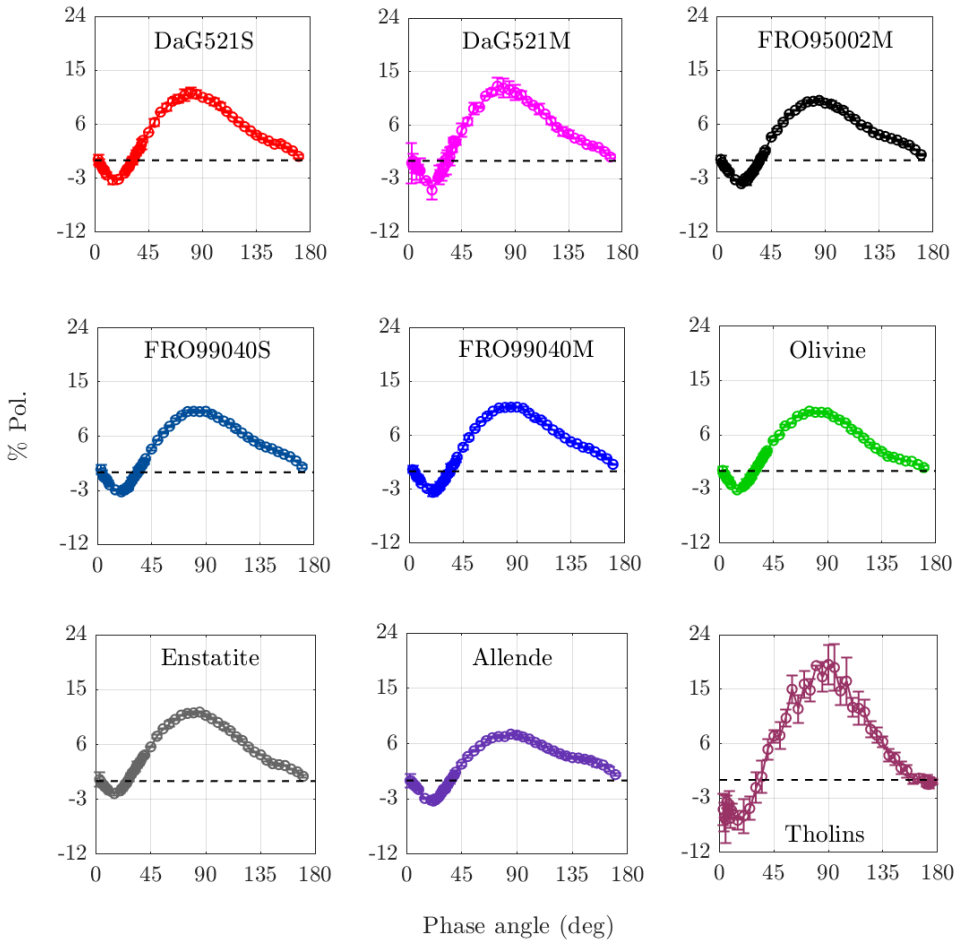

FIGURE 5.11: Polarization curve of the complete set of samples.

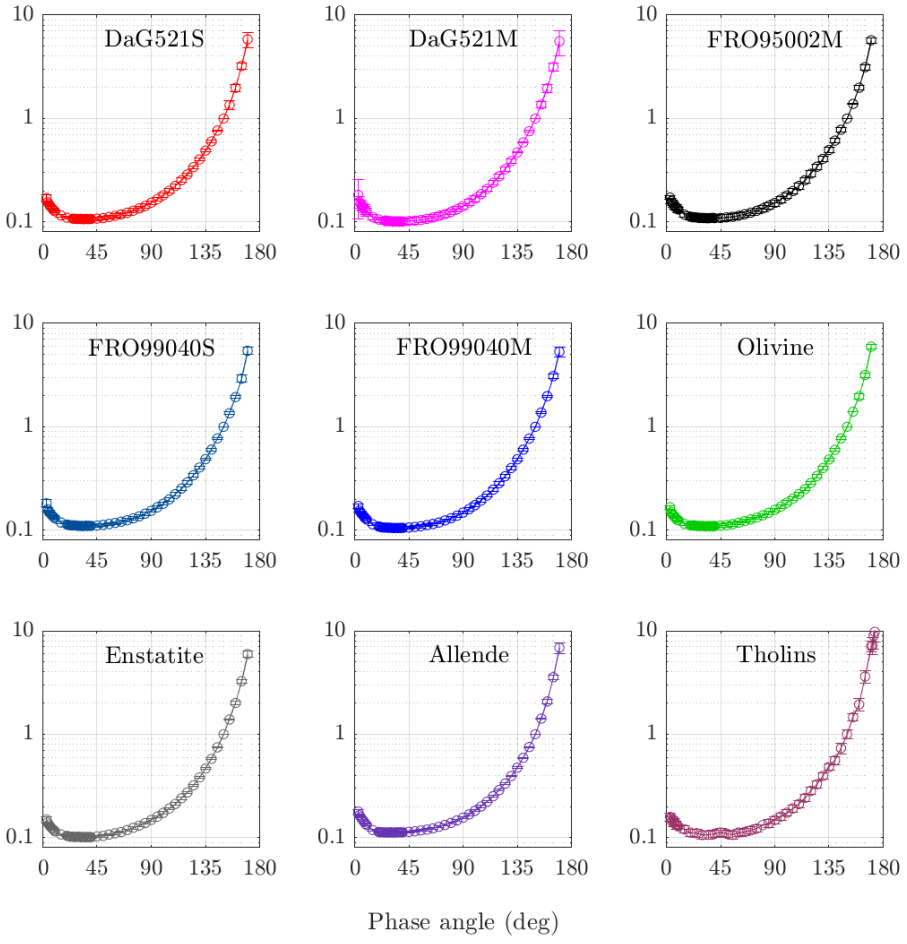

FIGURE 5.12: Phase function of the complete set of samples.

Chapter 6

Observational constraints to the dynamics of single grains

6.1 Abstract

In this work we aim to characterize the dust motion inside the coma of comet 67P-Churyumov-Gerasimenko. The OSIRIS camera on board the Rosetta mission, was able for the first time to acquire images single grains directly from inside the cometary coma, very close to the nucleus. We analyzed these tracks given an estimate of the rotating periods of the grains and we performed a strong statistic of their behavior during the post perihelion period, when the spacecraft covered distances from the nucleus ranging between 80 km to 400 km. We found an average value for the period of 1 second. The subgroup of rotating grains analyzed was about the 10-50 % of the overall grains population, suggesting that the remaining particles ware slow rotators. We computed also the ratio between the projected area onto the plane of the image of the sample of rotating grains, obtaining the most probable value of 1.4, which revealed a little flattening for these particles. Moreover, we performed a statistic on the overall population of grains, in order to define the alignment of their direction of motion with the solar and nuclear position. We found that the dust grains moves on a radial trajectory with respect to the nucleus in all the sample investigated. Our study provide some useful constraints for the models of grains dynamics in the cometary coma. This is still a work in progress and in the future we would like to increase the statistic and try to map the direction of motion of dust grains in the coma environment.

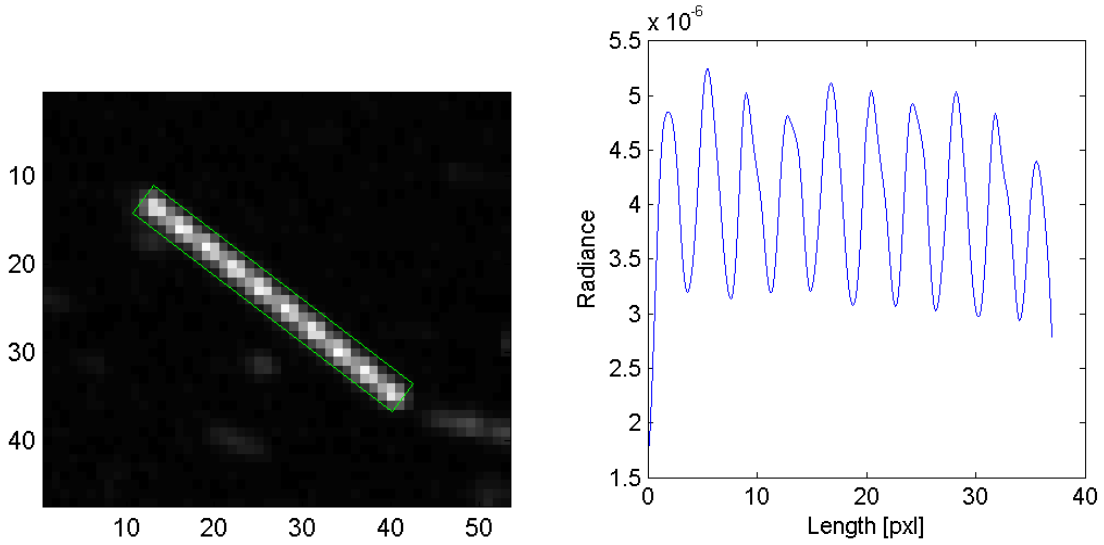

FIGURE 6.1: An example of rotating grain on the left panel and its rotational curve on the right panel.

6.2 Introduction

During its trajectory around the comet 67P, the OSIRIS camera on board the Rosetta mission was able to acquire images from inside the cometary coma, very close to the nucleus. From the period just before the perihelion from July 2015 to January 2016 the spacecraft reached distances from 80 km to 400 km from the nucleus (with one configuration at 1200 km). For the first time it was possible to directly observe tracks of single grains, to measure their typical parameters (value of flux, FWHM and orientation, etc.) and to provide a good statistic of the quantities involved thanks to the huge amount of data collected.

Cometary coma is a complex environment in which take place several physical and chemical processes, such as fragmentation, sublimation and photoionization. Several models have been developed during the years in order to describe the motion of the dust and the more reliable ones need to take into account the interactions between the two components of the coma: the gas and the dust. The main forces that define the motion of the grains are the gravitational force, the aerodynamical force generated by the gas drag and the solar radiation pressure.

The gas is considered the driver of the motion until a certain distance from the nucleus at which the particles reach their terminal velocity, and that occurs at about 10 nucleus radii from the center of mass (Crifo et al., 2005, 2002). Fulle et al. (2015b) and Ivanovski et al. (2017b) computed the exact distances at which single particles reach the terminal velocity varying their masses and obtained values that range between 10 to 100 Km. Clearly the dust production rate leads the process and it changes during the comet trajectory before and after perihelion.

The solar radiation becomes dominant when the gas drag decreases, and its typical distance depends on the models, taking values of 20 km for Skorov et al. (2018), or 5.5 nucleus radius for Ivanovski et al. (2017b), or 20 nucleus radius for Moreno et al. (2017). Moreover, the shape of the grains plays an important role in the dynamical models. The spherical particles models are no longer suitable to describe the dust motion after the evidences of irregular shape of dust grains revealed by the Stardust mission, by the IDPs analysis (Rotundi et al., 2008, 2007) and nowadays by the measurements obtained by GIADA and COSIMA for the Rosetta mission. Also the images provided by OSIRIS revealed the presence of non spherical particles, given by the brightness variation in the tracks of single grains, interpreted as rotational motion of irregular particles (Fulle et al., 2015b).

Therefore refined models, based on the aspherical shape of dust aggregates, have been developed by Ivanovski et al. (2017b) and Skorov et al. (2016).

In this work we present the analysis of the light curves of rotating grains, providing a statistic of their rotational periods and their possible variations depending on parameters such as the area of the coma analyzed or the nucleocentric distance. Moreover, we evaluate their flattening, given an estimate of their shape. From the preliminary analysis of the orientation of the tracks, the grains seem to follow a radial motion with respect to the nucleus up to 145 km from it.

The statistic performed in this work provides useful parameters for the still poorly constrained grains dynamical models.

6.3 Geometry

The tracks detected on the images are the 2D projection of the 3D grain motion. Considering the NAC reference system, the plane of the image is oriented such as the x axis of the images is roughly aligned with the y axis of the NAC reference system, while the y axis of the image coincides with the x axis of the NAC (Hviid, 2010). The camera is able to see objects within a certain distance, likely of few tenth of km, depending on size and composition of the particles (Frattin et al., 2017).

For this work we have analyzed 20 set of images taken in various epoch for a total of 809 images. We noticed 3 specific geometries of observation:

1. The line of sight (axis z) lies on the plane Sun-nucleus and the x axis points toward the Sun. The camera maps always the same area of the coma with respect to the nucleus, during a specific interval of time. Therefore the images are taken with the same configuration and clearly the angle between line of sight and Sun (ϵ) is maintained constant.
2. The line of sight moves on a plane perpendicular to the plane defined by Sun and

STP	epoch	r_c (km)	$R_\odot$ (AU)	$\alpha(^\circ)$	$\epsilon(^\circ)$	#rot	#im	#m	# tot	%rot	T (sec)	a/b	bkg (W/m^2 nm sr)
66GC	2015.07.24	184	1.26	99	90	31+20	4	8	314	16	0.5	1.2	$1 \cdot 10^{-6}$
67GC2	2015.08.04	238	1.25	89	135	89+61	8	11	599	25	1	1.4	$1 \cdot 10^{-6}$
78GC5	2015.10.18	435	1.40	65	107-95	15+15	6	2	104	28	1	1.2	$3.3 \cdot 10^{-7}$
81GT3	2015.11.10	202	1.61	62	137	43+21	12	4	284	22	1	1.4	$1 \cdot 10^{-6}$
83GT1	2015.11.27	142	1.70	88	122	70+35	6	12	355	30	1	1.4	$9 \cdot 10^{-7}$
84GT2	2015.11.30	111	1.70	89	120	9+3	7	1	107	11	1	1.2	$7 \cdot 10^{-7}$
86GT3	2015.12.10	99	1.86	89	76	74+52	10	8	301	41	1	1.4	$2.8 \cdot 10^{-6}$
87GT1	2015.12.17	100	1.9	89	105	50+42	12	5	198	46	1-2	1.4	$9 \cdot 10^{-7}$
89GC2	2016.01.04	79	2.0	89	91	140+154	19	7	1083	27	1	1.4	$2.3 \cdot 10^{-7}$
90GT3	2016.01.06	84	2.06	89	75	13+15	9	1	72	38	1	1.4	$2 \cdot 10^{-6}$

TABLE 6.1: Dataset of images used to compute periods and axis ratio. r_c is the nucleocentric distance, $R_\odot$ the heliocentric distance, α is the phase angle, ϵ is the elongation of the Sun, #rot is the number of rotating grains individuated in each set: the number on the left represents the grain with regular light curve, used to compute the period, while the add number is the number of grains that show evidence of rotation but not regular light curve. #set is the number of images analyzed for each set, #m is the average number of grains in each image of the set # tot the total number of grains in the set, %rot is the percentage of rotating grains with respect to the total. T is the average rotating period, a/b the axis ratio and bkg the value of the background.

nucleus. The Sun lies on the x axis. In this case each image samples a different part of the coma but always in the plane perpendicular to the Sun so the angle ϵ is still constant.
3. The configuration in this case is quite variable. The line of sight moves on a plane inclined with respect to the plane Sun nucleus. The camera samples different part of the coma and this time also the angle ϵ varies.
An exhaustive description of the geometry of observation is given in A.

6.4 Methods

The images analyzed in this work were acquired from July 2015 and January 2016 (perihelion passage August 2015) by the OSIRIS NAC (Narrow Angle Camera) in the Orange filter (λ = 649nm). For the study of the rotational state we decided to focus on set of images for which the geometric configuration formed by the spacecraft, the comet and the Sun is such as to remain stable during time. It means that the camera points always the same area with respect to the nucleus during a day (which is an important reference to consider in order to be sure to analyze the same coma area even if it changes due to the flow of material passing through). The data are reported in Tab. 6.1. Otherwise, for the analysis of the direction of motion of the particles we chose set of images which configuration changes among the same set, in order to map as much coma area as possible. The set is reported in Tab. 6.2. See A to have an exhaustive description of the geometry of observation.
We used an automatic method to detect the tracks from the images and to provide physical parameters as the flux, the FWHM and the orientation (Frattin et al., 2017). Then we evaluated each track to distinguish between a rotating grain and those that do not show evidence of rotation. The criterion we used was based on the amplitude between the maximum and the minimum, which must be bigger than the background error. We decided also to not consider those tracks that showed only two peaks of brightness, in order to avoid possible contamination from two different tracks (Fulle et al., 2015b). Overall we analyzed 534 grain light curves. An example of the detection is given in Fig. 6.1.

6.5 Rotational state of dust grains

We considered only those light curves that show regular brightness variations (see fig. 6.1). Since the image exposure time is known, it is straightforward to obtain the rotational period directly from the division of that exposure time for the number of maximum

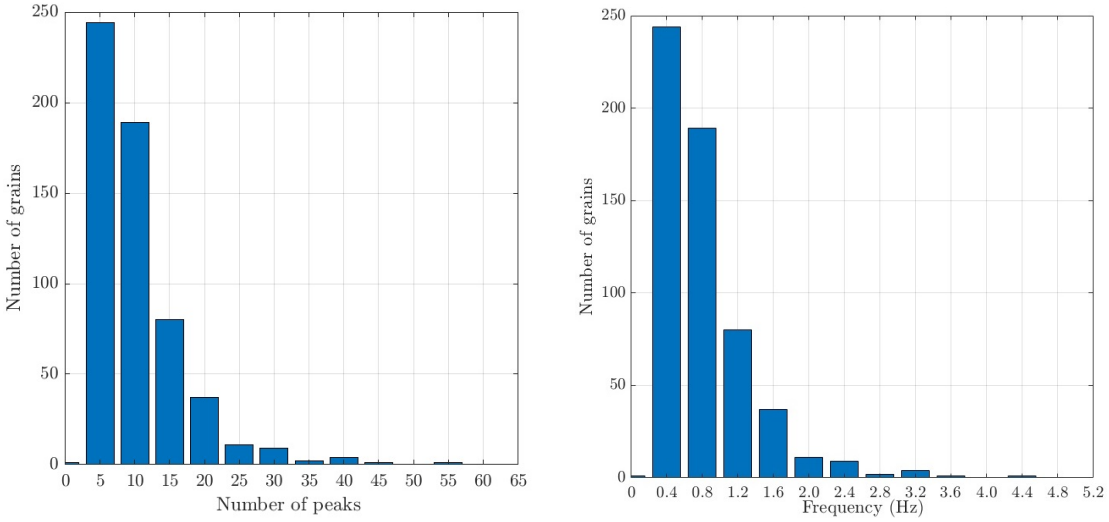

FIGURE 6.2: The histogram on the left panel represents the cumulative values for grain rotational periods in terms of number of peaks in the light curves, while the histogram on the right panel represents the cumulative values for grain rotational frequencies.

brightness peaks in the light curves. It does not depend on the track length neither on the track distance nor on the flux, but only on the number of peaks.

The highest probability for each set is reported in Tab. 6.1 and corresponds to value of rotational period of 1 second, which results approximately the same for each epoch. Since the periods statistic does not show any particular evidence of variation with respect to the epoch nor to the nucleocentric distance, a cumulative study of those grains is allowed. In Fig. 6.2 we report the histograms representing the rotational periods statistic in terms of number of peaks counted in the light curves and the respective rotational frequencies.

The observational bias plays a decisive role. There is a minimum number of detected peaks equal to 2, unless the periodic oscillations would result not visible. Anyway in this work we decided to be conservative and consider only those tracks with at least three peaks. The maximum number instead is related with the length of the track: it is possible to count high number of grain rotations only in the long tracks. The small tracks can show only a restricted number of rotation peaks. In order to quantify this bias we have analyzed the distribution of the number of peaks in relation with the tracks length, see Fig. 6.3. The majority of the population is distributed compactly and homogeneously in a certain area of the space parameter, while is possible to recognize some deviations from this average behavior. There are indeed very long tracks showing only few rotations and moderately long tracks presenting high rotational spin. Obviously there are not short tracks with high number of peaks, due to the observational bias.

The number of peaks depends on the particles rotational frequency which results, for the majority of them, in the range ν =0.2-0.6 Hz. On the other side, the length depend on the velocity of the particles and on the distance at which they are located.

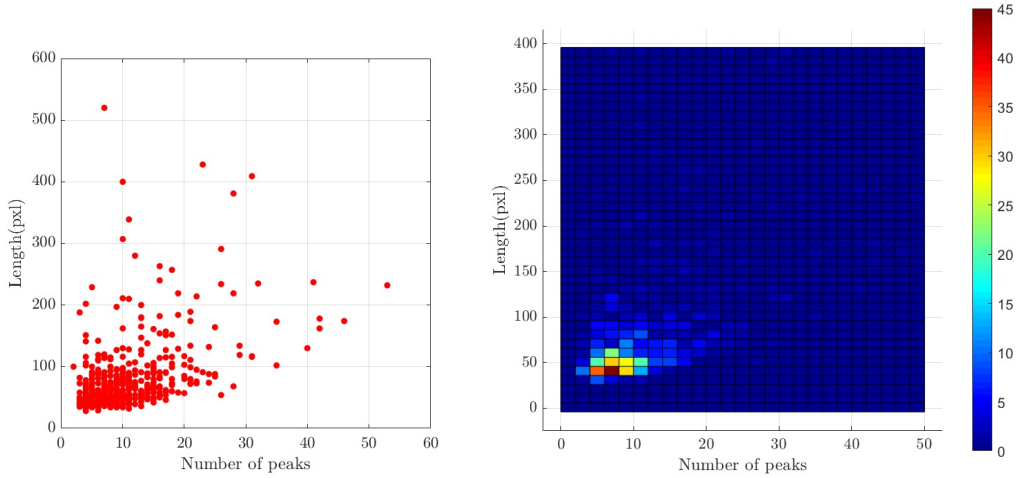

FIGURE 6.3: Space parameter defined by the tracks length and the rotational periods.

We know that the velocity at which the particles move inside the coma can be approximated with the value of 1 m/s. This implies that, at first approximation, within the same image the longest tracks represent on average closer particles, while the shorter ones are particles far away from the spacecraft.

Looking deeper in the problem we see that the length and the number of rotations depend also on other factors, as the mass and the size of the particles. Following the simulation of Ivanovski et al. (2017b) we expect that the smaller grains will reach higher terminal velocity rather than the larger ones. Moreover, among grains with different density, the porous ones reach higher terminal velocity with respect to the dense ones. Consequently, long tracks could be assigned both to close particles, but also to fast small grains, while short tracks could be generated by grains far away from the spacecraft, but also from slow bigger grains. Also the rotational velocity is higher for small and porous aggregates rather than for bigger and dense ones.

It is actually complex to disentangle all these factors in order to recognize grains populations with different characteristic relying upon the distribution on this parameter space. However, through a comparison with the values simulated by Ivanovski et al. (2017b) we can verify that the high frequencies found with our analysis are better represented by less dense and small aggregates with size of mm (or smaller) than by bigger particles, for which they should reach very low values.

It is important to notice that the tracks that show brightness variation are a percentage that range between 10-50% of the average number of tracks observed on an image, therefore all those tracks without brightness variation could be representative of very slow rotators or of grains that do not rotate at all or at least of grains with spherical shape (see Tab. 6.1). From the simulations it results that the grains are mainly slow rotators, with an average frequency of 0.03-0.2 Hz (Ivanovski et al., 2017a). Therefore

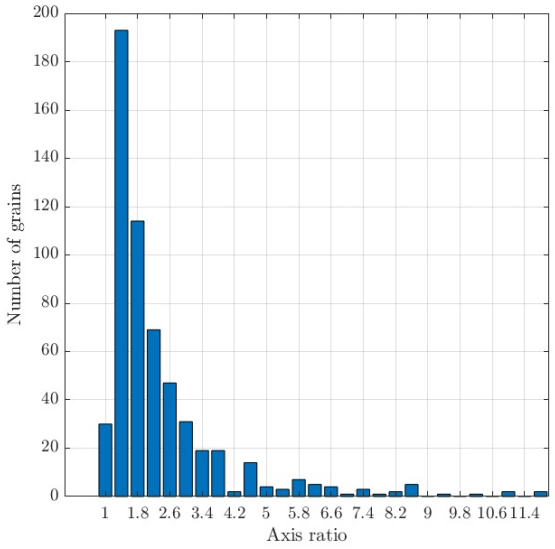

FIGURE 6.4: In the figure is shown the statistics of axis ratio of ellipsoidal particles.

the fast rotators we are looking at belong to a subgroup of the total population that can be used as a proxy to give an estimate of the small, porous grains with respect to the bigger and compact ones, supporting the idea of a coma composed by a significant amount of big particles.

6.6 Shape-axis ratio

Dust grains have irregular shapes, they can be fluffy aggregates or more compact particles. To give an estimate of how elongated the particles are, we measured the ratio between the maximum and the minimum of the light curves which represent the projected area of the grains on the plane of the image. We decided to approximate these shapes with an ellipsoid, precisely with a spheroid. Clearly the finding values are always major than 1 (which is the value for a perfect sphere), cause we cannot discriminate between oblate and prolate spheroids. It means that a value equal to 2, for instance, could be attribute to a prolate spheroid but also to an oblate spheroid with axis ratio 0.5. Following the results of Fulle et al. (2015b) we might suppose a higher percentage of oblate spheroids.

In Fig. 6.4, we see that the most probable value for axis ratio is 1.4, therefore the particles will be almost spherical, with little flattening. In Fig. 6.5, is shown the space parameter defined by the axis ratio (of an ellipsoidal grain model) and number of rotations. The majority of the grains fill homogeneously an area defined by value of axis ratio between 1 and 2 and number of peaks between 5 and 15. Therefore, for those grains will not be possible to infer a relation between rotational frequency and shape. Furthermore we recognize two populations that deviate from the majority: one with high

rotational frequency, to which corresponds low values of axis ratio so more spherical particles, the other population has high values of axis ratio, up to 4-5, which corresponds to very elongated particles with relatively slow rotational frequency. Indeed more elongated particles are expected to rotate slower than the spherical one, and this is linked to their moment of inertia (Ivanovski et al., 2017a). Likely the grain we see are small and little elongated particles, the only one that are allowed to be so fast in rotation. If they represent only a small percentage (10-50%) of the overall population of grains, it means that the majority is well represented by big and elongated grains, with low values of rotational velocity.

6.7 Coma interaction with solar radiation

In this section we study the direction of motion of the dust in the inner coma of comet 67P. There are several processes that contribute to the dust transport in the coma as the rocket force, the gas drag, the gravity and the solar radiation. At certain distance from the nucleus the gas drag reduces its power and the radiation pressure becomes dominant. We aim to provide an estimate of the distance at which the solar radiation pressure becomes dominant.

In order to measure the direction of motion of the particles we evaluated the angle between the velocity vector of the grain, defined by the track itself, and the projected position vector of the Sun and of the nucleus on the plane of the image, in the NAC reference system (see A for the observational geometry of each set). The positions of the Sun and the nucleus were derived using the Spice Kernels. The cosine between the two vectors is representative of their similarity: the closer to 1 it results and the more parallel are the vectors, meaning that the grains have a component of the motion that points away from the nucleus (or the Sun). Otherwise, if the cosine has a value closer to 0 it means that the particle has not a component of the velocity in the nucleus (or the Sun) direction. Since we are not able to discriminate the initial and final point of the tracks we have decided to consider the absolute value of the cosine. In this way we loose the information about the emission direction of the grains, therefore it is not possible to know which are the grains that come from the nucleus and those that fall back to the nucleus.

We have analyzed 5 set of images in the post-perihelion period. The data are reported in Tab. 6.2. In this case the configuration changes so the region of the coma investigated changes too. With this analysis it is possible to give an estimation of the direction of motion of the particles in different zones of the coma. Our results are shown in B, where for each set we have provided the histogram of the values of the cosine for each image belonging to the set. The appropriate configurations are illustrated in A. From these

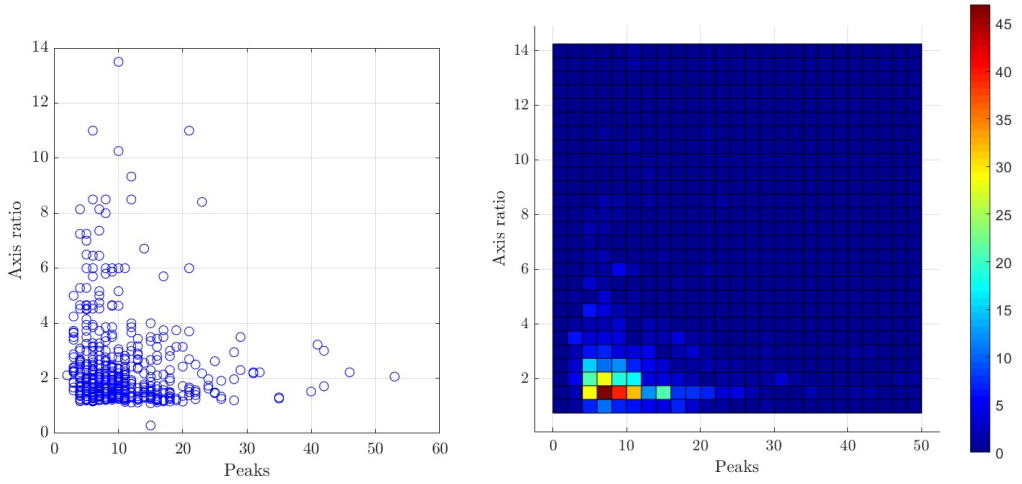

FIGURE 6.5: The graphic shows the parameters space of axis ratio and number of peaks in the light curves.

MTP	STP	series	epoch	r_c (km)	$R_\odot$ (AU)	$\alpha(^\circ)$	$\epsilon(^\circ)$
022	82	DP4	2015.11.16	145	1.68	75	104
023	83	GC1	2015.11.19	126	1.70	74	50-130
023	85	GC5	2015.12.14	100	1.90	89	90
024	89	GC2	2016.01.04	79	2.0	89	91
024	89	DP2	2016.01.04	80	2.04	90	90

TABLE 6.2: The complete data set for the measurements of the particles trajectories alignment with nucleus and Sun directions.

results it is clear that the particles are aligned with the nucleus position direction for the majority of the configurations. To have an estimate of the distance at which the particles are located we consider their velocity. Simulations by Ivanovski et al. (2017b) and measurements by Rotundi et al. (2015) and Ott et al. (2017) defined the average particles velocity $v = 1$ m/s. The length of the tracks range between 20 to 400 pixels, the majority of them having a value less than 100 pixels. Since the exposure time of our images is $t = 12.5$ seconds we can compute the maximum distances of the particles from the spacecraft as:

$$d = \frac{t_{exp} \cdot v}{sin(l \cdot 2.2^\circ/2048)} \tag{6.1}$$

where l is the length of the track, 2.2° the NAC field of view ans 2048 the pixel length of the images. The results are reported in Tab. 6.3. We should keep in mind that this is a maximum value for the distance since the tracks are projected onto the plane of the images loosing the information of the radial component of the velocity with respect to the plane of the image. For instance, if the image was taken at 80 km from the nucleus (as the closest case of set 89GC2) we would expect to see particles up to 10 km from it in the direction of the nucleus as maximum limit. However, the images do not point toward the nucleus but away from it at least of 15°. In that case, the maximum distance

length (pxl)	10	100	400
dist (km)	70	7	1.7

TABLE 6.3: Maximum distances at which the particles are suppose to be if we consider a average value for the velocity of 1 m/s.

at which the camera should be able to reveal the grain tracks is located at 20 km from the nucleus (from geometrical construction).
In our preliminary results we found that up to nucleocentric distance of 145 km the grains show evidences of radial motion from the nucleus. This is roughly consistent with the aforementioned dynamical models in which the particles motion appears to be still dominate by the gas drag. However, the dataset is still incomplete and we need to explore the series of images taken at larger distances to draw reliable conclusions.

6.8 Conclusions

In this ongoing work we have examined the dynamical properties of dust grains in the coma with the aim to provide constraints for modeling. The observational conclusions are the following:
1. The most probable frequency of rotation measured for our dust grains sample is in the range of $\nu = 0.2 - 0.6$ Hz.
2. The rotation frequencies distribution strongly increases as the sample rotation frequency decreases, showing that the most probable rotation period is lower than the lowest period that could be evaluated.
3. The percentage of rotating grains ranges between 10-50 % of the all population. Therefore we are seeing quite fast rotators, better represented by small porous aggregates (with size of mm or smaller) than by bigger particles, for which they should reach very low values of rotational frequency.
4. The most probable axis ratio for an ellipsoidal shaped aggregate is equal to 1.4, which means that the detected rotating grains are relatively elongated.
5. Our preliminary results suggest that the grains trajectory is radial to the nucleus up to 145 km from it.

Chapter 7

Conclusions

In conclusion we could say that the analysis of images of comet 67P/Churyumov-Gerasimenko taken by OSIRIS, the camera on board the Rosetta mission, provided essential information on the nature and behavior of cometary dust. Moreover, the laboratory experiment we performed, allowed the comparison with Rosetta and ground-based observational data, deriving some constraints on the properties of dust grains in the coma. Our work inserts in the complex framework delineated by Rosetta observations and contributes to the huge challenge of characterizing cometary dust.

The photometric investigation of more than 2000 dust grains in the period from July 2015 to January 2016 revealed several characteristics. We have found that the grains have average value of the spectral slope of 13%/100 nm in the wavelength range of [649-882] nm and a spectral slope of 7%/100 nm in the range [480-649] nm. The values of spectral slopes computed for each day show small variations depending on the distance from the Sun and from the nucleus suggesting certain degree of heterogeneity in the coma properties, depending on the ongoing evolution of comet environment. The 3-point spectra of a subgroup of 339 grains reveals the presence of three types of composition: a) the 13% of very steep slope spectra with values >15 %/100 nm, which may be connected with the presence of organics; b) the 77 % of spectra with intermediate slope values ranging between 5 and 15 %/100 nm; likely a mixture of silicates and organics and c) the 10% of flat spectra with spectral slope less than 5 %/100 nm, most likely due to much higher abundance of water ice.

Then, the laboratory experiments on cometary analogs we performed in collaboration with the Instituto de Astrofisica de Andalusia, Granada, allowed us to measure the phase function and the linear polarization curve of 7 different samples: 4 meteorites, 2 silicates and 1 organic compound. The direct comparison of our results with the phase

function measured by OSIRIS and with the polarization curves obtained by ground-based observations, reveals significant differences, suggesting that the main scatterers in the comet coma are not randomly oriented micrometer particles, but chunks of mm-dm with surface features of the order of the incident wavelength, as revealed by the multi-instrumentation analysis. We measured also the polarization curves for different size distribution of two samples, observing that bigger material produces higher value of maximum polarization. This evidence can help in the interpretation of observational data from comets as for example the case of 67P for which it was measured a decrease of polarization with nucleocentric distance that can be interpreted as a decrease in particle size.

The examination of the dynamical state of dust particles allows us to put some constraints to the dynamical models that try to reproduce the dust behavior in the coma. From the analysis of brightness variation in the tracks generated by the motion of the particles we have measured the rotational period of dust grains. We have found that the grains that show rotation are the 10-50 % of the total population with the most probable period of 1 second. This suggests that the majority of the grains have a period of rotation less than the one measured, not detectable in a pose of 12.5 seconds. Therefore, no fragmentation for centrifugal force is expected. Moreover, from the analysis of the light curves we were able to infer the ratio between the emitting areas of the aggregates. We found that the most probable value was 1.4, suggesting a shape not very elongated for those particles. Another parameter we were able to compute was the radial component of the particles motion on a dataset of 5 series taken at distances from the nucleus ranging from 80 km to 145 km. From our analysis the grains seem to be aligned with the nucleus direction, as we expect in the inner part of the coma still dominated by the gas drag.

Regarding the future perspectives we plan to deepen and extend the the spectrophotometric and dynamical analysis of dust grains to the entire set of suitable OSIRIS data. Moreover, it will be interesting to characterize those boulders emitted by the nucleus that have been observed into the inner coma.
Then, we plan to focus on the research of natural satellites possibly released during the perihelion passage. We will take advantage of those images taken at high distance from the nucleus in order to test as much area as possible around it.
Another future development will consists in the production of synthetic cometary analogs, as similar as possible to the coma dust, with particular attention on their structure and composition, in order to investigate their optical properties in the laboratory.

Appendix A

Observational configurations

MTP	STP	series	epoch	r_c (km)	$R_\odot$ (AU)	α (°)	ϵ (°)	# set
018	66	GC	2015.07.24	184	1.26	99	90	4
019	67	GC2	2015.08.04	238	1.25	89	135	8
019	70	GC3	2015.08.25	403	1.25	85	115-145	8
020	71	GC3	2015.08.31	404	1.26	70	(?)40-120	9
020	73	GC1	2015.09.11	326	1.31	119	29	3
020	73	GC4	2015.09.15	327	1.31	92	95-135	6
021	75	GC2	2015.09.28	1220	1.37	50	90-160	6
021	78	GC4	2015.10.18	437	1.47	65	70-150	5
021	78	GC5	2015.10.18	435	1.40	65	107-95	6
022	79	GC1	2015.10.23	389	1.51	63	70-150	8
022	81	GC2	2015.11.06	244	1.61	63	45-140	10
022	81	GT3	2015.11.10	202	1.61	62	137	12
022	82	GT4	2015.11.17	141	1.68	62	138	11
022	82	DP4	2015.11.16	145	1.68	75	104	19
023	83	GC1	2015.11.19	126	1.70	74	50-130	5
023	83	GT1	2015.11.27	142	1.70	88	122	6
023	84	GT2	2015.11.30	111	1.70	89	120	7
023	85	GC5	2015.12.14	100	1.90	89	90	10
023	86	GT3	2015.12.10	99	1.86	89	76	10
024	87	GT1	2015.12.17	100	1.9	89	105	12
024	89	GC2	2016.01.04	79	2.0	89	91	19
024	89	DP2	2016.01.04	80	2.04	90	90	18
024	90	GT3	2016.01.06	84	2.06	89	75	9

TABLE A.1: The complete data set analyzed. MTP: Medium Term Planning (1 month); STP: Short Term Planning (1 week); Series: Grain Colours, Grain Track or Dust Phase; r_c (km) is the nucleocentric distance; $R_\odot$ (AU) the heliocentic distance; α (°) is the phase angle; ϵ (°) the elongation; # set the number of set of 4 images for each STP .

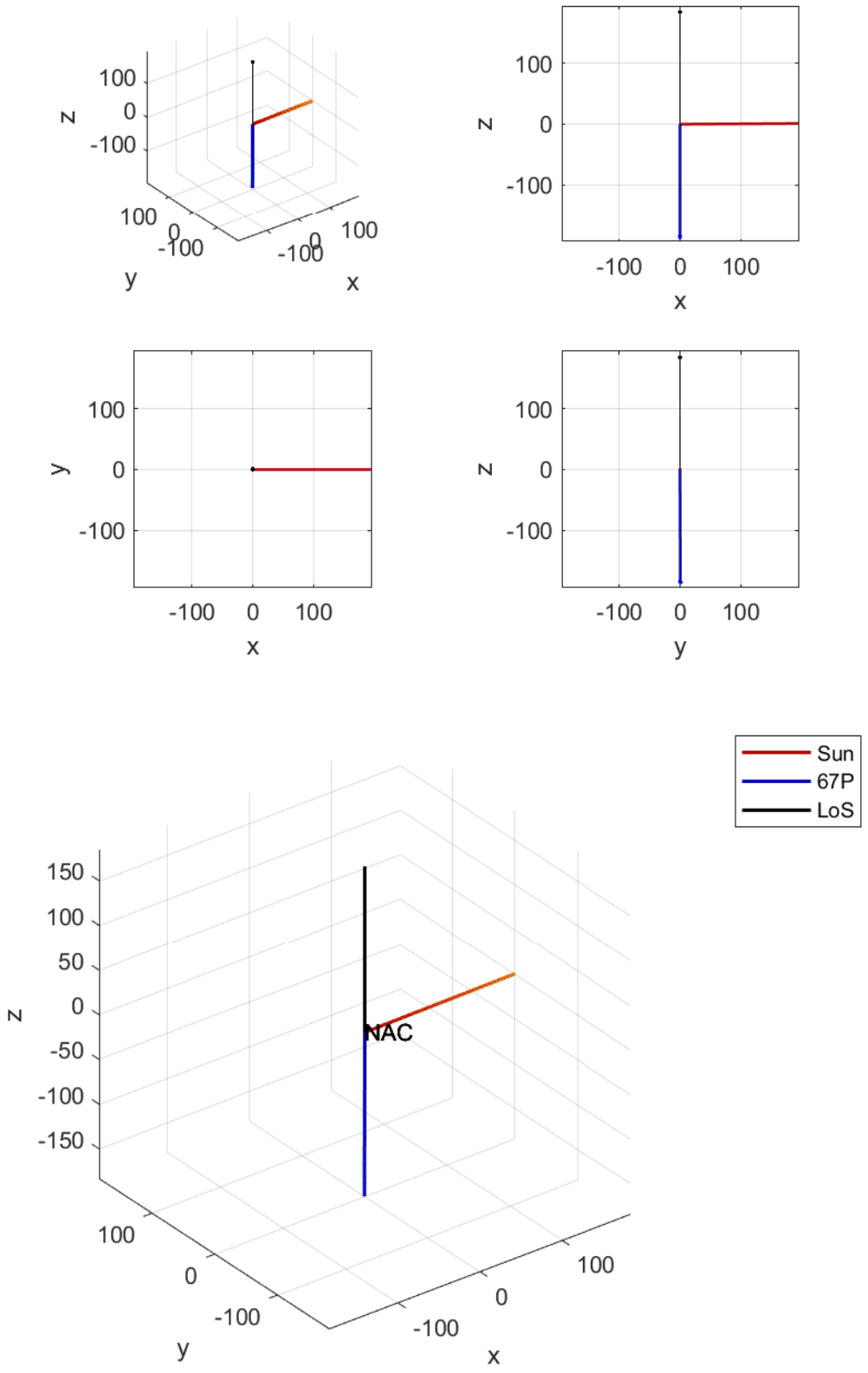

FIGURE A.1: 66GC

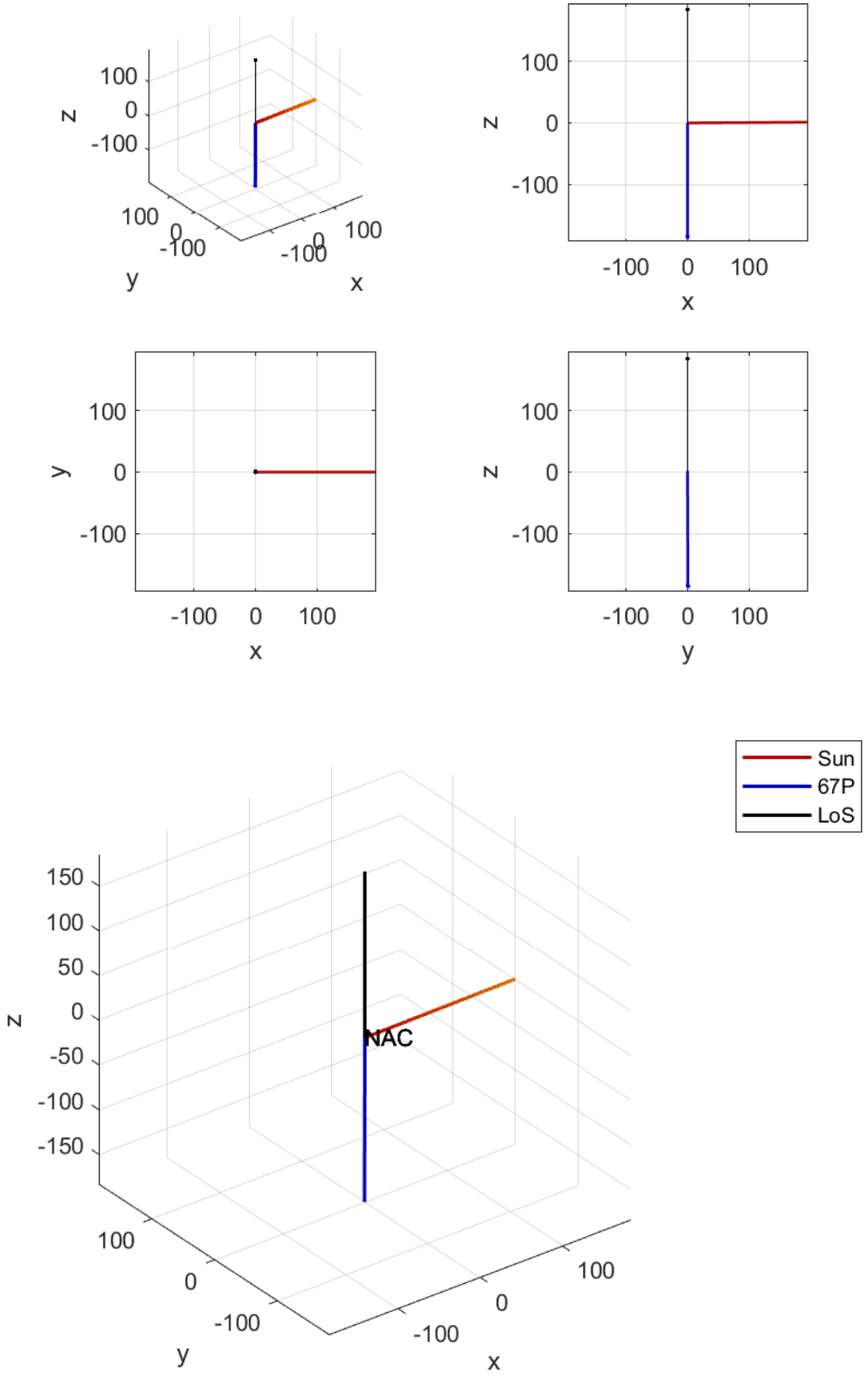

FIGURE A.2: 67GC2

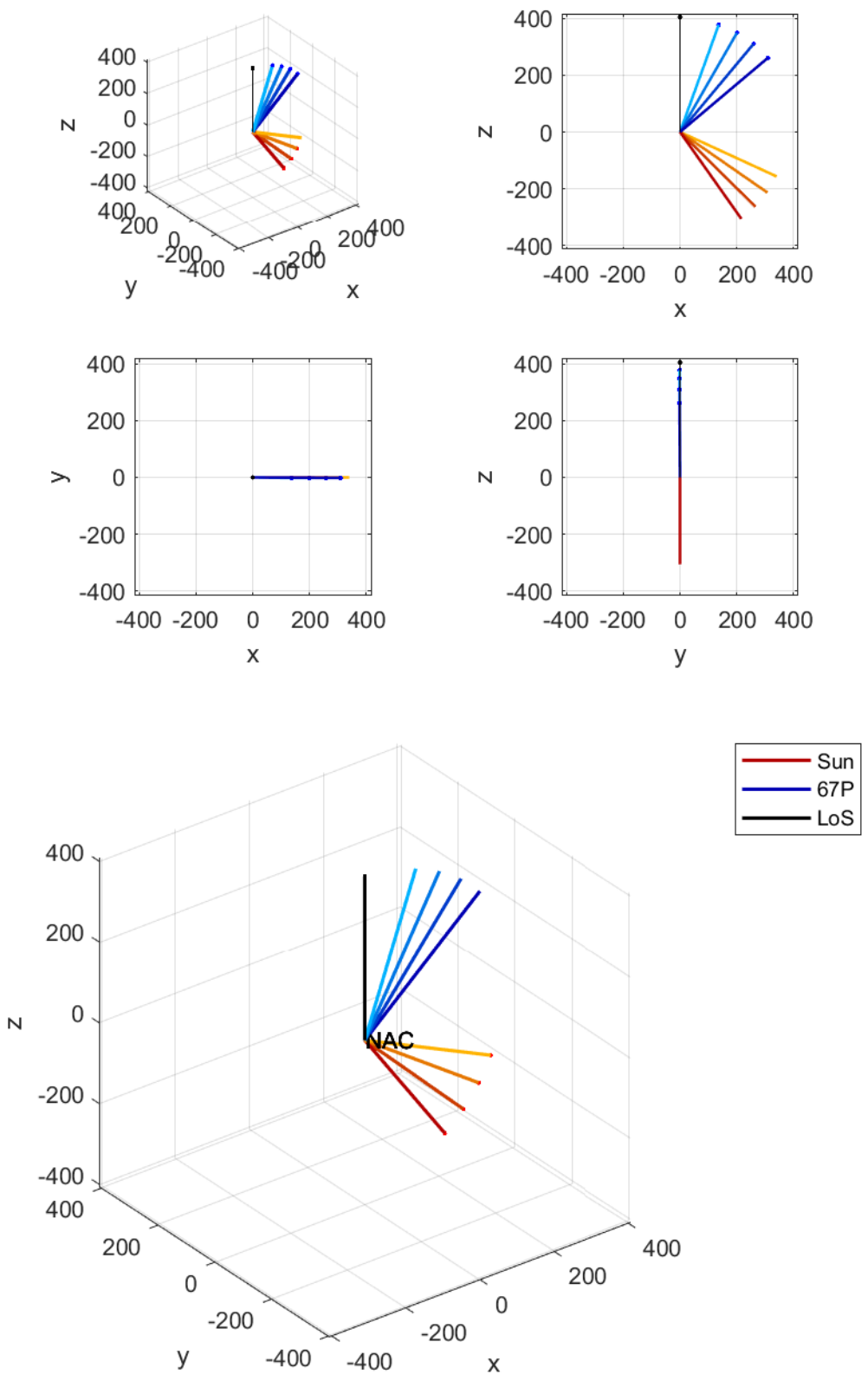

FIGURE A.3: 70GC3

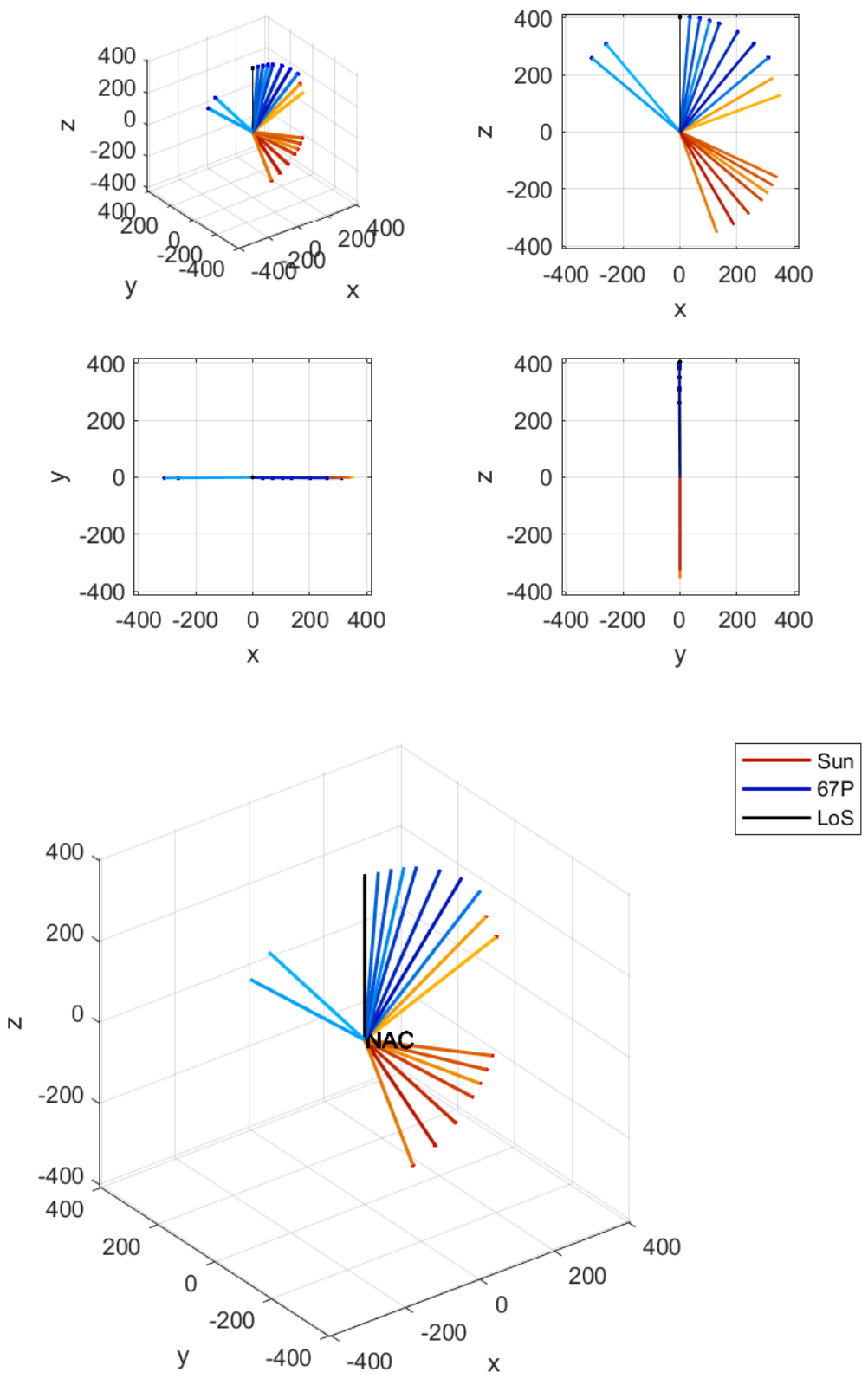

FIGURE A.4: 71GC3

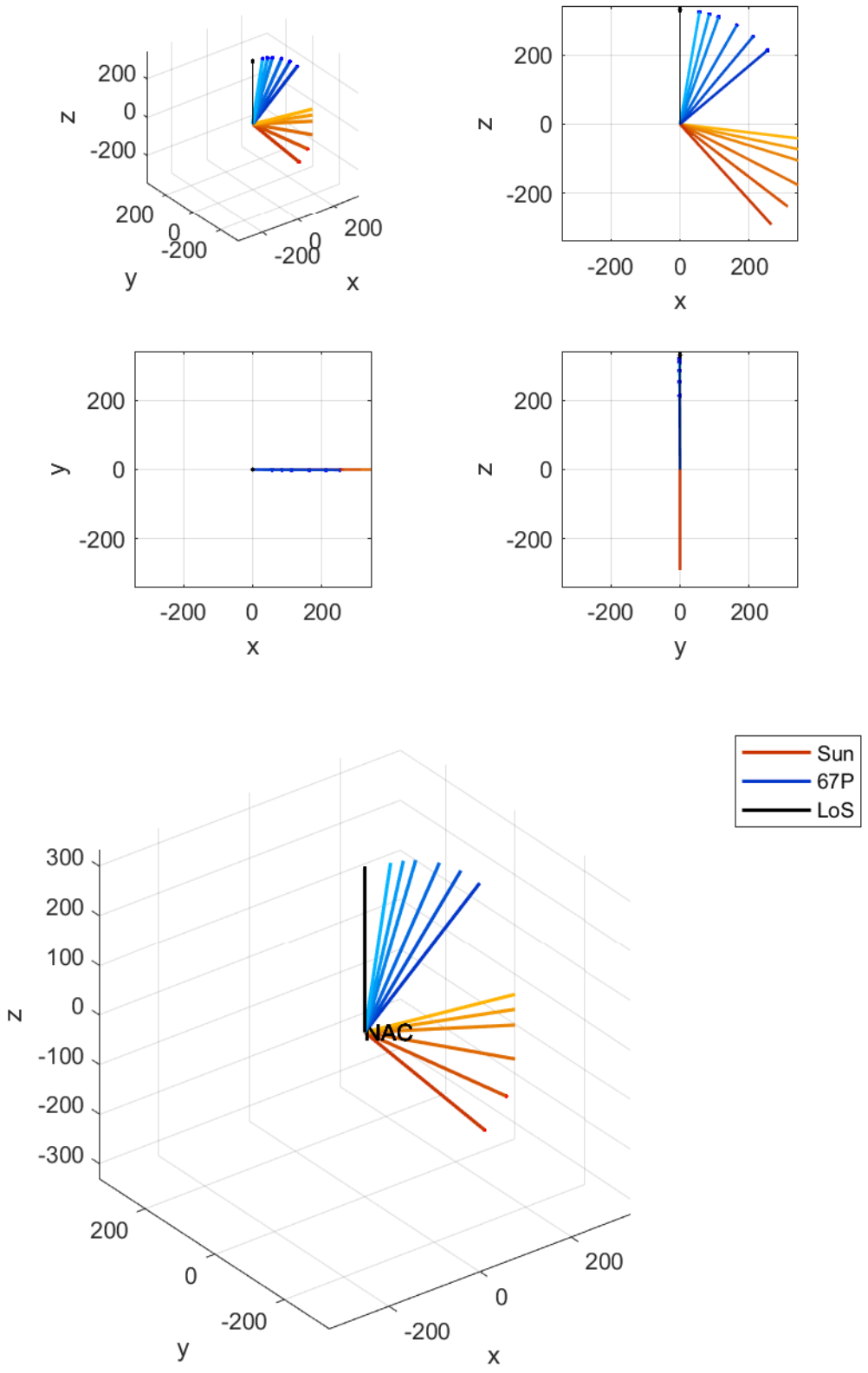

FIGURE A.5: 73GC4

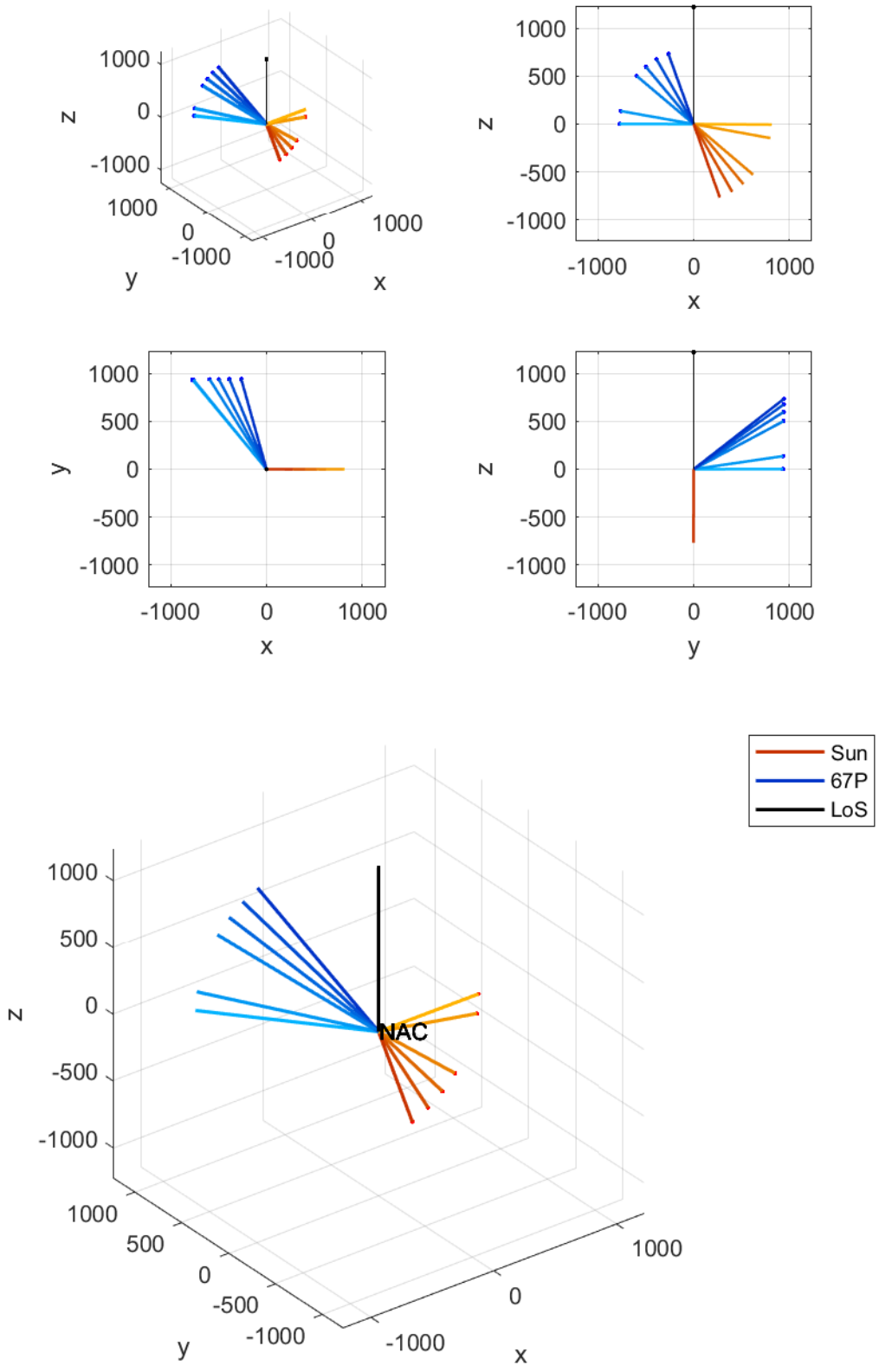

FIGURE A.6: 75GC2

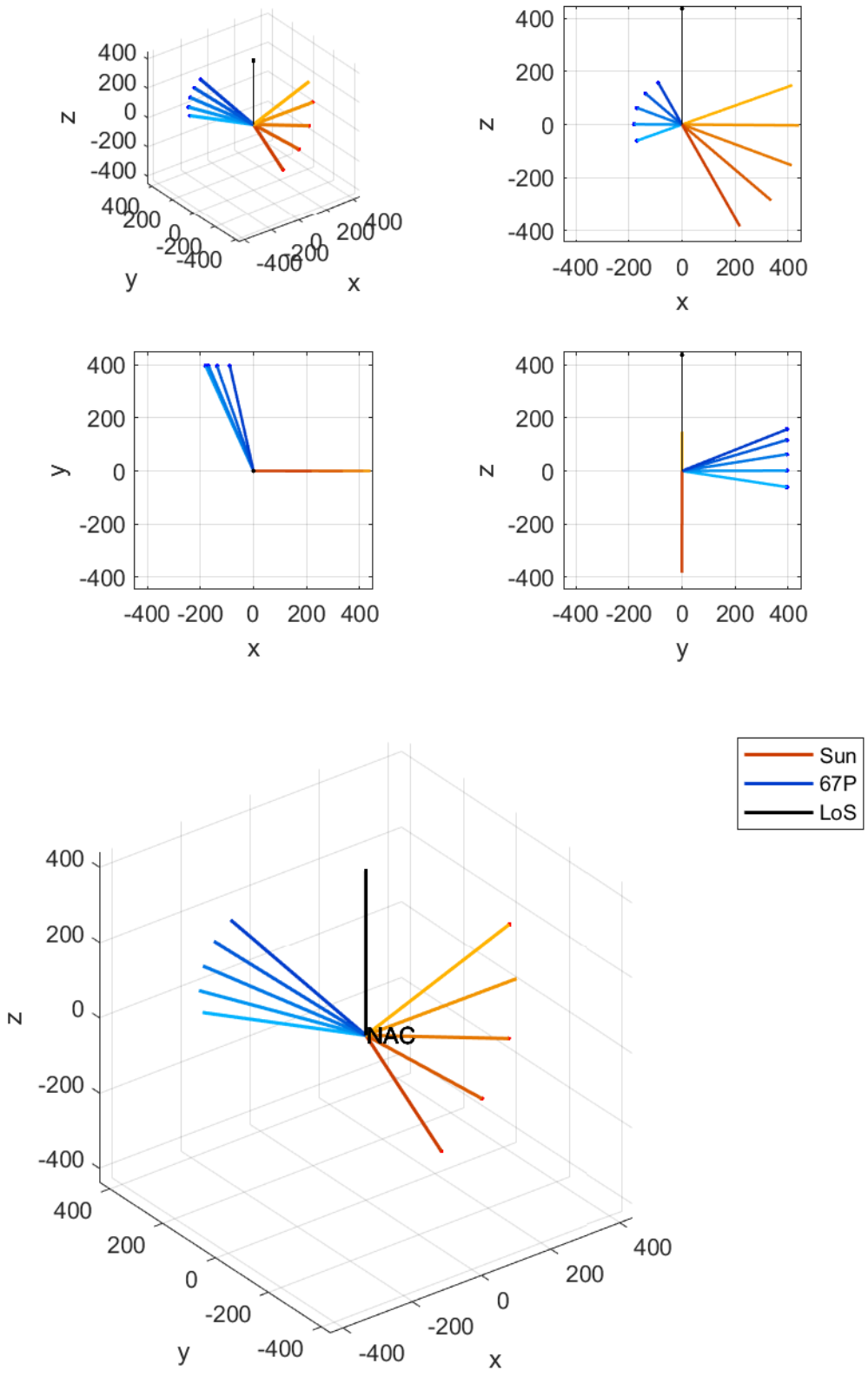

FIGURE A.7: 78GC4

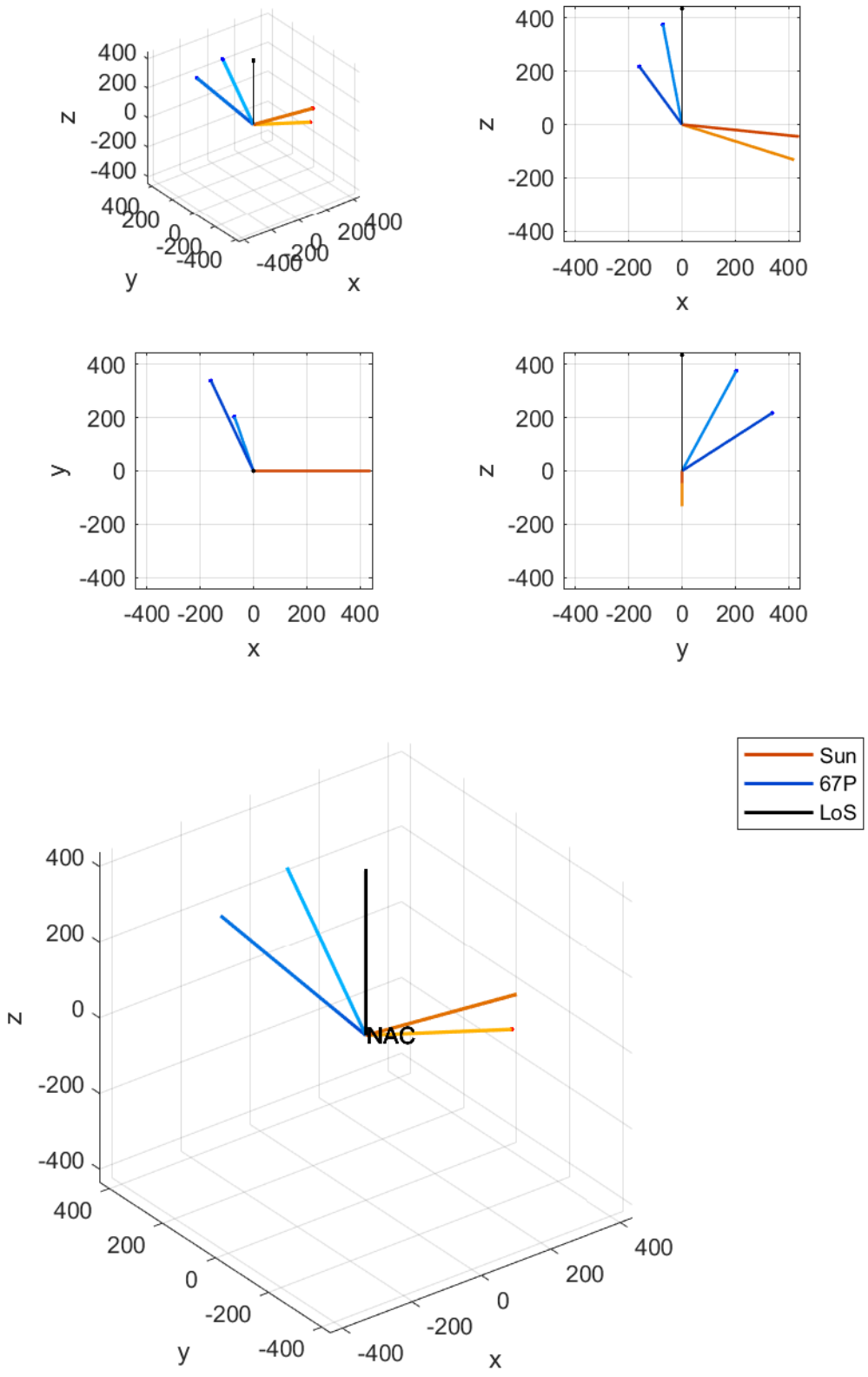

FIGURE A.8: 78GC5

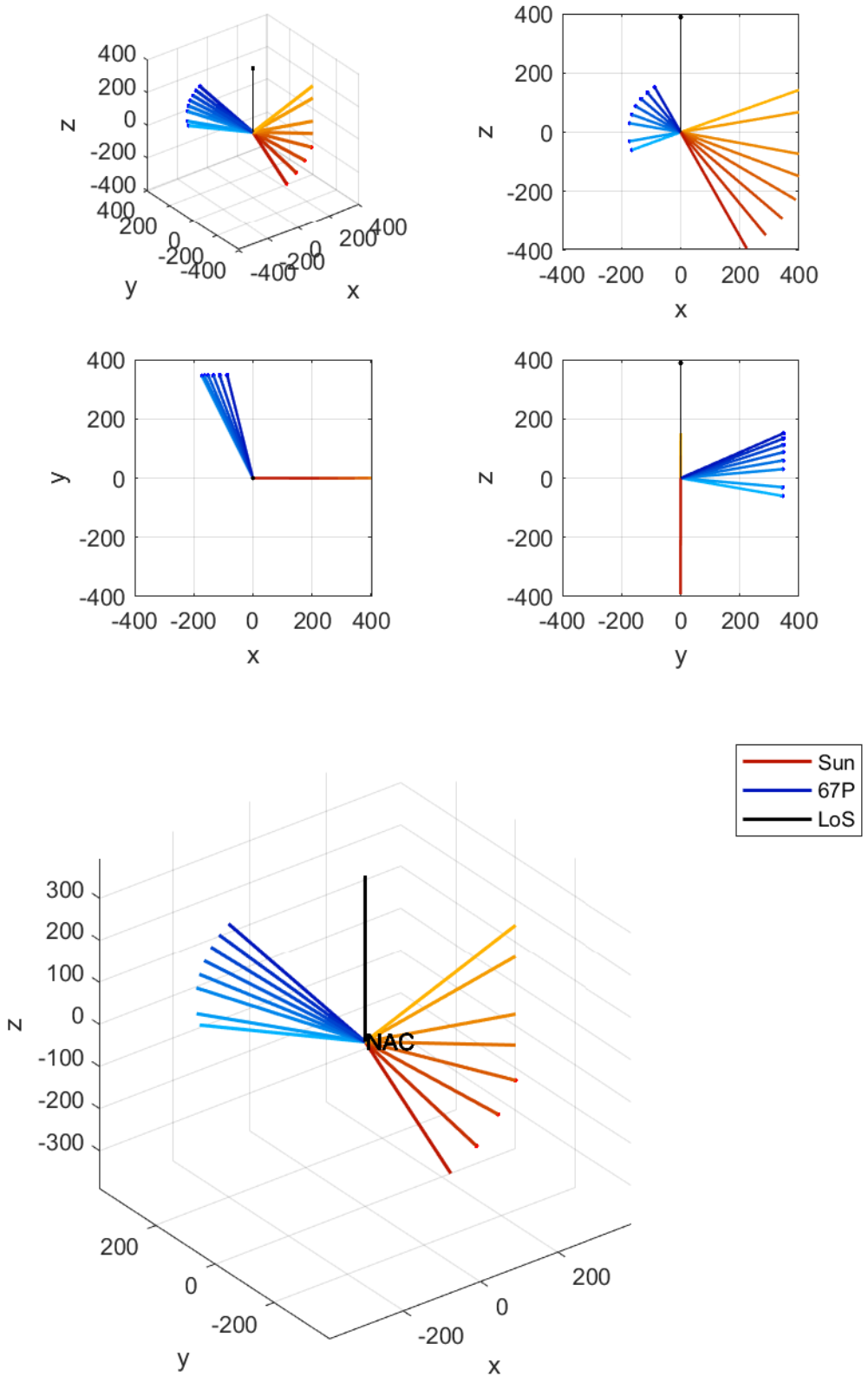

FIGURE A.9: 79GC1

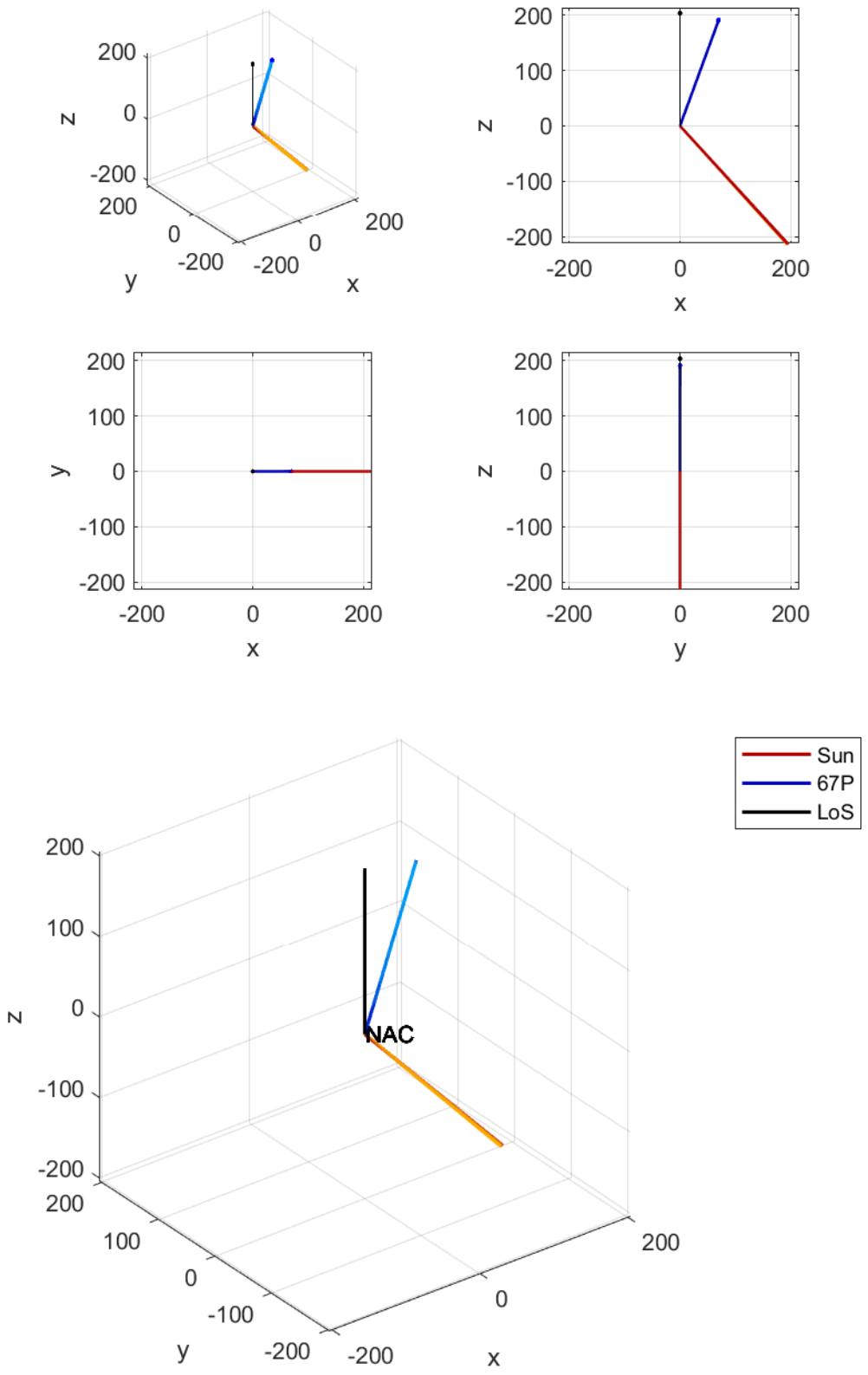

FIGURE A.10: 81GT3

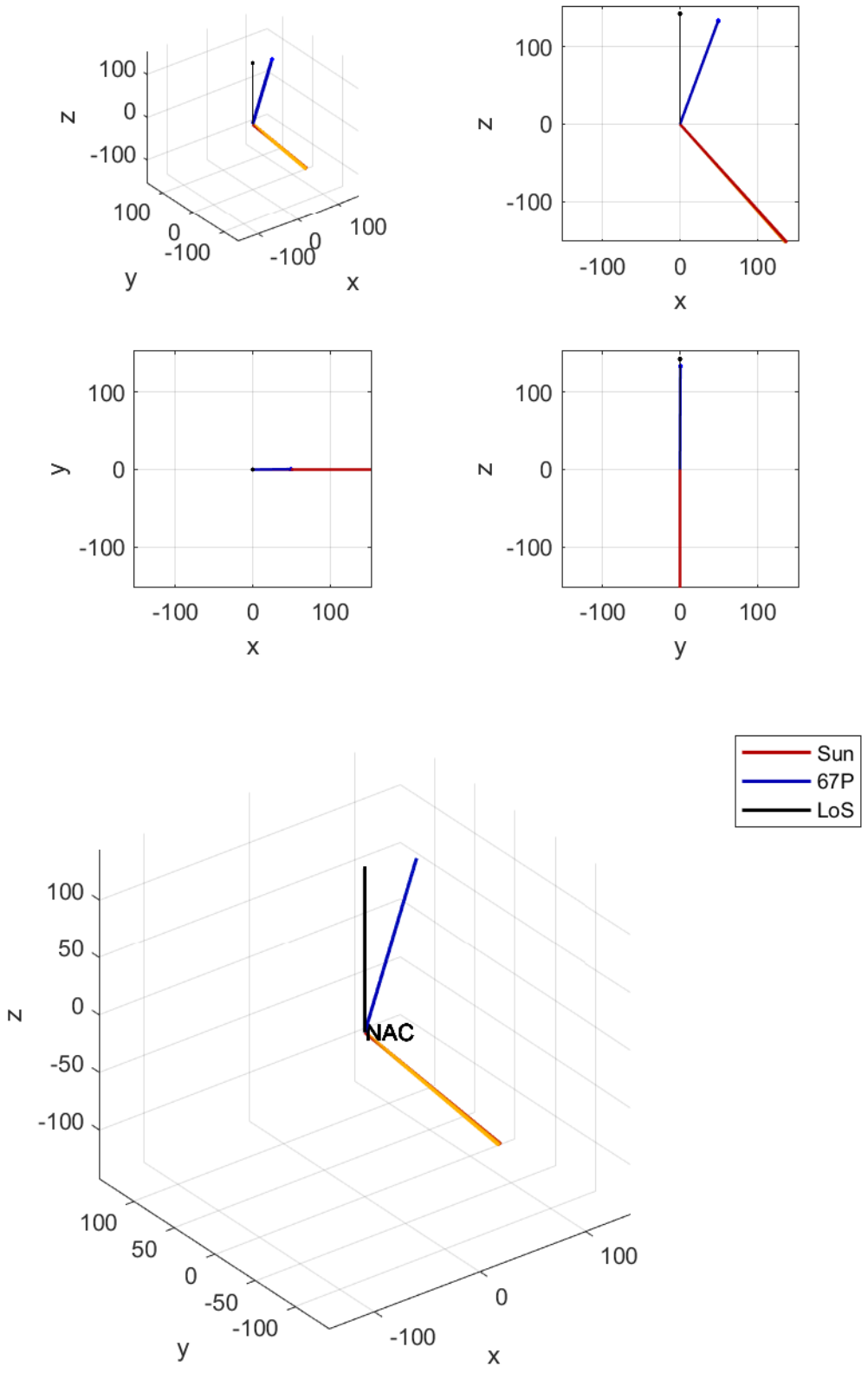

Figure A.11: 82GT4

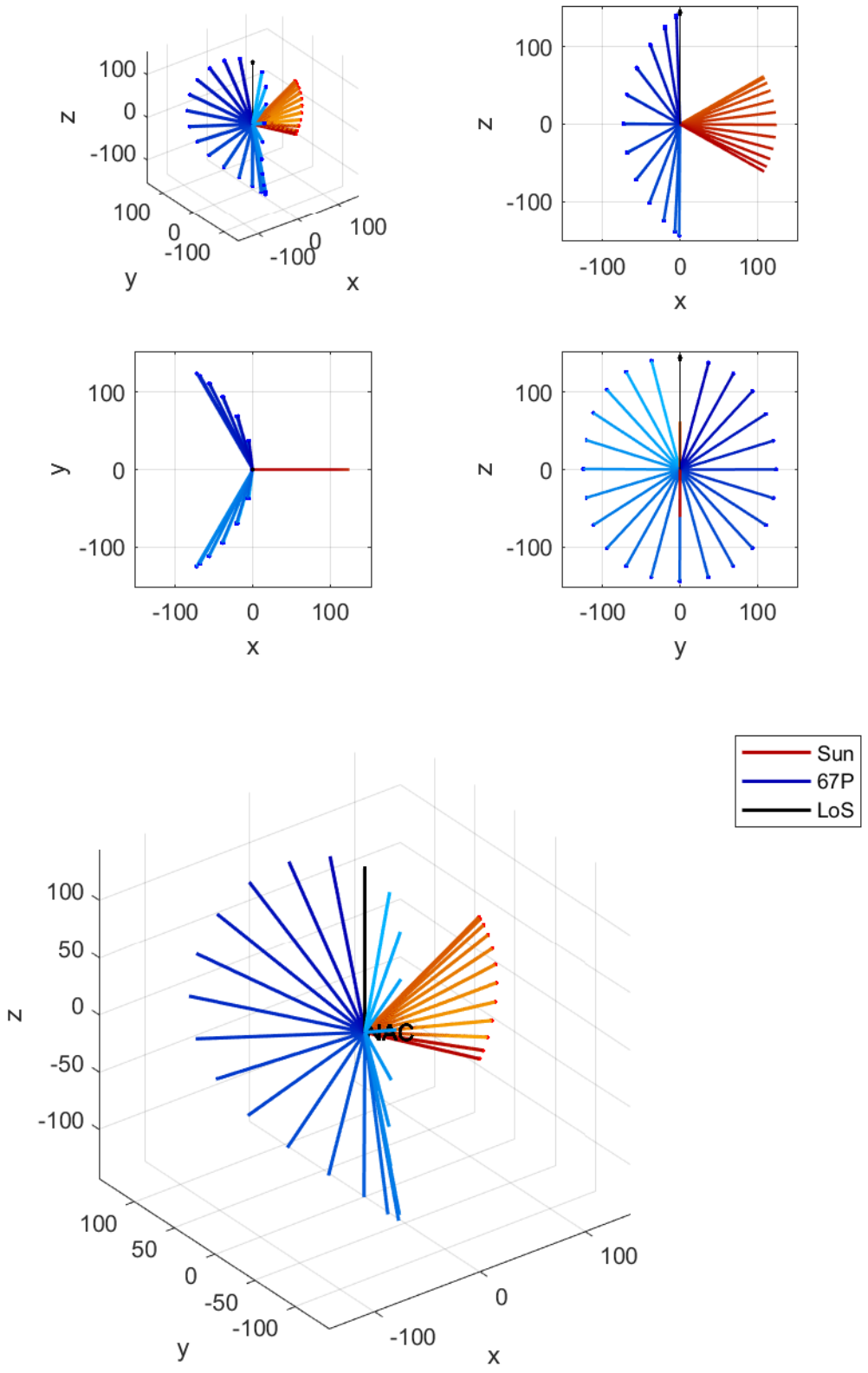

FIGURE A.12: 82DP4

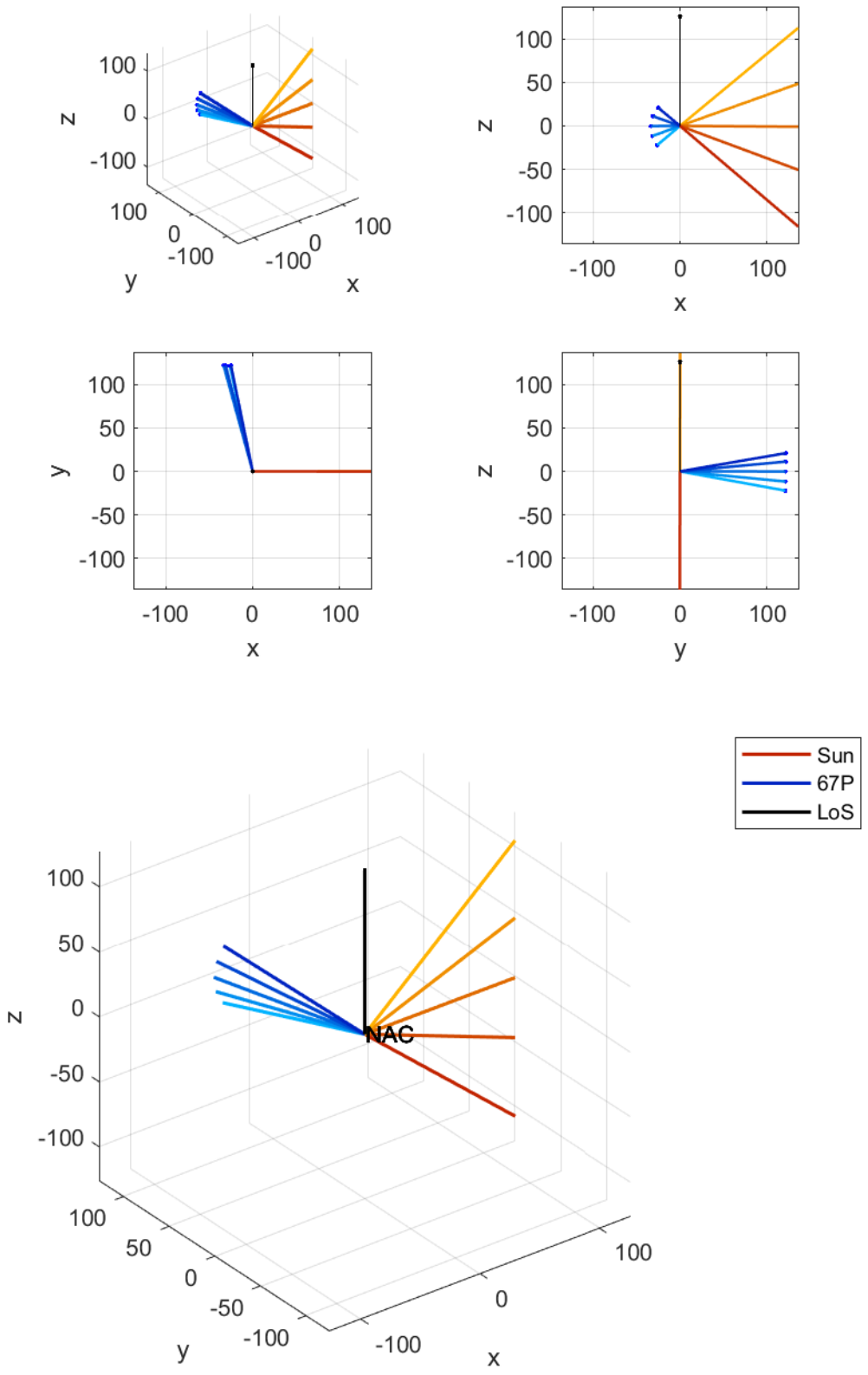

FIGURE A.13: 83GC1

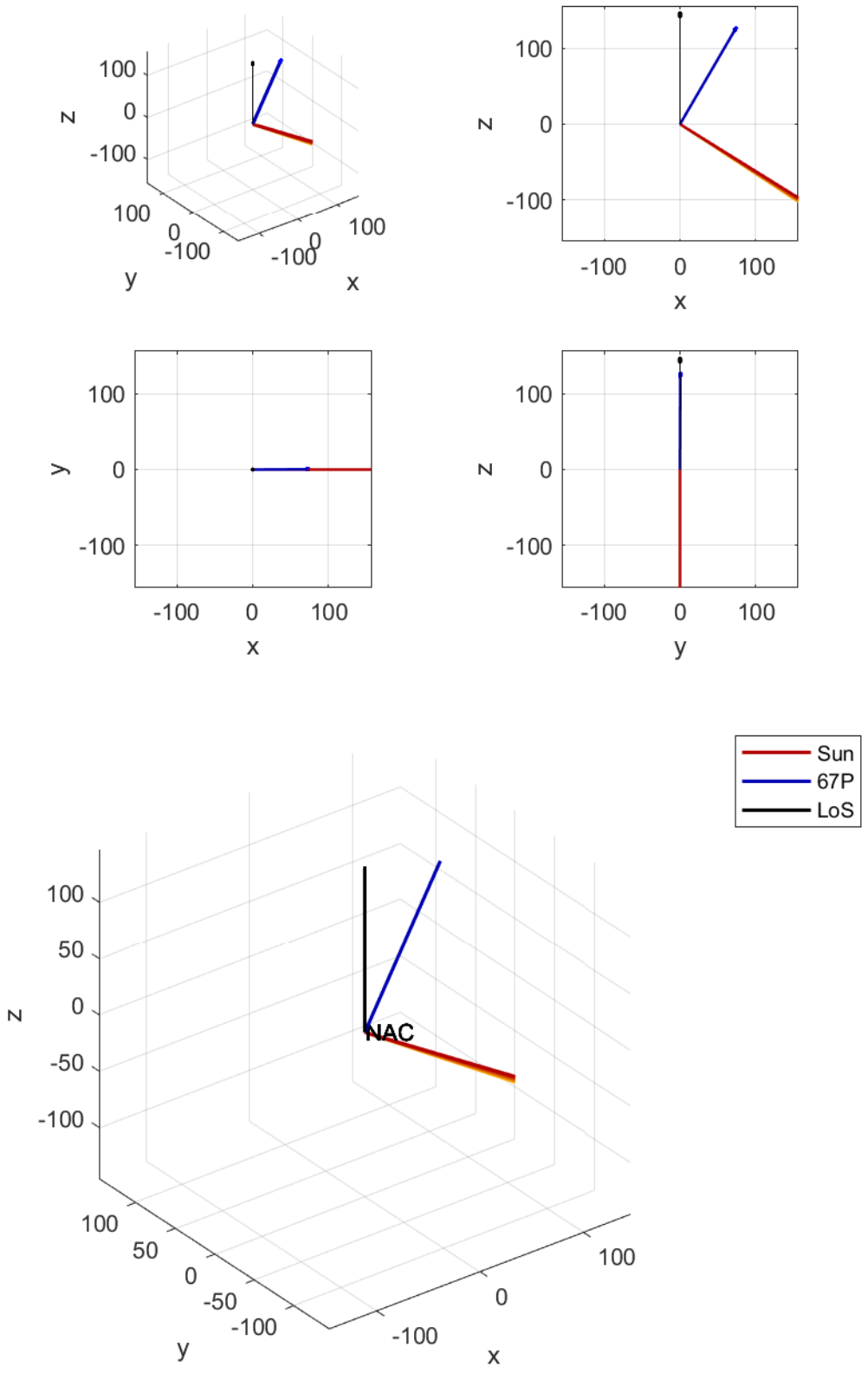

FIGURE A.14: 83GT1

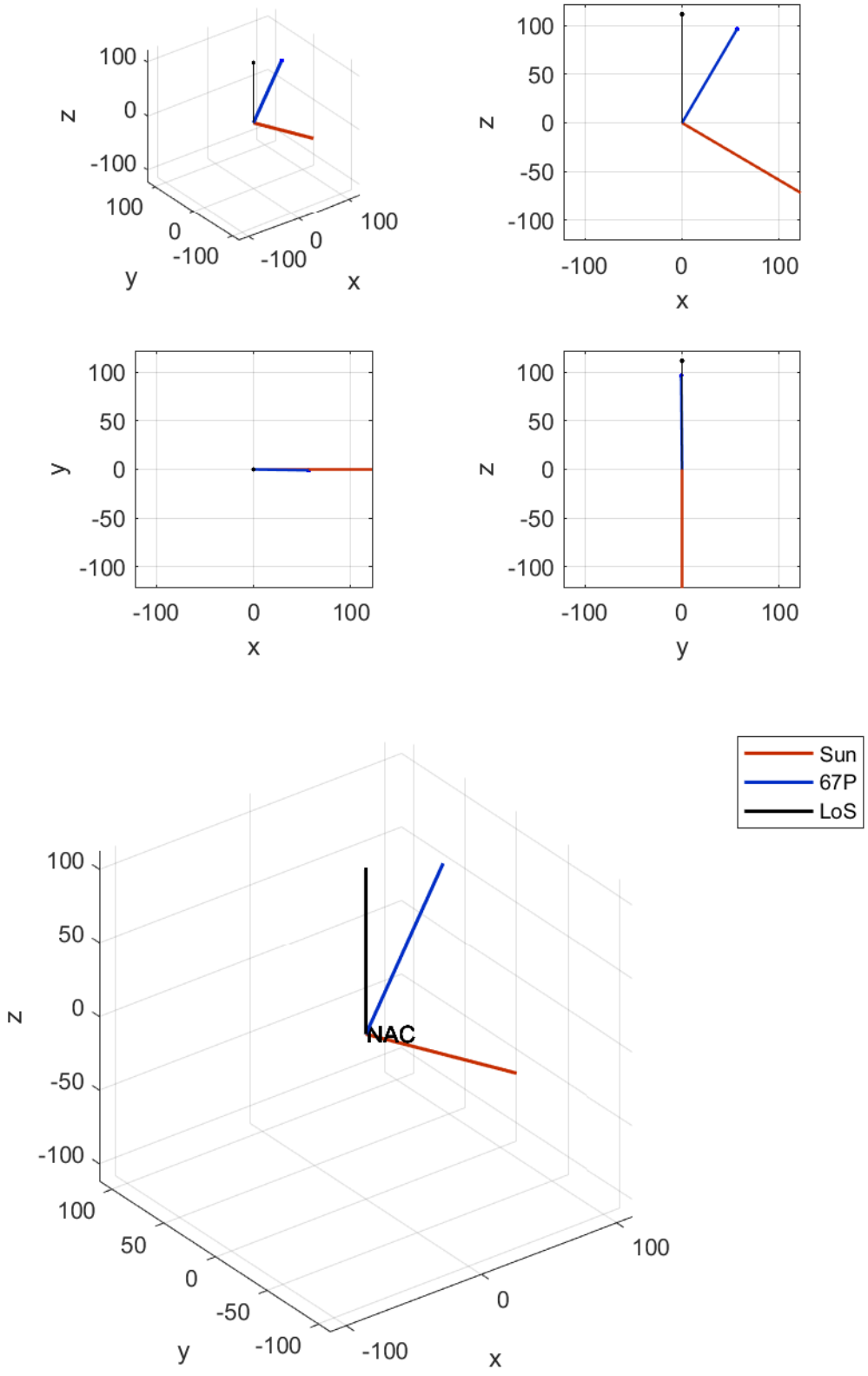

Figure A.15: 84GT2

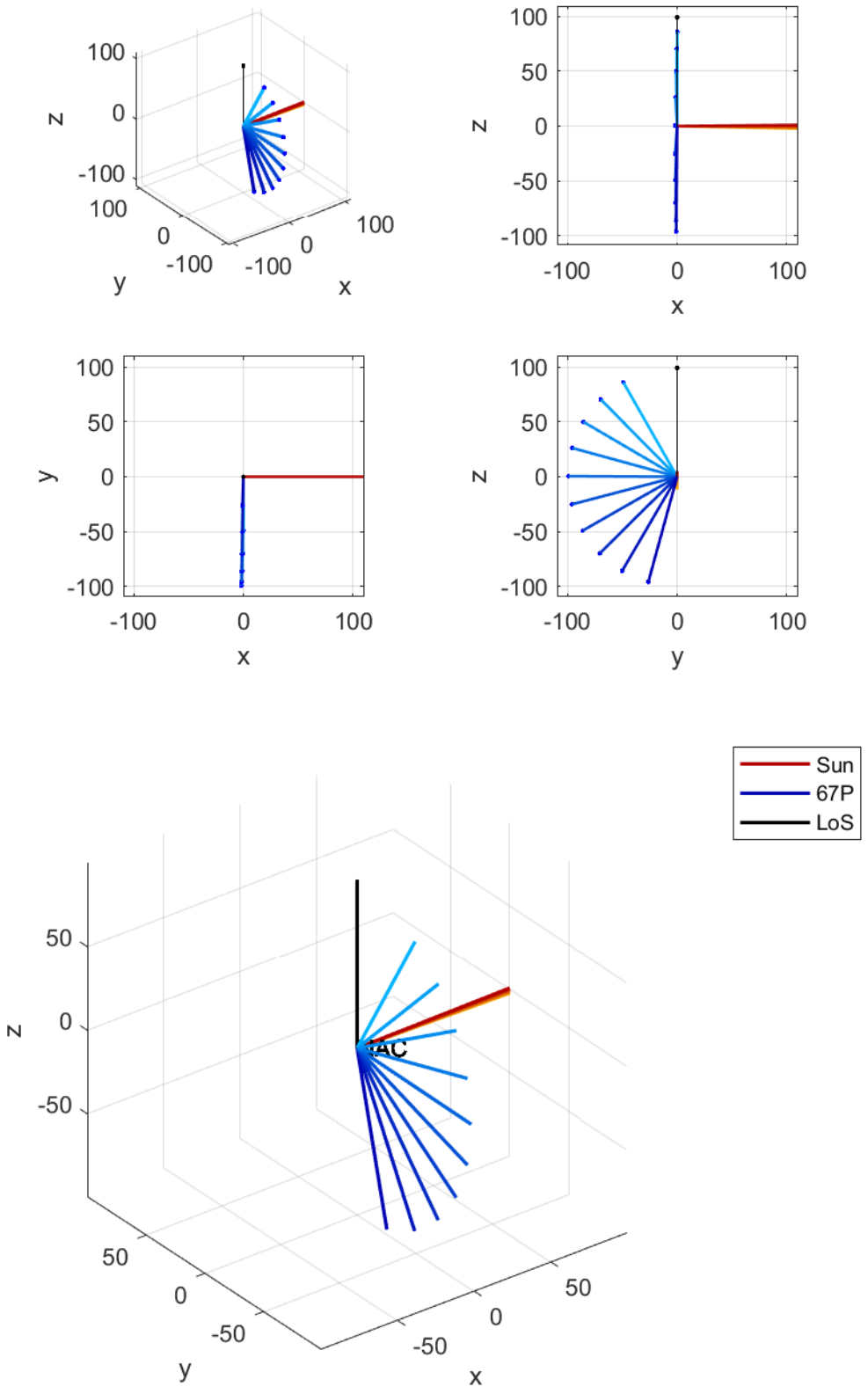

FIGURE A.16: 85GC5

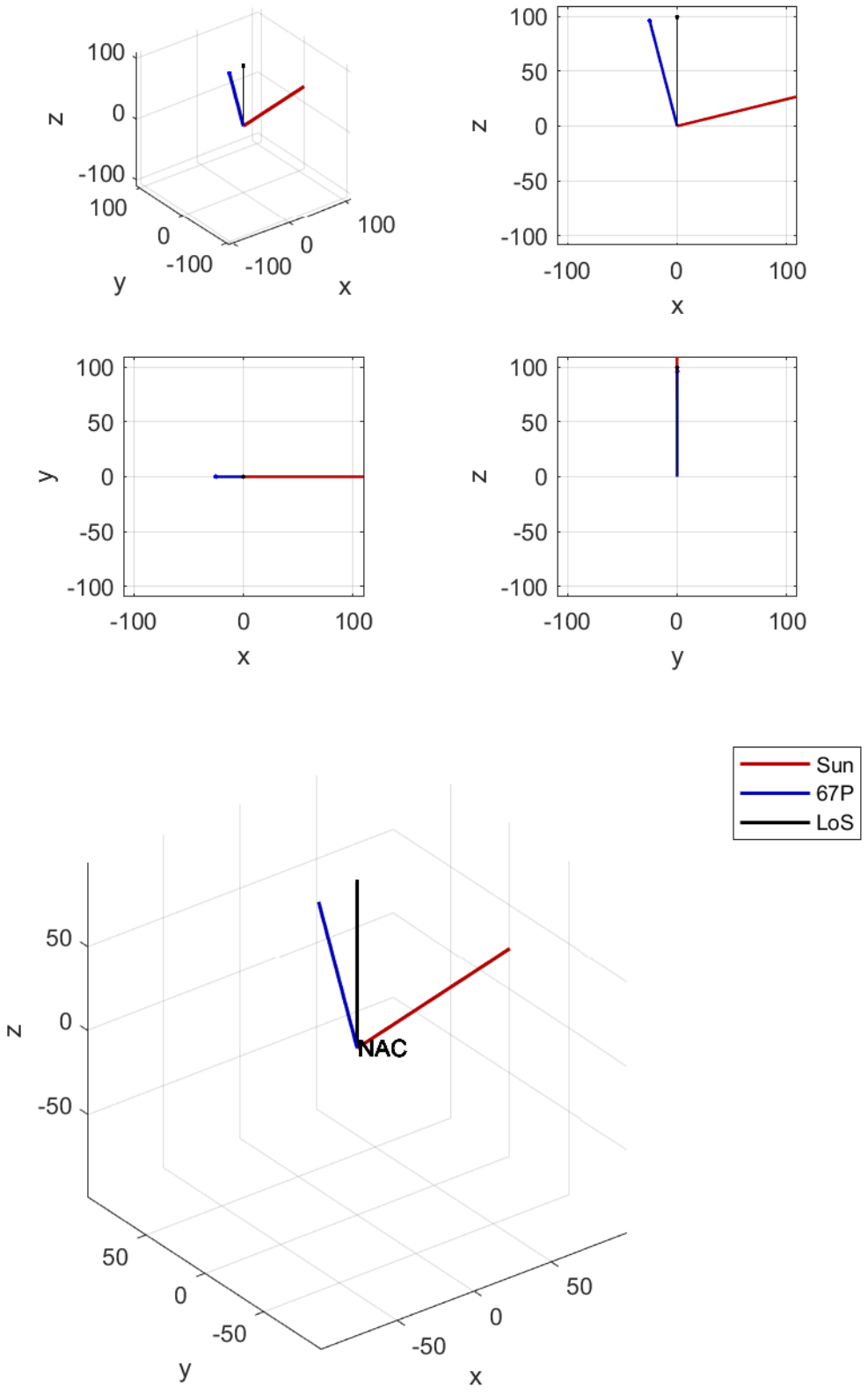

FIGURE A.17: 86GT3

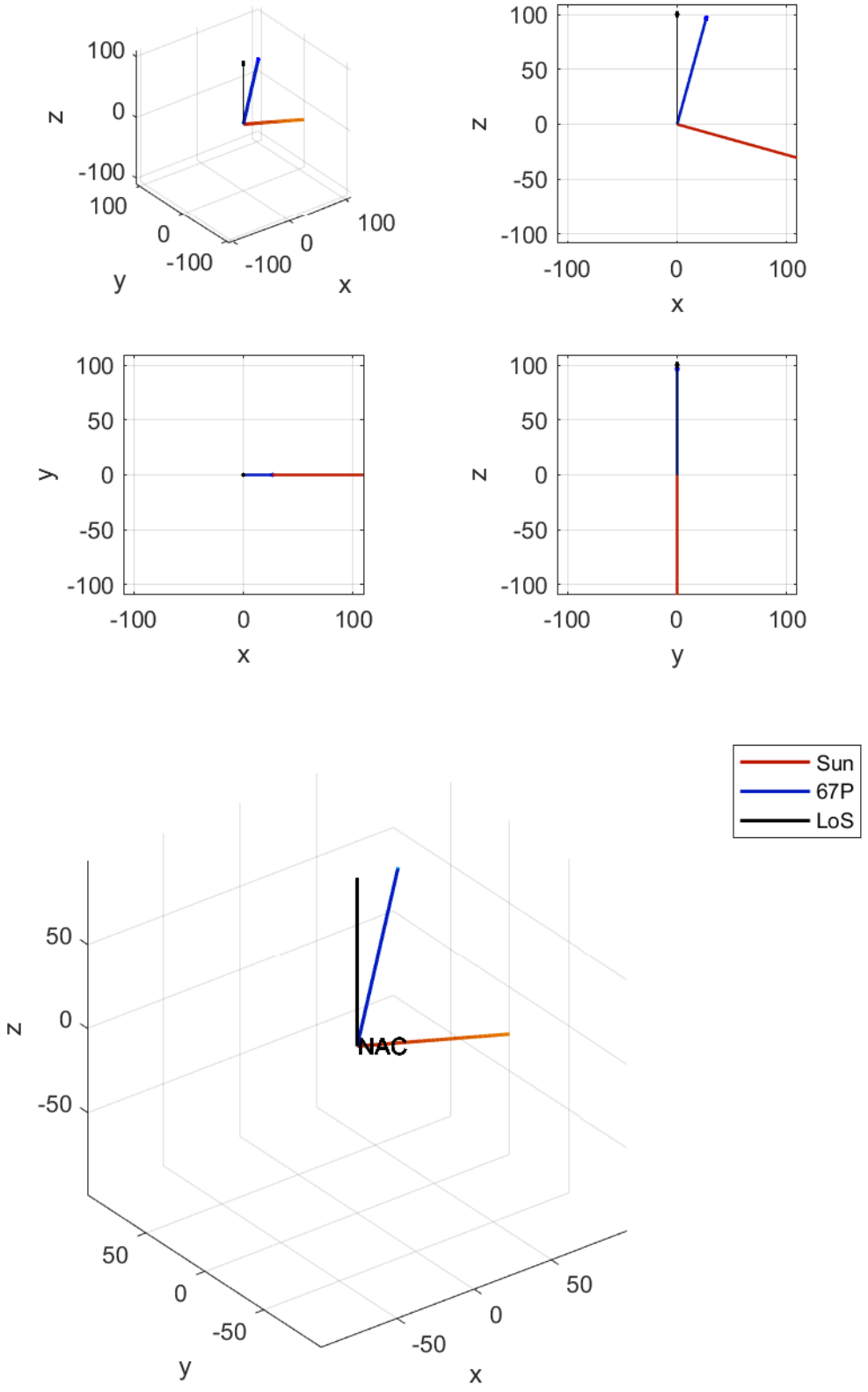

FIGURE A.18: 87GT1

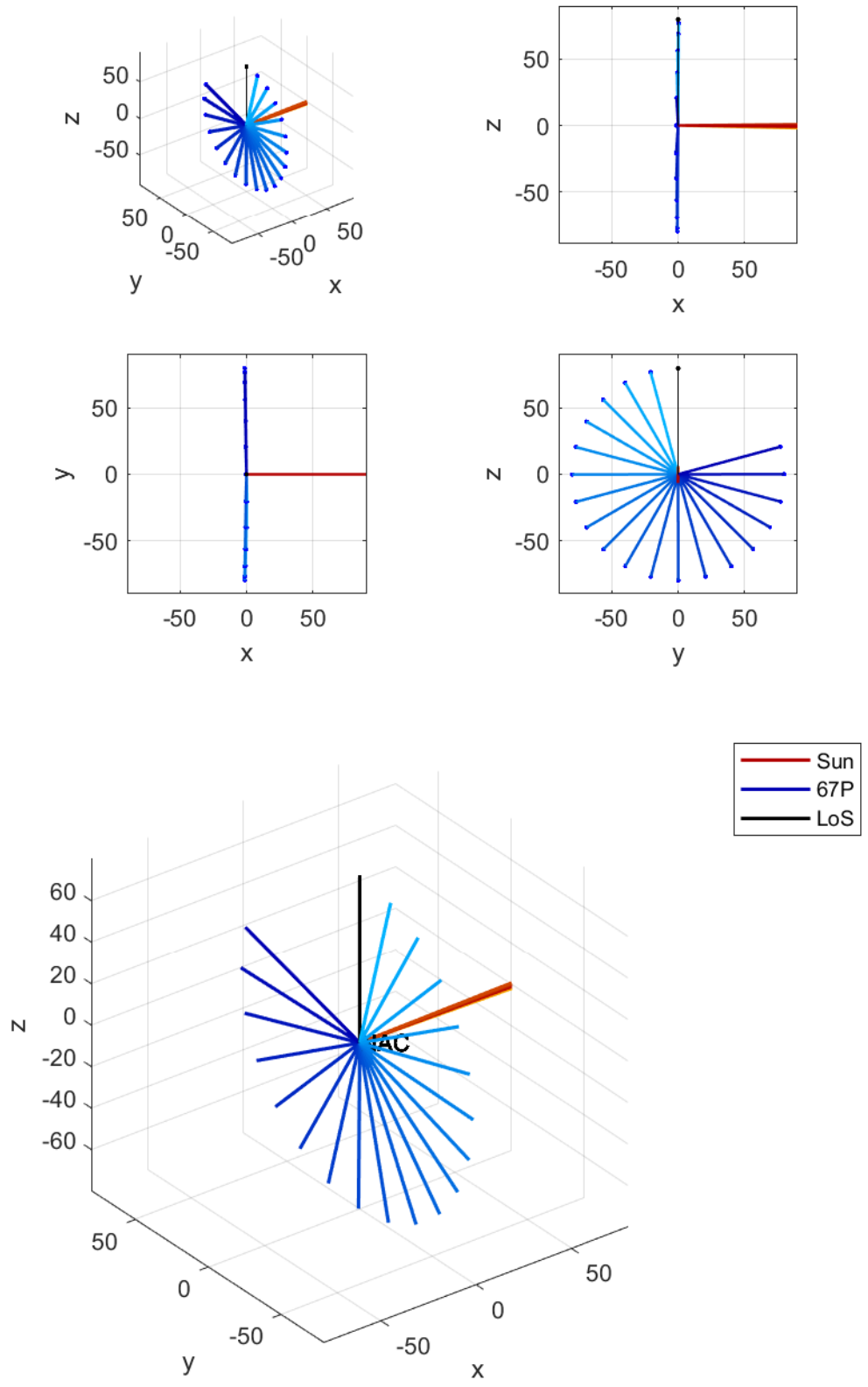

FIGURE A.19: 89GC2

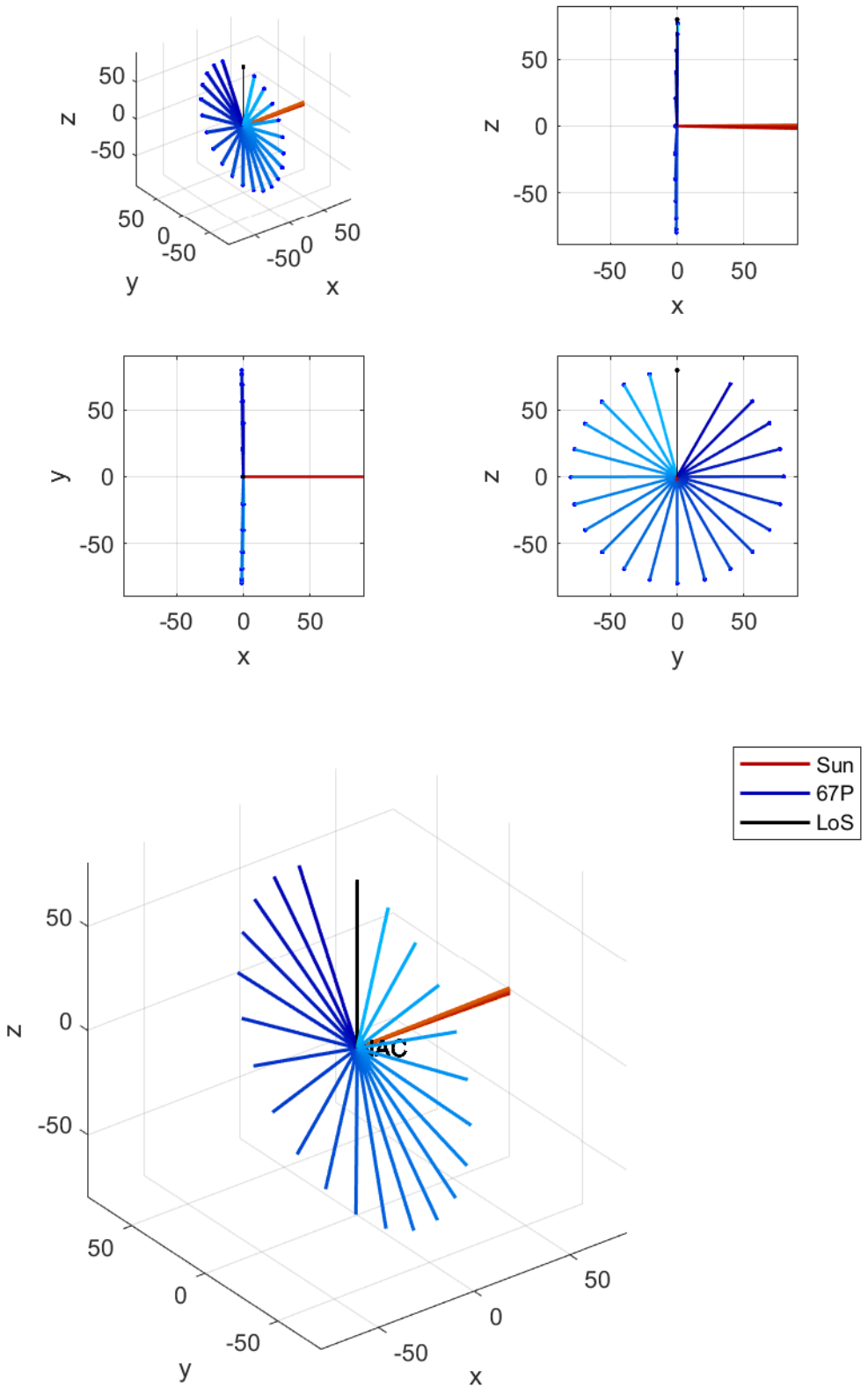

FIGURE A.20: 89DP2

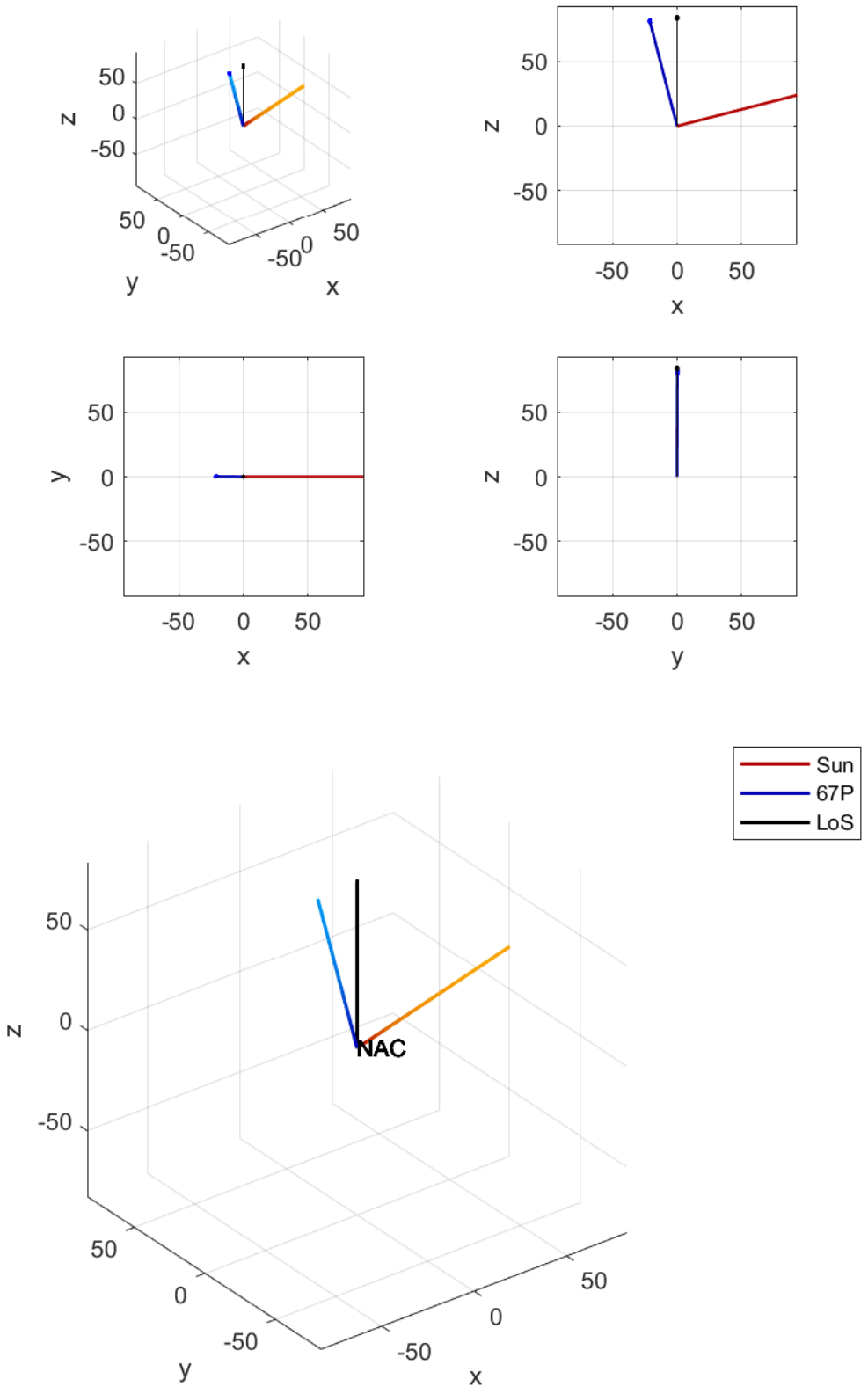

FIGURE A.21: 90GT3

Appendix B

Dust direction of motion

In this Appendix we show the alignment of the direction of motion of the dust grains with the nucleus and Sun position.
The histograms represent the value of cosine between the velocity vector of the grains and the position of the nucleus and the Sun. When the cosine is close to the value 1 the vectors are aligned, otherwise they are not. Each panel represents an image of the set defined in the caption.

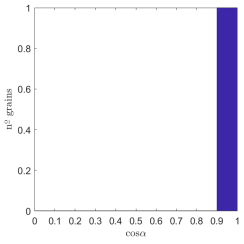

(A)

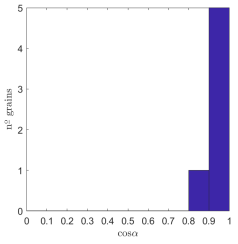

(B)

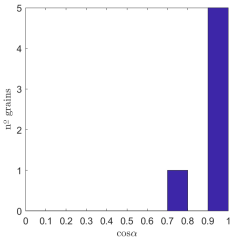

(C)

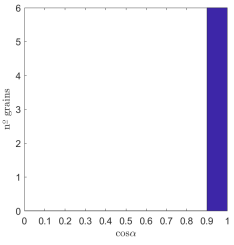

(D)

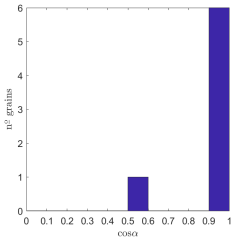

(E)

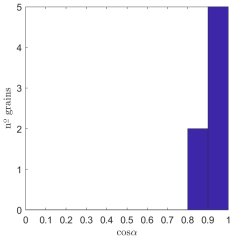

(F)

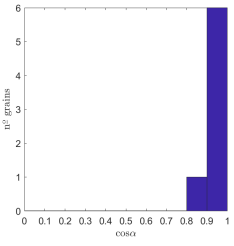

(G)

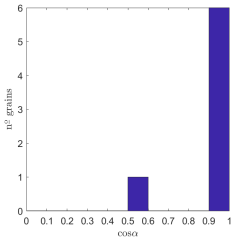

(H)

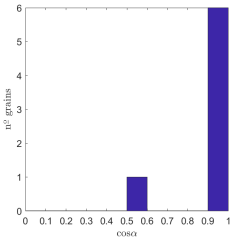

(I)

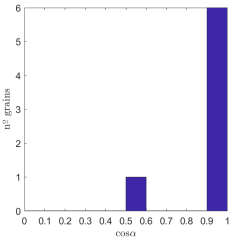

(J)

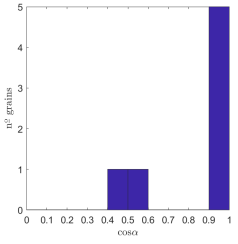

(K)

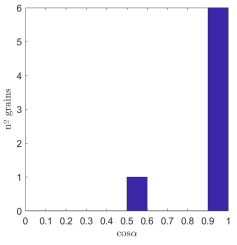

(L)

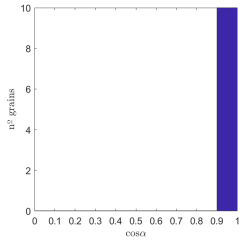

(M)

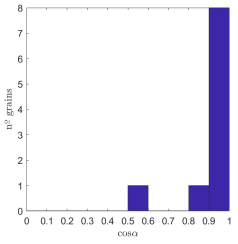

(N)

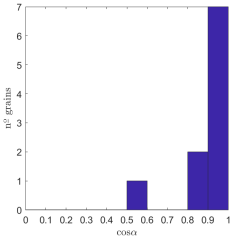

(O)

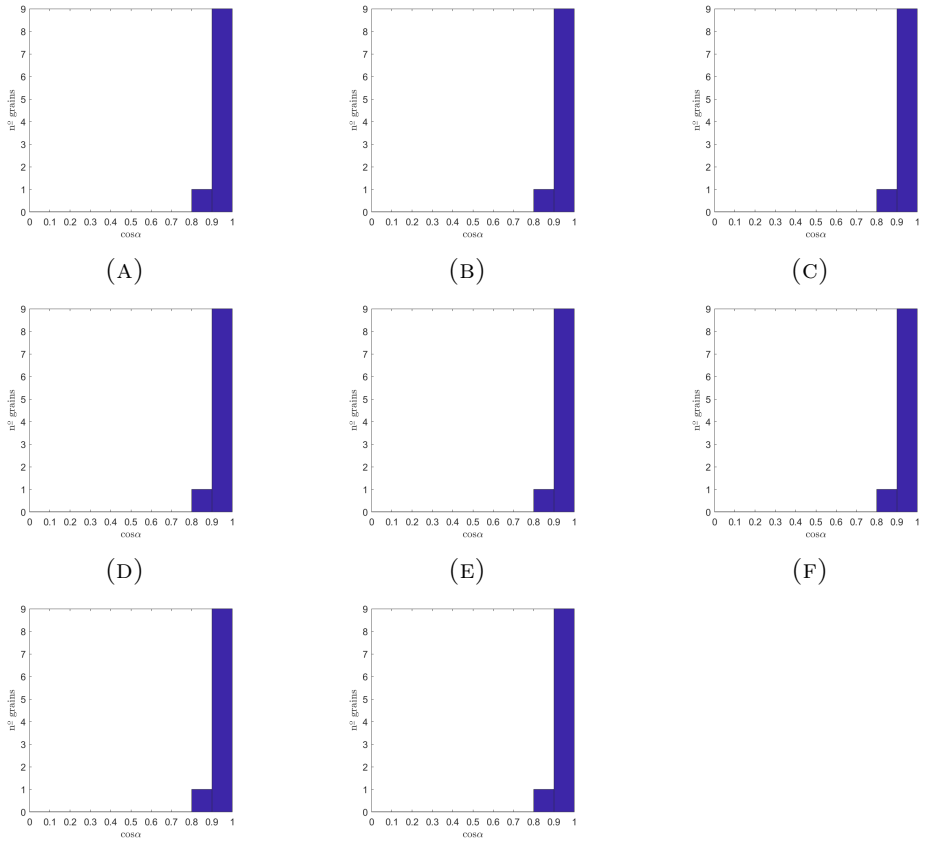

(A) (B) (C)

(D) (E) (F)

(G) (H)

FIGURE B.2: Alignment with the nucleus. Set 82DP4.

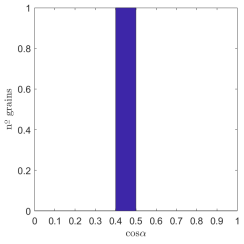

(A)

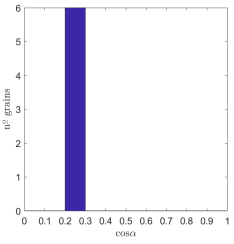

(B)

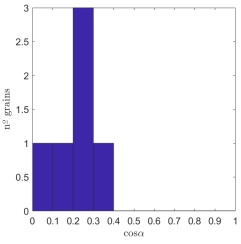

(C)

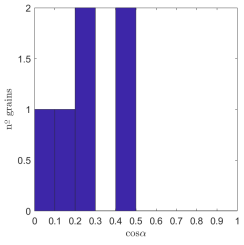

(D)

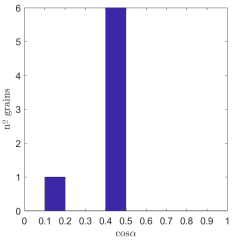

(E)

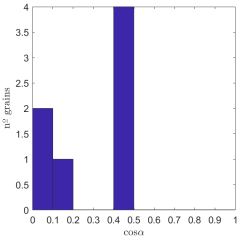

(F)

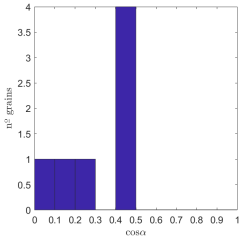

(G)

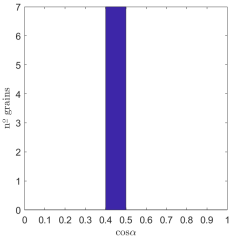

(H)

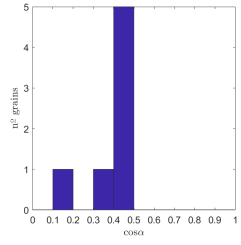

(I)

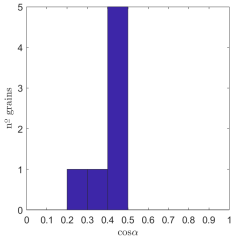

(J)

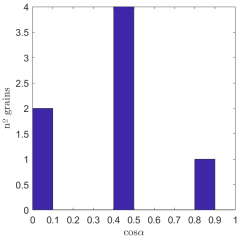

(K)

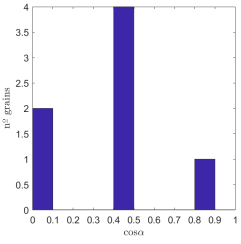

(L)

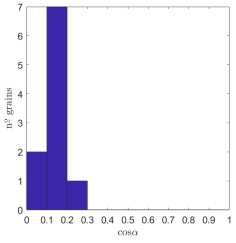

(M)

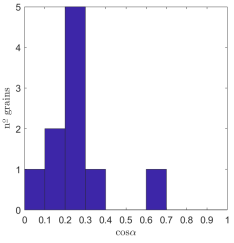

(N)

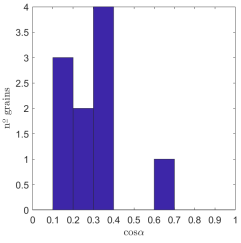

(O)

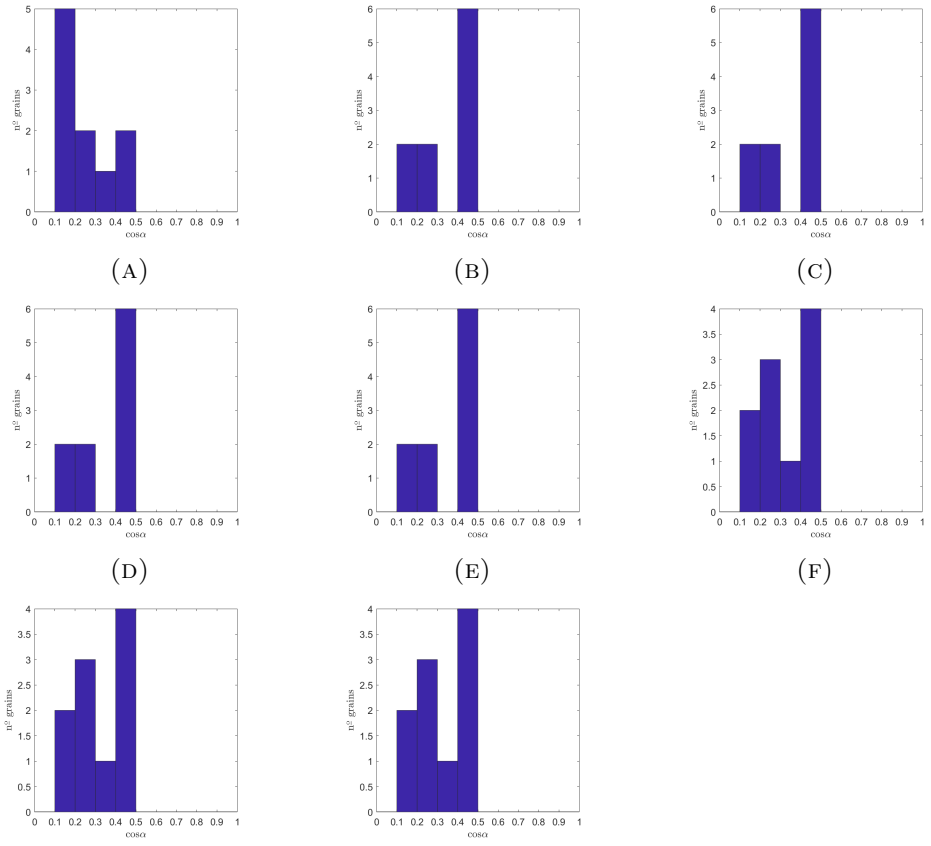

(A) (B) (C)

(D) (E) (F)

(G) (H)

FIGURE B.4: Alignment with the Sun. Set 82DP4.

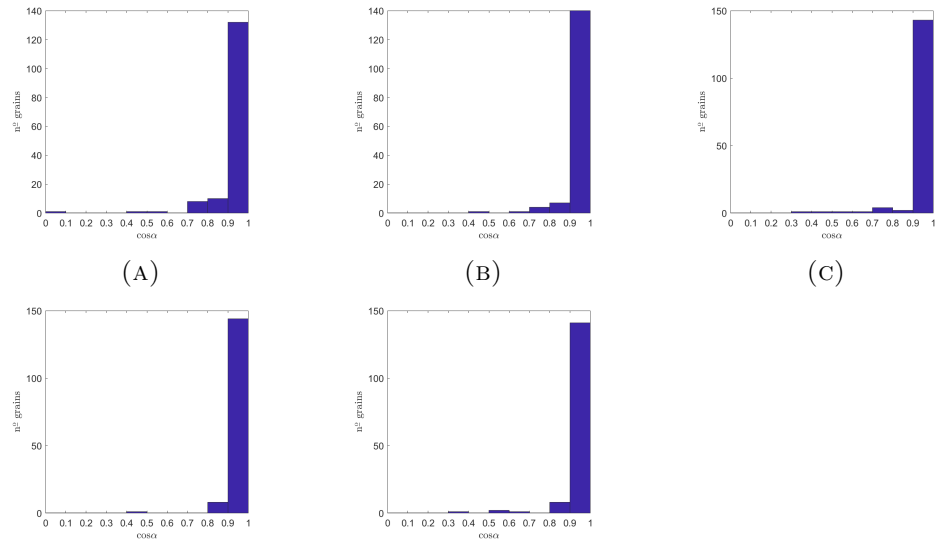

(A) (B) (C)

(D) (E)

FIGURE B.5: Alignment with the nucleus. Set 83 GC1.

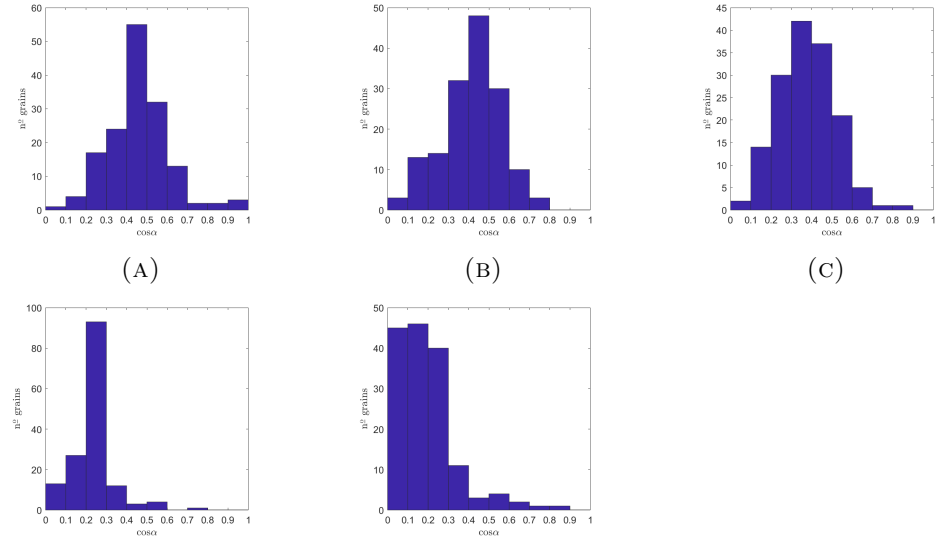

(A) (B) (C)

(D) (E)

FIGURE B.6: Alignment with the Sun. Set 83 GC1.

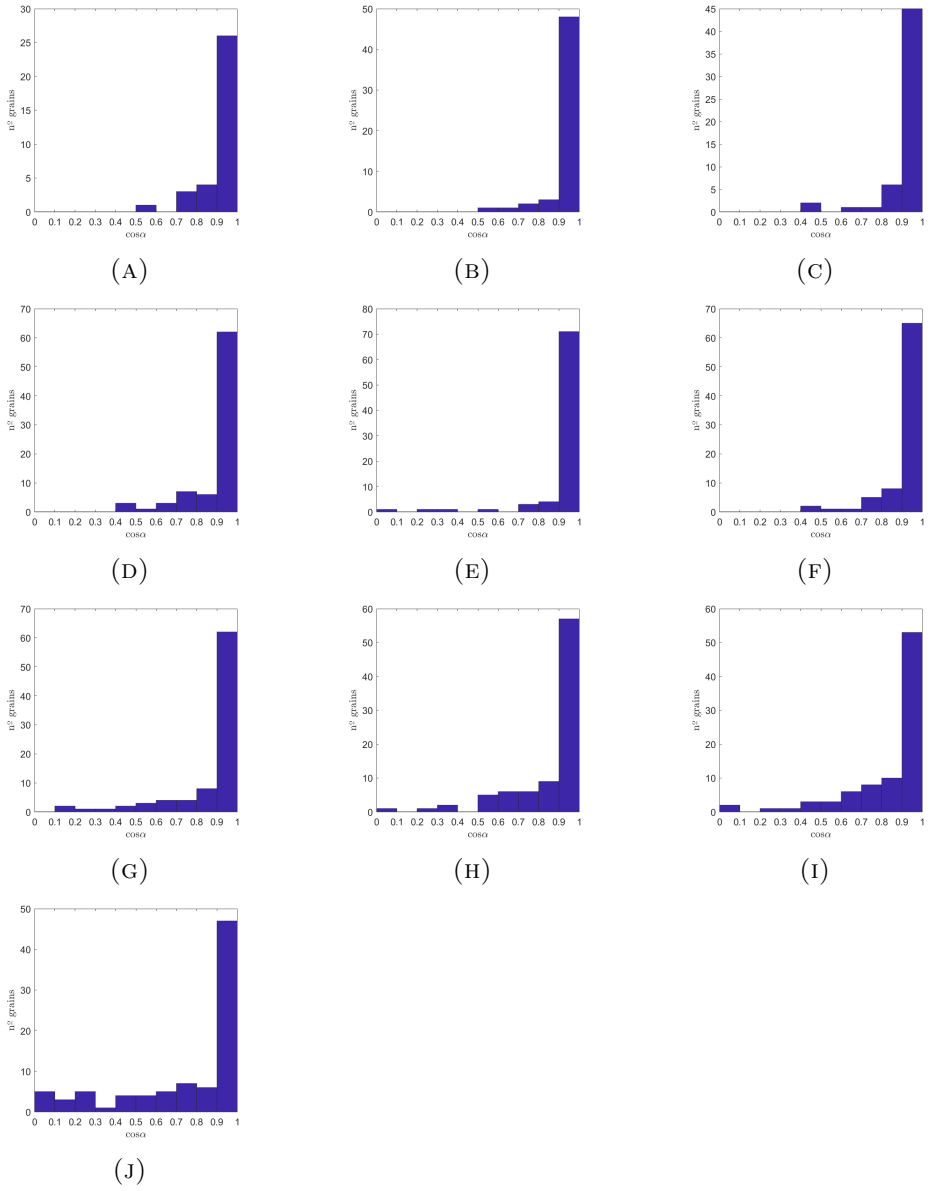

FIGURE B.7: Alignment with the nucleus. Set 85 GC5.

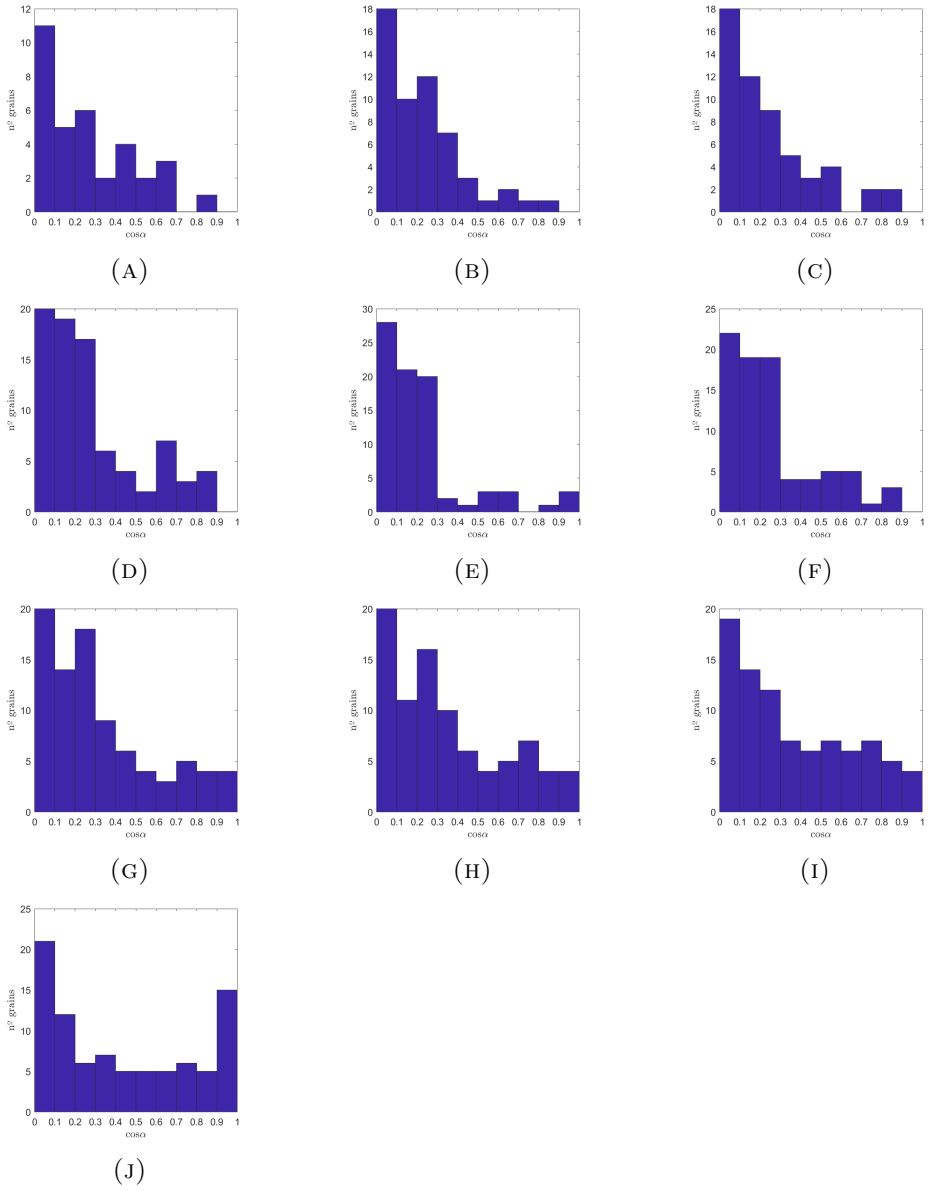

FIGURE B.8: Alignment with the Sun. Set 85 GC5.

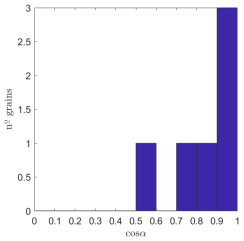

(A)

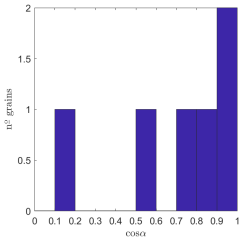

(B)

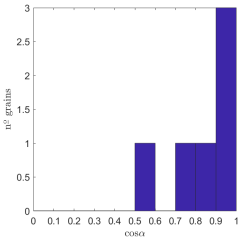

(C)

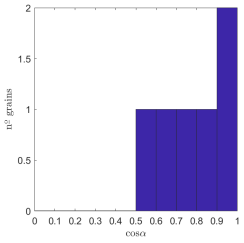

(D)

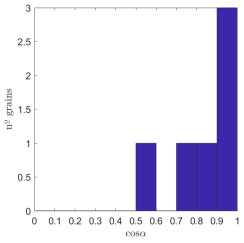

(E)

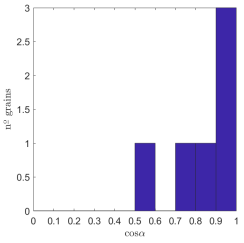

(F)

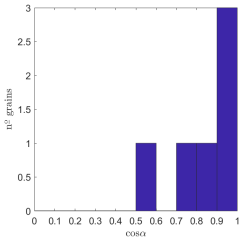

(G)

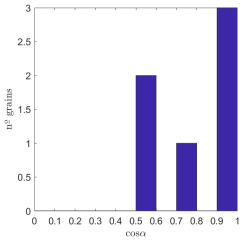

(H)

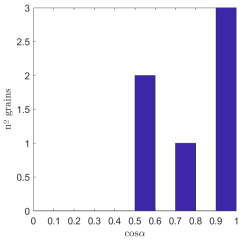

(I)

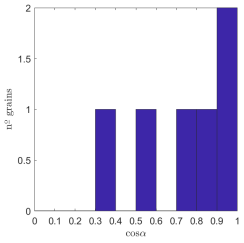

(J)

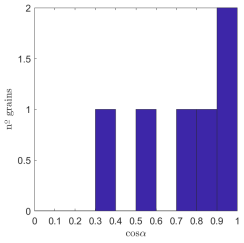

(K)

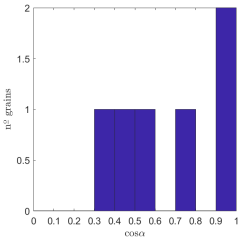

(L)

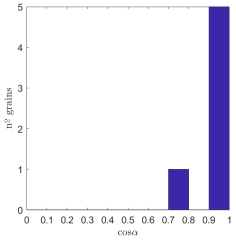

(M)

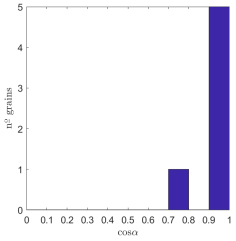

(N)

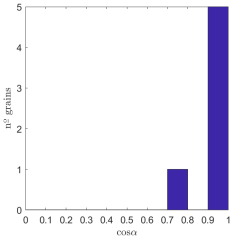

(O)

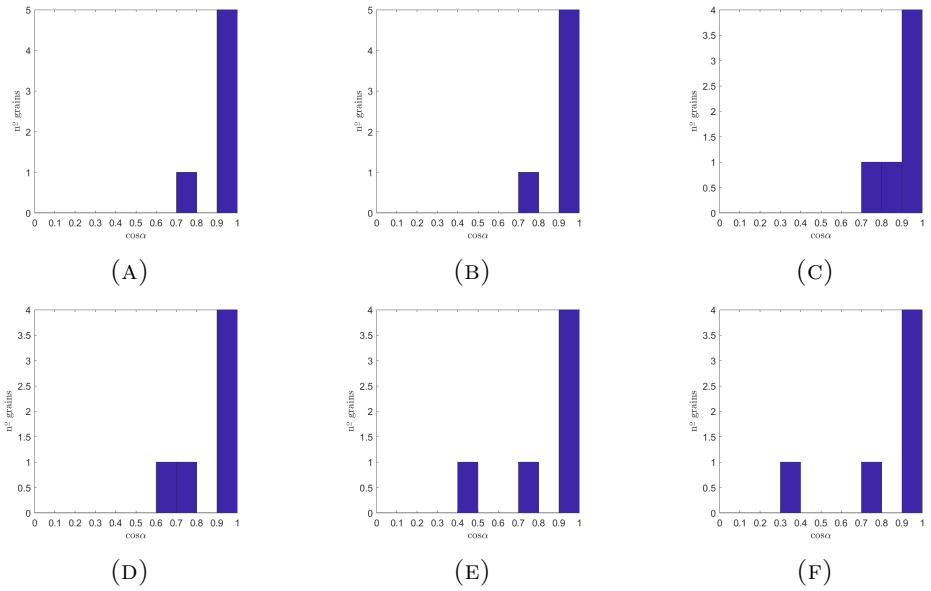

(A) (B) (C)

(D) (E) (F)

FIGURE B.10: Alignment with the nucleus. Set 89DP2

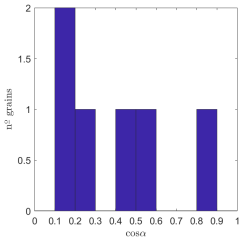

(A)

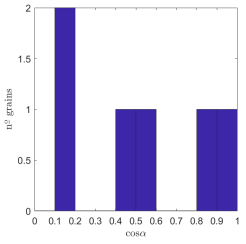

(B)

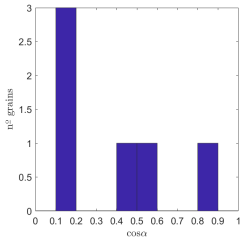

(C)

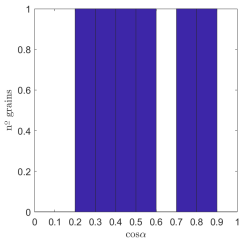

(D)

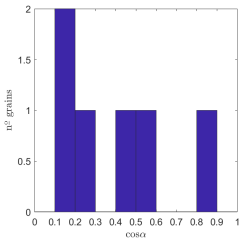

(E)

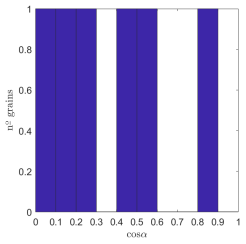

(F)

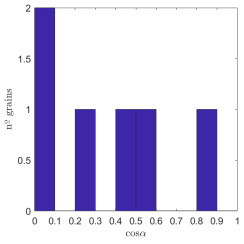

(G)

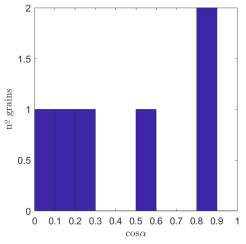

(H)

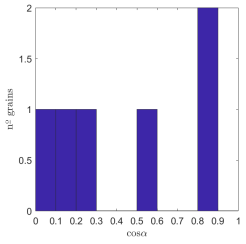

(I)

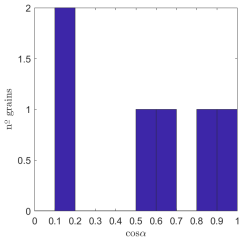

(J)

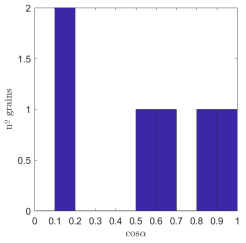

(K)

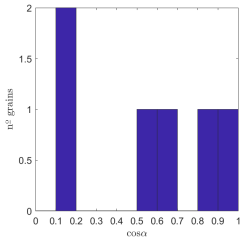

(L)

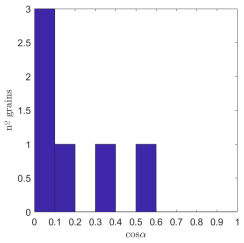

(M)

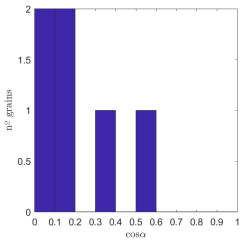

(N)

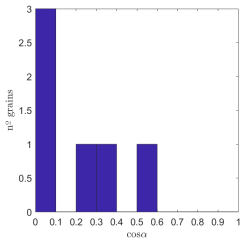

(O)

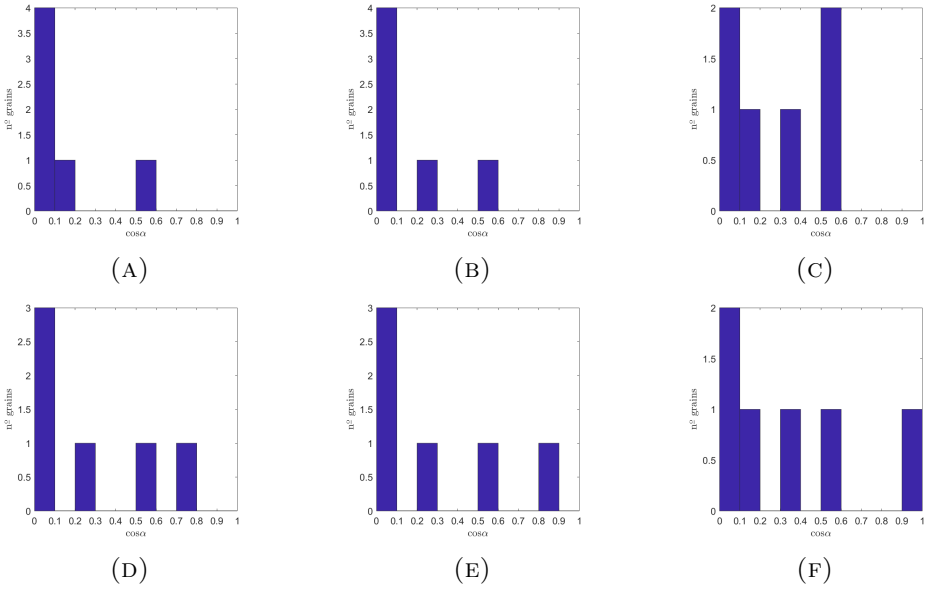

(A) (B) (C)

(D) (E) (F)

FIGURE B.12: Alignment with the Sun. Set 89DP2.

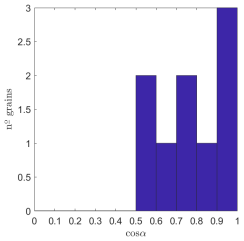

(A)

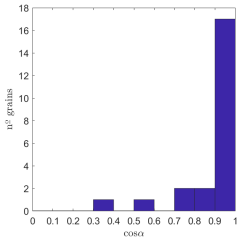

(B)

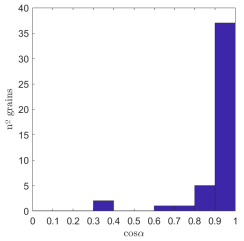

(C)

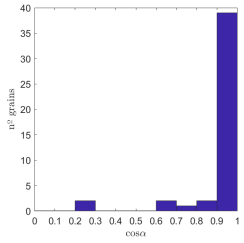

(D)

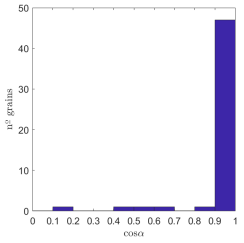

(E)

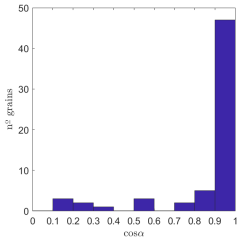

(F)

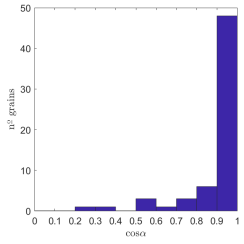

(G)

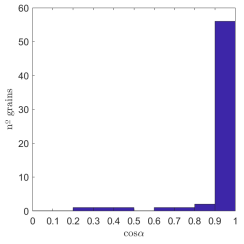

(H)

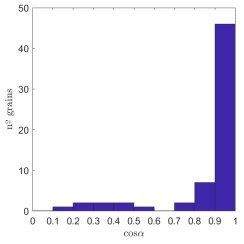

(I)

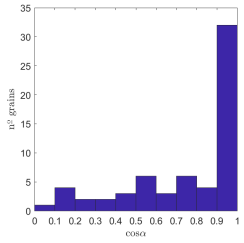

(J)

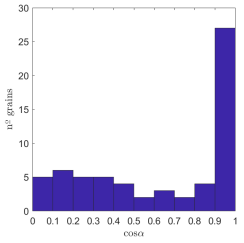

(K)

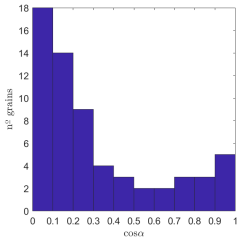

(L)

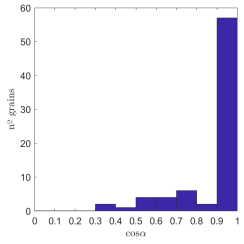

(M)

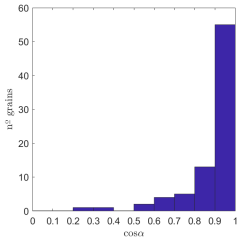

(N)

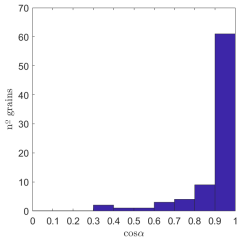

(O)

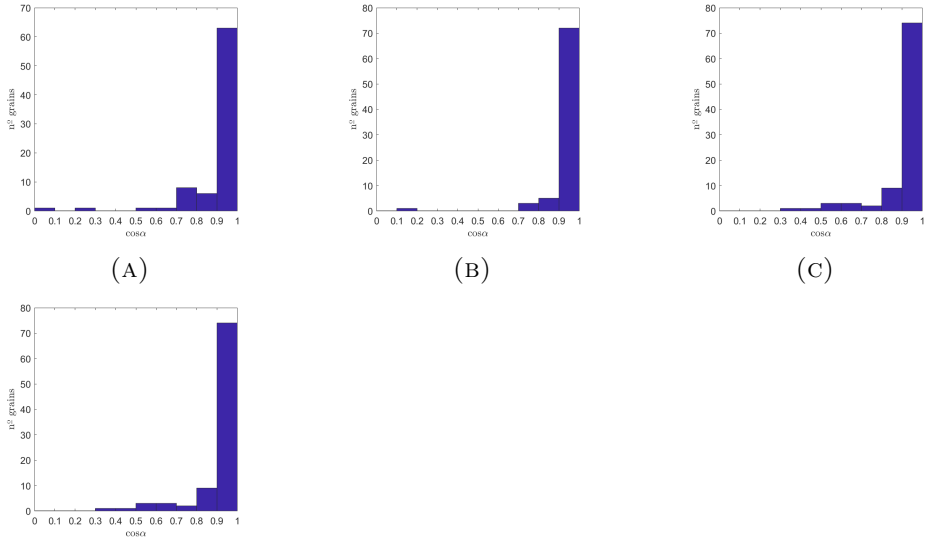

(A) (B) (C)

(D)

FIGURE B.14: Alignment with the nucleus. Set 89GC2.

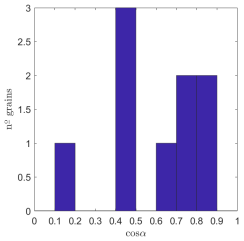

(A)

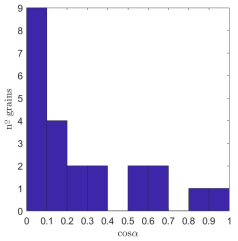

(B)

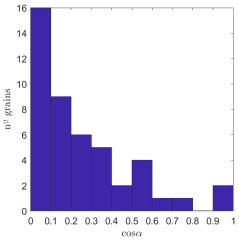

(C)

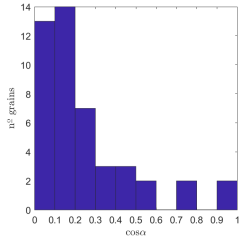

(D)

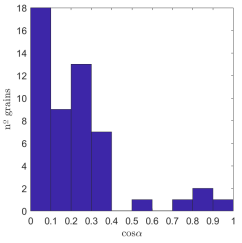

(E)

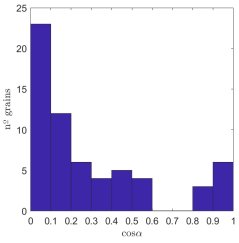

(F)

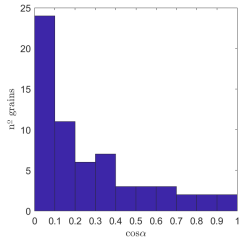

(G)

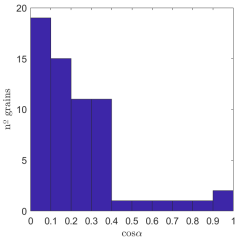

(H)

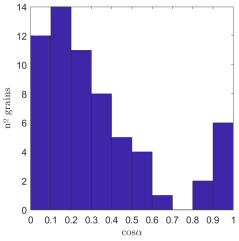

(I)

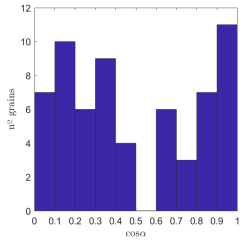

(J)

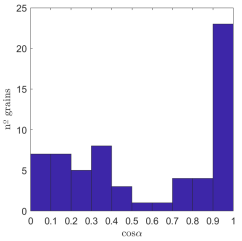

(K)

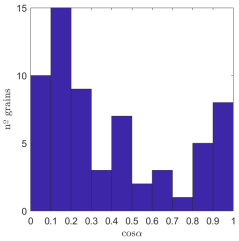

(L)

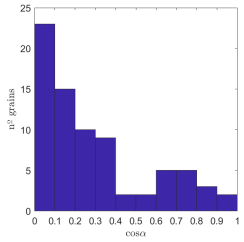

(M)

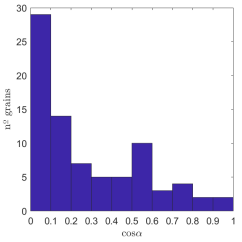

(N)

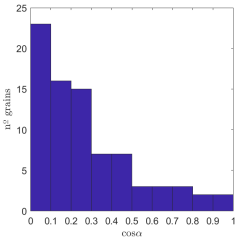

(O)

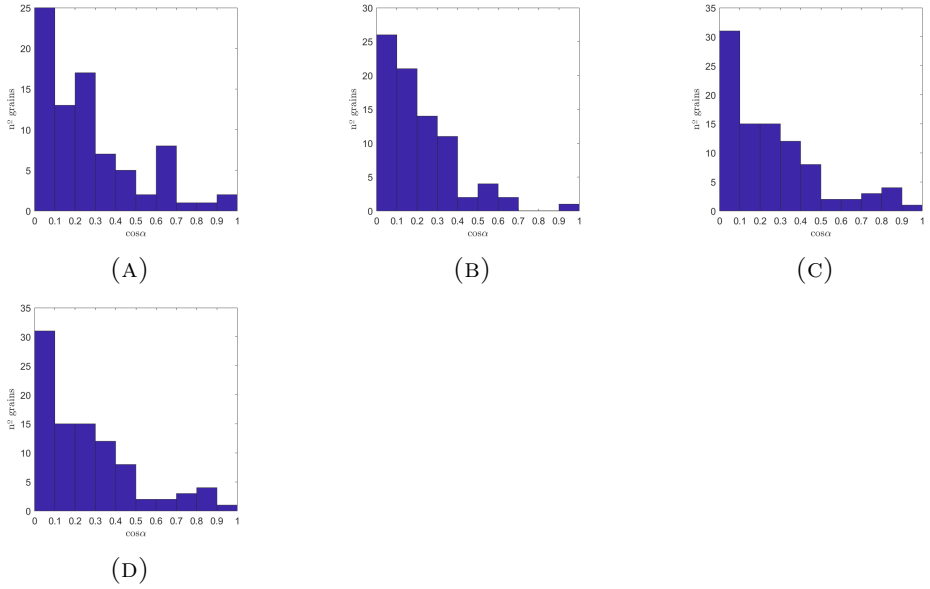

(A) (B) (C)

(D)

FIGURE B.16: Alignment with the Sun. Set 89GC2.

Appendix C

Rotational periods

In this Appendix we report the histogram of the rotational periods and their relative frequencies, related to each set of images analyzed in chapter 6.

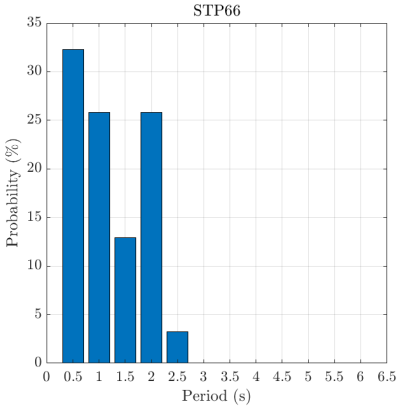

(A) 66

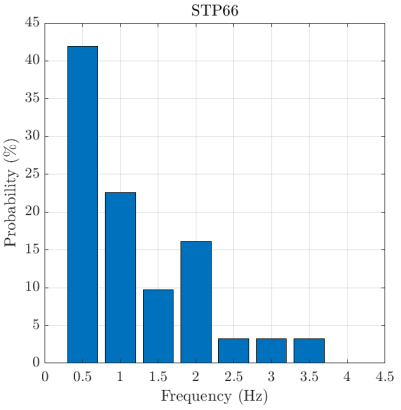

(B) 66

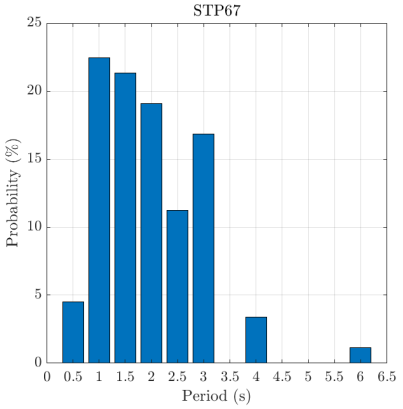

(C) 67

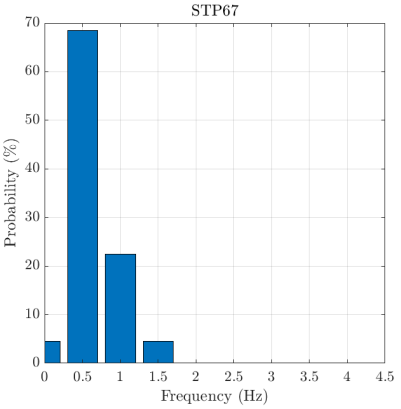

(D) 67

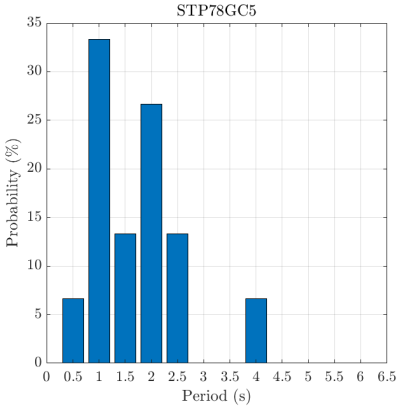

(E) 78

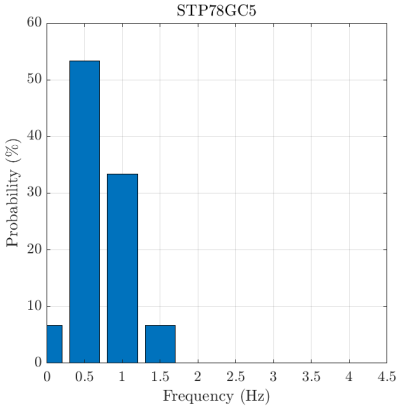

(F) 78

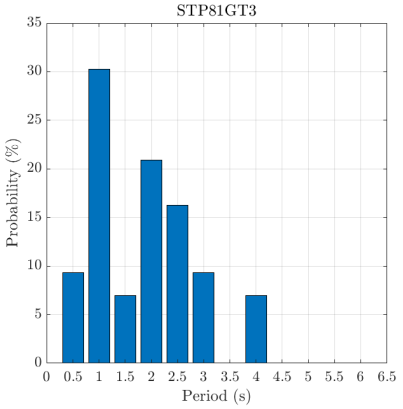

(G) 81

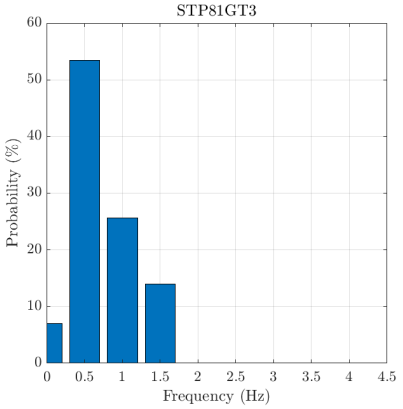

(H) 81

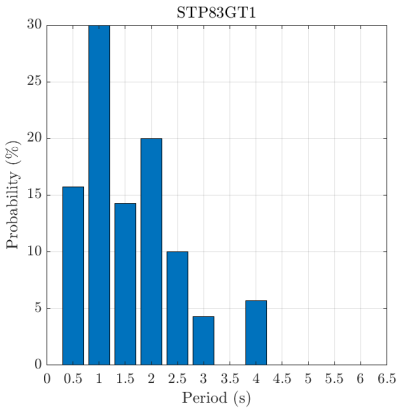

(I) 83

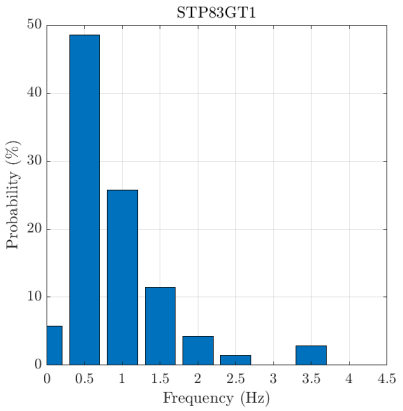

(J) 83

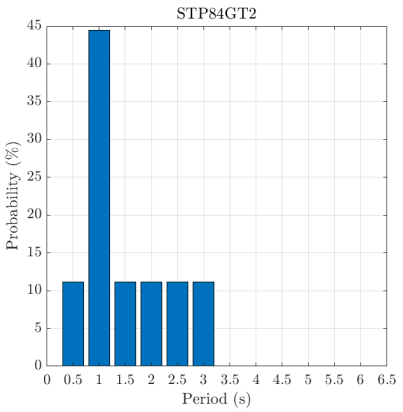

(K) 84

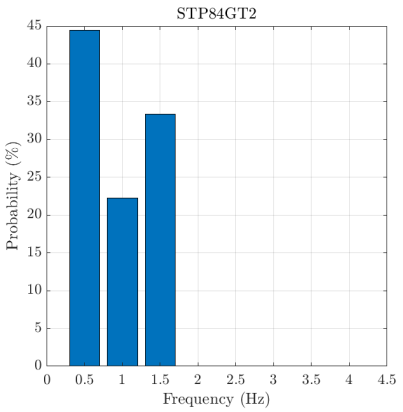

(L) 84

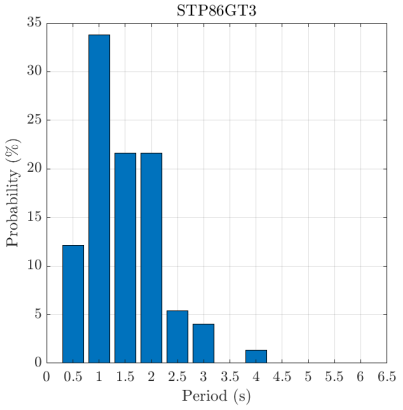

(M) 86

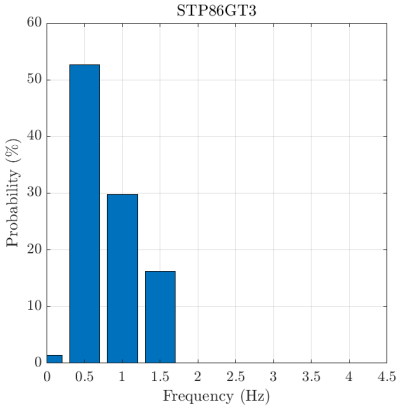

(N) 86

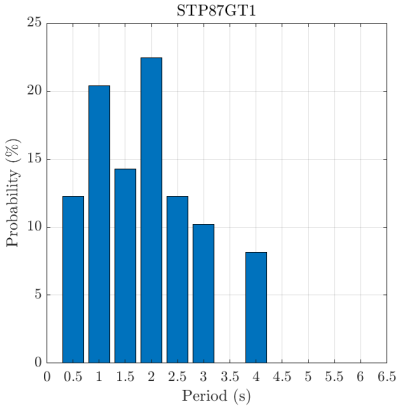

(O) 87

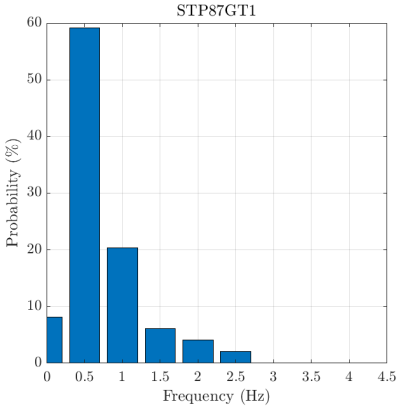

(P) 87

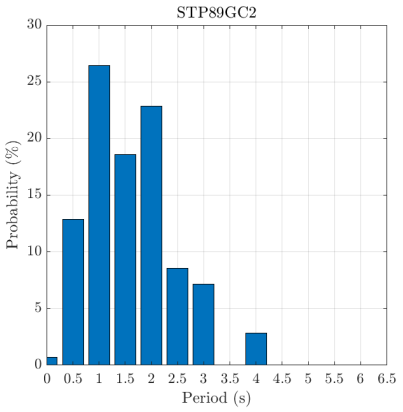

(Q) 89

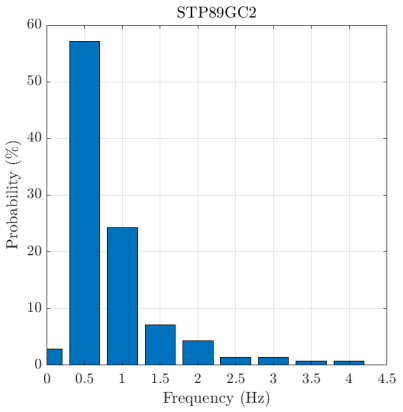

(R) 89

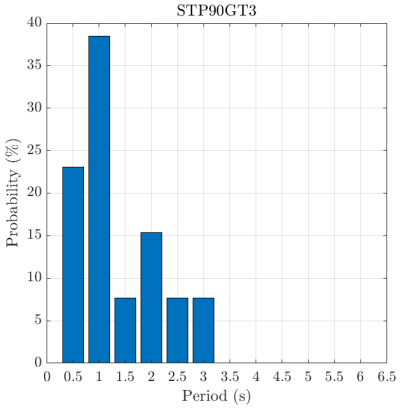

(S) 90

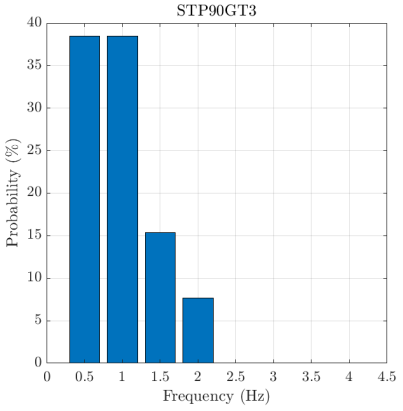

(T) 90

FIGURE C.1: The histograms show the rotational periods of the grains (left) and the relative frequencies (right).

Bibliography

Agarwal, J., A'Hearn, M. F., Vincent, J.-B., et al. 2016, ArXiv e-prints [[arXiv]1608.07933]

Altwegg, K., Balsiger, H., Bar-Nun, A., et al. 2015, Science, 347, 1261952

Altwegg, K., Balsiger, H., Bar-Nun, A., et al. 2016, Science Advances, 2, e1600285

Bagnulo, S., Cellino, A., & Sterzik, M. F. 2015, MNRAS, 446, L11

Bardyn, A., Baklouti, D., Cottin, H., et al. 2017, MNRAS, 469, S712

Barucci, M. A., Filacchione, G., Fornasier, S., et al. 2016, ArXiv e-prints [[arXiv]1609.00551]

Belskaya, I., Fornasier, S., Tozzi, G. P., et al. 2017, European Planetary Science Congress, 11, EPSC2017

Bertini, I. 2011, Planet. Space Sci., 59, 365

Bertini, I., La Forgia, F., & Fulle, M. in prep.

Bertini, I., La Forgia, F., Tubiana, C., et al. 2017, MNRAS, 469, S404

Bertini, I., Thomas, N., & Barbieri, C. 2007, A&A, 461, 351

Bieler, A., Altwegg, K., Balsiger, H., et al. 2015, Nature, 526, 678

Biermann, L. 1951, ZAp, 29, 274

Blum, J. 2018, Space Sci. Rev., 214, 52

Blum, J., Gundlach, B., Mühle, S., & Trigo-Rodriguez, J. M. 2014, Icarus, 235, 156

Blum, J. & Münch, M. 1993, Icarus, 106, 151

Blum, J. & Wurm, G. 2008, ARA&A, 46, 21

Brassé, C. 2014, University Paris Est Créteil

Brassé, C., Buch, A., Coll, P., & Raulin, F. 2017, Astrobiology, 17, 8

Brassé, C., Muñoz, O., Coll, P., & Raulin, F. 2015, Planet. Space Sci., 109, 159

Brearley, A. J. & Jones, R. H. 1998, Chondritic meteorites, ed. J. J. Papike, 3–36

Cellino, A., Bagnulo, S., Gil-Hutton, R., et al. 2016, MNRAS, 455, 2091

Cellino, A., Bagnulo, S., Tanga, P., Novaković, B., & Delbò, M. 2014, MNRAS, 439, L75

Cellino, A., Belskaya, I. N., Bendjoya, P., et al. 2006, Icarus, 180, 565

Chen, J. H. & Wasserburg, G. J. 1981, Earth and Planetary Science Letters, 52, 1

Ciarletti, V., Herique, A., Lasue, J., et al. 2017, MNRAS, 469, S805

Clarke, Jr., R. S. 1970, Meteoritics, 5, 189

Clemett, S. J., Nakamura-Messenger, K., McKay, D. S., & Sandford, S. A. 2007, in Lunar and Planetary Inst. Technical Report, Vol. 38, Lunar and Planetary Science Conference, 2091

Combe, J.-P., Singh, S., Johnson, K. E., et al. 2017, in Lunar and Planetary Inst. Technical Report, Vol. 48, Lunar and Planetary Science Conference, 2849

Combi, M. R., Harris, W. M., & Smyth, W. H. 2004, Gas dynamics and kinetics in the cometary coma: theory and observations, ed. M. C. Festou, H. U. Keller, & H. A. Weaver, 523–552

Cremonese, G., Boehnhardt, H., Crovisier, J., et al. 1997, ApJ, 490, L199

Cremonese, G., Borin, P., Martellato, E., Marzari, F., & Bruno, M. 2012, ApJ, 749, L40

Cremonese, G., Simioni, E., Ragazzoni, R., et al. 2016, A&A, 588, A59

Crifo, J.-F., Loukianov, G. A., Rodionov, A. V., & Zakharov, V. V. 2005, Icarus, 176, 192

Crifo, J. F., Lukianov, G. A., Rodionov, A. V., Khanlarov, G. O., & Zakharov, V. V. 2002, Icarus, 156, 249

Crovisier, J., Leech, K., Bockelee-Morvan, D., et al. 1997, Science, 275, 1904

Davidsson, B. J. R., Gutiérrez, P. J., Sierks, H., et al. 2015, A&A, 583, A16

Davidsson, B. J. R., Sierks, H., Güttler, C., et al. 2016, A&A, 592, A63

DeMeo, F. & Binzel, R. P. 2008, Icarus, 194, 436

DeMeo, F. E. & Carry, B. 2013, Icarus, 226, 723

Deshapriya, J. D. P., Barucci, M. A., Fornasier, S., et al. 2018, A&A, 613, A36

Devogèle, M., Tanga, P., Cellino, A., et al. 2018, Icarus, 304, 31

Dorschner, J., Begemann, B., Henning, T., Jaeger, C., & Mutschke, H. 1995, A&A, 300, 503

Draine, B. T. & Flatau, P. J. 2000, ArXiv Astrophysics e-prints [astro-ph/0008151]

Duda, R. O. & Hart, P. E. 1973, New York: Wiley

El-Maarry, M. R., Thomas, N., Giacomini, L., et al. 2015, A&A, 583, A26

Elsila, J. E., Glavin, D. P., & Dworkin, J. P. 2009, Meteoritics and Planetary Science, 44, 1323

Escobar-Cerezo, J., Muñoz, O., Moreno, F., et al. 2018, ApJS, 235, 19

Escobar-Cerezo, J., Palmer, C., Muñoz, O., et al. 2017, ApJ, 838, 74

Feldman, P. D., A'Hearn, M. F., Feaga, L. M., et al. 2016, ApJ, 825, L8

Fernandez, J. A. 1980, MNRAS, 192, 481

Festou, M. C. 1981, A&A, 95, 69

Festou, M. C., Keller, H. U., & Weaver, H. A. 2004, Comets II

Fink, U. & Rinaldi, G. 2015, Icarus, 257, 9

Fornasier, S., Hasselmann, P. H., Barucci, M. A., et al. 2015, A&A, 583, A30

Fornasier, S., Mottola, S., Keller, H. U., et al. 2016, Science, 354, 1566

Frattin, E., Cremonese, G., Simioni, E., et al. 2017, MNRAS, 469, S195

Frattin, E., Munoz, O., Moreno, F., et al. 2018, submitted

Fray, N., Bardyn, A., Cottin, H., et al. 2017, MNRAS, 469, S506

Fulle, M., Altobelli, N., Buratti, B., et al. 2016a, MNRAS, 462, S2

Fulle, M. & Blum, J. 2017, MNRAS, 469, S39

Fulle, M., Della Corte, V., Rotundi, A., et al. 2016b, MNRAS, 462, S132

Fulle, M., Della Corte, V., Rotundi, A., et al. 2015a, ApJ, 802, L12

Fulle, M., Ivanovski, S. L., Bertini, I., et al. 2015b, A&A, 583, A14

Fulle, M., Leblanc, F., Harrison, R. A., et al. 2007, ApJ, 661, L93

Fulle, M., Marzari, F., Della Corte, V., et al. 2016c, ApJ, 821, 19

Gicquel, A., Vincent, J.-B., Agarwal, J., et al. 2016, MNRAS[[arXiv]1608.08774]

Gladstone, e. a. 2016, Science, 351, aad8866

Gombosi, T. I., Cravens, T. E., & Nagy, A. F. 1985, ApJ, 293, 328

Gooding, J. L., Keil, K., Fukuoka, T., & Schmitt, R. A. 1980, Earth and Planetary Science Letters, 50, 171

Grossman, J. N. 1999, Meteoritics and Planetary Science Supplement, 34, 169

Guettler, C. in prep.

Hadamcik, E., Levasseur-Regourd, A. C., Hines, D. C., et al. 2016, MNRAS, 462, S507

Hallis, L. J. 2017, Philosophical Transactions of the Royal Society of London Series A, 375, 20150390

Hanner, M. S. & Bradley, J. P. 2004, Composition and mineralogy of cometary dust, ed. M. C. Festou, H. U. Keller, & H. A. Weaver, 555–564

Hanner, M. S. & Campins, H. 1986, Icarus, 67, 51

Hansen, J. E. & Travis, L. D. 1974a, Space Sci. Rev., 16, 527

Hansen, J. E. & Travis, L. D. 1974b, Space Sci. Rev., 16, 527

Hansen, K. C., Altwegg, K., Berthelier, J.-J., et al. 2016, MNRAS, 462, S491

Hapke, B. 2012, Theory of Reflectance and Emittance Spectroscopy, ed. Cambrige

Hasenkopf, C. A., Beaver, M. R., Trainer, M. G., et al. 2010, Icarus, 207, 903

Haser, L. 1957, Bulletin de la Societe Royale des Sciences de Liege, 43, 740

Hässig, M., Altwegg, K., Balsiger, H., et al. 2015, Science, 347, aaa0276

Hörz, F., Bastien, R., Borg, J., et al. 2006, Science, 314, 1716

Hovenier, J. W. & Guirado, D. 2014, J. Quant. Spectr. Rad. Transf., 133, 596

Hsieh, H. H. & Jewitt, D. 2006, Science, 312, 561

Hsieh, H. H., Jewitt, D. C., & Fernández, Y. R. 2004, AJ, 127, 2997

Huebner, W. F. 1990, Physics and Chemistry of Comets, ed. S.-V. B. H. Dr. Walter F. Huebner

Hviid, S. F. 2010

Irvine, W. M., Leschine, S. B., & Schloerb, F. P. 1980, Nature, 283, 748

Ishiguro, M., Yang, H., Usui, F., et al. 2013, ApJ, 767, 75

Ivanovski, S. L., Della Corte, V., Rotundi, A., et al. 2017a, MNRAS, 469, S774

Ivanovski, S. L., Zakharov, V. V., Della Corte, V., et al. 2017b, Icarus, 282, 333

Jenniskens, P., Blake, D. F., & Kouchi, A. 1998, in Astrophysics and Space Science Library, Vol. 227, Solar System Ices, ed. B. Schmitt, C. de Bergh, & M. Festou, 139

Jewitt, D., Chizmadia, L., Grimm, R., & Prialnik, D. 2007, Protostars and Planets V, 863

Jewitt, D. & Luu, J. 1993, Nature, 362, 730

Jewitt, D. & Meech, K. J. 1986, ApJ, 310, 937

Johansen, A. & Youdin, A. 2007, ApJ, 662, 627

Jorda, L., Gaskell, R., Capanna, C., et al. 2016, Icarus, 277, 257

Jost, B., Pommerol, A., Poch, O., et al. 2017, Planet. Space Sci., 148, 1

Keeney, B. A., Stern, S. A., A'Hearn, M. F., et al. 2017, MNRAS, 469, S158

Keller, H. U., Barbieri, C., Lamy, P., et al. 2007, Space Sci. Rev., 128, 433

Keller, H. U., Britt, D., Buratti, B. J., & Thomas, N. 2004, In situ observations of cometary nuclei, ed. M. C. Festou, H. U. Keller, & H. A. Weaver, 211–222

Kelley, M. S., Lindler, D. J., Bodewits, D., et al. 2013, Icarus, 222, 634

Kimura, H., Kolokolova, L., Li, A., & Lebreton, J. 2016, ArXiv e-prints [[arXiv]1603.03123]

Kissel, J. & Krueger, F. R. 1987a, Nature, 328, 117

Kissel, J. & Krueger, F. R. 1987b, Nature, 326, 755

Kofman, W., Herique, A., Barbin, Y., et al. 2015, Science, 349

Kolokolova, L., Hanner, M. S., Levasseur-Regourd, A.-C., & Gustafson, B. Å. S. 2004, Physical properties of cometary dust from light scattering and thermal emission, ed. M. C. Festou, H. U. Keller, & H. A. Weaver, 577–604

Kowal, C. T., Liller, W., & Marsden, B. G. 1979, in IAU Symposium, Vol. 81, Dynamics of the Solar System, ed. R. L. Duncombe, 245–250

Kramer, T. & Noack, M. 2015, ApJ, 813, L33

Krot, A. N., Petaev, M. I., Scott, E. R. D., et al. 1998, Meteoritics and Planetary Science, 33, 1065

Krot, A. N., Scott, E. R. D., & Zolensky, M. E. 1995, Meteoritics, 30, 748

La Forgia, F., Giacomini, L., Lazzarin, M., et al. 2015, A&A, 583, A41

Lai, I.-L., Su, C.-C., Ip, W.-H., et al. 2016, in EGU General Assembly Conference Abstracts, Vol. 18, EGU General Assembly Conference Abstracts, 3655

Langevin, Y., Hilchenbach, M., Ligier, N., et al. 2016, Icarus, 271, 76

Lee, T., Papanastassiou, D. A., & Wasserburg, G. J. 1976, Geophys. Res. Lett., 3, 41

Levasseur-Regourd, A.-C., Agarwal, J., Cottin, H., et al. 2018, Space Sci. Rev., 214, 64

Levasseur-Regourd, A. C., Hadamcik, E., & Renard, J. B. 1996, A&A, 313, 327

Levison, H. F. 1996, in Astronomical Society of the Pacific Conference Series, Vol. 107, Completing the Inventory of the Solar System, ed. T. Rettig & J. M. Hahn, 173–191

Lisse, C. M., Kraemer, K. E., Nuth, J. A., Li, A., & Joswiak, D. 2007, Icarus, 187, 69

Liu, J., Yang, P., & Muinonen, K. 2015, J. Quant. Spectr. Rad. Transf., 161, 136

Liu, L., Mishchenko, M. I., Hovenier, J. W., Volten, H., & Muñoz, O. 2003, J. Quant. Spectr. Rad. Transf., 79, 911

Lugaro, M. 2007, in Proceedings of the International Meteor Conference, 25th IMC, Roden, Netherlands, 2006, ed. F. Bettonvil & J. Kac, 146–153

Maas, R. W., Ney, E. P., & Woolf, N. J. 1970, ApJ, 160, L101

Mackowski, D. W. & Mishchenko, M. I. 1996, J. Opt. Soc. Am. A, 13, 2266

Mahnes, G., Göpel, C., & Allégre, C. J. 1987, Meteoritics, 22, 453

Mannel, T., Bentley, M. S., Schmied, R., et al. 2016, MNRAS, 462, S304

Massironi, M., Simioni, E., Marzari, F., et al. 2015, Nature, 526, 402

McSween, Jr., H. Y. 1977, Geochim. Cosmochim. Acta, 41, 477

Meech, K. J. & Svoren, J. 2004, Using cometary activity to trace the physical and chemical evolution of cometary nuclei, ed. M. C. Festou, H. U. Keller, & H. A. Weaver, 317–335

Merouane, S., Stenzel, O., Hilchenbach, M., et al. 2017, MNRAS, 469, S459

Mishchenko, M. I., Travis, L. D., & Macke, A. 2000, T-Matrix Method and Its Applications, ed. M. I. Mishchenko, J. W. Hovenier, & L. D. Travis, 147

Morbidelli, A. & Brown, M. E. 2004, The kuiper belt and the primordial evolution of the solar system, ed. M. C. Festou, H. U. Keller, & H. A. Weaver, 175–191

Moreno, F., Licandro, J., Ortiz, J. L., et al. 2011, ApJ, 738, 130

Moreno, F., Muñoz, O., Gutiérrez, P. J., et al. 2017, MNRAS, 469, S186

Muñoz, O., Moreno, F., Guirado, D., et al. 2012, J. Quant. Spectr. Rad. Transf., 113, 565

Muñoz, O., Moreno, F., Guirado, D., et al. 2010, J. Quant. Spectr. Rad. Transf., 111, 187

Muñoz, O., Moreno, F., Guirado, D., et al. 2011, Icarus, 211, 894

Muñoz, O., Moreno, F., Vargas-Martín, F., et al. 2017, ApJ, 846, 85

Muñoz, O., Volten, H., de Haan, J. F., Vassen, W., & Hovenier, J. W. 2000, A&A, 360, 777

Muñoz, O., Volten, H., & Hovenier, J. W. 2002, Electromagnetic and Light Scattering by Nonspherical Particle, 227

Muinonen, K., Mishchenko, M. I., Dlugach, J. M., et al. 2012, ApJ, 760, 118

Muinonen, K. & Saarinen, K. 2000, J. Quant. Spectr. Rad. Transf., 64, 201

Nesvorný, D., Vokrouhlický, D., Dones, L., et al. 2017, ApJ, 845, 27

Oklay, N., Vincent, J.-B., Fornasier, S., et al. 2016, A&A, 586, A80

Oort, J. H. 1950, Bull. Astron. Inst. Netherlands, 11, 91

Ott, T., Drolshagen, E., Koschny, D., et al. 2017, MNRAS, 469, S276

Patashnick, H. 1974, Nature, 250, 313

Penasa, L., Massironi, M., Naletto, G., et al. 2017, MNRAS, 469, S741

Poch, O., Pommerol, A., Jost, B., et al. 2016a, Icarus, 266, 288

Poch, O., Pommerol, A., Jost, B., et al. 2016b, Icarus, 266, 288

Poch, O., Pommerol, A., Jost, B., et al. 2016c, Icarus, 267, 154

Pommerol, A., Thomas, N., El-Maarry, M. R., et al. 2015, A&A, 583, A25

Poppe, T., Blum, J., & Henning, T. 2000, ApJ, 533, 454

Prialnik, D. 1997, Earth Moon and Planets, 77, 223

Prialnik, D., Benkhoff, J., & Podolak, M. 2004, Modeling the structure and activity of comet nuclei, ed. M. C. Festou, H. U. Keller, & H. A. Weaver, 359–387

Prior, G. T. 1920, Mineralogical Magazine, 19, 51

Purcell, E. M. & Pennypacker, C. R. 1973, ApJ, 186, 705

Rawle, A. F. 1993, The Basic Principles of Particle Size Analysis

Reinhard, R. 1986, Nature, 321, 313

Richard Norton, O. 2002, The Cambrige Encyclopedia of Meteorites, ed. C. U. Press

Rickman, H. 2017, Origin and evolution of comets

Robert, F. 2006, Solar System Deuterium/Hydrogen Ratio, ed. D. S. Lauretta & H. Y. McSween, 341–351

Rosenbush, V. K., Ivanova, O. V., Kiselev, N. N., Kolokolova, L. O., & Afanasiev, V. L. 2017, MNRAS, 469, S475

Rotundi, A., Baratta, G. A., Borg, J., et al. 2008, Meteoritics and Planetary Science, 43, 367

Rotundi, A., Ferrini, G., Baratta, G. A., et al. 2007, Dust in Planetary Systems, 643, 149

Rotundi, A., Rietmeijer, F. J. M., Ferrari, M., et al. 2014, Meteoritics and Planetary Science, 49, 550

Rotundi, A., Sierks, H., Della Corte, V., et al. 2015, Science, 347, aaa3905

Rubin, A. E. 1997, Meteoritics and Planetary Science, 32

Sagan, C. & Khare, B. N. 1979, Nature, 277, 102

Sagdeev, R. Z., Szabo, F., Avanesov, G. A., et al. 1986, Nature, 321, 262

Schloerb, F. P., Keihm, S., von Allmen, P., et al. 2015, A&A, 583, A29

Schmitt, B., Espinasse, S., Grim, R. J. A., Greenberg, J. M., & Klinger, J. 1989, in ESA Special Publication, Vol. 302, Physics and Mechanics of Cometary Materials, ed. J. J. Hunt & T. D. Guyenne

Schulze, H., Kissel, J., & Jessberger, E. K. 1997, in Astronomical Society of the Pacific Conference Series, Vol. 122, From Stardust to Planetesimals, ed. Y. J. Pendleton, 397

Shestopalov, D. I. & Golubeva, L. F. 2017, Advances in Space Research, 59, 2658

Shkuratov, Y., Bondarenko, S., Kaydash, V., et al. 2007, J. Quant. Spectr. Rad. Transf., 106, 487

Shkuratov, Y., Bondarenko, S., Ovcharenko, A., et al. 2006, J. Quant. Spectr. Rad. Transf., 100, 340

Shkuratov, Y., Ovcharenko, A., Zubko, E., et al. 2004, J. Quant. Spectr. Rad. Transf., 88, 267

Sierks, H., Barbieri, C., Lamy, P. L., et al. 2015, Science, 347, aaa1044

Skorov, Y., Reshetnyk, V., Lacerda, P., Hartogh, P., & Blum, J. 2016, MNRAS, 461, 3410

Skorov, Y., Reshetnyk, V., Rezac, L., et al. 2018, MNRAS, 477, 4896

Soderblom, L. A., Becker, T. L., Bennett, G., et al. 2002, Science, 296, 1087

Swamy, K. 2010a, Origin, ed. W. S. P. C. P. L. Jayant V. Narlikar, 381–399

Swamy, K. 2010b, Physics of comets, ed. W. S. P. C. P. L. Jayant V. Narlikar

Tancredi, G., Rickman, H., & Greenberg, J. M. 1994, A&A, 286, 659

Thomas, N., Davidsson, B., El-Maarry, M. R., et al. 2015, A&A, 583, A17

Tubiana, C., Güttler, C., Kovacs, G., et al. 2015, A&A, 583, A46

Van de Hulst, H. C. 1957, Light scattering by small particles, ed. I. N. Y. Dover Publications

van de Hulst, H. C. 1957, Light Scattering by Small Particles

Van Schmus, W. R. & Wood, J. A. 1967, Geochim. Cosmochim. Acta, 31, 747

Volten, H., Muñoz, O., Brucato, J. R., et al. 2006, J. Quant. Spectr. Rad. Transf., 100, 429

Volten, H., Muñoz, O., Hovenier, J. W., et al. 2007, A&A, 470, 377

Weidenschilling, S. J. 1977, MNRAS, 180, 57

Weisberg, M. K., McCoy, T. J., & Krot, A. N. 2006, Systematics and Evaluation of Meteorite Classification, ed. D. S. Lauretta & H. Y. McSween, 19–52

Weissman, P. 1991, Nature, 353, 793

Weissman, P. R. & Lowry, S. C. 2008, Meteoritics and Planetary Science, 43, 1033

Whipple, F. L. 1950, ApJ, 111, 375

Whipple, F. L. & Stefanik, R. P. 1965, SAO Special Report, 182

Zubko, E. 2015, Optics Letters, 40, 1204

Zubko, E., Kimura, H., Shkuratov, Y., et al. 2009, J. Quant. Spectr. Rad. Transf., 110, 1741

Zubko, E., Videen, G., Hines, D. C., & Shkuratov, Y. 2016, Planet. Space Sci., 123, 63

Zubko, E., Videen, G., & Shkuratov, Y. 2015, J. Quant. Spectr. Rad. Transf., 151, 38

Zubko, E., Videen, G., Shkuratov, Y., Muinonen, K., & Yamamoto, T. 2011, Icarus, 212, 403

Zubko, E., Videen, G., Zubko, N., & Shkuratov, Y. 2017, J. Quant. Spectr. Rad. Transf., 190, 1

Zubko, E., Videen, G., Zubko, N., & Shkuratov, Y. 2018, MNRAS